Development of Iron-based Oxyfluoride Cathodes for High Energy Density All-Solid-State Fluoride-ion Batteries

Yanchang Wang

Development of Iron-based Oxyfluoride Cathodes for High Energy Density All-Solid-State Fluoride-ion Batteries

Yanchang Wang

Graduate School of Human and Environmental Studies

Kyoto University

Supervised by

Prof. Dr. Yoshiharu Uchimoto

Contents

Chapter 1 General introduction

1.1 Background

Since primitive humans first used fire, energy has been a necessary resource for human survival. From the 17th century to the present, mankind has undergone two major transitions in the choice of energy sources: wood to coal, and coal to petroleum, each of which has been an increase in energy density. From the age of steam to the age of electrification, the switch in energy sources has been made throughout the three recent industrial revolutions, but with them came serious environmental problems such as the London smog incident.[1]

With the development of society and the advancement of globalization, the increasing carbon emissions have caused serious global environmental problems. International Energy Agency (IEA) data shows that the global transportation industry is the second largest emitting industry in the world, accounting for 25% of CO_2 emissions, increasing year by year.[1] Specifically, within the transport sector, road transport accounts for 75% of the industry's carbon emissions, shipping and water transport for 11%, and railroads for 3%. The world's energy development is entering a new historical period, and the third major shift from traditional fossil energy sources to new and clean energy sources has become inevitable in order to achieve sustainable social development. On December 12, 2015, 195 member states of the United Nations adopted the Paris Agreement at the 2015 United Nations Climate Change Conference[2], expecting to work together to curb global warming trends. According to the Paris Agreement, the concord countries will make finance flows consistent with a pathway towards low greenhouse gas emissions and climate-resilient development, including the introduction of policies to limit the growth of fuel vehicles and accelerate the transition to electrification, which has greatly contributed to the development of electric vehicles (EVs) and their related industries.[2]

At the present stage, EVs are mainly driven by lithium-ion secondary batteries.[3] Although Toyota Motor Corporation and other companies have introduced fuel cell electric vehicles (FCEVs), the current market share is small due to the production and storage of hydrogen resource. Lithium-ion batteries (LIBs) were first successfully commercialized by Sony in 1991.[4] Compared with lead-acid and nickel-hydrogen secondary batteries, which were widely used in the past, lithium-ion batteries have higher operating voltage, charging and discharging capacity and cycle life, and are currently the most suitable energy supply system for electric vehicles. As electric vehicle production surges, LIBs production also grows from about 64 GWh in 2016 to 631 GWh in 2022, and by 2030, global production will approach 3,000 GWh (Figure 1).[5]

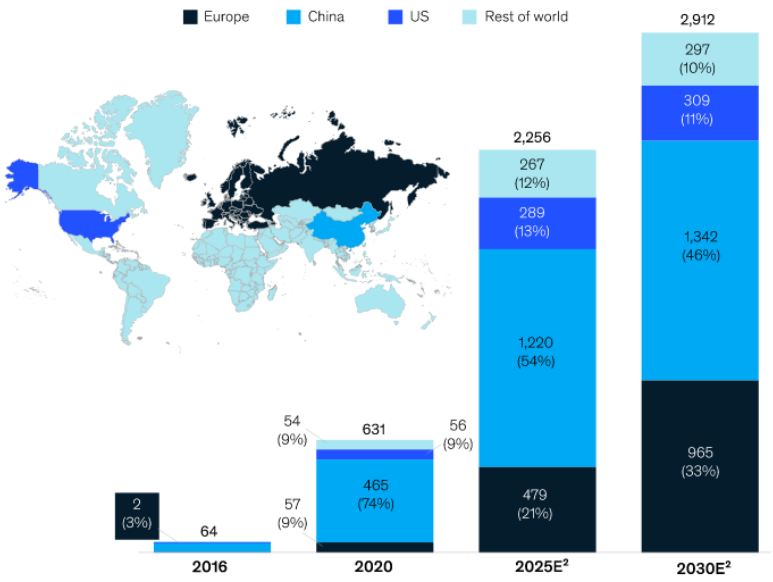

Figure 1.1 Battery cell production capacity, GWh annually.[5]

Although LIBs virtually rule the power battery market now, it still has some pain points that are difficult to solve. First of all, the energy density of the existing cathode material under working conditions is not ideal, and the energy density of most package batteries lands in the range of 220 ~ 250Wh kg^{-1}, causing mileage anxiety as a power battery for EVs.[3] This leads to the current EVs temporarily dominated by personal consumption, and the share in production and transportation is almost negligible. Although many new LIBs cathode materials are continuously developed (such as

lithium-excess cathode materials), they still cannot meet the demand for energy density of EVs. Second, commercial LIBs also face a series of safety problems.[6] Since the organic electrolyte used is flammable, there is a risk of explosion after overcharging and collision. And the lithium dendrites generated during the charging and discharging process can also lead to a short circuit in the battery, resulting in thermal runaway problem. Finally, due to the uneven distribution of lithium, cobalt and nickel mines, prices and supply are probably affected by geopolitics.[7] Therefore, limited by the above-mentioned points, LIBs may be difficult to support the sustainable development of power batteries.

In recent years, researchers have tried to improve the energy density of packed LIBs by making them all-solid state, and the use of solid-state electrolytes can also solve the flammability problem caused by organic electrolytes, however, the problem of lithium dendrites still exists in all-solid-state LIBs.[8, 9] Therefore, other researchers have introduced a new battery concept based on the operating principle of LIBs using ions other than Li-ion as carriers, including cations such as Na^+, K^+, Ca^{2+}, Mg^{2+}, Zn^{2+}, Al^{3+}, and even anions such as F^-, Cl^-.[10-20] Among them, fluoride ion batteries (FIBs) show great potential for applications in terms of energy/power density and safety.[12] Due to the highest electronegativity of fluorine and the high redox potential of F^-/F_2, fluoride ion exhibits high electrochemical stability, which allows the utilization of cathode materials with higher potentials for FIBs. Through the multi-electron reaction during charge and discharge, fluorine ion batteries can achieve higher energy density than traditional LIBs. Furthermore, it means that metal anodes can be used because the movable ions are anions and dendrite growth does not occur. A challenge that must be solved for current FIBs is the development of high-capacity cathodes.

In this thesis, we systematically investigated the cathode materials having high-capacities for all-solid-state FIBs: from the basic metal/metal fluoride conversion-type electrodes to the intercalation-type electrodes with layered structure, and studied their reaction mechanisms such as charge compensation, crystal changes, etc. during the (de)fluorination process. Since FIBs are developed based on the operating principle of

LIBs, in the remainder of this chapter, the operating principle of LIBs will first be discussed. This will be followed by an introduction to the concept of the FIBs, their development to date, and issues for continued improvement. Finally, the other chapters of the thesis will be outlined and the motivation for starting each work will also be briefly introduced.

1.2 Lithium-ion batteries

In order to design materials for FIBs, it is demanding to know the working principle of lithium-ion batteries, which are currently the most energy dense batteries. The technology to use LIBs was proposed in 1976 by Professor M. S. Whittingham, then a technician at Exxon.[21] Using TiS_2 as the cathode material and Li as the anode material, a chemical to electrical energy conversion was achieved by the single-phase reaction (Equation 1-1).[21]

$$x\mathrm{Li} + \mathrm{TiS_2} \rightarrow \mathrm{Li}_x\mathrm{TiS_2} \tag{1-1}$$

In 1980, Professor J. B. Goodenough expanded on Professor M. S. Whittingham's previous research and proposed the use of $LiCoO_2$ as the cathode material[22], and the following year, in collaboration with Professor A. Yoshino, proposed the combination of $LiCoO_2$ cathode and polyacetylene cathode, laying the foundation for the commercialization of LIBs as secondary batteries[23]. For their outstanding contributions to the field of lithium-ion batteries, the three professors were awarded the Nobel Prize in Chemistry in 2019.

1.2.1 Working principle of lithium-ion batteries

LIBs, also known as rocking chair batteries, are charged and discharged by shuttling lithium ions (charge carrier) between the cathode and anode.[24] When a LIB is located in an external circuit containing a load, the Li^+ are driven by the potential difference between the cathode and anode to detach from the cathode active material and travel through the electrolyte to the anode. Simultaneously, as the Li^+ are detached

from the positive active material, the electrons are also released from the cathode active material to maintain the electrical neutrality. Because the electron conductivity of the electrolyte is extremely low, the electrons released from the cathode active material do not pass through the electrolyte but arrive at the anode via an external circuit, providing electrical energy to the load of the external load (Figure 1.2).[25]

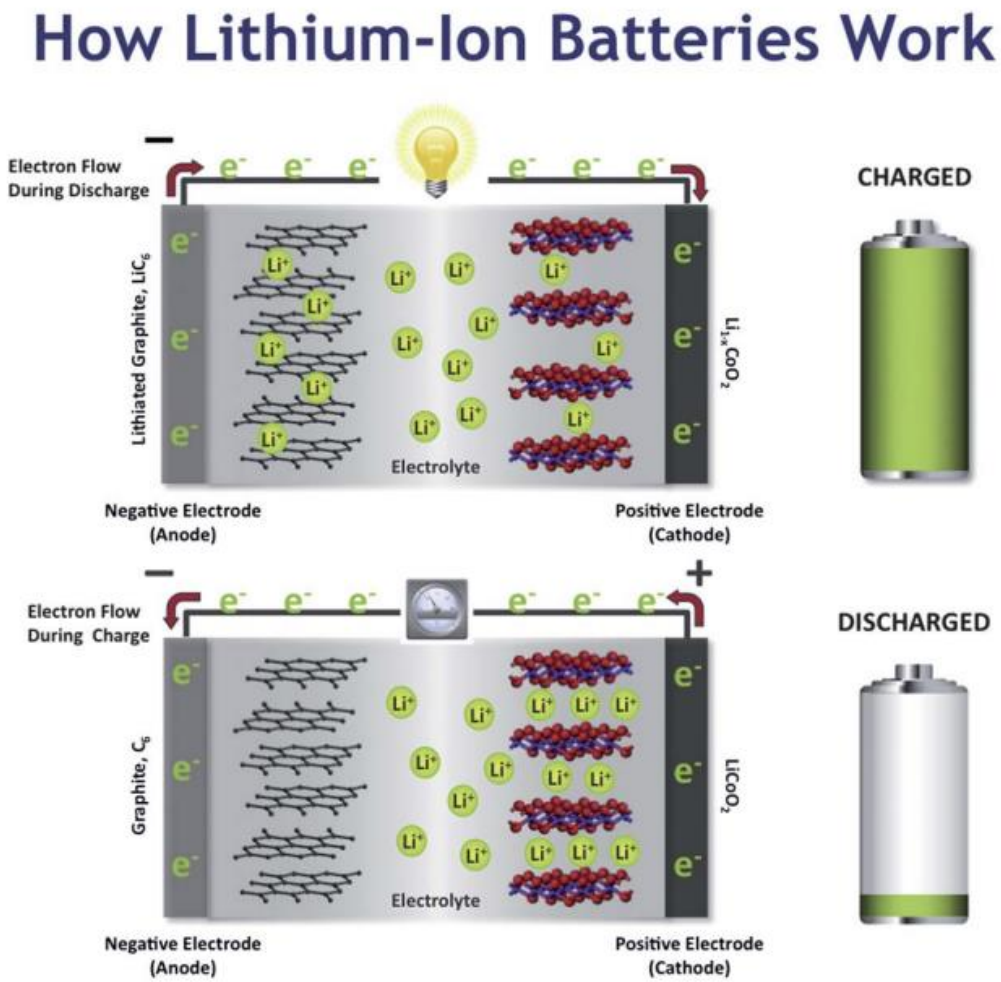

Figure 1.2 A schematic illustration of the working principles of a Li_xC_6/ $Li_{1-x}CoO_2$ LIBs. During discharge, lithium ions diffuse from a lithiated graphite (Li_xC_6) structure (the anode) into a delithiated $Li_{1-x}CoO_2$ structure (the cathode) with concomitant oxidation and reduction of the two electrodes, respectively. The reverse process occurs during charge.[25]

When evaluating the performance of a LIB, we usually focus on the following parameters: voltage, capacity, energy density, rate performance and cycle stability.

Voltage and capacity are the two most basic parameters of a LIB. The open circuit voltage of the battery is the voltage difference between the cathode and anode materials, but when the battery is connected to an external load and current pass through, the working voltage will deviate from the open circuit voltage due to the existence of the internal resistance of the battery, which we call the voltage polarization. Regarding the capacity of the battery, it is mainly determined by the type of cathode material because the capacity of the anode is much higher than that of the cathode. Take a typical $LiCoO_2$ as an example, its theoretical capacity is provided by Li ion fully detaching. However, due to the limitation of thermodynamics and other factors, the utilization rate of Li ion usually does not reach 100%, which leads to the working capacity of most materials is lower than their theoretical capacity. Usually, the capacity can also be subdivided into gravimetric capacity and volumetric capacity.

The energy density of a battery can be defined by equation (1-2),

$$energy\ density = capacity \times voltage \tag{1-2}$$

this parameter is mainly influenced by the capacity and voltage mentioned above. The energy density of current lithium-ion batteries mainly falls in the range of 220 ~ 250 Wh kg^{-1}.[3] Under the circumstance that the volume and mass of electric vehicle power batteries are strictly limited, the energy density of batteries determines the maximum driving range of electric vehicles in a single trip, so it becomes crucial to improve the energy density of power batteries for the development of electric vehicles.

In the case of rate performance, this indicator affects the continuous current, peak current and charge/discharge time of the battery, the unit is generally C (abbreviation of c rate).[26] For a battery with a calibrated charge rate of *x*C, it takes 1/*x* hour to fully charge it at the calibrated current. For example, if the capacity of a battery is 10Ah, and the calibrated rate is 1C, it means that the battery can be fully charged and discharged with 10A current within 1 hour.

Finally, about the cycle stability of the battery, it is affected by all parts of the whole battery. In the cathode material, as the lithium ions are detached and re-inserted, the

structural change upon this process is one of the important reasons for the performance decay of the cathode material.[27] Irreversible phase transition can lead to capacity and voltage fade of the cathode material[28-30], and excessive volume changes will lead to the stripping of the cathode material from the electrode.[31-33] Therefore, it is crucial to consider the structural stability during cycling when designing and developing new cathode materials.

1.2.2 Cathode materials for LIBs

Cathode materials for commercial LIBs

The cathode materials for commercial LIBs can be basically divided into three categories:

(1) lithium transition-metal oxides ($LiTmO_2$, Tm: Transition-metal)

The most representative cathode material in this category is $LiCoO_2$, which was synthesized and applied to LIBs by Prof. Goodenough's group in 1980, is the first cathode material to be commercialized.[22] $LiCoO_2$ has an α-$NaFeO_2$-type layered structure (space group: $R\bar{3}m$) based on the cubic sphere packing of oxygen atoms, with Li^+ and Co^{3+} each located at alternating [CoO_6] and [LiO_6] octahedral center, and is a typical cathode material with two-dimensional Li^+ channels (Fig. **1.3**).[34]

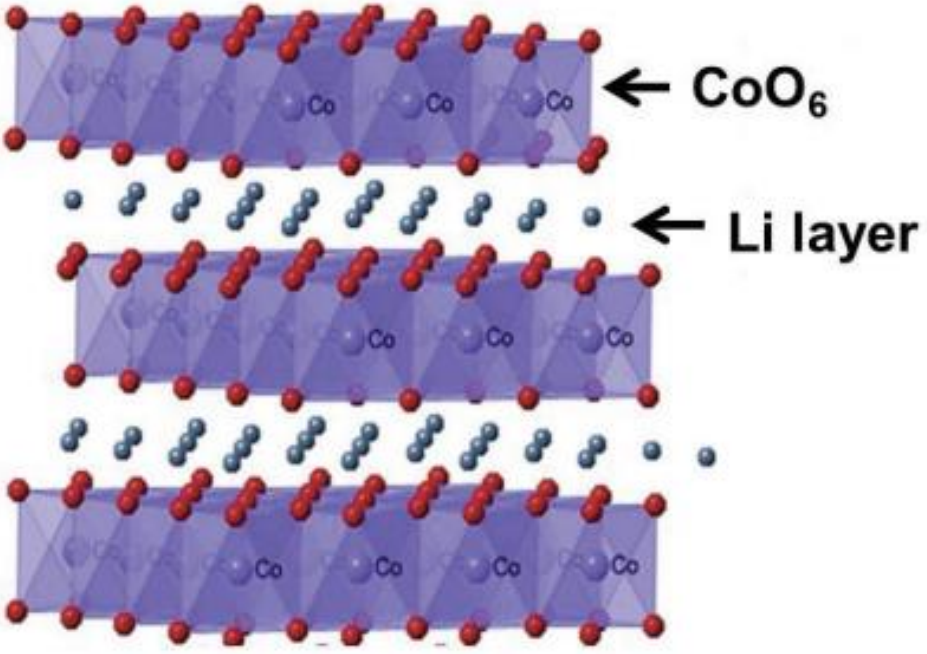

Figure 1.3 Crystal structure of $LiCoO_2$.[34]

$LiCoO_2$ has the advantages of high and smooth operating voltage (over 3.5 V vs. Li/Li^+), ideal specific energy, and good cycling performance; however, $LiCoO_2$ cannot withstand over-voltage charging, and its crystal structure will change irreversibly after charging to 4.2 V, which will cause a decrease in cycling stability and capacity decay. Moreover, due to the high cost and low utilization rate of Co (about 50% in unmodified $LiCoO_2$), other transition metals and even aluminum are used to substitute for cobalt in view of future application prospects.[35, 36] By optimizing the species and ratio of elements, several ternary-type materials have been designed successfully, such as NMC, NCA, which have the advantages of $LiCoO_2$ in high operating voltage and increase the working capacity to 200 mAh g^{-1}, and are popular choices for commercial Li-ion battery cathodes.

(2) Spinel $LiMn_2O_4$

$LiMn_2O_4$ was first proposed by Prof. Goodenough's group in 1984 and has a theoretical capacity of 148 mAh g^{-1}.[37] The oxygen in the spinel $LiMn_2O_4$ structure is arranged in a cubic sphere packing, where Li^+ occupies 1/8 of the oxygen tetrahedra at 8*a* site and Mn atoms occupy 1/2 of the oxygen octahedra at 16*d* site. There are two valence states of manganese in $LiMn_2O_4$, Mn^{3+} and Mn^{4+}, each accounting for 50%, and the material structure is shown in Fig. 1.4.

The $LiMn_2O_4$ structure has face-shared empty oxygen tetrahedra and edge-shard oxygen octahedra, and these empty sites constitute three-dimensional (3D) Li^+ diffusion channels, thus the material has good lithium conductivity. The most crucial problem of spinel $LiMn_2O_4$ material is the capacity decay upon cycling, the main reasons are: (1) $LiMn_2O_4$ is converted to $Li_2Mn_2O_4$ in tetragonal phase during deep discharging or high-rate charge/discharge, and Mn in the material is reduced to trivalent. This valence change will lead to distortion of the material caused by the Jahn-Teller effect, which will destroy the Lattice structure and cause capacity decay. (2) During cycling, Mn^{3+} will disproportionate to form Mn^{4+} and Mn^{2+}, and the Mn^{2+} will dissolve into the

electrolyte, resulting in the loss of active material.[38-40]

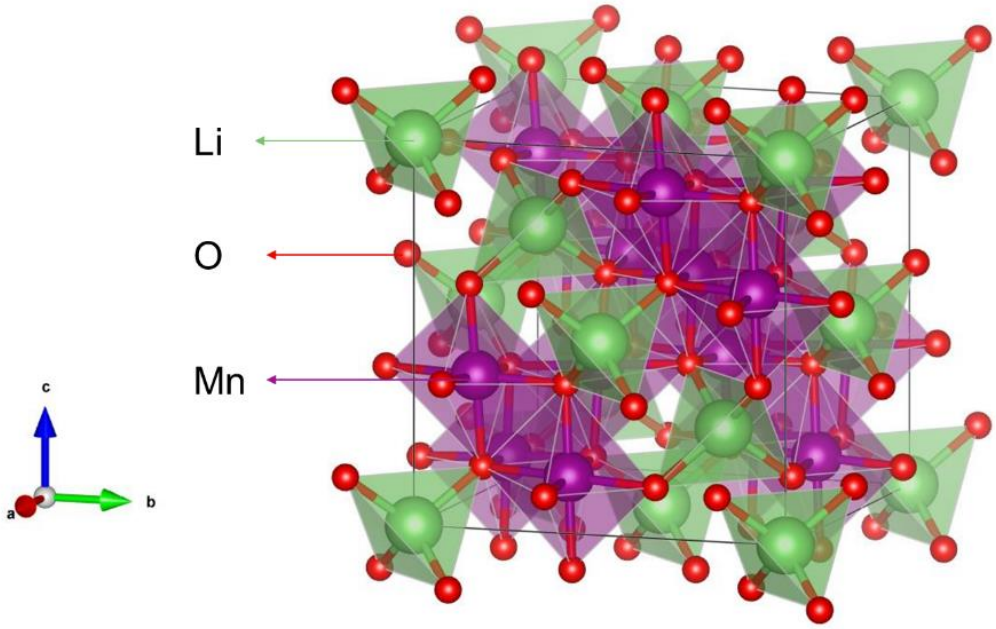

Figure 1.4 Crystal structure of $LiMn_2O_4$.[37]

(3) lithium Olivine-structured orthophosphates ($LiTmPO_4$)

The most representative material in this category is $LiFePO_4$ (space group: *Pnma*), which was first synthesized and applied to LIBs by Prof. Goodenough's group in 1997, with a theoretical capacity of 170 mAh g^{-1}.[41] The oxygen atoms form the basic skeleton of the lattice in a slightly distorted hexagonal sphere packing, and the FeO6 octahedra are connected by a corner-shared geometry (Fig. 1.5).[42] All oxygen ions are combined with pentavalent phosphorus atoms through covalent bonding.[43] Due to the strong P-O bonding, P plays a role in stabilizing the overall lattice and the material has very good thermal stability and high overcharge tolerance. Nevertheless, in practice, the operating capacity and rate property of $LiFePO_4$ materials are much lower than the theoretical values, mainly due to the fact that in $LiFePO_4$ materials, the diffusion pathway of Li^+ is one-dimensional and lithium ions can only diffuse along the *c*-axis direction (corresponding to the [010] direction of the lattice).[44-47] Besides, since the FeO6 octahedra are only connected to each other by a corner-shared geometry but not edge-shared or face-shared, there is no continuous net structure formed, resulting in a low

electronic conductivity of the material.[48, 49]

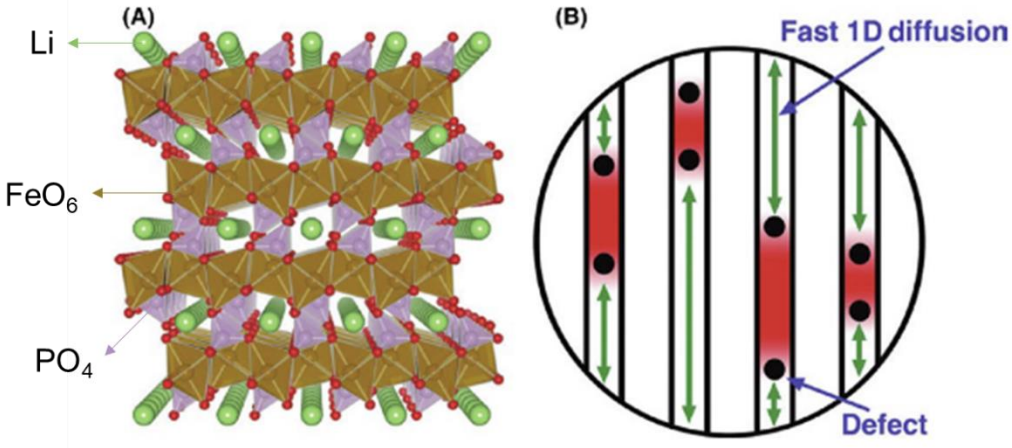

Figure 1.5 (A) Crystal structure of $LiFePO_4$ illustrating 1D Li^+ diffusion channels along the [010] direction; (B) Illustration of Li^+ diffusion impeded by immobile points defects in the channels.[42]

Cathode materials for next-generation LIBs

Because the theoretical capacity of conventional cathode materials is limited by the intrinsic stoichiometry of lithium-ion in host lattice, and lithium-ion utilization is usually less than 100%. Li-excess cathode materials, described as $Li_{1+x}Tm_{1-x}O_2$, have attracted much attention as a promising alternative toward high-capacity cathode materials for LIBs. By introducing Li_2MnO_3, a Li-excess phase which can also be written as $Li[Li_{1/3}Mn_{2/3}]O_2$, into the $LiTmO_2$ host phase, two types of Li-excess cathodes can be formed, namely, layered Li-excess oxides (LLOs) and cation-disordered Li-excess rocksalt (DRXs) (Fig. 1.6).[50, 51] These cathodes can deliver a large reversible capacity of > 250 mAh g^{-1} through the charge compensation of transition metals and oxygen. And due to its three-dimensional (3D) percolation Li^+ diffusion pathway, the DRX cathode ensures more ideal kinetic performances and maintains a higher structural integrity after delithiation then LLOs cathodes.[55-57] However, the development of Li-excess materials is still in the experimental stage, and capacity and

voltage fade issues still need to be addressed before commercial deployment.

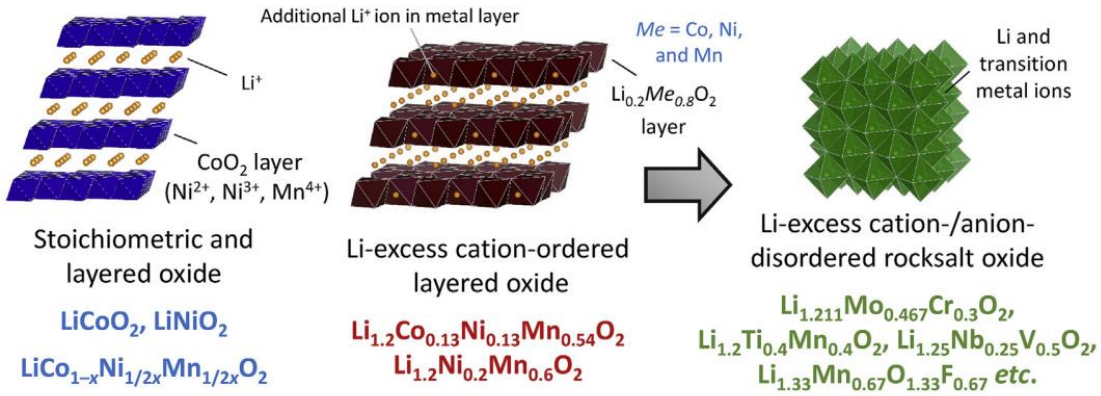

Figure 1.6 Comparison of schematic illustrations of the crystal structures for stoichiometric and Li-excess oxides (oxyfluorides) with cation-ordered layered and cation-disordered rock salt structures.[50]

Normally, the cathode of LIBs is compensated by the charge of the transition metal (Tm) that forms the crystal skeleton, and when the Tm is oxidized to a higher valence state, it can no longer provide electrons. In the past few years, reversible oxygen redox in LIBs has become a hot research topic.[50,51,58-63] The results of these studies show that oxygen redox at high potentials is a common phenomenon in LIBs and sodium-ion batteries (NIBs), and that reversible oxygen redox can be obtained by modulating the coordination state of Tm and oxygen (more toward covalent or ionic bonding).[58,59,64-66] Even in the latest study results, reversible molecular oxygen generation in the crystal cell were observed by various means. trapped molecular O_2 in a charged Li-rich cathode. In 2020, House et al. observed vibrational signals of molecular oxygen in $Na_{0.6}[Li_{0.2}Mn_{0.8}]O_2$ and $Li_{1.2}Ni_{0.13}Co_{0.13}Mn_{0.54}O_2$ electrodes, respectively, by means of resonant inelastic X-ray scattering (RIXS).[52-54] In 2022, House et al. trapped molecular O_2 in a charged Li-rich cathode was also confirmed by neutron pair distribution function (PDF) characterization.[67]

1.3 All-solid-state Fluoride-ion Batteries

Before liquid fluoride ion conductors were purposefully designed, good fluoride

ion conductors were in solid state. Therefore, unlike LIBs, the evolution of FIBs did not undergo a transition to a liquid system but emerged directly in an all-solid-state. As early as 1976, J. Schoonman experimentally demonstrated that $BiO_{0.09}F_{2.82}$ and β-PbF_2:AgF could be used as solid-state fluoride ion electrolytes in chemical batteries, and in 1981, he first proposed the concept of 'solid-state fluoride-ion battery'.[68-71] Subsequently, the study of all-solid-state FIBs stalled until Fichtner et al. constructed tysonite-type $La_{1-x}Ba_xF_{3-x}$ electrolytes and the first reversibly operated prototype of all-solid-state FIBs.[12] In the following part of this chapter, the research progress of FIBs, the problems to be solved and the future prospects will be described in detail.

1.3.1 Research progress of all-solid-state FIBs

Solid electrolyte

The exploration of fluoride ion conductor laid the groundwork for the research of all-solid-state FIBs. The fluorite-type difluoride MF_2 (M = Ca, Sr, Ba) and tysonite-type trifluoride MF_3 (M = La, Ce) are known to offer good fluoride ion conductivity at elevated temperatures (usually above 150 °C).[72-79] It has reported that single-crystal LaF_3 exhibits a fluoride ion conductivity of 1×10^{-6} S cm^{-1} at room temperature[77], but the single-crystal material is complicated to prepare and difficult to apply to all-solid-state batteries. Further studies revealed that by performing partial substitution of aliovalent fluorides into the tysonite-type fluoride, the resulting anionic defect can significantly improve the ionic conductivity of the material. Moreover, nanocrystals exhibit higher ionic conductivity than microcrystals. Based on these previous experiences, the landmark electrolyte for FIBs, $La_{1-x}Ba_xF_{3-x}$ (LBF), was proposed by Fichtner et al., its lattice structure is shown in Fig. 1.7.[80] A series of tysonite-type solid solutions can be produced using mechanical ball milling by a tuned La/Ba ratio. Compared to pure LaF_3, the $La_{1-x}Ba_xF_{3-x}$ compounds improved the ionic conductivity by more than two orders of magnitude (2×10^{-4} S cm^{-1}) at 160 °C with superior thermal stability[80], are widely used in the research of all-solid-state FIBs.

On the other hand, the $La_{1-x}Ba_xF_{3-x}$ compounds have a theoretically wide electrochemical window. The decomposition reactions of electrolytes are as follows:

$$MF_{x(s)} \rightarrow M_{(s)} + \frac{x}{2}F_{2(g)} \quad (1\text{-}3)$$

The theoretical potential of the above reaction can be calculated using the following equation:

$$\Delta_r G^{\ominus} = -nF\Delta E^{\ominus} = \Delta_f H^{\ominus} - T\Delta S^{\ominus} \quad (1\text{-}4)$$

with n the number of moles of electrons exchanged upon reaction, F the Faraday constant (96485 C.mol^{-1}), T the absolute temperature (K), and $\Delta_f H^{\ominus}$ (kJ mol^{-1}) and $\Delta S^{\ominus}$ (kJ mol^{-1} K^{-1}) are the standard enthalpy and entropy, respectively. The theoretical decomposition potentials of LaF_3 and BaF_2 were calculated to be 5.73 and 6.0 V at 293 K, respectively. The experimental data shows that $La_{0.95}Ba_{0.05}F_{2.95}$ has an electrochemical window over 5 V, which is consistent with the results obtained from theoretical calculations.[81]

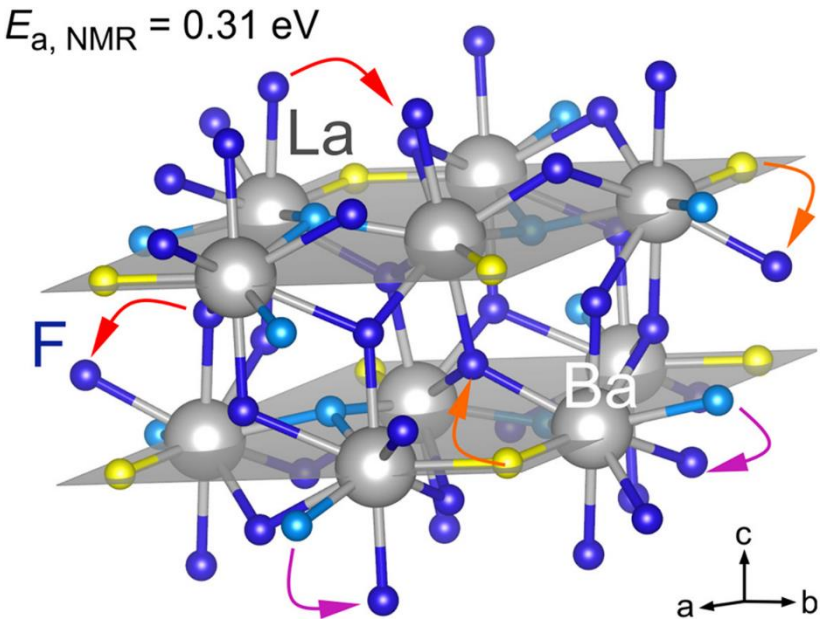

Figure 1.7 Lattice structure of $La_{1-x}Ba_xF_{3-x}$.[80]

Moreover, based on the forementioned fluorite-to-tysonite design principle, Dieudonné et al. reported $Sm_{1-x}Ca_xF_{3-x}$ and $Ce_{1-x}Sr_xF_{3-x}$ compounds.[82,83] The

introduction of aliovalent metals (Sr to Ce, and Ca to Sm) creates local distortions around them (Sr and Ca), that will hamper the mobility of fluoride ions in the tysonite network and thus achieve high fluorine ion conductivity of 10^{-4} S cm^{-1} at room temperature.

Another type of electrolyte commonly used in the study of all-solid-state FIBs is $M_xSn_{2-x}F_4$ (M = Pb, Ba, Sr), of which the most representative is $PbSnF_4$.[84-89] $PbSnF_4$ has 4 configurations: *o*-, *α*-, *β*-, and *γ*-; among them, *β*-$PbSnF_4$ exhibits the highest room temperature ionic conductivity of 2-3 mS cm^{-1}, which is much higher than LBF. Fig. 1.8 shows the crystal structure of *β*- $PbSnF_4$, the lattice is constructed by modulated [-Pb-Pb-Sn-Sn-Pb-Pb-] slabs and fluoride ions are located in the Pb-Sn and Pb-Pb slabs.[90] The Sn(II) lone pairs of electrons lead to local distortion and partially occupancy, create a zigzag two-dimensional fluoride-ion diffusion pathway on the *a-b* plane between Pb-Sn layers, while the fluoride ions between Pb-Pb layers are considered immovable. However, the relatively narrow electrochemical window of $M_xSn_{2-x}F_4$ compounds due to the high formation potential of Sn, hinders the operation of high potential electrodes in the study of all-solid-state FIBs.[90]

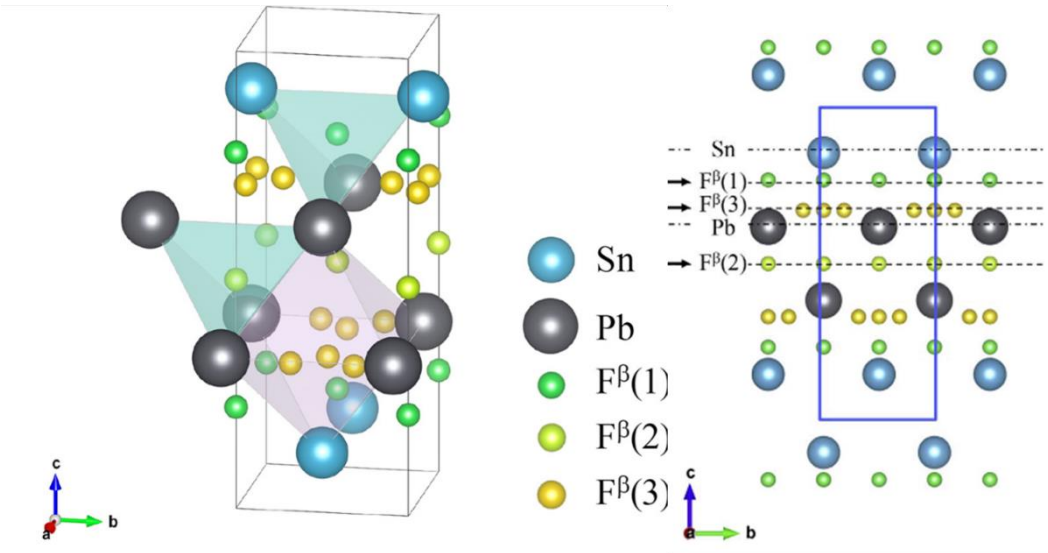

Figure 1.8 Lattice structure of *β*- $PbSnF_4$.[90]

Anode

When evaluating the electrochemical performance of a LIBs electrode material,

lithium metal half-cells are widely used because the redox of lithium ions can be plated directly on the lithium metal and the Li/Li^+ redox couple has the lowest potential (–3.04 V) against the standard hydrogen electrode among all solid-state redox couples. However, in FIBs, the redox of fluoride ions generates the release of F_2, so metal fluorides were firstly applied as a stable and readily available fluoride ion donor for the studies of electrode materials for FIBs. The M/MF_x transformation is typically accompanied by a large change in free energy, leading to high theoretical voltages in chemical batteries.[12] The relative potentials of each M/MF_x redox couples are summarized in Table 1.1. Li/LiF has the lowest redox potential of all M/MF_x and is the most ideal candidate for anode of FIBs. Nevertheless, due to its contact toxicity and flammability, Li/LiF has not been applied to FIBs. The first anode system to be used in FIBs was Ce/CeF_2. Subsequent studies have shown that Pb/PbF_2 is considered to be the most reliable anode system in terms of ionic conductivity, capacity, cycling stability and safety.[91]

Table 1.1 Theoretical capacities* and of various M/MF_x couples and their relative potential vs. Pb/PbF_2.

M/MF_x Couples	Gravimetric capacity (mAh g^{-1})	Volumetric capacity (mAh cm^{-3})	*E* vs. Pb/PbF_2 (V)
Li/LiF	3861	2062	-2.89
Ca/CaF_2	1337	2073	-2.85
Ba/BaF_2	390	1402	-2.80
Sr/SrF_2	612	1554	-2.78
Na/NaF	1166	1132	-2.44
La/LaF_3	579	3560	-2.41
K/KF	685	591	-2.38
Ce/CeF_3	574	3885	-2.37

Mg/MgF_2	2205	3832	-2.35
Al/AlF_3	2980	8052	-1.73
Ti/TiF_4	2240	10167	-0.84
Cr/CrF_3	1546	11117	-0.56
Zn/ZnF_2	820	5847	-0.50
Mn/MnF_3	1463	10874	-0.26
V/VF_4	2105	12859	-0.20
Fe/FeF_3	1440	3301	-0.16
Sn/SnF_2	452	2936	-0.07
Pb/PbF_2	259	8129	0.00
Ni/NiF_2	913	3751	0.07
Bi/BiF_3	385	14275	0.32
Mo/MoF_5	1397	8095	0.54
Co/CoF_3	1364	7558	0.64
Cu/CuF_2	843	2608	0.64
Ag/AgF	248	7887	1.26
Au/AuF_3	408	11336	2.19

*The capacities are calculated based on metal mass.

Cathode

(1) Conversion-type cathodes

The first to be used in FIBs cathodes are M/MF_x (Bi/BiF_3, Sn/SnF_2, and Cu/CuF_2) systems with high potentials.[12] Difluorides and trifluorides benefit from their multi-electron reactions during defluorination, can provide energy densities far exceeding those of LIBs and are considered promising alternatives for FIBs. Table 1.1 summarizes

the theoretical capacities of each M/MF_x system. However, it is difficult to achieve 100% utilization of the cathode active material in an all-solid-state system; Thieu et al. reported that 68% of the theoretical capacity was obtained in the first cycle by a setting of CuF_2|LBF|La, but only 10% of capacity remained after 23 cycles.[92]

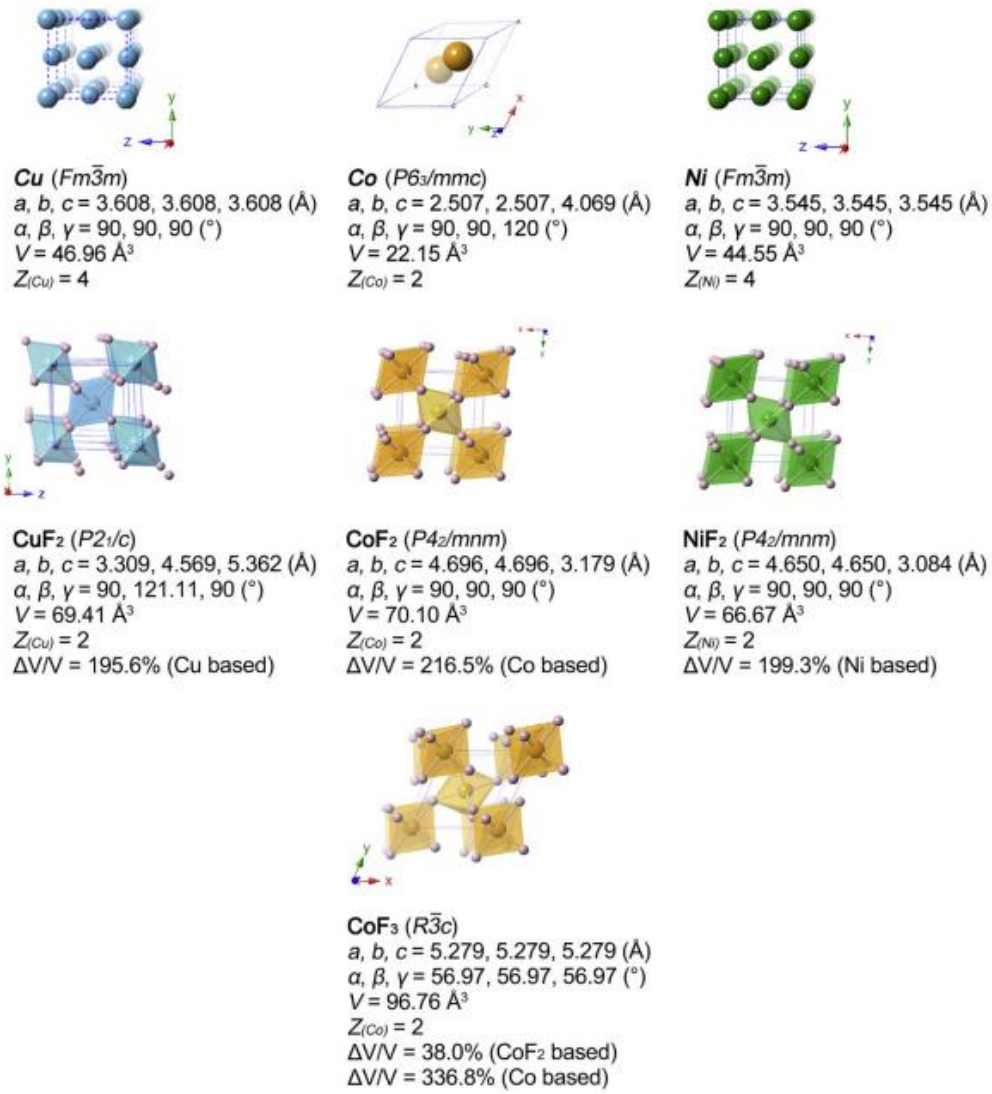

Figure 1.9 The crystallographic models of Cu, Co, Ni and their fluorides. The volumetric changes are listed under each model.[93]

Zhang et al. achieved nearly 100% utilization of the active material in the first cycle using a thin-film electrode with 3d-transition metal (Cu, Co, Ni) cathode generated on a LaF_3 single-crystal substrate by radio-frequency magnetron sputtering.[93] Further analysis of the reaction mechanism shows that the (de)fluorination of M/MF_x is

achieved by a two-phase reaction without the presence of a stable intermediate phase.[94] This observation is also supported by other experimental as well as theoretical density functional theory calculations.[95] It is noteworthy that the two-phase transition of M/MF_x is accompanied by a huge volume change of lattice; for instance, the phase transition of Cu and CuF_2 has to undergo a volume change of approximately 200% (Fig. 1.9). Additionally, this process generates a two-phase mismatch as well as a phase with low fluoride-ion conductivity, which explains the low utilization of the cathode active material and the poor cycling stability in the all-solid-state system. Although thin film electrode using Cu-Pb nanocomposite can provide an additional fluoride ion diffusion pathway during the fluorination process, this concept cannot be realized in an all-solid-state system.[96]

(2) Intercalation-type cathodes

Prior to the reversible (de)intercalation of fluoride ions into a host lattice via electrochemical means, there have been reports on topotactic fluorination that does not change the fundamental framework of the host lattice.[97-104] A variety of layered oxyfluorides with perovskite-related structure have been synthesized through various fluorination agents (metal fluorides with strong oxidizing properties: e.g., AgF_2; polyvinylidene difluoride (PVDF); XeF_2; F_2 gas, etc.). [97-104] Some of these fluorinations can result in fluoride ions not only occupying the interstitial sites but also replacing some of the original oxygen in the host lattice; for example, $Sr_2CuO_2F_{2+\delta}$ (prepared using Sr_2CuO_3 and gaseous F_2) and $Sr_2TiO_3F_2$ (produced by Sr_2TiO_4 and PVDF or NH_4F). Whether the fluoride ion is directly bonded to the metal ion or not might affect

its mobility under electrochemistry.

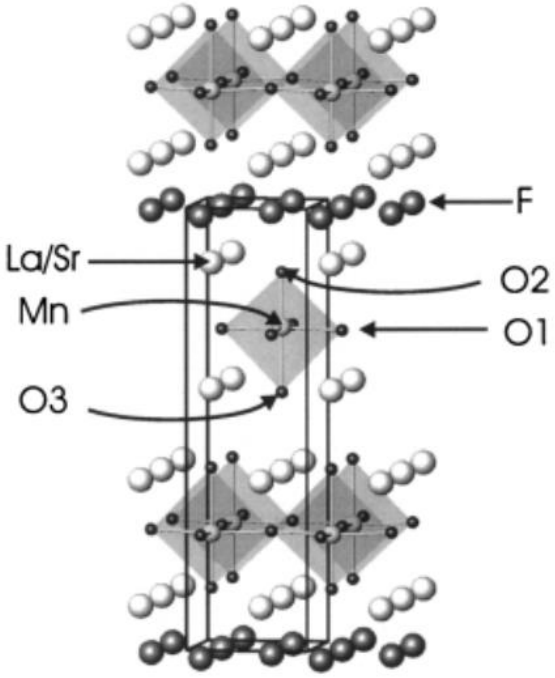

Figure 1.10 Structure of $LaSrMnO_4F$ showing the unit cell.[109]

As mentioned above, the huge volume expansion/shrink of M/MF_x conversion-type cathodes during (de)fluorination hinders their application as cathode materials for all-solid-state FIBs.[105-107] Therefore, intercalation-type materials like $LiCoO_2$ with a rigid metal oxide framework have attracted the attention of researchers. The first application of $BaFeO_{2.5}$ as an intercalation-type cathode for all-solid-state FIBs was reported by Clements et al.; Perovskite-type $BaFeO_{2.5}F_{0.5}$ was synthesized by electrochemical fluorination and a three-cycle reversible electrochemical (de)fluorination behavior was achieved.[108] However, it is not a material that can be used in practical batteries due to its lack of reversibility and low capacity.

Aikens et al. reported that, $LaSrMnO_4$, a perovskite-related material with layered Ruddlesden-Popper (R-P) phase can topotactically accommodate fluoride ions in its rocksalt blocks (Fig. 1.10).[109, 110] R-P phase are a type of perovskite compound that consists of alternate perovskite and rocksalt slabs, the general R-P phase can be written as $A_{n+1}B_nX_{3n+1}$, in which *A* is a rare earth or alkaline earth element and *B* is a transition

metal, *X* is an anion, *n* is the number of octahedral layers in the perovskite stack.[111] Nowroozi et al. experimentally revealed that $LaSrMnO_4$ has the ability to reversibly (de)insert fluoride ions into rocksalt layers by electrochemical. After the two rocksalt layers are fully occupied by fluoride ions, the lattice produced significant expansion only in the *c*-axis due to the Coulomb repulsion, and the fluorinated $LaSrMnO_4F_2$ produced only 16% volume expansion than $LaSrMnO_4$.[112] This topotactical fluoride-ion (de) insertion behavior suppressed the volume change issue that accompany (de)fluorination in the M/MF_x conversion-type cathodes. Subsequently, a series of n = 1 R-P-phase materials were proposed one after another.[113-115] Although they succeeded in suppressing the volume expansion, the fact that these materials have heavier and more complex host lattices, resulting in their energy density lower than that of M/MF_x conversion-type cathodes.

1.3.2 Challenges and Prospects for Fluoride-ion Batteries

From the time the first all-solid-state FIBs prototype was proposed in 2011, research on it has made considerable progress in the last 10 years. However, the performance of all-solid-state FIBs to date is not sufficient to allow it as a challenger to the position of LIBs.

In terms of cathode materials, the proposed intercalation-type cathode material is of great significance because it solves the problem of volume expansion that cannot be avoided with M/MF_x cathodes. We strongly believe that the intercalation-type cathode material is the ultimate solution for the cathode of all-solid-state FIBs, but a further increase in charge/discharge capacity has become an essential issue. To further improve charge and discharge capacity, there are major issues such as the application of anion redox as described for LIBs. Finally, the volume change upon charging/discharging of the current intercalation-type cathodes is still larger than that of LIBs; for example, the volume change of $LaSrMnO_4$/ $LaSrMnO_4F_2$ is 16%, while the volume change of $LiCoO_2$ before and after charging is only 4%.[116] Especially for the electrode materials of all-solid-state batteries, this volume expansion needs to be further suppressed.

With the increasing sophistication of material synthesis and characterization techniques, FIBs are expected to become the successor to LIBs in the future through proper material design and targeted analytical characterization.

1.4 Objective

As previously mentioned, the low capacity and reversibility of the intercalation-type cathodes in current FIBs has been a problem. Therefore, it becomes particularly important to find new solutions for the design of cathodes.

A mixed-anion compound is a solid-state material containing more than one anionic species in a single phase, such as oxyfluorides (oxide-fluoride) and oxynitrides (oxidenitride).[117] The $LaSrMnO_4F_x$ obtained by electrochemical fluorination can then be considered as a mixed-anion compound. In a mixed-anion compound, the metal can bind to more than one anionic ligand to form a heteroleptic polyhedron, unexpected properties can be obtained by modulation of the local structure (Fig. 1.11). As an example, MO_4X_2 octahedra obtained by anion substitution changes its original binding energy, which may enhance its anion diffusion.[118, 119] A further interesting concept for complex anions is the molecular formation shown in Fig. 1.11(h). The introduction of a hole into an anion species that occupies an orbital closer to the Fermi level may allow for effective anion redox to be utilized through the occurrence of molecular formation.

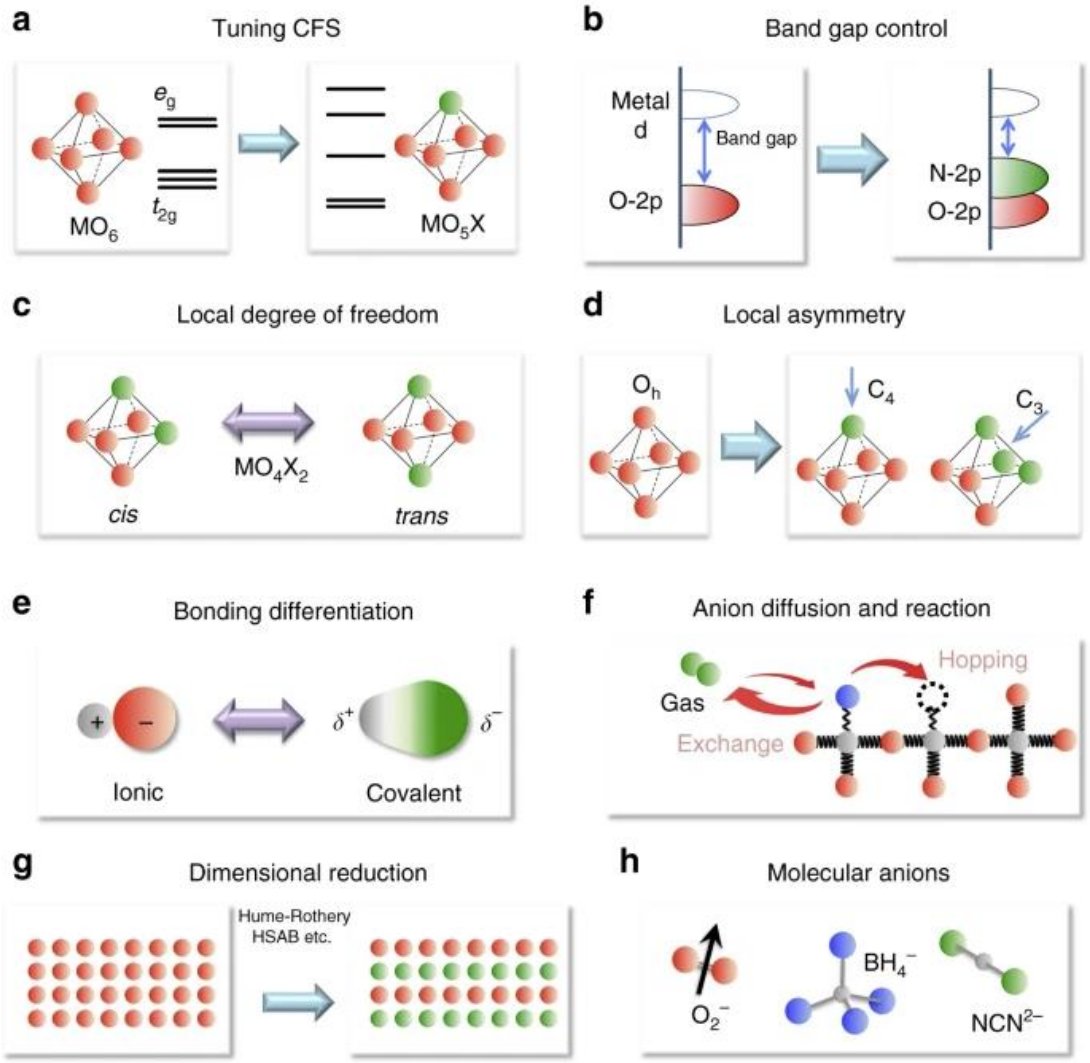

Figure 1.11 What mixed-anion compounds can do.[117]

In this thesis, we developed a series iron-based oxyfluoride compounds as cathodes for FIBs. These oxyfluoride cathodes show a significant improvement in energy density and power density compared to conventional oxide cathodes. Through systematic analysis of their local structure changes and the charge compensation mechanism during the (de)fluorination, the enhancement of the electrochemical performance by the design of the mixed-anion principle is explained. Besides, we also discussed a new process of fabricating the composite electrode. We believe that this thesis will bring new perspectives to the design of high-performance cathode materials for FIBs.

1.5 Outline of the present thesis

This thesis consists of 8 chapters, which report the designs and studies of oxyfluoride cathodes with layered structure for all-solid-state FIBs and a new fabrication process of composite electrode.

In Chapter 1, we briefly describe the fundamental principles of batteries, the development and design principles of electrode materials, and the encountered problems based on the widely used LIBs. Afterwards, we discussed the research achievement and urgent problems, and gave an outlook on the design concepts of cathode for FIBs based on the experience drawn from the cathodes of LIBs.

In Chapter 2, by high-temperature and high-pressure synthesis, we fabricated the oxyfluoride Sr_2MnO_3F with half of the apical site occupied by F, and the introduction of F into the apical site reduces the Coulomb repulsion after charging (electrochemical insertion of F) compared with the general metal oxide $LaSrMnO_4$. Electrochemical and XAS analyses show that the charging and discharging of the oxyfluoride proceeds in a smooth solid-solution reaction, effectively avoiding the two-phase transition route of the pure oxide, and thus achieving better high-rate performance.

In Chapter 3, we demonstrate the first synthesis of layered oxyfluoride $Sr_3Fe_2O_5F_2$ as an intercalation-type cathode material for FIBs via a $Sr_3Fe_2O_5$ intermediate. The results of electrochemical measurement demonstrate that the F could be reversible (de)inserted into the anion vacancies via a solid-solution route, and exhibit excellent stable cycle performance.

In Chapter 4, $SrFeO_2$ with infinite-layer structure, after undergoing the electrochemical activation process, the in-situ generated $SrFeO_2F_x$ cathode exhibits a high capacity overriding LIBs by accommodating more than the stoichiometric ratio of F. The synchrotron XRD results indicate that the $SrFeO_2F_x$ cathode exhibit zero-strain property (~0.5% volume change) upon charging/discharging, which is essential for all-solid-state batteries.

In Chapter 5, based on our experience with $SrFeO_2$ cathode, we obtained a series of $Ca_ySr_{1-y}FeO_2$ ($0 \leq y \leq 1$) cathodes with substantially increased capacities by using low-cost and lightweight Ca as a substitute for Sr; among them, $Ca_{0.8}Sr_{0.2}FeO_2$ reached the highest energy density, about 2.5 times higher than that of $LiCoO_2$. XAS measurements reveal that both the cation (Fe^{2+}/Fe^{3+}) as well as the anion (O^{2-}/O^0) are involved in charge compensation, and that the stably generated oxygen molecules are trapped in the lattice and provide space for additional fluoride ion insertion.

In Chapter 6, a series of $Sr_{1-y}Ba_yFeO_2$ cathodes were proposed by modulating the local construction of infinite-layer structure; in comparison with $SrFeO_2$, the $Sr_{0.7}Ba_{0.3}FeO_2$ cathode successfully increased the high-rate electrochemical performance by 20%. The results of extended X-ray absorption fine structure (EXAFS) and synchrotron XRD cross-support that the bottle-neck area of fluoride-ion diffusion is amplified after the introduction of Ba^{2+} with larger ionic radius.

In Chapter 7, we suggest the HPT deformation as a new approach to the fabrication of composite electrode for all-solid-state FIBs. The particle size of the active material and solid electrolyte in the treated composites was significantly reduced and a more homogeneous distribution was obtained. The electrochemical results reveal that the HPT deformation effectively lowers the impedance within the composite electrode, thus reducing the voltage polarization during charging/discharging.

In Chapter 8, we summarized the above research and provide an outlook on the prospects of all-solid-state FIBs.

Reference

1. Berdysheva, S.; Ikonnikova, S., The Energy Transition and Shifts in Fossil Fuel Use: The Study of International Energy Trade and Energy Security Dynamics. *Energies* **2021,** *14* (17), 5396.
2. Agreement, P. In *Paris agreement*, Report of the Conference of the Parties to the United Nations Framework Convention on Climate Change (21st Session, 2015: Paris). Retrived December, HeinOnline: 2015; p 2017.
3. Chu, S.; Cui, Y.; Liu, N., The path towards sustainable energy. *Nat. Mater.* **2017,** *16* (1), 16-22.
4. SONY Corp. https://www.sony.com/en/SonyInfo/News/Press_Archive/200412/04-060E/.
5. Jakob Fleischmann, D. H., Friederike Liebach, and Martin Linder Unlocking growth in battery cell manufacturing for electric vehicles. https://www.mckinsey.com/capabilities/operations/our-insights/unlocking-growth-in-battery-cell-manufacturing-for-electric-vehicles.
6. Liu, K.; Liu, Y.; Lin, D.; Pei, A.; Cui, Y., Materials for lithium-ion battery safety. *Sci. Adv.* **2018,** *4* (6), eaas9820.
7. Fu, X.; Beatty, D. N.; Gaustad, G. G.; Ceder, G.; Roth, R.; Kirchain, R. E.; Bustamante, M.; Babbitt, C.; Olivetti, E. A., Perspectives on cobalt supply through 2030 in the face of changing demand. *Environ. Sci. Technol.* **2020,** *54* (5), 2985-2993.
8. Cao, D.; Sun, X.; Li, Q.; Natan, A.; Xiang, P.; Zhu, H., Lithium dendrite in all-solid-state batteries: growth mechanisms, suppression strategies, and characterizations. *Matter* **2020,** *3* (1), 57-94.
9. Li, Q.; Yi, T.; Wang, X.; Pan, H.; Quan, B.; Liang, T.; Guo, X.; Yu, X.; Wang, H.; Huang, X., In-situ visualization of lithium plating in all-solid-state lithium-metal battery. *Nano Energy* **2019,** *63*, 103895.
10. Delmas, C.; Braconnier, J.-J.; Fouassier, C.; Hagenmuller, P., Electrochemical

intercalation of sodium in Na_xCoO_2 bronzes. *Solid State Ionics* **1981,** *3*, 165-169.

11. Aurbach, D.; Lu, Z.; Schechter, A.; Gofer, Y.; Gizbar, H.; Turgeman, R.; Cohen, Y.; Moshkovich, M.; Levi, E., Prototype systems for rechargeable magnesium batteries. *Nature* **2000,** *407* (6805), 724-727.

12. Anji Reddy, M.; Fichtner, M., Batteries based on fluoride shuttle. *J. Mater. Chem.* **2011,** *21* (43).

13. Xu, C.; Li, B.; Du, H.; Kang, F., Energetic zinc ion chemistry: the rechargeable zinc ion battery. *Angew. Chem. Int. Ed. Engl.* **2012,** *124* (4), 957-959.

14. Zhao, X.; Zhao-Karger, Z.; Wang, D.; Fichtner, M., Metal oxychlorides as cathode materials for chloride ion batteries. *Angew. Chem. Int. Ed. Engl.* **2013,** *52* (51), 13621-4.

15. Jian, Z.; Luo, W.; Ji, X., Carbon electrodes for K-ion batteries. *J. Am. Chem. Soc.* **2015,** *137* (36), 11566-11569.

16. Lin, M.-C.; Gong, M.; Lu, B.; Wu, Y.; Wang, D.-Y.; Guan, M.; Angell, M.; Chen, C.; Yang, J.; Hwang, B.-J., An ultrafast rechargeable aluminium-ion battery. *Nature* **2015,** *520* (7547), 324-328.

17. Gao, P.; Reddy, M. A.; Mu, X.; Diemant, T.; Zhang, L.; Zhao-Karger, Z.; Chakravadhanula, V. S.; Clemens, O.; Behm, R. J.; Fichtner, M., VOCl as a Cathode for Rechargeable Chloride Ion Batteries. *Angew. Chem. Int. Ed. Engl.***2016,** *55* (13), 4285-90.

18. Ponrouch, A.; Frontera, C.; Bardé, F.; Palacín, M. R., Towards a calcium-based rechargeable battery. *Nat. Mater.* **2016,** *15* (2), 169-172.

19. Davis, V. K.; Bates, C. M.; Omichi, K.; Savoie, B. M.; Momcilovic, N.; Xu, Q.; Wolf, W. J.; Webb, M. A.; Billings, K. J.; Chou, N. H.; Alayoglu, S.; McKenney, R. K.; Darolles, I. M.; Nair, N. G.; Hightower, A.; Rosenberg, D.; Ahmed, M.; Brooks, C. J.; Miller, T. F., 3rd; Grubbs, R. H.; Jones, S. C.,

Room-temperature cycling of metal fluoride electrodes: Liquid electrolytes for high-energy fluoride ion cells. *Science* **2018,** *362* (6419), 1144-1148.

20. Wang, M.; Jiang, C.; Zhang, S.; Song, X.; Tang, Y.; Cheng, H.-M., Reversible calcium alloying enables a practical room-temperature rechargeable calcium-ion battery with a high discharge voltage. *Nat. Chem.* **2018,** *10* (6), 667-672.

21. Whittingham, M. S., Electrical energy storage and intercalation chemistry. *Science* **1976,** *192* (4244), 1126-1127.

22. Mizushima, K.; Jones, P.; Wiseman, P.; Goodenough, J. B., Li_xCoO_2 (0< x<-1): A new cathode material for batteries of high energy density. *Mater. Res. Bull.* **1980,** *15* (6), 783-789.

23. Nakajima, T. Sanechika, K.-i.; Yoshino, A. Secondary battery. US4668595A, May 9.1986.

24. Koksbang, R.; Barker, J.; Shi, H.; Saidi, M., Cathode materials for lithium rocking chair batteries. *Solid State Ionics* **1996,** *84* (1-2), 1-21.

25. Thackeray, M. M.; Wolverton, C.; Isaacs, E. D., Electrical energy storage for transportation—approaching the limits of, and going beyond, lithium-ion batteries. *Energy Environ. Sci.* **2012,** *5* (7), 7854-7863.

26. Merryweather, A. J.; Schnedermann, C.; Jacquet, Q.; Grey, C. P.; Rao, A., Operando optical tracking of single-particle ion dynamics in batteries. *Nature* **2021,** *594* (7864), 522-528.

27. Qian, J.; Liu, L.; Yang, J.; Li, S.; Wang, X.; Zhuang, H. L.; Lu, Y., Electrochemical surface passivation of $LiCoO_2$ particles at ultrahigh voltage and its applications in lithium-based batteries. *Nat. Commun.* **2018,** *9* (1), 1-11.

28. Reimers, J. N.; Dahn, J., Electrochemical and in situ X-ray diffraction studies of lithium intercalation in Li_xCoO_2. *J. Electrochem. Soc.* **1992,** *139* (8), 2091.

29. Lee, J. I.; Lee, E. H.; Park, J. H.; Park, S.; Lee, S. Y., Ultrahigh-Energy-

Density Lithium-Ion Batteries Based on a High-Capacity Anode and a High-Voltage Cathode with an Electroconductive Nanoparticle Shell. *Adv. Energy Mater.* **2014,** *4* (8), 1301542.

30. Kalluri, S.; Yoon, M.; Jo, M.; Park, S.; Myeong, S.; Kim, J.; Dou, S. X.; Guo, Z.; Cho, J., Surface Engineering Strategies of Layered $LiCoO_2$ Cathode Material to Realize High-Energy and High-Voltage Li-Ion Cells. *Adv. Energy Mater.* **2017,** *7* (1), 1601507.

31. Sharifi-Asl, S.; Lu, J.; Amine, K.; Shahbazian-Yassar, R., Oxygen Release Degradation in Li-Ion Battery Cathode Materials: Mechanisms and Mitigating Approaches. *Adv. Energy Mater.* **2019,** *9* (22).

32. Yamada, A.; Chung, S.-C.; Hinokuma, K., Optimized $LiFePO_4$ for lithium battery cathodes. *J. Electrochem. Soc.* **2001,** *148* (3), A224.

33. Zaghib, K.; Dubé, J.; Dallaire, A.; Galoustov, K.; Guerfi, A.; Ramanathan, M.; Benmayza, A.; Prakash, J.; Mauger, A.; Julien, C., Enhanced thermal safety and high power performance of carbon-coated $LiFePO_4$ olivine cathode for Li-ion batteries. *J. Power Sources* **2012,** *219*, 36-44.

34. Daniel, C.; Mohanty, D.; Li, J.; Wood, D. L. In *Cathode materials review*, AIP Conference Proceedings, American Institute of Physics: 2014; pp 26-43.

35. Armstrong, A. R.; Bruce, P. G., Synthesis of layered $LiMnO_2$ as an electrode for rechargeable lithium batteries. *Nature* **1996,** *381* (6582), 499-500.

36. Thomas, M.; David, W.; Goodenough, J.; Groves, P., Synthesis and structural characterization of the normal spinel $Li[Ni_2]O_4$. *Mater. Res. Bull.* **1985,** *20* (10), 1137-1146.

37. Thackeray, M.; Johnson, P.; De Picciotto, L.; Bruce, P.; Goodenough, J., Electrochemical extraction of lithium from $LiMn_2O_4$. *Mater. Res. Bull.* **1984,** *19* (2), 179-187.

38. Aurbach, D.; Levi, M.; Gamulski, K.; Markovsky, B.; Salitra, G.; Levi, E.; Heider, U.; Heider, L.; Oesten, R., Capacity fading of $Li_xMn_2O_4$ spinel

electrodes studied by XRD and electroanalytical techniques. *J. Power Sources* **1999,** *81*, 472-479.

39. Shin, Y.; Manthiram, A., Factors influencing the capacity fade of spinel lithium manganese oxides. *J. Electrochem. Soc.* **2004,** *151* (2), A204.

40. Dai, Y.; Cai, L.; White, R. E., Capacity fade model for spinel $LiMn_2O_4$ electrode. *J. Electrochem. Soc.* **2012,** *160* (1), A182.

41. Padhi, A. K.; Nanjundaswamy, K. S.; Goodenough, J. B., Phospho-olivines as positive-electrode materials for rechargeable lithium batteries. *J. Electrochem. Soc.* **1997,** *144* (4), 1188.

42. Malik, R.; Burch, D.; Bazant, M.; Ceder, G., Particle size dependence of the ionic diffusivity. *Nano Letters* **2010,** *10* (10), 4123-4127.

43. Zhang, W.-J., Structure and performance of $LiFePO_4$ cathode materials: A review. *J. Power Sources* **2011,** *196* (6), 2962-2970.

44. Wang, Y.; He, P.; Zhou, H., Olivine $LiFePO_4$: development and future. *Energy Environ. Sci.* **2011,** *4* (3), 805-817.

45. Morgan, D.; Van der Ven, A.; Ceder, G., Li conductivity in Li_xMPO_4 (M= Mn, Fe, Co, Ni) olivine materials. *ECS Solid State Lett.* **2003,** *7* (2), A30.

46. Islam, M. S.; Driscoll, D. J.; Fisher, C. A.; Slater, P. R., Atomic-scale investigation of defects, dopants, and lithium transport in the $LiFePO_4$ olivine-type battery material. *Chem. Mater.* **2005,** *17* (20), 5085-5092.

47. Nishimura, S.-i.; Kobayashi, G.; Ohoyama, K.; Kanno, R.; Yashima, M.; Yamada, A., Experimental visualization of lithium diffusion in Li_xFePO_4. *Nat. Mater.* **2008,** *7* (9), 707-711.

48. Chung, S.-Y.; Bloking, J. T.; Chiang, Y.-M., Electronically conductive phospho-olivines as lithium storage electrodes. *Nat. Mater.* **2002,** *1* (2), 123-128.

49. Wang, G.; Bewlay, S.; Needham, S. A.; Liu, H.-K.; Liu, R.; Drozd, V.; Lee, J.-F.; Chen, J., Synthesis and characterization of $LiFePO_4$ and

LiuTi$_{0.01}$Fe$_{0.99}$PO$_4$ cathode materials. *J. Electrochem. Soc.* **2005,** *153* (1), A25.

50. Yabuuchi, N., Rational Material Design of Li-excess Metal Oxides with Disordered Rocksalt Structure. *Curr. Opin. Electrochem.* **2022**, 100978.

51. Yabuuchi, N.; Kubota, K.; Aoki, Y.; Komaba, S., Understanding particle-size-dependent electrochemical properties of Li_2MnO_3-based positive electrode materials for rechargeable lithium batteries. *J. Phys. Chem. C.* **2016,** *120* (2), 875-885.

52. House, R. A.; Playford, H. Y.; Smith, R. I.; Holter, J.; Griffiths, I.; Zhou, K.-J.; Bruce, P. G., Detection of trapped molecular O_2 in a charged Li-rich cathode by Neutron PDF. *Energy Environ. Sci.* **2022,** *15* (1), 376-383.

53. House, R. A.; Rees, G. J.; Pérez-Osorio, M. A.; Marie, J.-J.; Boivin, E.; Robertson, A. W.; Nag, A.; Garcia-Fernandez, M.; Zhou, K.-J.; Bruce, P. G., First-cycle voltage hysteresis in Li-rich 3d cathodes associated with molecular O_2 trapped in the bulk. *Nat. Energy* **2020,** *5* (10), 777-785.

54. Zhuo, Z.; Liu, Y. S.; Guo, J.; Chuang, Y. D.; Pan, F.; Yang, W., Full Energy Range Resonant Inelastic X-ray Scattering of O_2 and CO_2: Direct Comparison with Oxygen Redox State in Batteries. *J. Phys. Chem. Lett.* **2020,** *11* (7), 2618-2623.

55. Clément, R.; Lun, Z.; Ceder, G., Cation-disordered rocksalt transition metal oxides and oxyfluorides for high energy lithium-ion cathodes. *Energy Environ. Sci.* **2020,** *13* (2), 345-373.

56. Chen, D.; Ahn, J.; Chen, G., An overview of cation-disordered lithium-excess rocksalt cathodes. *ACS Energy Lett.* **2021,** *6* (4), 1358-1376.

57. Zhao, X.; Tian, Y.; Lun, Z.; Cai, Z.; Chen, T.; Ouyang, B.; Ceder, G., Design principles for zero-strain Li-ion cathodes. *Joule* **2022**.

58. Yamamoto, K.; Zhou, Y.; Yabuuchi, N.; Nakanishi, K.; Yoshinari, T.; Kobayashi, T.; Kobayashi, Y.; Yamamoto, R.; Watanabe, A.; rikasa, Y.; Tsuruta, K.; Park, J.; Byon, H. R.; Tamenori, Y.; Ohta, T.; Uchimoto, Y., Charge

Compensation Mechanism of Lithium-Excess Metal Oxides with Different Covalent and Ionic Characters Revealed by Operando Soft and Hard X-ray Absorption Spectroscopy. *Chem. Mater.* **2019,** *32* (1), 139-147.

59. Hafiz, H.; Suzuki, K.; Barbiellini, B.; Tsuji, N.; Yabuuchi, N.; Yamamoto, K.; Orikasa, Y.; Uchimoto, Y.; Sakurai, Y.; Sakurai, H., Tomographic reconstruction of oxygen orbitals in lithium-rich battery materials. *Nature* **2021,** *594* (7862), 213-216.

60. Dai, K.; Wu, J.; Zhuo, Z.; Li, Q.; Sallis, S.; Mao, J.; Ai, G.; Sun, C.; Li, Z.; Gent, W. E.; Chueh, W. C.; Chuang, Y.-d.; Zeng, R.; Shen, Z.-x.; Pan, F.; Yan, S.; Piper, L. F. J.; Hussain, Z.; Liu, G.; Yang, W., High Reversibility of Lattice Oxygen Redox Quantified by Direct Bulk Probes of Both Anionic and Cationic Redox Reactions. *Joule* **2019,** *3* (2), 518-541.

61. Sharpe, R.; ouse, R. A.; Clarke, M. J.; Forstermann, D.; Marie, J. J.; Cibin, G.; Zhou, K. J.; Playford, H. Y.; Bruce, P. G.; Islam, M. S., Redox Chemistry and the Role of Trapped Molecular O_2 in Li-Rich Disordered Rocksalt Oxyfluoride Cathodes. *J. Am. Chem. Soc.* **2020,** *142* (52), 21799-21809.

62. Koo, S.; Lee, J.; Lee, J.; Yoon, S.; Kim, D., Importance of metal−oxygen bond for stable oxygen-redox reaction in Li-excess layered oxides. *Energy Stor. Mater.* **2021,** *42*, 764-772.

63. Li, Q.; Ning, D.; Wong, D.; An, K.; Tang, Y.; Zhou, D.; Schuck, G.; Chen, Z.; Zhang, N.; Liu, X., Improving the oxygen redox reversibility of Li-rich battery cathode materials via Coulombic repulsive interactions strategy. *Nature Commun.* **2022,** *13* (1), 1-13.

64. Hong, J.; Gent, W. E.; Xiao, P.; Lim, K.; Seo, D. H.; Wu, J.; Csernica, P. M.; Takacs, C. J.; Nordlund, D.; Sun, C. J.; Stone, K. H.; Passarello, D.; Yang, W.; Prendergast, D.; Ceder, G.; Toney, M. F.; Chueh, W. C., Metal-oxygen decoordination stabilizes anion redox in Li-rich oxides. *Nat. Mater.* **2019,** *18* (3), 256-265.

65. Sudayama, T.; Uehara, K.; Mukai, T.; Asakura, D.; Shi, X.-M.; Tsuchimoto, A.; Mortemard de Boisse, B.; Shimada, T.; Watanabe, E.; Harada, Y.; Nakayama, M.; Okubo, M.; Yamada, A., Multiorbital bond formation for stable oxygen-redox reaction in battery electrodes. *Energy Environ. Sci.* **2020,** *13* (5), 1492-1500.

66. Zhang, K.; Jiang, Z.; Ning, F.; Li, B.; Shang, H.; Song, J.; Zuo, Y.; Yang, T.; Feng, G.; Ai, X.; Xia, D., Metal-Ligand π Interactions in Lithium-Rich Li_2RhO_3 Cathode Material Activate Bimodal Anionic Redox. *Advanced Energy Materials* **2021,** *11* (30).

67. House, R. A. *et al.* Detection of trapped molecular O_2 in a charged Li-rich cathode by Neutron PDF. *Energy Environ. Sci.* **15**, 376-383 (2022).

68. Nowroozi, M. A.; Mohammad, I.; Molaiyan, P.; Wissel, K.; Munnangi, A. R.; Clemens, O., Fluoride ion batteries – past, present, and future. *J. Mater. Chem. A* **2021,** *9* (10), 5980-6012.

69. Schoonman, J.; Wolfert, A., Alloy-anodes in fluoride solid-state batteries. *J. Electrochem. Soc.* **1981,** *128* (7), 1522-1523.

70. Schoonman, J.; Wolfert, A., Solid-state galvanic cells with fast fluoride conducting electrolytes. *Solid State Ionics* **1981,** *3*, 373-379.

71. Schoonman, J., A solid-state galvanic cell with fluoride-conducting electrolytes. *J. Electrochem. Soc.* **1976,** *123* (12), 1772.

72. Ure Jr, R. W., Ionic conductivity of calcium fluoride crystals. *J. Chem. Phys.* **1957,** *26* (6), 1363-1373.

73. Van Gool, W., Fast ion transport in solids, solid state batteries and devices. (Proceedings of the NATO-sponsored advanced study institute of fast ion transport in solids, solid state batteries and devices, Belgirate, Italy 5-15 September 1972). **1973**.

74. Reau, J.; Lucat, C.; Campet, G.; Portier, J.; Hammou, A., Application du tracé des diagrammes d'impédance complexe à la détermination de la

conductivité ionique des solutions solides $Ca_{1-x}Y_xF_{2+x}$: Corrélations entre propriétés electriques et structurales. *J. Solid. State. Chem.* **1976,** *17* (1-2), 123-129.

75. Sher, A.; Solomon, R.; Lee, K.; Muller, M., Transport Properties of LaF_3. *Phys. Rev.* **1966,** *144* (2), 593.

76. Frant, M. S.; Ross Jr, J. W., Electrode for sensing fluoride ion activity in solution. *Science* **1966,** *154* (3756), 1553-1555.

77. Roos, A.; Schoonman, J., Electronic conductivity in $La_{1-x}Ba_xF_{3-x}$ crystals. *Solid State Ionics* **1984,** *13* (3), 205-211.

78. Takahashi, T.; Iwahara, H.; Ishikawa, T., Ionic conductivity of doped cerium trifluoride. *J. Electrochem. Soc.* **1977,** *124* (2), 280.

79. Sorokin, N.; Sobolev, B., Nonstoichiometric fluorides—Solid electrolytes for electrochemical devices: A review. *Crystallogr. Rep.* **2007,** *52* (5), 842-863.

80. Breuer, S.; Gombotz, M.; Pregartner, V.; Hanzu, I.; Wilkening, M., Heterogeneous F anion transport, local dynamics and electrochemical stability of nanocrystalline $La_{1-x}Ba_xF_{3-x}$. *Energy Stor. Mater.* **2019,** *16*, 481-490.

81. Grenier, A.; Porras-Gutierrez, A. G.; Body, M.; Legein, C.; Chretien, F.; Raymundo-Piñero, E.; Dollé, M.; Groult, H.; Dambournet, D., Solid fluoride electrolytes and their composite with carbon: issues and challenges for rechargeable solid state fluoride-ion batteries. *J. Phys. Chem. C.* **2017,** *121* (45), 24962-24970.

82. Dieudonné, B.; Chable, J.; Mauvy, F.; Fourcade, S.; Durand, E.; Lebraud, E.; Leblanc, M.; Legein, C.; Body, M.; Maisonneuve, V., Exploring the $Sm_{1-x}Ca_xF_{3-x}$ Tysonite Solid Solution as a Solid-State Electrolyte: Relationships between Structural Features and F^- Ionic Conductivity. *J. Phys. Chem. C.* **2015,** *119* (45), 25170-25179.

83. Dieudonné, B.; Chable, J.; Body, M.; Legein, C.; Durand, E.; Mauvy, F.; Fourcade, S.; Leblanc, M.; Maisonneuve, V.; Demourgues, A., The key role

of the composition and structural features in fluoride ion conductivity in tysonite $Ce_{1-x}Sr_xF_{3-x}$ solid solutions. *Dalton Trans.* **2017,** *46* (11), 3761-3769.

84. Liu, L.; Yang, L.; Liu, M.; Li, X.; Shao, D.; Luo, K.; Wang, X.; Luo, Z., SnF_2-based fluoride ion electrolytes $MSnF_4$ (M= Ba, Pb) for the application of room-temperature solid-state fluoride ion batteries. *J. Alloys Compd.* **2020,** *819*, 152983.

85. Castiglione, M.; Madden, P.; Berastegui, P.; Hull, S., The crystal structure of α-$PbSnF_4$ and its anion diffusion mechanism. *J. Phys. Condens. Matter.* **2005,** *17* (6), 845.

86. Murakami, M.; Morita, Y.; Yonemura, M.; Shimoda, K.; Mori, M.; Koyama, Y.; Kawaguchi, T.; Fukuda, K.; Ishikawa, Y.; Kamiyama, T.; Uchimoto, Y.; Ogumi, Z., High Anionic Conductive Form of $Pb_xSn_{2-x}F_4$. *Chem. Mater.* **2019,** *31* (18), 7704-7710.

87. Zhang, D.; Nakano, H.; Yamamoto, K.; Tanaka, K.; Yahara, T.; Imai, K.; Mori, T.; Miki, H.; Nakanishi, S.; Iba, H., Rate-determining process at electrode/electrolyte interfaces for all-solid-state fluoride-ion batteries. *ACS Appl. Mater. Interfaces* **2021,** *13* (25), 30198-30204.

88. Denes, G.; Milova, G.; Madamba, M.; Perfiliev, M., Structure and ionic transport of $PbSnF_4$ superionic conductor. *Solid State Ionics* **1996,** *86*, 77-82.

89. Hagenmuller, P.; Réau, J.-M.; Lucat, C.; Matar, S.; Villeneuve, G., Ionic conductivity of fluorite-type fluorides. *Solid State Ionics* **1981,** *3*, 341-345.

90. Fujisaki, F.; Mori, K.; Yonemura, M.; Ishikawa, Y.; Kamiyama, T.; Otomo, T.; Matsubara, E.; Fukunaga, T., Mechanical synthesis and structural properties of the fast fluoride-ion conductor $PbSnF_4$. *J Solid State Chem.* **2017,** *253*, 287-293.

91. Nowroozi, M. A.; Clemens, O., Insights on the behavior of conversion-based anode materials for fluoride ion batteries by testing against an intercalation-based reference cathode. *ACS Appl. Energy Mater.* **2018,** *1* (11), 6626-6637.

92. Thieu, D. T.; Fawey, M. H.; Bhatia, H.; Diemant, T.; Chakravadhanula, V. S. K.; Behm, R. J.; Kübel, C.; Fichtner, M., CuF_2 as reversible cathode for fluoride ion batteries. *Adv. Funct. Mater.* **2017,** *27* (31), 1701051.

93. Zhang, D.; Yamamoto, K.; Ochi, A.; Wang, Y.; Yoshinari, T.; Nakanishi, K.; Nakano, H.; Miki, H.; Nakanishi, S.; Iba, H.; Uchiyama, T.; Watanabe, T.; Amezawa, K.; Uchimoto, Y., Understanding the reaction mechanism and performances of 3*d* transition metal cathodes for all-solid-state fluoride ion batteries. *J. Mater. Chem. A* **2021,** *9* (1), 406-412.

94. Nakano, H.; Matsunaga, T.; Mori, T.; Nakanishi, K.; Morita, Y.; Ide, K.; Okazaki, K.-i.; Orikasa, Y.; Minato, T.; Yamamoto, K., Fluoride-ion shuttle battery with high volumetric energy density. *Chem. Mater.* **2020,** *33* (1), 459-466.

95. Haruyama, J.; Okazaki, K. I.; Morita, Y.; Nakamoto, H.; Matsubara, E.; Ikeshoji, T.; Otani, M., Two-Phase Reaction Mechanism for Fluorination and Defluorination in Fluoride-Shuttle Batteries: A First-Principles Study. *ACS Appl. Mater. Interfaces* **2020,** *12* (1), 428-435.

96. Zhang, D.; Yoshinari, T.; Yamamoto, K.; Kitaguchi, Y.; Ochi, A.; Nakanishi, K.; Miki, H.; Nakanishi, S.; Iba, H.; Watanabe, T.; Uchiyama, T.; Orikasa, Y.; Amezawa, K.; Uchimoto, Y., Cu–Pb Nanocomposite Cathode Material toward Room-Temperature Cycling for All-Solid-State Fluoride-Ion Batteries. *ACS Appl. Energy Mater.* **2021,** *4* (4), 3352-3357.

97. Greaves, C.; Francesconi, M. G., Fluorine insertion in inorganic materials. *Current Opinion in Solid State and Materials Science* **1998,** *3* (2), 132-136.

98. McCabe, E. E.; Greaves, C., Fluorine insertion reactions into pre-formed metal oxides. *J. Fluor. Chem.* **2007,** *128* (4), 448-458.

99. Clemens, O.; Slater, P. R., Topochemical modifications of mixed metal oxide compounds by low-temperature fluorination routes. *Rev. Inorg. Chem.* **2013,** *33* (2-3), 105-117.

100. Ai-Mamouri, M.; Edwards, P.; Greaves, C.; Slaski, M., Synthesis and

superconducting properties of the strontium copper oxy-fluoride $Sr_2CuO_2F_{2+\delta}$. *Nature* **1994,** *369* (6479), 382-384.

101. Case, G. S.; Hector, A. L.; Levason, W.; Needs, R. L.; Thomas, M. F.; Weller, M. T., Syntheses, powder neutron diffraction structures and Mössbauer studies of some complex iron oxyfluorides: $Sr_3Fe_2O_6F_{0.87}$, Sr_2FeO_3F and $Ba_2InFeO_5F_{0.68}$. *J. Mater. Chem.* **1999,** *9* (11), 2821-2827.

102. Berry, F. J.; Heap, R.; Helgason, Ö.; Moore, E. A.; Shim, S.; Slater, P. R.; Thomas, M. F., Magnetic order in perovskite-related $SrFeO_2F$. *J. Phys. Condens. Matter.* **2008,** *20* (21).

103. Sivakumar, T.; Wiley, J. B., Topotactic route for new layered perovskite oxides containing fluorine: $Ln_{1.2}Sr_{1.8}Mn_2O_7F_2$ (Ln=Pr, Nd, Sm, Eu, and Gd). *Mater. Res. Bull.* **2009,** *44* (1), 74-77.

104. Tsujimoto, Y.; Yamaura, K.; Takayama-Muromachi, E., Oxyfluoride Chemistry of Layered Perovskite Compounds. *Appl. Sci.* **2012,** *2* (1), 206-219.

105. Shi, T.; Zhang, Y.-Q.; Tu, Q.; Wang, Y.; Scott, M.; Ceder, G., Characterization of mechanical degradation in an all-solid-state battery cathode. *J. Mater. Chem. A* **2020,** *8* (34), 17399-17404.

106. Koerver, R.; Zhang, W.; de Biasi, L.; Schweidler, S.; Kondrakov, A. O.; Kolling, S.; Brezesinski, T.; Hartmann, P.; Zeier, W. G.; Janek, J., Chemo-mechanical expansion of lithium electrode materials–on the route to mechanically optimized all-solid-state batteries. *Energy Environ. Sci.* **2018,** *11* (8), 2142-2158.

107. Sakuda, A.; Hayashi, A.; Tatsumisago, M., Sulfide solid electrolyte with favorable mechanical property for all-solid-state lithium battery. *Sci. Rep.* **2013,** *3* (1), 1-5.

108. Clemens, O.; Rongeat, C.; Reddy, M. A.; Giehr, A.; Fichtner, M.; Hahn, H., Electrochemical fluorination of perovskite type $BaFeO_{2.5}$. *Dalton Trans.* **2014,** *43* (42), 15771-8.

109. Aikens, L. D.; Gillie, L. J.; Li, R. K.; Greaves, C., Staged fluorine insertion into manganese oxides with Ruddlesden–Popper structures: $LaSrMnO_4F$ and $La_{1.2}Sr_{1.8}Mn_2O_7F$. *J. Mater. Chem.* **2002,** *12* (2), 264-267.

110. Aikens, L. D.; Li, R. K.; Greaves, C., The synthesis and structure of a new oxide fluoride, $LaSrMnO_4F$, with staged fluorine insertion. *Chem. Comm.* **2000,** (21), 2129-2130.

111. Wells, A. F., *Structural inorganic chemistry*. Oxford university press: 2012.

112. Nowroozi, M. A.; Wissel, K.; Rohrer, J.; Munnangi, A. R.; Clemens, O., LaSrMnO4: Reversible Electrochemical Intercalation of Fluoride Ions in the Context of Fluoride Ion Batteries. *Chem. Mater.* **2017,** *29* (8), 3441-3453.

113. Nowroozi, M. A.; Wissel, K.; Donzelli, M.; Hosseinpourkahvaz, N.; Plana-Ruiz, S.; Kolb, U.; Schoch, R.; Bauer, M.; Malik, A. M.; Rohrer, J.; Ivlev, S.; Kraus, F.; Clemens, O., High cycle life all-solid-state fluoride ion battery with La_2NiO_{4+d} high voltage cathode. *Comm. Mater.* **2020,** *1* (1).

114. Wissel, K.; Heldt, J.; Groszewicz, P. B.; Dasgupta, S.; Breitzke, H.; Donzelli, M.; Waidha, A. I.; Fortes, A. D.; Rohrer, J.; Slater, P. R.; Buntkowsky, G.; Clemens, O., Topochemical Fluorination of La_2NiO_{4+d}: Unprecedented Ordering of Oxide and Fluoride Ions in $La_2NiO_3F_2$. *Inorg. Chem.* **2018,** *57* (11), 6549-6560.

115. Nowroozi, M. A.; Ivlev, S.; Rohrer, J.; Clemens, O., La_2CoO_4: a new intercalation based cathode material for fluoride ion batteries with improved cycling stability. *J. Mater. Chem. A* **2018,** *6* (11), 4658-4669.

116. Luo, J.; Dai, C. Y.; Wang, Z.; Liu, K.; Mao, W. G.; Fang, D. N.; Chen, X., In-situ measurements of mechanical and volume change of $LiCoO_2$ lithium-ion batteries during repeated charge–discharge cycling by using digital image correlation. *Measurement* **2016,** *94*, 759-770.

117. Kageyama, H.; Hayashi, K.; Maeda, K.; Attfield, J. P.; Hiroi, Z.; Rondinelli, J. M.; Poeppelmeier, K. R., Expanding frontiers in materials chemistry and physics with multiple anions. *Nat. Commun.* **2018,** *9* (1), 772.

118. Yajima, T.; Takeiri, F.; Aidzu, K.; Akamatsu, H.; Fujita, K.; Yoshimune, W.; Ohkura, M.; Lei, S.; Gopalan, V.; Tanaka, K.; Brown, C. M.; Green, M. A.; Yamamoto, T.; Kobayashi, Y.; Kageyama, H., A labile hydride strategy for the synthesis of heavily nitridized $BaTiO_3$. *Nat. Chem.* **2015,** *7* (12), 1017-23.

119. Freysoldt, C.; Grabowski, B.; Hickel, T.; Neugebauer, J.; Kresse, G.; Janotti, A.; Van de Walle, C. G., First-principles calculations for point defects in solids. *Rev Mod Phys.* **2014,** *86* (1), 253-305.

Chapter 2. Anion Substitution at Apical Sites of Ruddlesden−Popper-type Cathodes toward High Power Density

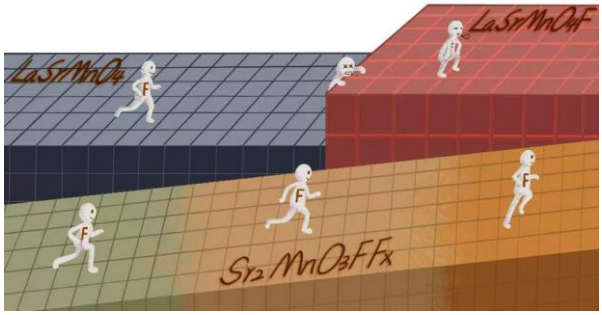

All-solid-state fluoride ion batteries (FIBs) that use fluoride ions as carrier ions offer a new horizon for next-generation energy storage devices owing to their high specific capacities. Materials that utilize topochemical insertion and desorption reactions of fluoride ions have been proposed as cathodes for FIBs; among them, Ruddlesden–Popper-type perovskite-related compounds are promising cathode materials owing to reversible fluoride ion (de)intercalations with low volume expansion compared to conversion-type cathode materials. Although it is essential to improve the power density of the compounds for practical application, the relationship between the structure and power density is still not clearly understood. In this study, we synthesized chemically fluorinated Ruddlesden–Popper compounds, $LaSrMnO_4$ and apical-site-substituted oxyfluoride Sr_2MnO_3F, and examined the correlations between their structures and electrochemical properties; Sr_2MnO_3F showed better power density. Open-circuit voltage measurements, X-ray absorption spectroscopy, and synchrotron X-ray diffraction revealed that electrochemical F^- insertion into $LaSrMnO_4$ proceeds via a two-phase reaction with relatively high volume expansion, whereas that into Sr_2MnO_3F proceeds via a solid-solution reaction with relatively low volume expansion. The substitution of oxygen in the apical sites with fluorine suppressed phase transitions with large volume changes, resulting in improved power density.

2.1 Introduction

On account of the rapid popularization of wearable electronic devices and electric vehicles, the demands for batteries with higher energy densities and that are safer compared to commercial Li-ion batteries have become increasingly urgent. To meet these demands, battery systems that use multivalent cations as charge carriers, such as Mg^{2+}, Ca^{2+}, and Al^{3+}, are attracting attention, and battery systems that use anions (e.g., Cl^{-}, F^{-}) as charge carriers are being actively studied to address the low mobility of multivalent cations.[1–8] Among these battery systems, all-solid-state fluoride ion batteries (FIBs) with fluoride ions as carriers and without a flammable organic electrolyte are highly promising with respect to theoretical high energy densities and safety.[9–11] Conversion-type metal/metal fluorides (Me/MeF_x) have undergone extensive development as cathode materials for all-solid-state fluoride batteries.[9,10] Although these cathodes exhibit high theoretical capacities, they suffer from high volume expansion and contraction during charging and discharging, resulting in poor cycle and rate characteristics.[12]

In order to avoid the volume changes, several intercalation cathodes with Ruddlesden–Popper $A_{n+1}B_nO_{3n+1}$ (n = 1, 2) perovskite structures, in which A is a rare-earth or alkaline earth element and B is a transition metal, were developed in the pioneering work of Clemens et al. to replace conversion-type cathodes for all-solid-state FIBs.[13–16] Interstitial sites in the rock-salt slabs of $A_{n+1}B_nO_{3n+1}$ (n = 1, 2) compounds are available for fluoride ion intercalation.[17–22] It has been reported that the volume changes of $A_{n+1}B_nO_{3n+1}$ (n = 1, 2) cathodes upon F^{-} intercalation are smaller than those of conversion cathodes, allowing reversible charging and discharging.[16] However, owing to the relatively large polarization of $A_{n+1}B_nO_{3n+1}$ (n = 1, 2), further improvement of the power density is required.

In order to improve the power density of cathode materials for lithium-ion batteries and/or magnesium batteries, it is effective to suppress the volume expansion/shrinkage during the insertion and desorption of ion carriers.[23,24] That material design should be

applicable to cathode material design for FIBs. Because the lattice constant increase along the *c*-axis of $A_{n+1}B_nO_{3n+1}$ (n = 1, 2) with F^- intercalation is due to the Coulomb repulsion between the intercalated F^- and the anion at the nearest apical site in the host lattice,[19,25] suppressing this Coulomb repulsion is an effective strategy for reducing lattice expansion.

In this study, we focused on $LaSrMnO_4$[13] and Sr_2MnO_3F[26] as model A_2BO_4 (n = 1) compounds; the apical sites of the perovskite interlayer in $LaSrMnO_4$ only contain oxygen, and 50% of the oxygen in the apical sites of the perovskite layer in Sr_2MnO_3F is substituted with F. Substitution of the oxide ions in the apical sites with fluoride ions may reduce the Coulomb repulsion with inserted fluoride ions between the lattices, thus reducing lattice expansion during the insertion and desorption of fluoride ions. We examined the electrochemical performances and crystal structure changes with fluoride ion (de)intercalation of chemically fluorinated $LaSrMnO_4$ and Sr_2MnO_3F to clarify the effect of anion substitution in the apical sites on the power density and lattice volume change. Sr_2MnO_3F showed significantly higher power density than $LaSrMnO_4$. The reason was that the electrochemical intercalation of F^- into $LaSrMnO_4$ proceeds via a two-phase coexistence reaction with a large volume change, whereas that into Sr_2MnO_3F proceeds via a solid-solution reaction with a small volume change.

2.2 Experimental

2.2.1 Material synthesis

Sr_2MnO_3F. Sr_2MnO_3F was synthesized via a high-pressure-assisted solid-state reaction.[26] SrO was prepared by heating $SrCO_3$ (99.9%, FUJIFILM Wako Pure Chemical Corp.) at 800 °C in flowing O_2 gas, and Mn_2O_3 was prepared by heating $MnCO_3$ (99.9%, FUJIFILM Wako Pure Chemical Corp.) at 800 °C overnight. SrF_2 (99.9%, Rare Metallic Co., Ltd.), SrO, and Mn_2O_3 were mixed in a stoichiometric ratio in an agate mortar in an Ar-filled glove box. The mixture was transferred into a platinum capsule and sealed in a high-pressure cell. Sr_2MnO_3F was obtained after the cell was

maintained at 6 GPa at 1800 °C for 45 min.

$LaSrMnO_4$. $LaSrMnO_4$ was synthesized through a solid-state reaction as per a previous report.[13] A stoichiometric ratio of $SrCO_3$ (≥99.9%, FUJIFILM), Mn_2O_3 (99%, Sigma-Aldrich), and La_2O_3 (99.9%, Alfa Aesar), which was dried at 100 °C under vacuum overnight, were ground using a mortar and then pelletized. The mixture of the starting materials was heated at 1450 °C for 24 h twice in flowing Ar gas with one intermediate re-grinding.

Solid electrolyte. $La_{0.9}Ba_{0.1}F_{2.9}$ (LBF) was employed as the electrolyte in this study.[27] A stoichiometric ratio of LaF_3 (99.9%, Kojundo Chemical Laboratory Co., Ltd.) and BaF_2 (99.9%, Kojundo Chemical Laboratory Co., Ltd.) were thoroughly ground using a mortar and the mixture was subsequently sealed into an agate ball milling pot and milled at 600 rpm for 10 h. Finally, the ball-milled mixture was pelletized and sintered at 1000 °C for 4 h. All of the above operations were completed in an Ar-filled glove box.

Chemical fluorination. Fluorine was inserted into the as-prepared materials via a chemical method.[13,28] The as-prepared precursors ($LaSrMnO_4$ or Sr_2MnO_3F) and the fluorinating agent, AgF_2 (≥98%, Sigma-Aldrich), were ground in a stoichiometric ratio using a mortar and pelletized. The pellet was then loaded into a polytetrafluoroethylene sleeve and sealed in a steel autoclave. All operations were carried out in an Ar-filled glove box. Finally, the reactor was heated at 250 °C for 48 h.

2.2.2 Electrochemical measurements

Electrochemical measurements of chemically fluorinated $LaSrMnO_4$ and Sr_2MnO_3F were performed using two-electrode cells. For the cathode composite, fluorinated $LaSrMnO_4$ or Sr_2MnO_3F was mixed with the solid electrolyte, LBF, and vapor grown carbon fiber (VGCF, Showa Denko K.K.) at a weight ratio of 3:6:1 by ball milling for 10 h. For the anode composite, elemental Pb (99.9%, Kojundo Chemical Laboratory Co., Ltd.), PbF_2 (99.9%, Kojundo Chemical Laboratory Co., Ltd.), LBF, and VGCF were ball-milled at a weight ratio of 3:2:4:1. The powders of the cathode

composite, solid electrolyte, and anode composite were pressed into a pellet under 360 MPa for 5 min, holding by two pieces of gold foil as current collectors.

The electrochemical performances of chemically fluorinated Sr_2MnO_3F and $LaSrMnO_4$ were examined using an HJ1010SD8 (Hokuto Denko Corporation) electrochemical workstation. For galvanostatic charge/discharge tests, a current density of 5 mA g^{-1} was employed to evaluate the cycling stabilities; current densities up to 100 mA g^{-1} were used for rate capabilities. The cutoff voltage was set to −1.5 to 0.6 V vs. Pb/PbF_2. The open-circuit voltages (OCVs) at various states of charge (SOCs) were examined through galvanostatic measurements; the cell was relaxed for 12 h after each 5 mA g^{-1} current pulse.

2.2.3 Characterization

Synchrotron X-ray diffraction (XRD) measurements were performed at room temperature at synchrotron radiation facility SPring-8 (BL02B2), Japan. Ex situ samples upon charging/discharging were peeled off the cathode side and sealed in a capillary tube. The synchrotron radiation X-rays were monochromatized to a wavelength of 0.41373 Å, which was calibrated using a CeO_2 standard sample. Rietveld refinements were performed using the JANA2006 package[29] to obtain a detailed information on the structural changes during charging and discharging. The crystal structure models for chemically fluorinated Sr_2MnO_3F and $LaSrMnO_4F$ were drawn using the program VESTA.[30] X-ray absorption spectroscopy (XAS) measurements for Mn *K* and *L*-edge were performed at beamlines BL14B2 and BL27SU in SPring-8, Japan. All spectra were collected in the partial fluorescence mode. The morphologies of chemically fluorinated $LaSrMnO_4$ and Sr_2MnO_3F were observed using field emission scanning electron microscope (FE-SEM, Hitachi SU-8000).

2.3 Results and discussion

2.3.1 Crystal structures of $LaSrMnO_4F$ and $Sr_2MnO_3F_2$

The crystal structures of as-prepared $LaSrMnO_4$, fluorinated $LaSrMnO_4$, Sr_2MnO_3F, and fluorinated $LaSrMnO_4$ were examined using synchrotron XRD coupled with Rietveld refinement (Fig. 2.1, Figure 2.2, and Table 2.1).

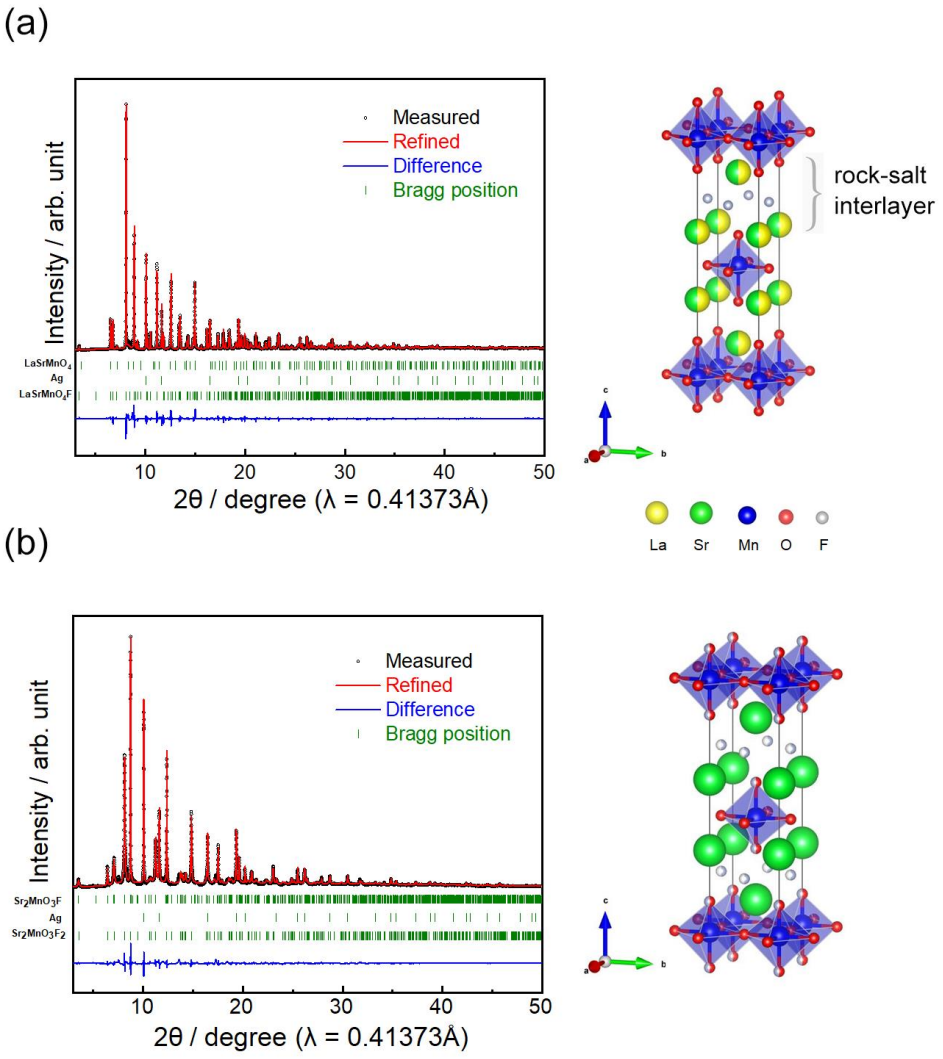

Figure 2.1 Crystal structures of chemically fluorinated $LaSrMnO_4$ and Sr_2MnO_3F. XRD patterns coupled with Rietveld analysis refinement and refined crystal structures of (a) $LaSrMnO_4F$ and (b) $Sr_2MnO_3F_2$.

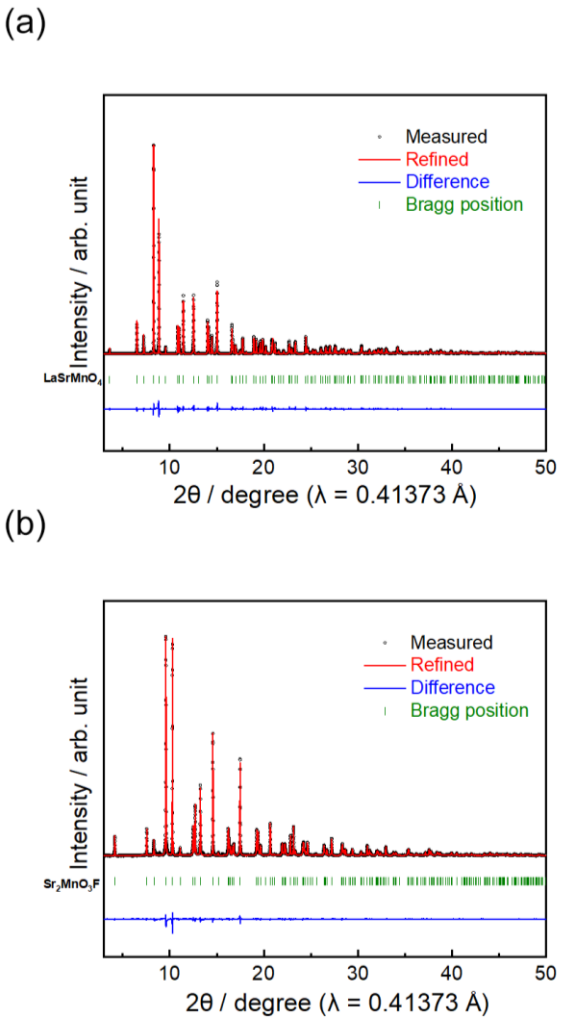

Figure 2.2 X-ray diffraction pattern and Rietveld refinement of (a) $LaSrMnO_4$, (b) Sr_2MnO_3F.

Table 2.1 (a) Refined structural data for chemically fluorinated Sr_2MnO_3F.

Atom	Wyckoff position	x	y	z	Occupancy
Sr	4e	0	0	0.35828	1
Mn	2a	0	0	0.00000	1
O1	4c	0	0.5	0.00000	1
O2	4e	0	0	0.11656	0.5
F1	4e	0	0	0.11656	0.5
F2	4d	0	0.5	0.25000	0.5

Wavelength = 0.41391 Å; Space group: *I*4/*mmm*; $R_p = 3.44\%$; $R_{wp} = 6.54\%$; $a = b =$ 3.833910 Å; $c = 13.45916$ Å.

(b) Refined structural data for chemically fluorinated $LaSrMnO_4$.

Atom	Wyckoff position	x	y	z	Occupancy
La1	2c	0.5	0	0.59875	0.5
Sr2	2c	0.5	0	0.59875	0.5
La2	2c	0.5	0	0.88312	0.5
Sr2	2c	0.5	0	0.88312	0.5
Mn1	2c	0	0.5	0.72889	1
O1	4f	0	0	0.72202	1
O2	2c	0	0.5	0.58088	1
O3	2c	0	0.5	0.85491	1
F1	2a	0	0	0.00000	1

Wavelength = 0.41391 Å; Space group: *P*4/*nmm*; R_p = 2.90%; R_{wp} = 5.11 %; $a = b$ = 3.77962 Å; c = 14.08493 Å.

(c) Refined structural data for Sr_2MnO_3F.

Atom	Wyckoff position	x	y	z	Occupancy
Sr	4e	0	0	0.36045	1
Mn	2a	0	0	0.00000	1
O1	4c	0	0.5	0.00000	1
O2	4e	0	0	0.17150	0.5
F	4e	0	0.5	0.17150	0.5

Wavelength = 0.41391 Å; Space group: *I*4/*mmm*; R_p = 4.87%; R_{wp} = 7.11%; $a = b$ = 3.79955 Å; c = 13.29342 Å.

(d) Refined structural data for $LaSrMnO_4$.

Atom	Wyckoff position	x	y	z	Occupancy
La	4e	0	0	0.35651	0.5
Sr	4e	0	0	0.35651	0.5
Mn	2a	0	0	0.00000	1
O1	4c	0	0.5	0.00000	1
O2	4e	0	0	0.17454	1

Wavelength = 0.41391 Å; Space group: *I*4/*mmm*; R_p = 4.77%; R_{wp} = 6.35%; $a = b$ = 3.79577 Å; c = 13.14748 Å.

For $LaSrMnO_4$, all peaks were indexed to a space group of *I*4/*mmm* without any impurities and the lattice constants were a = 3.79577(99) and c = 13.14748(30) Å. For fluorinated $LaSrMnO_4$, the XRD patterns were fitted using $LaSrMnO_4F$ with a space group of *P*4/*mmm*, $LaSrMnO_4$, and Ag. The lattice constants of $LaSrMnO_4F$ were a = 3.77962(36) and c = 14.08493(44) Å. Rietveld refinement showed that the inserted fluoride ions occupied every second rock-salt interlayer (Figure 1a and Supplementary Table 1), and the c-axis expansion in $LaSrMnO_4F/LaSrMnO_4$ was $\Delta c/c \approx 7.13\%$. These crystal structure changes of $LaSrMnO_4$ with fluoride ions are in agreement with the results of previous studies.[13,19,25] For $SrMnO_3F$, all peaks were indexed to a space group of *I*4/*mmm* without any impurities. The lattice constants were a = 3.79955(16) and c = 13.29342(69) Å, which were consistent with those from a previous study.[30] Both materials suffer from the Jahn-Teller effect because the valence of Mn is trivalent in Sr_2MnO_3F and $LaSrMnO_4$. As is shown in Table 2.2 and Fig. 2.3, the Mn – (O_{ap}/F_{ap}) and Mn – O_{eq} bond lengths of the Sr_2MnO_3F are 2.2780 and 1.8998 Å, respectively, and the ratio of the apical bond to the equatorial bond is 1.20. The Mn – O_{ap} and Mn – O_{eq} bond lengths of the $LaSrMnO_4$ are 2.295 and 1.898 Å, respectively and the ratio of the apical bond to the equatorial bond is 1.21. The ratio of the Mn− O_{ap}/Mn−O_{eq} bond length in Sr_2MnO_3F is comparable to that of the Mn− O_{ap}/Mn−O_{eq} bond length in $LaSrMnO_4$, implying that the Jahn-Teller effect is not the main reason that why the c-axis value of Sr_2MnO_3F is larger than that of $LaSrMnO_4$. Therefore, the difference in the initial state lattice constants ($LaSrMnO_4$ and Sr_2MnO_3F) is due to the difference in the ionic radii of the A-site cations (Sr^{2+}: 131, La^{3+}: 121.6 pm).[31]

Table 2.2 Lattice constant and bond length that extracted from the result of Rietveld refinement.

		Sr_2MnO_3F	**$LaSrMnO_4$**	**$Sr_2MnO_3F_2$**	**$LaSrMnO_4F$**
Lattice constant / Å	a axis	3.79955(16)	3.79577(99)	3.83391(41)	3.77962(36)
	c axis	13.29342(69)	13.14748(30)	13.45916(84)	14.08493(44)
Bond length / Å	Mn-O_{ap}/F_{ap}	2.27982(12)	2.29470(6)	1.56880(9)	1.77552(0) 2.14783(0)*
	Mn-O_{eq}	1.89978(8)	1.89790(5)	1.91950(7)	1.89158(0)
	La/Sr-O_{ap}/F_{ap}	2.51179(14)	2.39240(6)	3.25330(17)	2.46753(0) 3.70377(0)*
	La/Sr-$F_{interlayer}$			1.45736	1.65089
	O_{ap}/F_{ap}-$F_{interlayer}$			1.79599	2.05288

* is the value of bond length in the fluoride ion occupied interlayer.

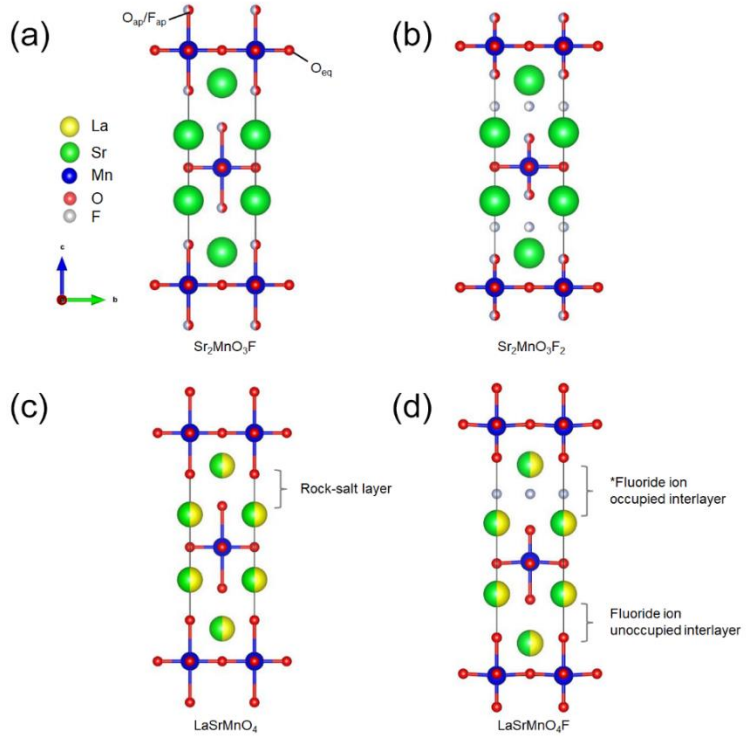

Figure 2.3 Crystal structure of (a) Sr_2MnO_3F, (b)$Sr_2MnO_3F_2$, (c)$LaSrMnO_4$, and $LaSrMnO_4F$ viewed along the *a* axis.

For fluorinated Sr_2MnO_3F, the XRD patterns were fitted using $Sr_2MnO_3F_2$ with a space group of *I*4/*mmm*, Sr_2MnO_3F, and Ag. The lattice constants of $Sr_2MnO_3F_2$ were a = 3.833910(41) and c = 13.45916(84) Å. Rietveld refinement showed that half of the accessible sites for F^- intercalation in $Sr_2MnO_3F_2$ were occupied by chemically inserted F^- and the c-axis expansion in $Sr_2MnO_3F_2/Sr_2MnO_3F$ was $\Delta c/c \approx 1.25\%$ (Figure 2.1b and Table 2.1), indicating the successful chemical fluorination of Sr_2MnO_3F. The O_{ap}/F_{ap} - $F_{interlayer}$ bond length in $Sr_2MnO_3F_2$ (1.79599 Å) is smaller than the O_{ap}-$F_{interlayer}$ bond length in $LaSrMnO_4$ (2.05288 Å) as shown in Table 2.2. The crystal structure changes of Sr_2MnO_3F with chemical fluorination are completely different from those of $LaSrMnO_4$.[19,25] The lower c-axis expansion of $Sr_2MnO_3F_2/Sr_2MnO_3F$ compared to that of $LaSrMnO_4F/LaSrMnO_4$ is attributed to the weaker electrostatic repulsions between inserted F^- and apical-site anions because 50% of O^{2-} at apical site is substituted to F^- in the $Sr_2MnO_3F_2$, compared to $LaSrMnO_4$.[19,25] The particle sizes of $LaSrMnO_4F$ and $Sr_2MnO_3F_2$ were approximately 5–10 μm (Fig. 2.4).

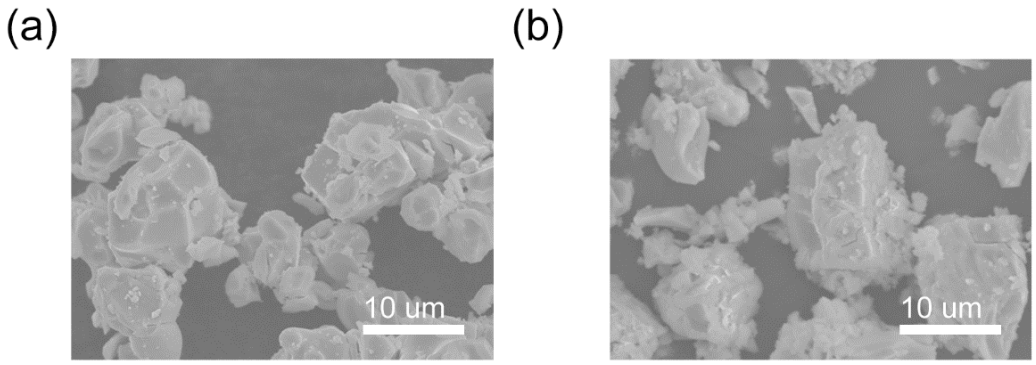

Figure 2.4 SEM images of (a) $LaSrMnO_4F$, (b) $Sr_2MnO_3F_2$.

2.3.2 Electrochemical performance

The electrochemical properties of $LaSrMnO_4F$ and $Sr_2MnO_3F_2$ obtained through chemical fluorination were evaluated. The discharge/charge measurements for $LaSrMnO_4F$ revealed a capacity of 70 mAh g^{-1} with a clear plateau at −0.1 V during the discharge process, a capacity of 72 mAh g^{-1} with a flat plateau at 0.2 V during the charge process (Fig. 2.5a), and good cyclability (Fig. 2.6a). The clear plateau at around 0.2 V was also observed in previous study.[17] $Sr_2MnO_3F_2$ gave a capacity of 84 mAh g^{-1}

with plateaus at 0.2 and −0.2 V during the discharge process and a capacity of 83 mAh g^{-1} with plateaus at −0.2 and 0.3 V during the charge process (Figure 2.5b). Although the cyclability of $Sr_2MnO_3F_2$ was worse than that of $LaSrMnO_4F$ (Fig. 2.6b), it was significantly better than those of the conversion-type electrodes.[1,9,32,33] Comparing the capacity retention at various current densities of $LaSrMnO_4F$ and $Sr_2MnO_3F_2$, the $Sr_2MnO_3F_2$ showed better capacity retention at high current densities to $LaSrMnO_4F$ (Fig. 2.5c).

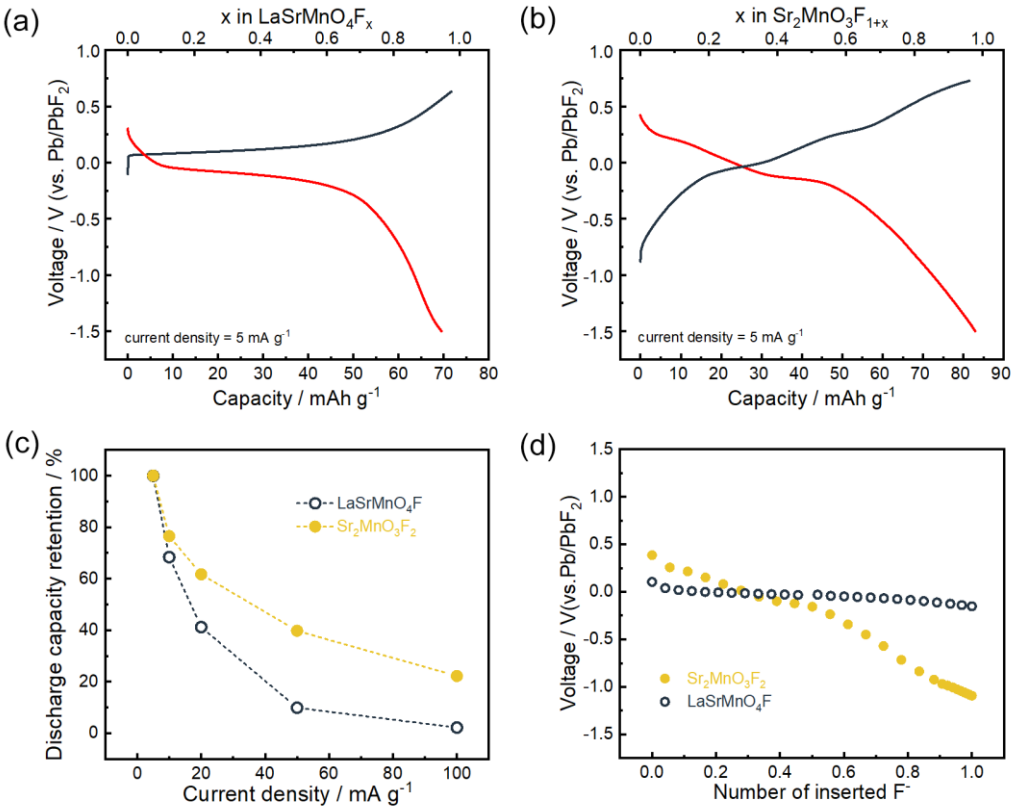

Figure 2.5 Electrochemical performances of $LaSrMnO_4F$ and $Sr_2MnO_3F_2$. Discharge/charge profiles of (a) $LaSrMnO_4F$ and (b) $Sr_2MnO_3F_2$. (c) Rate performance of discharge capacity retentions of the two active materials; the capacity was normalized for more intuitive comparison. (d) OCVs at various F^- contents.

The open-circuit voltage (OCVs) at various F contents during discharge for $LaSrMnO_4F$ and $Sr_2MnO_3F_2$ were measured and are shown in Fig. 2.5d and Fig. 2.7 For $LaSrMnO_4F$, a significantly flat OCV similar to that seen for $LiFePO_4$[34,35] was obtained over a wide range of F contents. In contrast, the OCV for $Sr_2MnO_3F_2$

decreased gradually with increasing amount of inserted F. It is difficult to identify the reason of the polarization change observed while x > 0.5 in the $LaSrMnO_4$ at present stage because there are many factors that affect polarization such as phase transition of $LaSrMnO_4$ with volume change, the associated changes in the diffusion coefficient of F^- in the host lattice and electronic conductivity occur during charging/discharging processes.

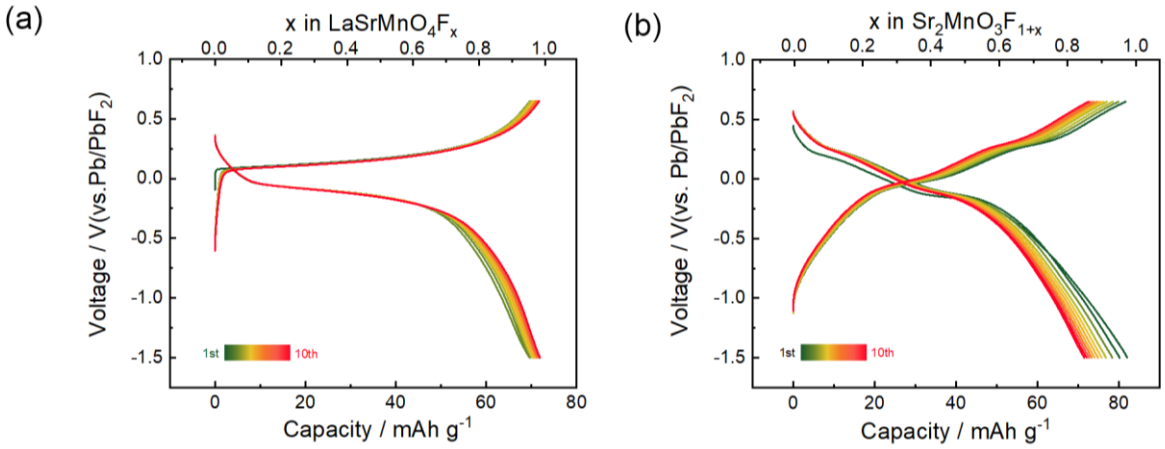

Figure 2.6 Cycle performance of the $LaSrMnO_4F$ and $Sr_2MnO_3F_2$ at 5 mA g^{-1} under 140°C.

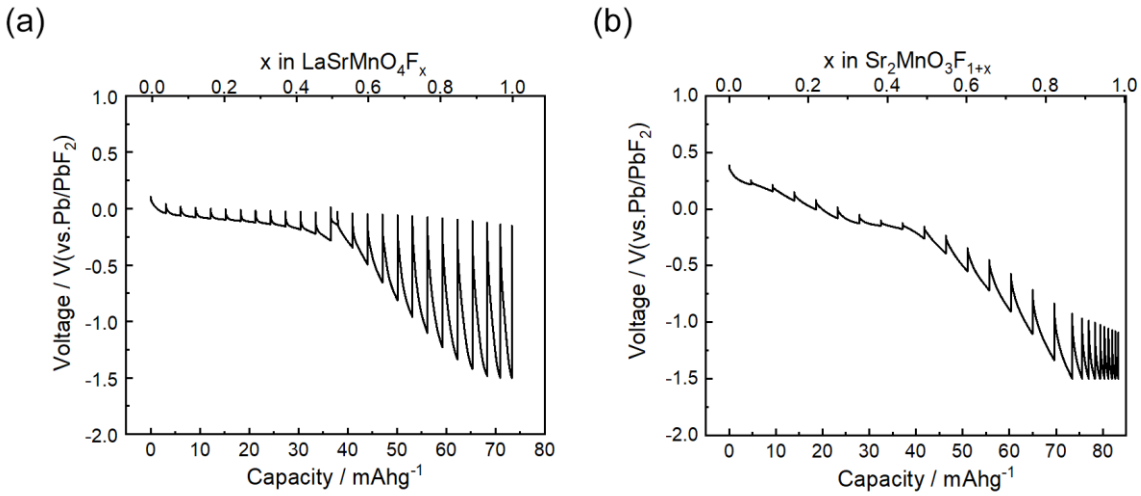

Figure 2.7. The OCV measurements of (a) the $LaSrMnO_4F$ and $Sr_2MnO_3F_2$. Discharge process was separated into 25 steps follows by 12 hours of rest.

2.3.3 X-ray absorption spectroscopy and reaction mechanism

The XAS spectra of the Mn *K*-edge and Mn *L*-edge for the $LaSrMnO_4F$ and $Sr_2MnO_3F_2$ during F^- insertion were obtained to examine the charge compensation of Mn in these compounds (Fig. 2.8). In the Mn *K*-edge spectra of $LaSrMnO_4F$ (Fig. 2.8a), the absorption edge shifted to a higher energy with the insertion of F into the fully discharged state (x = 0.05). In the Mn *L*-edge spectrum of $LaSrMnO_4F$ (Fig. 2.9a), the spectra also shifted to a higher energy region with the insertion of F into the fully discharged state. These results indicate that Mn in $LaSrMnO_4$ is oxidized during F^- insertion. The X-ray absorption near-edge spectra (XANES) for Mn *K*-edge of $LaSrMnO_4F$ showed the isosbestic points at 6557.2 and 6560.5 eV that were also observed for $LiFePO_4$,[36,37] indicating that F^- insertion into $LaSrMnO_4F$ proceeds via a typical two-phase reaction comparable to that for $LiFePO_4$.

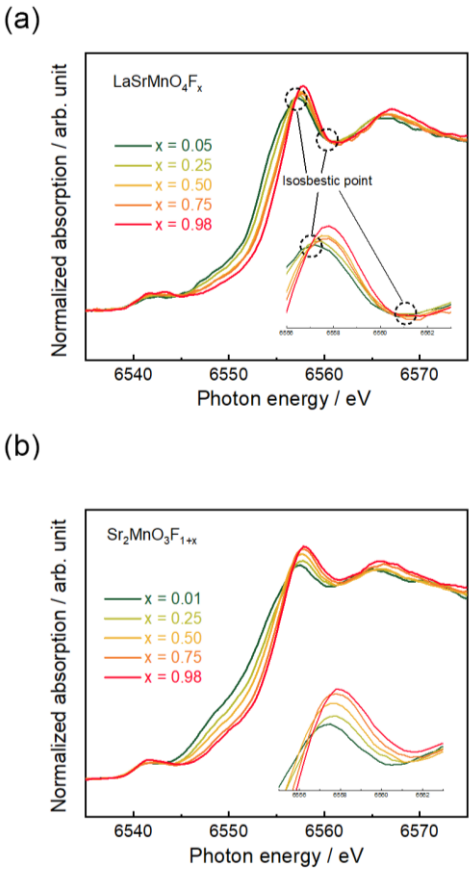

Figure 2.8. Mn *K*-edge spectra of (a) $LaSrMnO_4F_x$ and (b) $Sr_2MnO_3F_{1+x}$ in different SOCs.

Similar to $LaSrMnO_4F$, the XANES spectra for Mn *K*-edge and *L*-edge of $Sr_2MnO_3F_2$ (Fig. 2.8b and Fig. 2.9b) shifted to higher energies with the insertion of F^- into the fully discharged state (x = 0.01). This indicates that Mn in $Sr_2MnO_3F_2$ is oxidized during F^- insertion. However, in contrast to $LaSrMnO_4F$, the XANES spectra for Mn *K*-edge of $Sr_2MnO_3F_2$ did not show the isosbestic points, indicating that F^- insertion does not proceed via a typical two-phase reaction similar to that for $LiFePO_4$. These XAS results were in agreement with the charge/discharge curves and OCV plots.

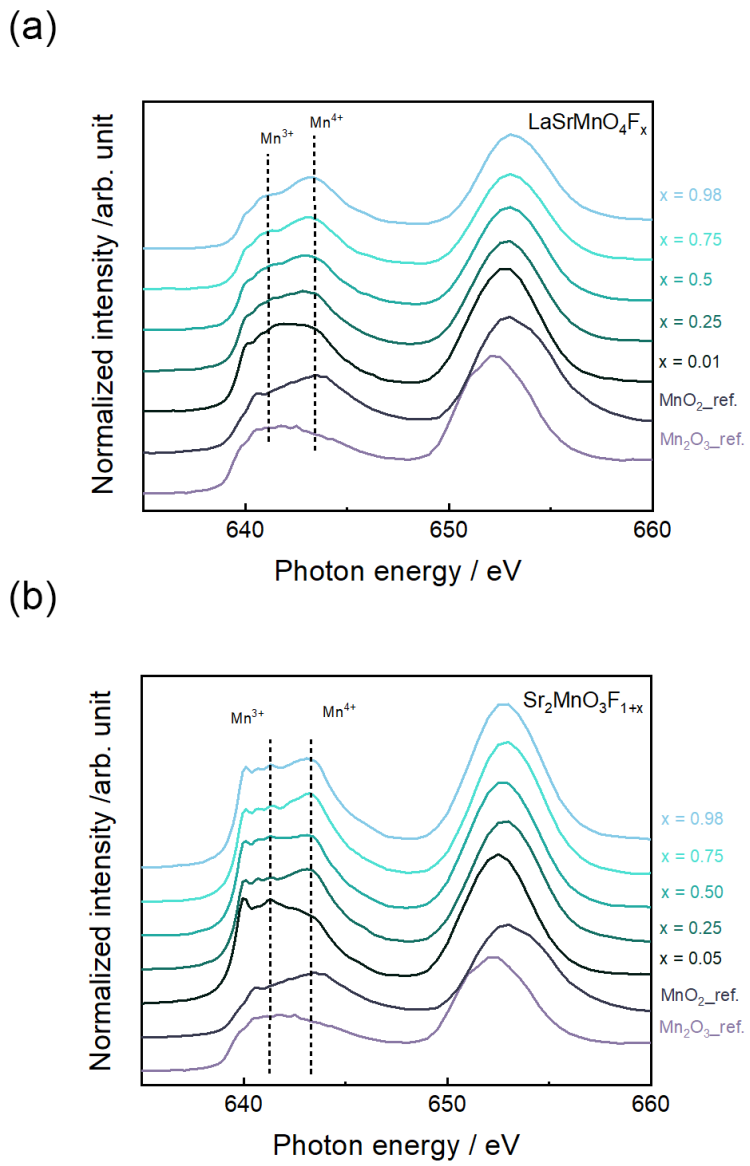

Figure 2.9 Mn *L*-edge XAS for (a) the $LaSrMnO_4F$ and (b) $Sr_2MnO_3F_{1+x}$.

The crystal structure changes of $LaSrMnO_4F$ and $Sr_2MnO_3F_2$ during the discharge and charge processes were analyzed using ex situ synchrotron XRD (Fig 2.10 and Fig. 2.11 and Fig. 2.12). Although the spectrum of each sample shows strong Bragg peaks for LBF, several Bragg peaks for $LaSrMnO_4F$ and $Sr_2MnO_3F_2$ in the discharged and charged states can be distinguished from the LBF peaks.

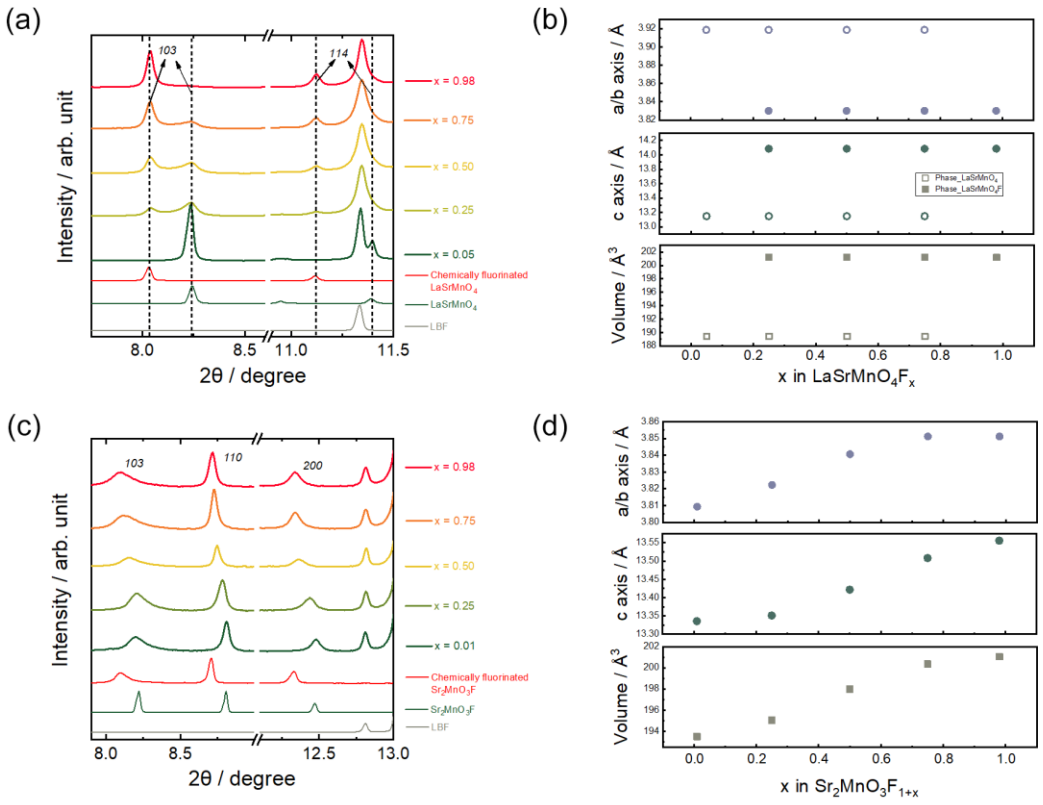

Figure 2.10. Structural changes with electrochemical fluoride ion extraction and insertion.

(a) XRD patterns and (b) calculated lattice constants of $LaSrMnO_4F_x$. (c) XRD patterns and (d) calculated lattice constants of $Sr_2MnO_3F_x$.

In the $LaSrMnO_4F$, when F was extracted from the pristine state (chemically fluorinated $LaSrMnO_4$) to afford the fully discharged state (x = 0.05), the intensities of the peaks at 8.11° and 11.1° attributed to the 103 and 114 planes of $LaSrMnO_4F$ decreased, while peaks at 8.25° and 11.4° attributed to the 103 and 114 planes of $LaSrMnO_4$ appeared. When the amount of F was increased from the fully discharged state (x = 0.05) to x = 0.25, the intensities of the peaks at 8.25° and 11.4° attributed to the 103 and 114 planes of $LaSrMnO_4$ decreased, while peaks at 8.1° and 11.1° attributed

to the 103 and 114 planes of $LaSrMnO_4F$ appeared. As F^- insertion progressed, the intensities of the 103 and 114 peaks of $LaSrMnO_4$ decreased, while those of the 103 and 114 peaks of $LaSrMnO_4F$ increased; at full charge (x = 0.98), the 103 and 114 peaks of $LaSrMnO_4$ disappeared. The lattice constants and volume of $LaSrMnO_4F$ during charging were constant regardless of the amount of F^- inserted (Fig 2.10b). These results indicate that F^- insertion/extraction with $LaSrMnO_4F$ proceeds via a two-phase coexistence reaction such as with $LiFePO_4/FePO_4$.[38]

For $Sr_2MnO_3F_2$, the peaks at 8.1°, 8.7°, and 12.3° attributed to the 103, 110, and 200 planes of the pristine state (chemically fluorinated Sr_2MnO_3F) shifted to higher angles after full discharge (x = 0.01), and then shifted back to lower angles with F^- insertion into the fully discharged state without the appearance of new peaks. The lattice constants and volume of $Sr_2MnO_3F_2$ increased continuously with the amount of F, according to Vegard's law (Fig. 2.10b). These results indicate that F^- insertion/extraction with Sr_2MnO_3F proceeds via a solid-solution reaction, in contrast to $LaSrMnO_4F$.

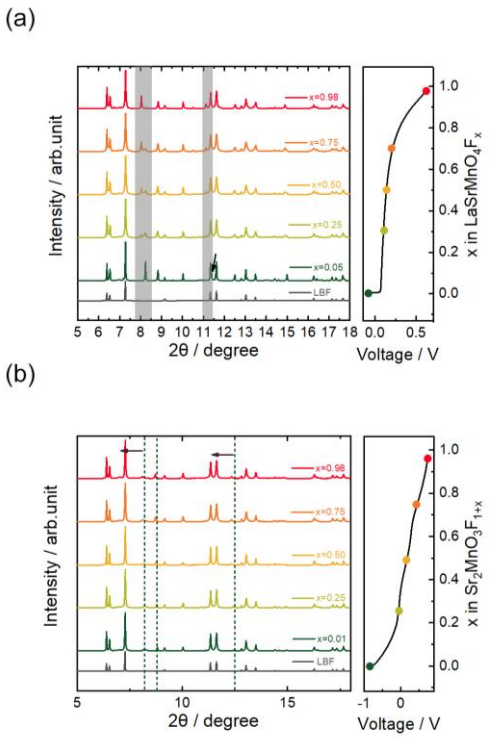

Figure 2.11. Structural changes with electrochemical fluoride ion insertion. (a) $LaSrMnO_4F_x$, (b) $Sr_2MnO_3F_{1+x}$.

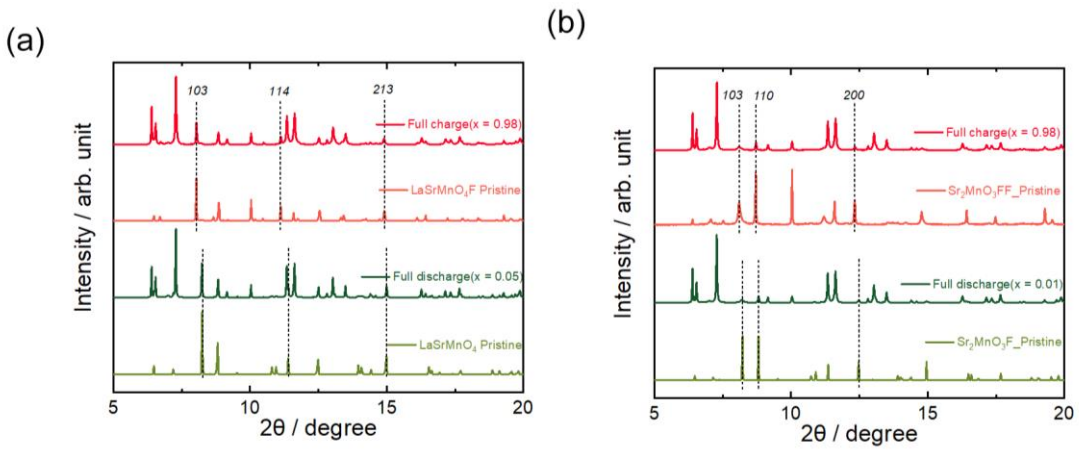

Figure 2.12. Comparison between chemical and electrochemical fluorination for (a) $LaSrMnO_4F_x$ and (b) $Sr_2MnO_3F_{1+x}$.

The relationships between the rate performances and phase transitions of chemically fluorinated $LaSrMnO_4$ and Sr_2MnO_3F are summarized in Figure 5, based on the results of electrochemical measurements, XAS, and synchrotron XRD. In the case of $LaSrMnO_4$, the charging process proceeds via a two-phase reaction with $LaSrMnO_4F$ with relatively high volume expansion of 6.22%. In contrast, the charging process of Sr_2MnO_3F proceeds via a solid-solution reaction with relatively low volume expansion of 3.08%. In the $Li_4Ti_5O_{12}$ spinel anode with the $Fd\bar{3}m$ space group for lithium-ion batteries, a two-phase reaction between two phases with almost identical lattice constants proceeds. In this system, Li^+ is inserted into the 16c site, and phase transition occurs when the lithium in the 8a site moves to the 16c site because the large Li-Li electrostatic repulsion between the Li^+ in the 8a site and the Li^+ in the 16c site are energetically unfavorable.[39-41] Similar to $Li_4Ti_5O_{12}$ system, in the $LaSrMnO_4$ cathode, the strong F-O electrostatic repulsion between the F^- inserted in the interlayer and the oxygen at the apical site would cause the phase transition, as the process of Li^+ insertion into $Li_4Ti_5O_{12}$ electrode. On the other hand, in the Sr_2MnO_3F system, because 50% of the apical site is replaced by F^-, the electrostatic repulsion between the F^- inserted in the interlayer and the anion in the apical position is relatively small, suppressing a phase transition. The smaller volume change of Sr_2MnO_3F compared to that of $LaSrMnO_4$ during the charging process leads to better power density.

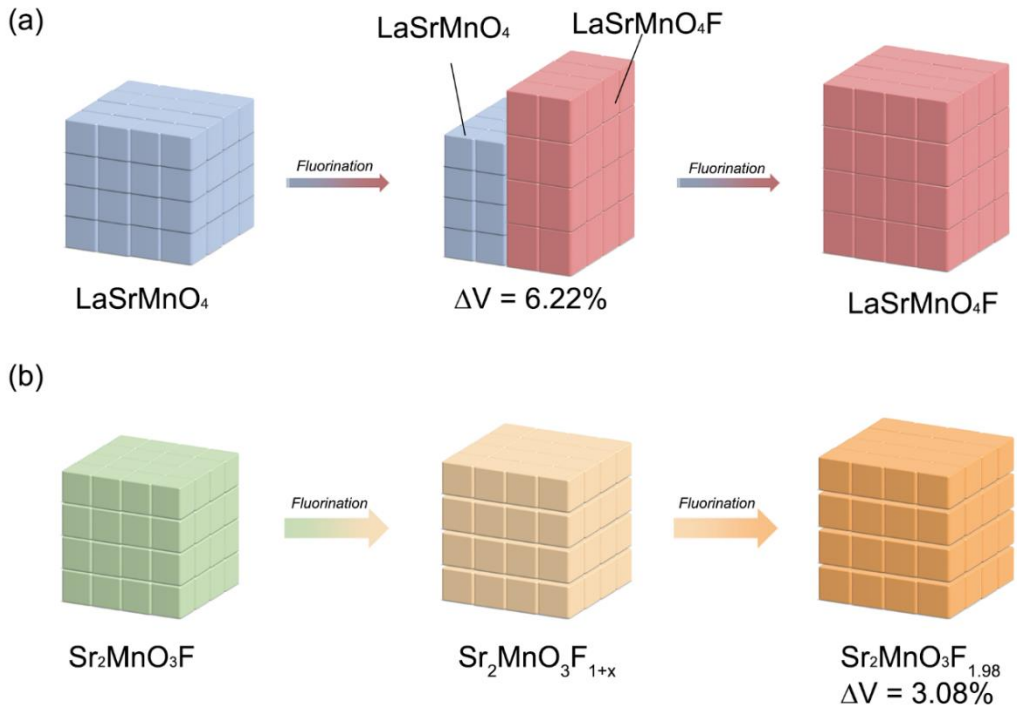

Figure 2.13. Schematic illustration of the volume changes and phase transition models during the charge processes for (a) $LaSrMnO_4F$ and (b) $Sr_2MnO_3F_2$.

2.4 Conclusions

In this study, chemically fluorinated Ruddlesden–Popper compounds, $LaSrMnO_4$ ($LaSrMnO_4F$) and apical-site-substituted oxyfluoride Sr_2MnO_3F ($Sr_2MnO_3F_2$), were synthesized and the correlations between their structures and electrochemical properties were examined. $LaSrMnO_4F$ and $Sr_2MnO_3F_2$ showed highly reversible charge/discharge capacities, compared to those of conversion-type metal/metal fluoride cathode materials, and $Sr_2MnO_3F_2$ showed better power density than $LaSrMnO_4F$. OCV measurements, XAS, and synchrotron XRD revealed that electrochemical F^- insertion into $LaSrMnO_4$ proceeds via a two-phase reaction with relatively high volume expansion of 6.22%, whereas that into Sr_2MnO_3F proceeds via a solid-solution reaction with relatively low volume expansion of 3.08%. Anion substitution from O to F in the apical sites of Sr_2MnO_3F reduced the volume expansion caused by Coulomb repulsion with the intercalated F^-, resulting in the higher power density. The smaller volume

change of Sr_2MnO_3F compared to that of $LaSrMnO_4$ during the charging process, which is comparably small to typical cathodes in all-solid-state lithium-ion batteries, are benefit for suppressing increase the interfacial resistance between cathode and electrolyte,[42] leading to better power density. These findings will be useful for designing intercalation-type cathode materials with high power densities for all-solid-state FIBs.

Reference

1. Anji Reddy, M.; Fichtner, M., Batteries based on fluoride shuttle. *J. Mater. Chem.* **2011,** *21* (43), 17059-17062.

2. Kato, Y.; Hori, S.; Saito, T.; Suzuki, K.; Hirayama, M.; Mitsui, A.; Yonemura, M.; Iba, H.; Kanno, R., High-power all-solid-state batteries using sulfide superionic conductors. *Nat. Energy* **2016,** *1* (4), 1-7.

3. Kamaya, N.; Homma, K.; Yamakawa, Y.; Hirayama, M.; Kanno, R.; Yonemura, M.; Kamiyama, T.; Kato, Y.; Hama, S.; Kawamoto, K., A lithium superionic conductor. *Nat. Mater.* **2011,** *10* (9), 682-686.

4. Bruce, P. G.; Freunberger, S. A.; Hardwick, L. J.; Tarascon, J.-M., Li–O_2 and Li–S batteries with high energy storage. *Nat. Mater.* **2012,** *11* (1), 19-29.

5. Aurbach, D.; Lu, Z.; Schechter, A.; Gofer, Y.; Gizbar, H.; Turgeman, R.; Cohen, Y.; Moshkovich, M.; Levi, E., Prototype systems for rechargeable magnesium batteries. *Nature* **2000,** *407* (6805), 724-727.

6. Zhao, X.; Ren, S.; Bruns, M.; Fichtner, M., Chloride ion battery: A new member in the rechargeable battery family. *J. Power Sources* **2014,** *245*, 706-711.

7. Davis, V. K.; Bates, C. M.; Omichi, K.; Savoie, B. M.; Momcilovic, N.; Xu, Q.; Wolf, W. J.; Webb, M. A.; Billings, K. J.; Chou, N. H.; Alayoglu, S.; McKenney, R. K.; Darolles, I. M.; Nair, N. G.; Hightower, A.; Rosenberg, D.; Ahmed, M.; Brooks, C. J.; Miller, T. F., 3rd; Grubbs, R. H.; Jones, S. C., Room-temperature cycling of metal fluoride electrodes: Liquid electrolytes for high-energy fluoride ion cells. *Science* **2018,** *362* (6419), 1144-1148.

8. Nowroozi, M. A.; Mohammad, I.; Molaiyan, P.; Wissel, K.; Munnangi, A. R.; Clemens, O., Fluoride ion batteries–past, present, and future. *J. Mater. Chem. A* **2021,** *9* (10), 5980-6012.

9. Gschwind, F.; Rodriguez-Garcia, G.; Sandbeck, D. J. S.; Gross, A.; Weil, M.; Fichtner, M.; Hörmann, N., Fluoride ion batteries: Theoretical performance, safety, toxicity, and a combinatorial screening of new electrodes. *J. Fluor. Chem.* **2016,** *182*, 76-90.

10. Thieu, D. T.; Fawey, M. H.; Bhatia, H.; Diemant, T.; Chakravadhanula, V. S. K.; Behm, R. J.; Kübel, C.; Fichtner, M., CuF_2 as Reversible Cathode for Fluoride Ion

Batteries. *Adv. Funct. Mater.* **2017,** *27* (31).

11. Rongeat, C.; Anji Reddy, M.; Diemant, T.; Behm, R. J.; Fichtner, M., Development of new anode composite materials for fluoride ion batteries. *J. Mater. Chem. A* **2014,** *2* (48), 20861-20872.

12. Yoshinari, T.; Zhang, D.; Yamamoto, K.; Kitaguchi, Y.; Ochi, A.; Nakanishi, K.; Miki, H.; Nakanishi, S.; Iba, H.; Uchiyama, T., Kinetic analysis and alloy designs for metal/metal fluorides toward high rate capability for all-solid-state fluoride-ion batteries. *J. Mater. Chem. A* 2021, 9 (11), 7018-7024.

13. Nowroozi, M. A.; Wissel, K.; Rohrer, J.; Munnangi, A. R.; Clemens, O., $LaSrMnO_4$: Reversible Electrochemical Intercalation of Fluoride Ions in the Context of Fluoride Ion Batteries. *Chem. Mater.* **2017,** *29* (8), 3441-3453.

14. Nowroozi, M. A.; Ivlev, S.; Rohrer, J.; Clemens, O., La_2CoO_4: a new intercalation based cathode material for fluoride ion batteries with improved cycling stability. *J. Mater. Chem. A* **2018,** *6* (11), 4658-4669.

15. Wissel, K.; Schoch, R.; Vogel, T.; Donzelli, M.; Matveeva, G.; Kolb, U.; Bauer, M.; Slater, P. R.; Clemens, O., Electrochemical Reduction and Oxidation of Ruddlesden–Popper-Type $La_2NiO_3F_2$ within Fluoride-Ion Batteries. *Chem. Mater.* **2021,** *33* (2), 499-512.

16. Nowroozi, M. A.; Wissel, K.; Donzelli, M.; Hosseinpourkahvaz, N.; Plana-Ruiz, S.; Kolb, U.; Schoch, R.; Bauer, M.; Malik, A. M.; Rohrer, J.; Ivlev, S.; Kraus, F.; Clemens, O., High cycle life all-solid-state fluoride ion battery with La_2NiO_{4+d} high voltage cathode. *Commun. Mater.* **2020,** *1*, No 27.

17. Clemens, O.; Berry, F. J.; Wright, A. J.; Knight, K. S.; Perez-Mato, J. M.; Igartua, J. M.; Slater, P. R., A neutron diffraction study and mode analysis of compounds of the system $La_{1-x}Sr_xFeO_{3-x}F_x$ (x=1, 0.8, 0.5, 0.2) and an investigation of their magnetic properties. *J. Solid State Chem.* **2013,** *206*, 158-169.

18. McCabe, E. E.; Greaves, C., Fluorine insertion reactions into pre-formed metal oxides. *J. Fluor. Chem.* **2007,** *128* (4), 448-458.

19. Aikens, L. D.; Li, R. K.; Greaves, C., The synthesis and structure of a new oxide fluoride, $LaSrMnO_4F$, with staged fluorine insertion. *Commun. Chem.* **2000,** (21), 2129-2130.

20. Sivakumar, T.; Wiley, J. B., Topotactic route for new layered perovskite oxides containing fluorine: $Ln_{1.2}Sr_{1.8}Mn_2O_7F_2$ (Ln= Pr, Nd, Sm, Eu, and Gd). *Mater. Res. Bull.* **2009,** *44* (1), 74-77.

21. Romero, F. D.; Bingham, P. A.; Forder, S. D.; Hayward, M. A., Topochemical fluorination of $Sr_3(M_{(0.5)}Ru_{(0.5)})_2O_7$ (M = Ti, Mn, Fe), n = 2, Ruddlesden-Popper phases. *Inorg. Chem.* **2013,** *52* (6), 3388-98.

22. Wissel, K.; Vogel, T.; Dasgupta, S.; Fortes, A. D.; Slater, P. R.; Clemens, O., Topochemical Fluorination of n = 2 Ruddlesden-Popper Type $Sr_3Ti_2O_7$ to $Sr_3Ti_2O_5F_4$ and Its Reductive Defluorination. *Inorg. Chem.* **2020,** *59* (2), 1153-1163.

23. Yoshinari, T.; Yamamoto, K.; Nishijima, M.; Fukuda, K.; Kuwabara, A.; Tanaka, I.; Maeda, K.; Kageyama, H.; Orikasa, Y.; Uchimoto, Y., High Rate Performance of Dual-Substituted $LiFePO_4$ Based on Controlling Metastable Intermediate Phase. *ACS Appl. Energy Mater.* **2018,** *1* (12), 6736-6740.

24. Tuerxun, F.; Otani, S.; Yamamoto, K.; Matsunaga, T.; Imai, H.; Mandai, T.; Watanabe, T.; Uchiyama, T.; Kanamura, K.; Uchimoto, Y., Phase Transition Behavior of $MgMn_2O_4$ Spinel Oxide Cathode during Magnesium Ion Insertion. *Chem. Mater.* **2021,** *33* (3), 1006-1012.

25. Aikens, L. D.; Gillie, L. J.; Li, R. K.; Greaves, C., Staged fluorine insertion into manganese oxides with Ruddlesden–Popper structures: $LaSrMnO_4F$ and $La_{1.2}Sr_{1.8}Mn_2O_7F$. *J. Mater. Chem.* **2002,** *12* (2), 264-267.

26. Su, Y.; Tsujimoto, Y.; Matsushita, Y.; Yuan, Y.; He, J.; Yamaura, K., High-Pressure Synthesis, Crystal Structure, and Magnetic Properties of Sr_2MnO_3F: A New Member of Layered Perovskite Oxyfluorides. *Inorg. Chem.* **2016,** *55* (5), 2627-2633.

27. Rongeat, C.; Anji Reddy, M.; Witter, R.; Fichtner, M., Solid Electrolytes for Fluoride Ion Batteries: Ionic Conductivity in Polycrystalline Tysonite-Type Fluorides. *ACS Appl. Mater. Interfaces* **2014,** *6* (3), 2103-2110.

28. Slater, P.; Driscoll, L., Modification of Magnetic and Electronic Properties, in Particular Superconductivity, by Low Temperature Insertion of Fluorine into Oxides. *Photonic and Electronic Properties of Fluoride Materials*; **2016** Elsevier press, pp 401-421.

29. Petříček, V.; Dušek, M.; Palatinus, L., Crystallographic computing system

JANA2006: general features. *Zeitschrift für Kristallographie-Crystalline Materials* **2014,** *229* (5), 345-352.

30. Momma, K.; Izumi, F., VESTA 3 for three-dimensional visualization of crystal, volumetric and morphology data. *J. Appl. Crystallogr* **2011,** *44* (6), 1272-1276.

31. Shannon, R. D., Revised effective ionic radii and systematic studies of interatomic distances in halides and chalcogenides. *Acta Crystallographica Section A* 1976, 32 (5), 751-767.

32. Zhang, D.; Yamamoto, K.; Ochi, A.; Wang, Y.; Yoshinari, T.; Nakanishi, K.; Nakano, H.; Miki, H.; Nakanishi, S.; Iba, H., Understanding the reaction mechanism and performances of 3d transition metal cathodes for all-solid-state fluoride ion batteries. *J. Mater. Chem. A* **2021,** *9* (1), 406-412.

33. Zhang, D.; Yoshinari, T.; Yamamoto, K.; Kitaguchi, Y.; Ochi, A.; Nakanishi, K.; Miki, H.; Nakanishi, S.; Iba, H.; Watanabe, T., Cu–Pb Nanocomposite Cathode Material toward Room-Temperature Cycling for All-Solid-State Fluoride-Ion Batteries. *ACS Appl. Energy Mater.* **2021,** *4* (4), 3352-3357.

34. Zhu, Y.; Wang, C., Galvanostatic intermittent titration technique for phase-transformation electrodes. *J. Phys. Chem. C* **2010,** *114* (6), 2830-2841.

35. Tang, X.; Wang, Y.; Chen, Z., A method for state-of-charge estimation of $LiFePO_4$ batteries based on a dual-circuit state observer. *J. Power Sources* **2015,** *296*, 23-29.

36. Orikasa, Y.; Maeda, T.; Koyama, Y.; Murayama, H.; Fukuda, K.; Tanida, H.; Arai, H.; Matsubara, E.; Uchimoto, Y.; Ogumi, Z., Transient phase change in two phase reaction between $LiFePO_4$ and $FePO_4$ under battery operation. *Chem. Mater.* **2013,** *25* (7), 1032-1039.

37. Orikasa, Y.; Maeda, T.; Koyama, Y.; Minato, T.; Murayama, H.; Fukuda, K.; Tanida, H.; Arai, H.; Matsubara, E.; Uchimoto, Y., Phase transition analysis between $LiFePO_4$ and $FePO_4$ by in-situ time-resolved X-ray absorption and X-ray diffraction. *J. Electrochem. Soc.* **2013,** *160* (5), A3061-A3065.

38. Liu, H.; Strobridge, F. C.; Borkiewicz, O. J.; Wiaderek, K. M.; Chapman, K. W.; Chupas, P. J.; Grey, C. P. Capturing metastable structures during high-rate cycling of $LiFePO_4$ nanoparticle electrodes. *Science* **2014,** *344* (6191), 1252817.

39. M. Wagemaker, A. Van Der Ven, D. Morgan, G. Ceder, F.M. Mulder, G.J. Kearley.

Thermodynamics of spinel Li_xTiO_2 from first principles. *Chem. Phys.* **2005**, *317*, 130–136.

40. W. Zhang, M. Topsakal, C. Cama, C. J. Pelliccione, H. Zhao, S. Ehrlich, L. Wu, Y. Zhu, A. I. Frenkel, K. J. Takeuchi, E. S. Takeuchi, A. C. Marschilok, D. Lu, F. Wang. Multi-Stage Structural Transformations in Zero-Strain Lithium Titanate Unveiled by in Situ X-ray Absorption Fingerprints. *J. Am. Chem. Soc.* **2017**, *139*, 16591−16603.

41. S. Ganapathy, A. Vasileiadis, J. R. Heringa, and M. Wagemaker. The Fine Line between a Two-Phase and Solid-Solution Phase Transformation and Highly Mobile Phase Interfaces in Spinel $Li_{4+x}Ti_5O_{12}$. *Adv. Energy Mater.* **2017**, *7*, 1601781.

42. A. Banerjee, X. Wang, C. Fang, E. A. Wu, and Y. S. Meng. Interfaces and Interphases in All-Solid-State Batteries with Inorganic Solid Electrolytes. *Chem. Rev.* **2020**, *120*, 6878−6933.

Chapter 3. Oxyfluoride Cathode with Small Volume Change Using Three-dimensional Diffusion Paths

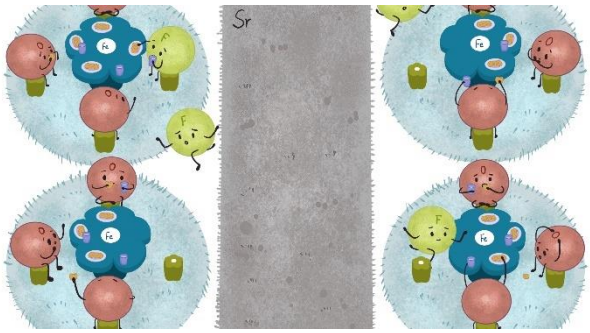

All-solid-state fluoride-ion batteries (FIBs) are expected to become the next generation of battery systems owing to their outstanding energy storage characteristics. However, the volume expansion of the cathode that accompanies the insertion of fluoride ions remains an urgent issue to be addressed. Even if an intercalation-type cathode is applied in FIBs, fluoride-ion insertion into the interstitial sites of two-dimensional materials such as $LaSrMnO_4$ still leads to non-negligible volume expansion. Here, we report a novel intercalation-type material, $Sr_3Fe_2O_5F_2$, possessing the Ruddlesden–Popper structure as a cathode material for FIBs that features not only interstitial sites but also anion vacancies as three-dimensional (3D) percolation sites to accommodate fluoride ions. This material exhibits a relatively high capacity of 118 mAh g^{-1} and good cycling stability over 70 cycles. Fe^{2+}/Fe^{3+} redox reactions are responsible for charge compensation during the charging and discharging processes. The crystal structure during the charging process changes from $Sr_3Fe_2O_5F_{0.46}$ to $Sr_3Fe_2O_5F_2$ by using the 3D percolation sites with an extremely small volume change of approximately 0.17% and thereafter changes to $Sr_3Fe_2O_5F_3$ with *P*4/*mmm* symmetry by using interstitial sites with a large volume change of approximately 11%. Our findings should pave the way for the design of new cathodes with excellent cycling stability and minimal volume expansion based on the percolation mechanism.

3.1 Introduction

Growing demands for reducing global carbon dioxide emissions are driving a shift from internal-combustion-engine-based mobility to electric vehicles. One of the most important requirements for improving the performance of electric vehicles is increasing the cruising range, which necessitates the development of storage batteries with high volumetric energy density.[1, 2] Lithium-ion batteries (LIBs) have dominated the market as a stable commercial energy storage system for over 30 years, but it is desirable to develop new battery systems with higher energy densities.[3] Recently, all-solid-state fluoride-ion batteries (FIBs) that use F^- as the charge carrier have attracted a great deal of attention as a next-generation energy storage technology.[4-10] Owing to the high electronegativity of fluorine, fluoride ions can be transferred between the electrodes in an electrochemically stable manner, and a high theoretical capacity is ensured by multiple electron transfer. Early FIB studies reported that conversion cathodes such as Bi/BiF_3 and Cu/CuF_2 exhibited large discharge capacities at 150 °C. However, our recent studies have clarified that the reaction in these metal/metal fluoride cathode materials proceeds through a two-phase mechanism.[9] We found that the inherent large volume expansion and contraction during (de)fluorination associated with charging and discharging makes the cycling and rate performance of these materials impractical.[6, 9, 11] Therefore, as with LIBs, the development of materials in which charging and discharging proceed by topochemical reactions is crucial for FIBs.[12-16]

To explore more potential cathode active materials for FIBs, perovskite-related oxides $A_{n+1}B_nO_{3n+1}$ (A: rare-earth or alkaline-earth element; B: transition metal) possessing the Ruddlesden–Popper structure were actively investigated in previous studies.[12, 13, 17-19] In this structure, the rigid void space between two octahedral layers (so-called interstitial site) provides several sites for the insertion of fluoride ions and their substitution fors oxide ions. By using oxidative (e.g., F_2 gas) or non-oxidative (e.g., polyvinylidene difluoride) fluorination agents, topochemical fluorination reactions can be realized, leading to the formation of oxyfluorides $A_{n+1}B_nO_{3n+1}F_x$ ($x \leq 2$) with fluoride

ions occupying the interstitial sites.[15, 20-22] These insertion/extraction reactions of fluoride ions into the interstitial sites are electrochemically feasible and have been proposed as the basis of cathode materials for FIBs.[12] Because this material system uses heavy elements such as La at the *A* site, the theoretical weight capacity is inferior to that of LIB cathodes, but the theoretical volumetric capacity is comparable ($LaSrMnO_4F_{1.7}$: 755 mAh cm^{-3}; $LiFePO_4$: 611.4 mAh cm^{-3}).[12] The volume expansion ratio of such Ruddlesden–Popper intercalation-type cathodes (e.g., $LaSrMnO_4$/$LaSrMnO_4F$: 6.22%)[15] is much smaller than that of two-phase reaction-type cathodes (e.g., Cu/CuF_2: 195.6%).[9] However, the former value resulting from the insertion of fluoride ions into interstitial sites still exceeds that of layered rock-salt-structured cathode materials for LIBs (e.g., $LiCoO_2$/$Li_{0.3}CoO_2$: 3.63%),[23] which is undesirable for application as an all-solid-state battery cathode. Therefore, it is necessary to develop material systems that undergo less volume expansion to serve as cathode materials for all-solid-state FIBs, but fewer examples of such materials have been reported than for lithium-ion secondary batteries, and the material design guidelines have yet to be established. In the case of LIB cathodes, the volume expansion has been reported to be more suppressed in disordered rock-salt-structured cathodes, in which the reaction proceeds by a percolation mechanism, than in layered rock-salt-structured cathodes.[24-26] We have focused on the previously unexplored volume expansion of FIB cathodes during the insertion and extraction of fluoride ions and attempted to clarify the relationship between the volume expansion and insertion sites using a model cathode material containing both two-dimensional (2D) interstitial sites and three-dimensional (3D) percolation sites.

In this study, we demonstrate the first synthesis of $Sr_3Fe_2O_5F_2$ as an intercalation-type cathode material for FIBs via a $Sr_3Fe_2O_5$ intermediate, which is obtained by introducing oxygen vacancies into $Sr_3Fe_2O_7$. Analysis of the experimental data indicates that $Sr_3Fe_2O_5F_2$ accommodates fluoride ions into both the oxygen vacancies at the apical sites of the perovskite slabs (3D diffusion sites) and the interstitial sites (2D diffusion sites). Furthermore, synchrotron X-ray diffraction (XRD) data suggest

that the volume expansion upon fluoride-ion insertion into the oxygen vacancies at the apical sites is significantly smaller than that upon fluoride-ion insertion into the interstitial sites.

3.2 Experimental

3.2.1 Material synthesis

$Sr_3Fe_2O_7$. $Sr_3Fe_2O_7$ was synthesized via a typical solid-state reaction method.[27] A stoichiometric mixture of pre-dried Sr_2CO_3 (Fujifilm, ≥99.9%) and Fe_2O_3 (Fujifilm, ≥99.9%) was finely ground using a mortar and pestle and the resulting powder was pressed into one pellet. The pellet was heated at 1000 °C under air for 24 h and then ground, pelletized again, and sintered for 48 h with one intermediate re-grinding.

$Sr_3Fe_2O_5$. $Sr_3Fe_2O_5$ was synthesized via a conventional CaH_2 reduction method.[27] $Sr_3Fe_2O_7$ was thoroughly ground with CaH_2 (Sigma-Aldrich, 99.9% trace metals basis), and sealed in an evacuated Pyrex glass tube, which was then heated at 350 °C for 72 h. The product was washed with 0.1 M NH_4Cl in dry methanol to remove the by-product CaO and residual CaH_2 impurities.

Chemical fluorination. XeF_2 (Sigma-Aldrich, 99.99% trace metals basis) was selected as a fluorination agent for synthesizing $Sr_3Fe_2O_5F_2$. $Sr_3Fe_2O_5$ and XeF_2 were separately sealed in a polytetrafluoroethylene reactor under an argon atmosphere and reacted at 150 °C for 48 h.

$La_{0.9}Ba_{0.1}F_{2.9}$ solid electrolyte. $La_{0.9}Ba_{0.1}F_{2.9}$ solid electrolyte was prepared according to our previous study.[28] LaF_3 (Kojundo Chemical Lab. Co. Ltd., 99.9%) and BaF_2 (Kojundo Chemical Lab. Co. Ltd., 99.9%) were mixed in a molar ratio of 9:1 and thoroughly ground using a mortar and pestle. The resulting powder was sealed in an agate ball milling jar and milled at 600 rpm for 10 h. Finally, the ball-milled mixture was pelletized and sintered at 1000 °C for 4 h. All operations were performed in an Ar-filled glovebox and the starting powders were stored under a water/oxygen-free

atmosphere.

3.2.2 Characterization and electrochemical measurement

A cathode composite was prepared by mixing $Sr_3Fe_2O_5F_2$, the $La_{0.9}Ba_{0.1}F_{2.9}$ solid electrolyte, and vapor-grown carbon fiber (VGCF, Showa Denko K.K.) in a weight ratio of 3:6:1 followed by ball milling for 10 h. An anode composite was obtained by mixing Pb powder (Kojundo Chemical Lab. Co. Ltd., 99.9%), PbF_2 (Kojundo Chemical Lab. Co. Ltd., 99.9%), $La_{0.9}Ba_{0.1}F_{2.9}$, and VGCF in a weight ratio of 3:2:4:1 followed by ball milling for 10 h. An electrochemical cell was then assembled by pressing the cathode composite, solid electrolyte, and anode composite (excess amount relative to the cathode) into a pellet with two pieces of gold foil as the current collectors. The cell was tested at 140 °C to ensure sufficient fluoride-ion conductivity of $La_{0.9}Ba_{0.1}F_{2.9}$.

The electrochemical performance of $Sr_3Fe_2O_5F_2$ was examined using an HJ1010SD8 electrochemical workstation (Hokuto Denko Corporation) with a lower cut-off voltage of −1.5 V vs. Pb/PbF_2 and a limited charge capacity of 118 mAh g^{-1}. Galvanostatic charge/discharge tests at a current density of 5 mA g^{-1} were employed to evaluate the cycling stability.

The average valence of iron ions was determined by iodometric titration, and nitrogen was continuously introduced into the sample solution throughout the experiment to prevent exposure of the sample to air.[29] Inductively coupled plasma (ICP) spectroscopy was performed using an ICPE-9820 instrument (Shimadzu Corporation). Information on the morphology of $Sr_3Fe_2O_5F_2$ was collected using an ultrahigh-resolution field-emission scanning electron microscope (SEM, Hitachi SU-8000). Energy-dispersive spectroscopy (EDS) mapping was also performed to confirm the uniform distributions of the elements. Synchrotron XRD measurements were conducted at room temperature on beamline BL02B2 of the synchrotron radiation facility SPring-8, Japan. The $Sr_3Fe_2O_5F_2$ composites after charging/discharging were peeled off from the cathode side and sealed in quartz glass capillary tubes. The synchrotron X-rays were monochromatized to a wavelength of 0.41337 Å, which was calibrated using a CeO_2

standard sample. Rietveld refinements were performed using the JANA2006 package to obtain detailed information on the structural changes during charge and discharge.[30] The crystal structure models presented in this paper were prepared using the VESTA program.[31] Soft X-ray absorption spectroscopy (XAS) measurements for the iron L_3-edge and oxygen *K*-edge were performed on beamline BL27SU of SPring-8. All spectra were collected in the partial fluorescence mode.

3.2.3 Density functional theory (DFT) calculations

First-principles calculations were performed using the FLAPW-Fourier program (WIEN 2k). Brillouin-zone integration was conducted on a 10 × 10 × 10 mesh with k-point sampling. The convergence condition was defined as a total energy of less than 0.0001 Ry. The calculation methods are reported in detail elsewhere.[32]

3.3 Result and discussion

3.3.1 Material characterization

Figure 3.1a shows the synchrotron XRD and Rietveld refinement patterns for $Sr_3Fe_2O_{6.7}$. All of the Bragg peaks were well fitted using the space group *I*4/*mmm*, and the lattice constants and oxygen vacancies at the *2a* site estimated from the refinement were $a = b = 3.874$ Å, $c = 20.199$ Å, and $\delta = 0.3$ (corresponding to $Sr_3Fe_2O_{6.7}$) (Table 3.1). $Sr_3Fe_2O_{6.7}$ synthesized by this method is likely to contain oxygen defects, and the amount of oxygen defects is in good agreement with previously reported values.[27] Figure 3.1b shows the synchrotron XRD and Rietveld refinement patterns for $Sr_3Fe_2O_5$, which was prepared by subjecting $Sr_3Fe_2O_{6.7}$ to reduction with CaH_2. All of the Bragg peaks were indexed to the tetragonal unit cell crystallizing in space group *Immm* and the lattice constants estimated from the refinement were $a = 3.515$ Å, $b = 3.954$ Å, and $c = 20.921$ Å (Table 3.2), which are consistent with the previous study.[27]

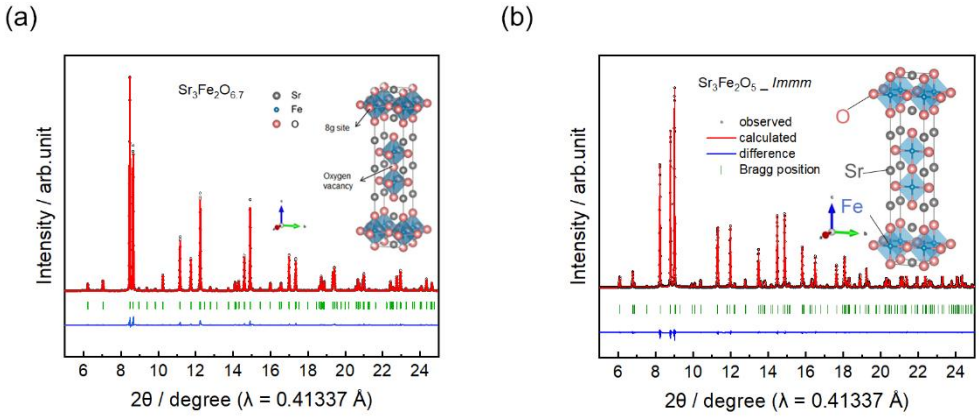

Figure 3.1 Crystal structure of (a) $Sr_3Fe_2O_{6.7}$, (b) $Sr_3Fe_2O_5$.

Table 3.1 Refined crystal parameters, space group, lattice parameters, reliability factorand agreement factor for $Sr_3Fe_2O_{6.7}$ at room temperature. Here, the reliability factor R_{WP} is the weightedprofile.

Atom	Wyckoff position	x	y	z	B_{iso} (Å^2)	Occupancy
Sr1	2b	0	0	0.5	0.516(4)	1
Sr2	4e	0	0	0.31740(1)	0.132(6)	1
Fe	4e	0	0	0.09982(2)	0.867(1)	1
O1	8g	0	0.5	0.09232(9)	0.878(24)	1
O2	4e	0	0	0.19500(0)	1.23(2)	1
O3	2a	0	0	0	0.648(3)	0.73

$Sr_3Fe_2O_{6.73}$ S.G. *I*4/*mmm*; R_{wp} = 5.42%, R_F = 4.11%; *a* = *b* = 3.8737(4) Å, *c* = 20.1992(0) Å

Table 3.2 Refined crystal parameters, space group, lattice parameters, reliability factorand agreement factor for $Sr_3Fe_2O_5$ at room temperature. Here, the reliability factor R_{WP} is the weightedprofile.

Atom	Wyckoff position	x	y	z	B_{iso} (Å^2)	Occupancy
Sr1	2c	0.5	0.5	0.00000	0.907(11)	1
Sr2	4i	0	0	0.31250(8)	1.59(5)	1
Fe	4i	0	0	0.09634(2)	1.33(1)	1
O1	2a	0	0	0.00000	0.942(17)	1
O2	4j	0.5	0	0.59581(3)	1.22(3)	1
O3	4i	0	0	0.19246(1)	0.771(8)	1

$Sr_3Fe_2O_5$ S.G. *Immm*; R_{wp} = 7.33%, R_F =1.37%; *a* = 3.515 Å, *b* = 3.954 Å, *c* = 20.921 Å

Next, $Sr_3Fe_2O_5$ with oxygen vacancies at the equatorial sites was subjected to chemical fluorination using XeF_2. SEM-EDS mapping revealed that the particle size of the chemically fluorinated $Sr_3Fe_2O_5$ was approximately 5 μm. The Fe, O, and F atoms were homogeneously distributed in the particles (Figure 3.2). The results of iodometric titration indicated that the average valence of the iron ions in the chemically fluorinated $Sr_3Fe_2O_5$ was +3, and ICP spectroscopy afforded a molar mass of 492 g/mol. By combining these two elemental analysis techniques, we deduced that the chemical composition of the synthesized material was $Sr_3Fe_2O_5F_2$. The crystal structure of $Sr_3Fe_2O_5F_2$ was examined by synchrotron XRD and Rietveld analysis (Figure 3.3 and Table 3.3). All of the Bragg peaks were indexed to an orthorhombic unit cell with the space group *Immm* (the fluoride ions occupy the generated vacancies) or *I*4/*mmm* (the fluoride ions occupy the apical sites of the FeO_6 slabs).[33] However, XRD with Rietveld analysis alone was unsuitable for unambiguously determining the space group of $Sr_3Fe_2O_5F_2$ because the small difference in atomic scattering factors between oxygen and fluorine made it difficult to assign these anion sites exactly.

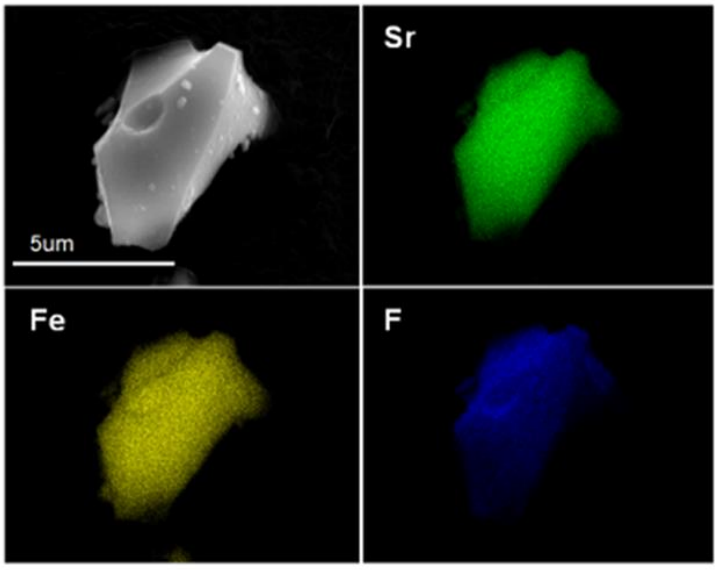

Figure 3.2 EDX mapping of $Sr_3Fe_2O_5F_2$.

Therefore, we performed theoretical calculations for the final determination of the space group. Figure 3.4 shows the densities of states calculated by DFT for both of the possible space groups of $Sr_3Fe_2O_5F_2$. The total energy was found to be 4.6 eV lower for the *I*4/*mmm* space group than for the *Immm* space group, indicating that the chemical fluorination leads to the rearrangement of O, and F occupies the apical site rather than vacancy. Such structural rearrangements accompanied with fluorination were also reported by *Case et al*. experimentally.[34]

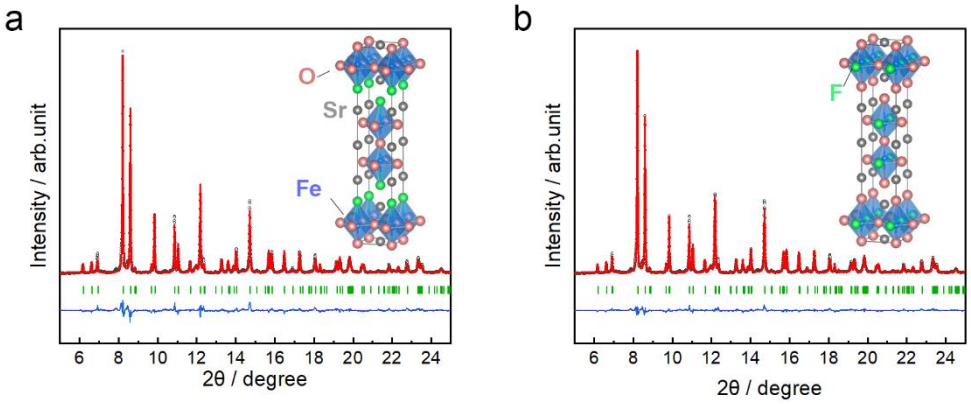

Figure 3.3 Crystal structure of chemical fluorinated $Sr_3Fe_2O_5F_2$ with space group of (a) *I*4/*mmm*, (b). *Immm*

Table 3.3 Refined crystal parameters, space group, lattice parameters, reliability factorand agreement factor for $Sr_3Fe_2O_5F_2$ at room temperature. Rietveld refinements were performed basedon (a) *Immm* and (b) *I*4/*mmm* space group. Here, the reliability factor R_{WP} is the weighted profile.

(a) *Immm*

Atom	Wyckoff position	x	y	z	B_{iso} (Å²)	Occupancy
Sr1	2c	0	0	0.5	1.10(8)	1
Sr2	4i	0	0	0.32218(8)	0.61(5)	1
Fe	4i	0	0	0.08876(20)	0.51(7)	1
O1	2a	0	0	0	0.46(39)	1
O2	4j	0	0.5	0.10027(66)	1.42(39)	1
O3	4i	0	0	0.21457(67)	5.0(5)	1
F	4j	0.5	0	0.10070(54)	0.84(29)	1

$Sr_3Fe_2O_5F_2$ S.G. *Immm*; R_{wp} = 8.44%, R_F = 2.84%; *a* = 3.88569(49) Å, *b* = 3.89229(60) Å, *c* = 21.4337(17) Å

(b) *I*4/*mmm*

Atom	Wyckoff position	x	y	z	B_{iso} (Å^2)	Occupancy
Sr1	2b	0	0	0.5	1.06(7)	1
Sr2	4e	0	0	0.32246(8)	0.62(5)	1
Fe	4e	0	0	0.08838(18)	0.51(6)	1
O1	2a	0	0	0	0.72(35)	1
O2	8g	0	0.5	0.10026(26)	0.45(15)	1
F	4e	0	0	0.21313(56)	7.8(4)	1

$Sr_3Fe_2O_5F_2$ S.G. *I*4/*mmm*; R_{wp} = 8.13%, R_F = 2.93%; *a* = 3.88860(23) Å, *c* = 21.4340(17) Å

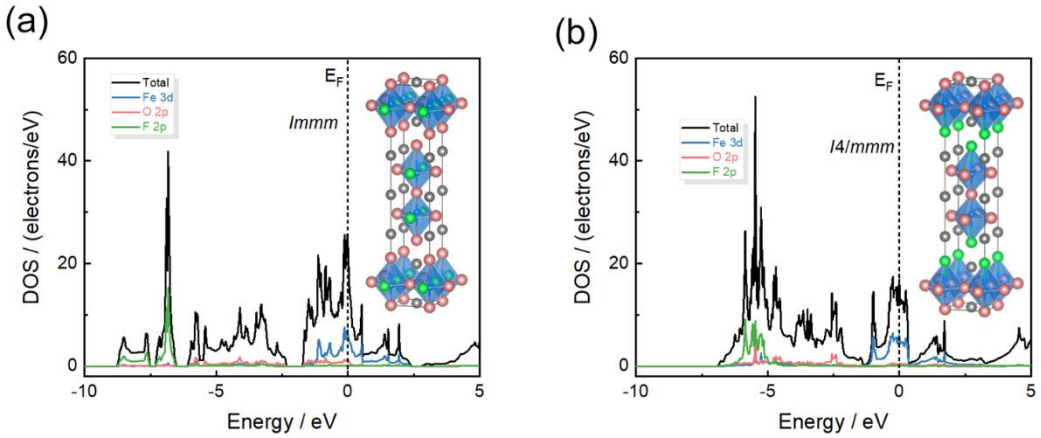

Figure 3.4 Calculated density of states for $Sr_3Fe_2O_5F_2$ with (a) the *Immm* symmetry and (b) the *I*4/*mmm* symmetry.

3.3.2 Electrochemical performance

In order to accurately study the properties of the cathode material, the Pb/PbF_2 anode was used in this study. The Pb/PbF_2 is one of most popular anode materials with ideal non-polarizing electrode behavior: the potential is always constant because the reaction proceeds in a two-phase routine,[35-37] and the potential does not change even when a small current flows due to the large exchange current density. Therefore, the Pb/PbF_2 anode helps to examine accurate electrochemical behavior on the chemically fluorinated $Sr_3Fe_2O_5F_2$; but Pb/PbF_2 has relatively high potential, which plays a role more like reference electrode. In some cases of employing Pb/PbF_2 as anode, the discharging cut-off voltage can be even minus, which was also called "forced discharge" by O. Clemens et al.[12] In terms of practical applications, the anodes with lower

potentials such as La/LaF_3 (-2.41 V vs. Pb/PbF_2) have be utilized.[7-11]

After considering the reduction potential window of the $La_{0.9}Ba_{0.1}F_{2.9}$ solid electrolyte, the lower potential limit of the chemically fluorinated $Sr_3Fe_2O_5F_2$ active material was fixed at −1.5 V for the discharge (defluorination) step.[38] As shown in Figure 3.5a, $Sr_3Fe_2O_5F_2$ exhibited an initial discharge capacity of 91 mAh g^{-1}, which corresponds to the extraction of 1.54 fluoride ions. The molecular formula of the cathode material after the first discharge step was thus assumed to be $Sr_3Fe_2O_5F_{0.46}$ based on Faraday's law. If we continuously decrease the lower potential below −1.5 V, fluoride ions may be completely removed. However, owing to the electrochemical window of solid electrolyte $La_{0.9}Ba_{0.1}F_{2.9}$, discharging below −1.5 V vs. Pb/PbF_2 will fall into electrolyte decomposition (Figure 3.6).

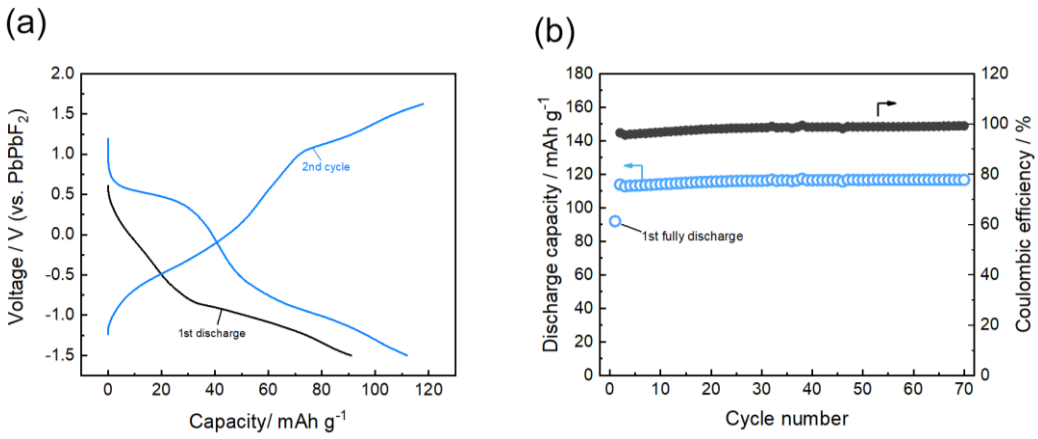

Figure 3.5 Electrochemical performance of $Sr_3Fe_2O_5F_2$. (a) Charge/discharge profiles for the first two cycles. (b) Capacity retention upon cycling under a current density of 5 mA g^{-1}, where the charge capacity was limited to 118 mAh g^{-1}.

In the following cycles, the charge capacities were set to 118 mAh g^{-1} to ensure the intercalation of two fluoride ions. Figure 2a clearly shows that the charging voltage increased gradually with fluoride intercalation until the charge capacity reached 58 mAh g^{-1} (equivalent to the insertion of 1.0 fluoride ions) and then increased greatly with fluoride intercalation until the charge capacity reached 94.4 mAh g^{-1} (equivalent to the insertion of 1.6 fluoride ions), whereas it increased slowly during the subsequent charging process. $Sr_3Fe_2O_5F_2$ shows the highly symmetrical charge/discharge profile in

the subsequent cycle, indicating highly reversible fluoride ion (de)insertion behavior during cycling. Furthermore, the $Sr_3Fe_2O_5F_2$ cathode also displayed excellent cycling stability. A discharge capacity of 116.7 mAh g^{-1} was obtained after 70 cycles without any capacity decay (Figure 3.5b), and the average coulombic efficiency over these cycles was 98%. The charge/discharge profiles of 70 cycles are showed in Figure 3.7 Some changes in the curves may be due to some structural changes such as fluoride-ion occupation of interlayer sites and/or the insertion site itself during the charge/discharge process. The volumetric capacity estimated from the discharge capacity of 116.7 mAh g^{-1} was 595 mAh cm^{-3}, which is comparable to those of commercial LIB cathode materials such as $LiCoO_2$ (514 mAh cm^{-3}) and $LiFePO_4$ (589 mAh cm^{-3}).[39]

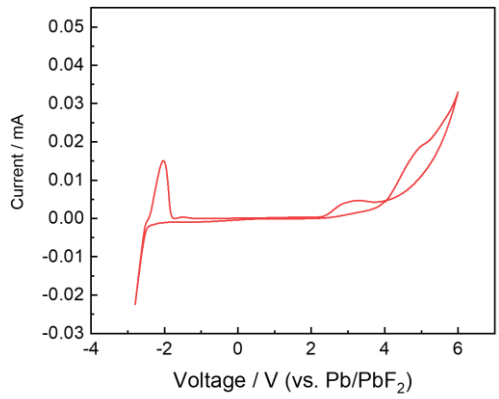

Figure 3.6 Electrochemical window of solid electrolyte $L_{0.9}Ba_{0.1}F_{2.9}$.

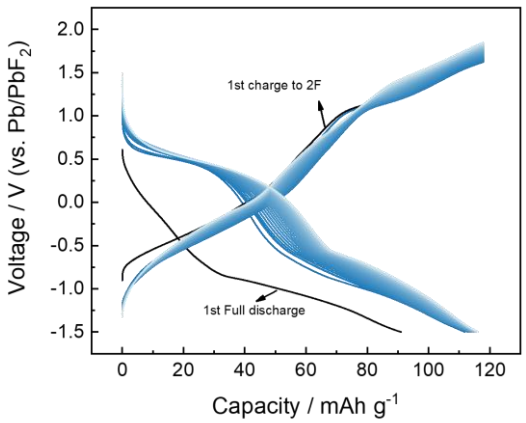

Figure 3.7 Charge/discharge profiles of 70 cycles.

We also evaluated the rate capability of $Sr_3Fe_2O_5F_2$ during discharging under the current densities from 5 mA g^{-1} to 200 mA g^{-1}, in which the charge capacity was set to 118 mAh g^{-1} (Figure 3.8). At a current density of 200 mA g^{-1}, $Sr_3Fe_2O_5F_2$ achieved a discharge capacity of 51 mAh g^{-1}, which is equivalent to 43% of the discharge capacity with 5 mA g^{-1}.

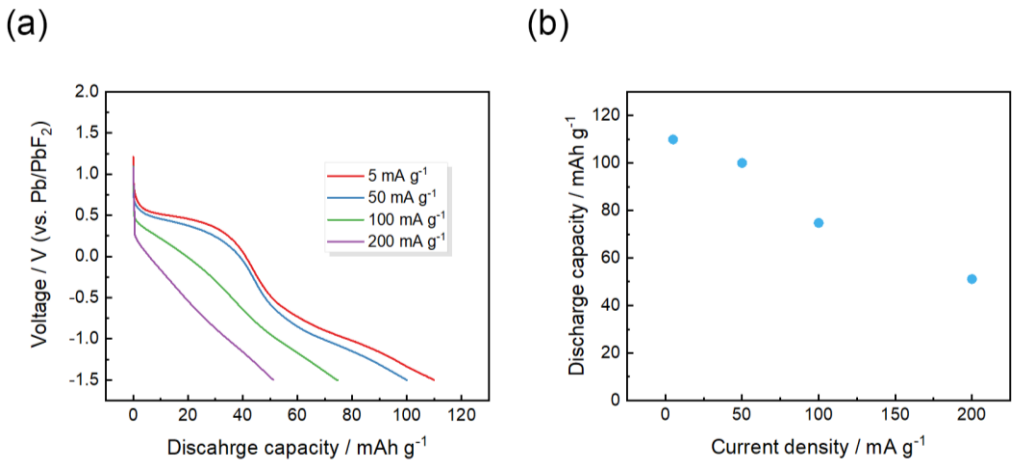

Figure 3.8 Rate performance of $Sr_3Fe_2O_5F_2$. (a) Discharge profiles with varying the current density. (b) Discharge capacity retention as a function of current density.

3.3.3 Charge compensation mechanism

The charge compensation mechanism during the cycle after the first discharge was analyzed by soft XAS for the iron L_3-edge and oxygen K-edge, as presented in Figure 3.9. Soft XAS is a powerful technique for examining the oxidation states of transition-metal 3d ions through dipole-allowed transitions.[40,41] The initially discharged $Sr_3Fe_2O_5F_2$ ($Sr_3Fe_2O_5F_{0.46}$) cathode and the $Sr_3Fe_2O_5F_{0.46+x}$ cathode at various states of charge during the subsequent cycle were prepared by regulating the fluoride-ion content x as shown in Figure 3.9a, and their iron L_3-edge XAS spectra are plotted in Figure 3.9b. After the first discharge to −1.5 V ($Sr_3Fe_2O_5F_{0.46}$, x = 0), the peak observed at approximately 708 eV shifted toward the lower-energy side, but it did not reach the energy for $Sr_3Fe_2O_5$. This result indicates that iron ions were reduced alongside the fluoride-ion extraction, but not all of the fluoride ions were extracted from the pristine state corresponding to the initial discharge capacity in Figure 3.5a. In the subsequent

charging process, the peak energy continuously shifted toward higher energy with fluoride-ion insertion until reaching a composition of $Sr_3Fe_2O_5F_2$ (x = 1.5). Finally, the peak energy remained almost constant from $Sr_3Fe_2O_5F_2$ (x = 1.5) to $Sr_3Fe_2O_5F_{2.5}$ (x = 2.0), indicating that iron ions were not oxidized in this region. During the subsequent discharge, the peak energy of the sample ($Sr_3Fe_2O_5F_{0.46}$, x = 0_re) reversibly returned to the same position as that of the initially discharged sample ($Sr_3Fe_2O_5F_{0.46}$, x = 0), indicating that reversible redox reactions of the iron ions occurred during fluoride-ion insertion/extraction.

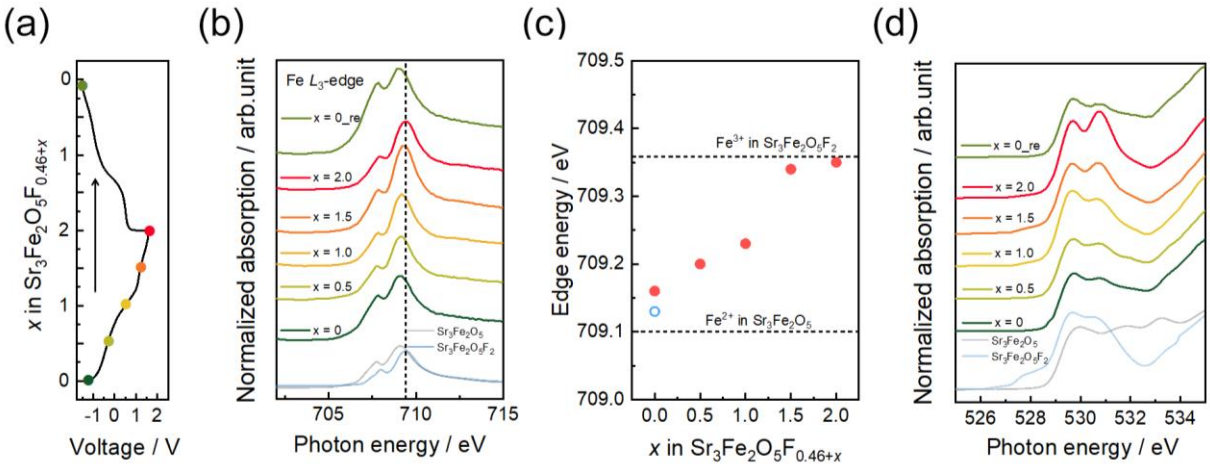

Figure 3.9 X-ray absorption spectra for the iron L_3-edge and oxygen K-edge. (a) Measurement points for XAS in the first charge and second discharge steps. (b) X-ray absorption spectra for the iron L_3-edge, in which the colors correspond to the measurement points in panel (a). (c) Energy of the peak around 708.5 eV in panel (b). (d) X-ray absorption spectra for the oxygen K-edge, in which the colors correspond to the measurement points in panel (a).

Figure 3.9d shows the oxygen K-edge XAS results for the $Sr_3Fe_2O_5F_{0.46+x}$ cathodes. All of the spectra exhibited two clear pre-edge features from 528 to 532 eV, which correlate to transitions occurring from the oxygen 1s orbital to the transition-metal 3d–oxygen 2p hybridized orbital.[42] During the early stage of charging to $Sr_3Fe_2O_5F_2$ ($0 < x < 1.5$), the pre-edge peak shifted toward lower energy because the hybridization between the iron 3d and oxygen 2p orbitals increased in strength owing to the oxidation of iron ions. In the late state of charging from $Sr_3Fe_2O_5F_2$ ($x \geq 1.5$), the intensity of the

peak at 531 eV increased, indicating that hole formation occurred in the oxygen 2*p* orbital as in the case of LIB cathodes.[23, 43-45] The characteristic peak is not attributed to superoxide because the observed peak energy is different from the superoxide derived-one.[42] Taking into account our previous studies on Li-excess cathode materials,[42] as the Fe 3*d* and O 2*p* forms strong covalent bond, we believe that the peak is not attributed to localized hole formation on O 2*p* orbital as particularly observed in Li-excess metal oxide but to the electron transfer from the O 2*p* orbital to the Fe 3*d* orbital (i.e. ligand hole formation). In particular, upon charging from $Sr_3Fe_2O_5F_2$ to $Sr_3Fe_2O_5F_{2.5}$, oxygen was largely responsible for the charge compensation with fluoride-ion insertion because iron ions were not oxidized in this region, as indicated by the iron L_3-edge (Figure 3.9b and c). Moreover, the intensity of the peak corresponding to the oxygen redox process decreased after discharging to −1.5 V ($Sr_3Fe_2O_5F_{0.46}$, $x = 0$_re), meaning that the oxygen redox process in the high-voltage region was reversible. Thus, the results of the iron L_3-edge and oxygen *K*-edge XAS indicate that iron ions, iron and oxide ions, and oxide ions were responsible for the charge compensation from $Sr_3Fe_2O_5F_{0.46}$ to $Sr_3Fe_2O_5F_{1.5}$, from $Sr_3Fe_2O_5F_{1.5}$ to $Sr_3Fe_2O_5F_2$, and from $Sr_3Fe_2O_5F_2$ to $Sr_3Fe_2O_5F_{2.5}$, respectively, during the charging process, corresponding to the charge/discharge profile shown in Figure 3.5a.

3.3.4 Structural evolution upon cycling

Because there are two sites in the host lattice that can accommodate fluoride ions (apical sites and interstitial sites, see Figure 3.10), it is important to determine the crystal structure during charging and discharging. Thus, the crystal structures of cathodes with different fluorine contents were analyzed by high-resolution synchrotron XRD (Figure 3.11).

After the initial discharging to −1.5 V, the observed Bragg peaks of $Sr_3Fe_2O_5F_{0.46}$ were indexed to the same structure as $Sr_3Fe_2O_5F_2$ and the $La_{0.9}Ba_{0.1}F_{2.9}$ solid electrolyte, suggesting that the fluoride ions were topotactically extracted from the host structure. In the subsequent charging process to $Sr_3Fe_2O_5F_2$ ($0 < x < 1.5$), the peaks corresponding

to the 015/105 and 110 planes shifted gradually. Upon further charging from $Sr_3Fe_2O_5F_2$ ($x \geq 1.5$), new Bragg peaks appeared at approximately 7.8° and 8.4°, and the peak intensity gradually increased with fluoride-ion insertion while the peak intensity for the pristine $Sr_3Fe_2O_5F_2$ phase gradually decreased. These results indicate that the solid-solution limit exists near the composition of $Sr_3Fe_2O_5F_2$ and the fluoride-ion insertion proceeds via a solid-solution reaction up to the limit and thereafter via a two-phase coexistence reaction. Upon the subsequent discharge, the XRD pattern of $Sr_3Fe_2O_5F_{0.46}$ (x = 0_re) reversibly returned to the same as that for the initially discharged $Sr_3Fe_2O_5F_{0.46}$ (x = 0), indicating that the crystal structure of the $Sr_3Fe_2O_5F_2$ cathode reversibly changed during fluoride-ion insertion/extraction.

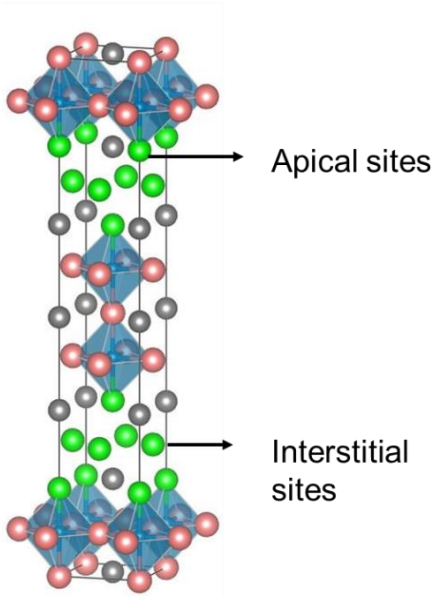

Figure 3.10 Possible sites in the $Sr_3Fe_2O_5F_{0.46+x}$ compound that can accommodate fluoride ions.

Owing to the high $La_{0.9}Ba_{0.1}F_{2.9}$ content in the composite electrode, the low intensity of the diffraction peaks of the active material made it impossible to precisely determine the crystal structures of the newly appeared phases observed from $Sr_3Fe_2O_5F_2$ ($x \geq 1.5$) using Rietveld analysis. However, it has been reported that the space group of layered perovskites in the Ruddlesden–Popper structure changes upon fluoride insertion in one layer of interstitial sites.[12] Considering this previous report, we

simulated the diffraction peaks of $Sr_3Fe_2O_5F_3$, where the interstitial sites in a layer of $Sr_3Fe_2O_5F_2$ are fully occupied. Consequently, the additional Bragg peaks could be reasonably interpreted as those of $Sr_3Fe_2O_5F_3$ with the *P*4/*mmm* space group.

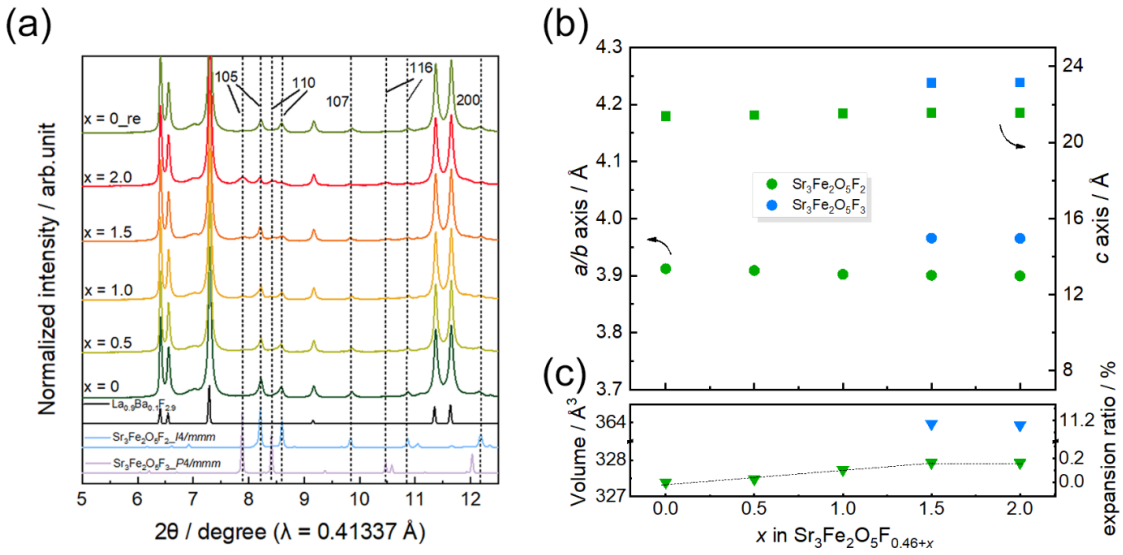

Figure 3.11 Crystal structure changes with electrochemical fluoride-ion extraction and insertion. (a) Synchrotron XRD data for $Sr_3Fe_2O_5F_{0.46+x}$ cathodes in various states of charge. The $Sr_3Fe_2O_5F_3$ reference is a simulated pattern based on *P*4/*mmm* symmetry, with one of the rock-salt layers fully occupied by fluoride ions. (b) Lattice parameter changes for the $Sr_3Fe_2O_5F_{0.46+x}$ cathode upon electrochemical fluoride-ion insertion. (c) Volume change of the $Sr_3Fe_2O_5F_{0.46+x}$ cathode.

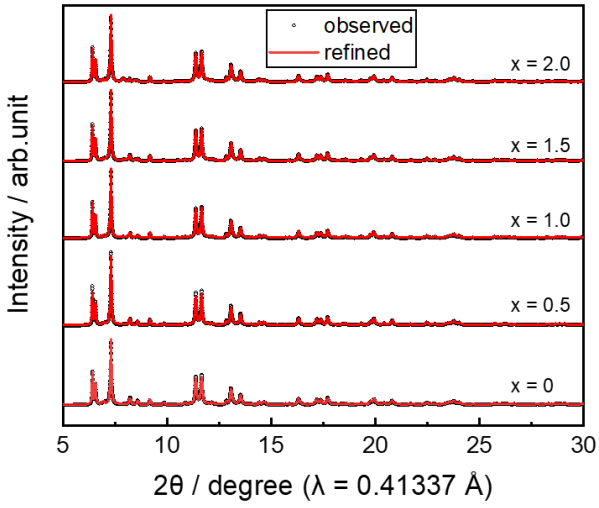

Figure 3.12 Respective XRD patterns and their Le bail refinement results of cathode in different states of charge.

To quantitatively analyze the crystal structure of $Sr_3Fe_2O_5F_{0.46+x}$ during the charging process, Le Bail refinement was performed, assuming that the new phase observed from $Sr_3Fe_2O_5F_2$ ($x \geq 1.5$) belonged to the *P*4/*mmm* space group (Figure 3.11b, Figure 3.12, and Table 3.4). During the insertion of fluoride ions until $Sr_3Fe_2O_5F_2$ ($0 < x < 1.5$), the lattice constant *c* continuously increased while the lattice constants *a* and *b* continuously decreased, and the corresponding volume expansion ratio was approximately 0.17%. These changes obey Vegard's rule, meaning that the fluoride-ion insertion proceeds via a solid-solution reaction in this region. Upon further fluoride-ion insertion from $Sr_3Fe_2O_5F_2$ ($x > 1.5$), the lattice constants of the $Sr_3Fe_2O_5F_2$ and $Sr_3Fe_2O_5F_3$ phases remained constant, indicating that the fluoride-ion insertion proceeded via the two-phase reaction in this region. The volume change ratio between the two phases was 11%, which is substantially larger compared with the solid-solution region.

Table 3.4 Refined crystal parameters, space group, lattice parameters for $Sr_3Fe_2O_5F_{0.46+x}$ during the charge process.

x in $Sr_3Fe_2O_5F_{0.46+x}$	$Sr_3Fe_2O_5F_{0.46+x}$ *I*4/*mmm*			$Sr_3Fe_2O_5F_3$ *P*4/*mmm*		
	a/*b* (Å)	*c* (Å)	*V* (Å^3)	*a*/*b* (Å)	*c* (Å)	*V* (Å^3)
0	3.9120(3)	21.3930(1)	327.3925(6)			
0.5	3.9089(2)	21.4326(4)	327.4805(9)			
1.0	3.9020(8)	21.5247(3)	327.7368(3)			
1.5	3.9005(1)	21.5551(7)	327.9353(7)	3.9657(4)	23.1433(3)	363.9639(2)
2.0	3.8995(1)	21.5654(4)	327.9316(7)	3.9652(3)	23.1479(7)	363.9223(6)

Figure 3.13 depicts the reaction mechanism of electrochemical fluoride-ion (de)intercalation for $Sr_3Fe_2O_5F_2$. The crystal structure of pristine $Sr_3Fe_2O_5F_2$ changes to $Sr_3Fe_2O_5F_{0.46}$ with the deintercalation of 1.56 fluoride ions after the initial discharge to −1.5 V, whereupon partial anion vacancies exist in the perovskite layer. In the subsequent charging process until $Sr_3Fe_2O_5F_2$ ($0 < x < 1.5$ in $Sr_3Fe_2O_5F_{0.46+x}$), the fluoride-ion intercalation proceeds primarily by the solid-solution reaction with a negligible volume change (ca. 0.17%). Once the anion vacancies are fully occupied ($1.5 < x < 2$ in $Sr_3Fe_2O_5F_{0.46+x}$), the fluoride-ion intercalation proceeds via the two-phase

reaction between $Sr_3Fe_2O_5F_2$ and $Sr_3Fe_2O_5F_3$ with a large volume expansion (11%), in which the phase transition is induced by fluoride-ion insertion into the rock-salt layer of $Sr_3Fe_2O_5F_2$. In the case of LIB cathodes, it has also been reported that the lattice volume change is very small for the (de)intercalation of lithium ions into random percolation sites in the rock-salt structure, compared with the lattice volume expansion associated with the (de)intercalation of lithium ions into a 2D layered rock-salt oxide cathode (e.g., layered $LiCoO_2$ (3.63%),[23] cation-disordered rock salt $Li_{1.25}Nb_{0.25}V_{0.5}O_2$ oxide (1%),[26] and $Li_{1.25}V_{0.55}Nb_{0.2}O_{1.9}F_{0.1}$ oxyfluoride (0.7%)[24]). Our finding that the volume change upon fluoride-ion insertion into perovskite layers is significantly smaller than that into the interlayer is expected to prove valuable for the development of cathodes for all-solid-state FIBs.

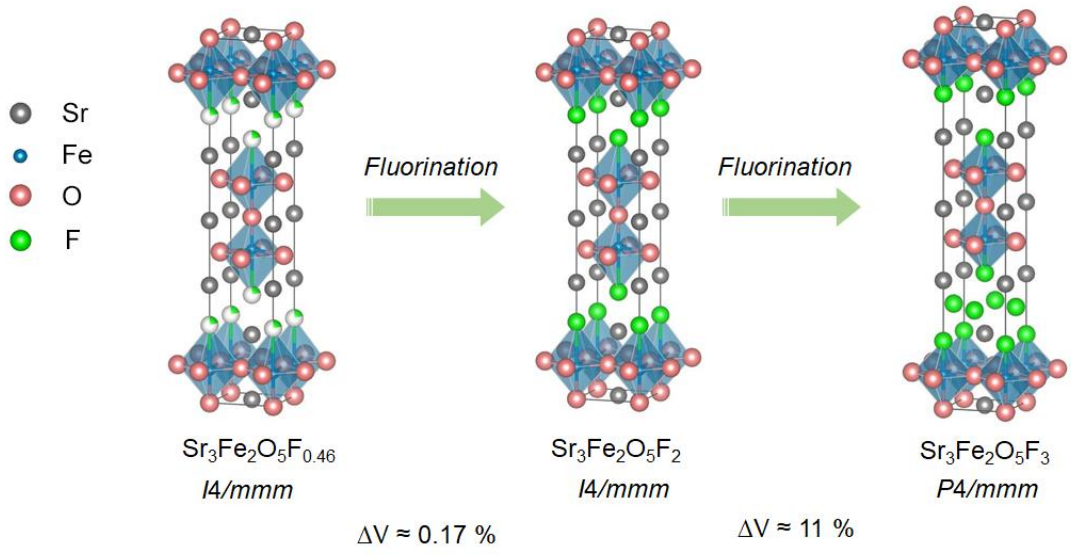

Figure 3.13. Schematic illustration of the volume changes and phase-transition models during the charging process for $Sr_3Fe_2O_5F_{0.46+x}$.

3.4 Conclusions

In summary, we have reported the synthesis of the new oxyfluoride $Sr_3Fe_2O_5F_2$ via a $Sr_3Fe_2O_5$ intermediate for the first time and evaluated its electrochemical performance as a cathode active material for FIBs. The crystal structure of $Sr_3Fe_2O_5F_2$ was elucidated by combining synchrotron XRD data and theoretical calculations. All of the results

indicate that $Sr_3Fe_2O_5F_2$ possesses *I*4/*mmm* symmetry. Fluoride ions were (de)inserted into lattice vacancies smoothly via 3D percolation sites, resulting in excellent cycling stability; that is, the capacity retention over 70 cycles reached 116.7 mAh g^{-1} with a coulombic efficiency of 98%. The crystal structure during the charging process retained the same space group until a composition of $Sr_3Fe_2O_5F_2$ with an extremely small volume change of approximately 0.17%. Fe^{2+}/Fe^{3+} redox reactions were responsible for the overall charge and discharge processes. All of the aforementioned processes are highly reversible. Although practical applications remain to be addressed, $Sr_3Fe_2O_5F_2$ represents a unique cathode material for FIBs based on the percolation mechanism.

References

1. Tarascon, J., The Li-ion battery: 25 years of exciting and enriching experiences. *Electrochem. Soc. Interface* **2016,** *25* (3), 79.

2. Janek, J.; Zeier, W. G., A solid future for battery development. *Nat. Energy* **2016,** *1*, *16141*.

3. Korthauer, R., *Handbuch lithium-ionen-batterien*. Springer: 2013.

4. Gschwind, F.; Rodriguez-Garcia, G.; Sandbeck, D. J. S.; Gross, A.; Weil, M.; Fichtner, M.; Hörmann, N., Fluoride ion batteries: Theoretical performance, safety, toxicity, and a combinatorial screening of new electrodes. *J. Fluor. Chem.* **2016,** *182*, 76-90.

5. Zhang, L.; Reddy, M. A.; Gao, P.; Diemant, T.; Jürgen Behm, R.; Fichtner, M., Study of all solid-state rechargeable fluoride ion batteries based on thin-film electrolyte. *J. Solid State Electrochem.* **2016,** *21* (5), 1243-1251.

6. Anji Reddy, M.; Fichtner, M., Batteries based on fluoride shuttle. *J. Mater. Chem.* **2011,** *21* (43), 17059-17062.

7. Zhang, D.; Yoshinari, T.; Yamamoto, K.; Kitaguchi, Y.; Ochi, A.; Nakanishi, K.; Miki, H.; Nakanishi, S.; Iba, H.; Watanabe, T.; Uchiyama, T.; Orikasa, Y.; Amezawa, K.; Uchimoto, Y., Cu–Pb Nanocomposite Cathode Material toward Room-Temperature Cycling for All-Solid-State Fluoride-Ion Batteries. *ACS Appl. Energy Mater.* **2021,** *4* (4), 3352-3357.

8. Yoshinari, T.; Zhang, D.; Yamamoto, K.; Kitaguchi, Y.; Ochi, A.; Nakanishi, K.; Miki, H.; Nakanishi, S.; Iba, H.; Uchiyama, T.; Watanabe, T.; Matsunaga, T.; Amezawa, K.; Uchimoto, Y., Kinetic analysis and alloy designs for metal/metal fluorides toward high rate capability for all-solid-state fluoride-ion batteries. *J. Mater. Chem. A* **2021,** *9* (11), 7018-7024.

9. Zhang, D.; Yamamoto, K.; Ochi, A.; Wang, Y.; Yoshinari, T.; Nakanishi, K.;

Nakano, H.; Miki, H.; Nakanishi, S.; Iba, H.; Uchiyama, T.; Watanabe, T.; Amezawa, K.; Uchimoto, Y., Understanding the reaction mechanism and performances of 3*d* transition metal cathodes for all-solid-state fluoride ion batteries. *J. Mater. Chem. A* **2021,** *9* (1), 406-412.

10. Zhang, D.; Nakano, H.; Yamamoto, K.; Tanaka, K.; Yahara, T.; Imai, K.; Mori, T.; Miki, H.; Nakanishi, S.; Iba, H., Rate-determining process at electrode/electrolyte interfaces for all-solid-state fluoride-ion batteries. *ACS Appl. Mater. & Interfaces* **2021,** *13* (25), 30198-30204.

11. Thieu, D. T.; Fawey, M. H.; Bhatia, H.; Diemant, T.; Chakravadhanula, V. S. K.; Behm, R. J.; Kübel, C.; Fichtner, M., CuF_2 as reversible cathode for fluoride ion batteries. *Adv. Funct. Mater.* **2017,** *27* (31), 1701051.

12. Nowroozi, M. A.; Wissel, K.; Rohrer, J.; Munnangi, A. R.; Clemens, O., $LaSrMnO_4$: reversible electrochemical intercalation of fluoride ions in the context of fluoride ion batteries. *Chem. Mater.* **2017,** *29* (8), 3441-3453.

13. Nowroozi, M. A.; Ivlev, S.; Rohrer, J.; Clemens, O., La_2CoO_4: a new intercalation based cathode material for fluoride ion batteries with improved cycling stability. *J. Mater. Chem. A* **2018,** *6* (11), 4658-4669.

14. Wissel, K.; Heldt, J.; Groszewicz, P. B.; Dasgupta, S.; Breitzke, H.; Donzelli, M.; Waidha, A. I.; Fortes, A. D.; Rohrer, J.; Slater, P. R.; Buntkowsky, G.; Clemens, O., Topochemical fluorination of La_2NiO_{4+d}: Unprecedented ordering of oxide and fluoride ions in $La_2NiO_3F_2$. *Inorg. Chem.* **2018,** *57* (11), 6549-6560.

15. Wang, Y.; Yamamoto, K.; Tsujimoto, Y.; Matsunaga, T.; Zhang, D.; Cao, Z.; Nakanishi, K.; Uchiyama, T.; Watanabe, T.; Takami, T.; Miki, H.; Iba, H.; Maeda, K.; Kageyama, H.; Uchimoto, Y., Anion substitution at apical sites of Ruddlesden–Popper-type cathodes toward high power density for all-solid-state fluoride-ion batteries. *Chem. Mater.* **2022,** *34* (2), 609-616.

16. Zhang, D.; Yamamoto, K.; Wang, Y.; Gao, S.; Uchiyama, T.; Watanabe, T.; Takami,

T.; Matsunaga, T.; Nakanishi, K.; Miki, H.; Iba, H.; Amezawa, K.; Maeda, K.; Kageyama, H.; Uchimoto, Y., Reversible and Fast (De)fluorination of High-Capacity Cu_2O Cathode: One Step Toward Practically Applicable All-Solid-State Fluoride-Ion Battery. *Adv. Energy Mater.* **2021,** *11* (45).

17. Wissel, K.; Schoch, R.; Vogel, T.; Donzelli, M.; Matveeva, G.; Kolb, U.; Bauer, M.; Slater, P. R.; Clemens, O., Electrochemical reduction and oxidation of Ruddlesden–Popper-type $La_2NiO_3F_2$ within fluoride-ion batteries. *Chem. Mater.* **2021,** *33* (2), 499-512.

18. Nowroozi, M. A.; Wissel, K.; Donzelli, M.; Hosseinpourkahvaz, N.; Plana-Ruiz, S.; Kolb, U.; Schoch, R.; Bauer, M.; Malik, A. M.; Rohrer, J.; Ivlev, S.; Kraus, F.; Clemens, O., High cycle life all-solid-state fluoride ion battery with La_2NiO_{4+d} high voltage cathode. *Commun. Mater.* **2020,** *1* (1).

19. Vasala, S.; Jakob, A.; Wissel, K.; Waidha, A. I.; Alff, L.; Clemens, O., Reversible tuning of magnetization in a ferromagnetic Ruddlesden–Popper-type manganite by electrochemical fluoride-ion intercalation. *Adv. Electron. Mater.* **2020,** *6* (2), 1900974.

20. McCabe, E. E.; Greaves, C., Fluorine insertion reactions into pre-formed metal oxides. *J. Fluor. Chem.* **2007,** *128* (4), 448-458.

21. Sivakumar, T.; Wiley, J. B., Topotactic route for new layered perovskite oxides containing fluorine: $Ln_{1.2}Sr_{1.8}Mn_2O_7F_2$ (Ln = Pr, Nd, Sm, Eu, and Gd). *Mater. Res. Bull.* **2009,** *44* (1), 74-77.

22. Tsujimoto, Y.; Yamaura, K.; Takayama-Muromachi, E., Oxyfluoride chemistry of layered Perovskite compounds. *Appl. Sci.* **2012,** *2* (1), 206-219.

23. Liu, Q.; Su, X.; Lei, D.; Qin, Y.; Wen, J.; Guo, F.; Wu, Y. A.; Rong, Y.; Kou, R.; Xiao, X.; Aguesse, F.; Bareño, J.; Ren, Y.; Lu, W.; Li, Y., Approaching the capacity limit of lithium cobalt oxide in lithium ion batteries via lanthanum and aluminium doping. *Nat. Energy* **2018,** *3* (11), 936-943.

24. Zhao, X.; Tian, Y.; Lun, Z.; Cai, Z.; Chen, T.; Ouyang, B.; Ceder, G., Design principles for zero-strain Li-ion cathodes. *Joule* **2022**, *6* (7), 1654-1671.

25. Lee, J.; Papp, J. K.; Clement, R. J.; Sallis, S.; Kwon, D. H.; Shi, T.; Yang, W.; McCloskey, B. D.; Ceder, G., Mitigating oxygen loss to improve the cycling performance of high capacity cation-disordered cathode materials. *Nat. Commun.* **2017,** *8* (1), 981.

26. Nakajima, M.; Yabuuchi, N., Lithium-excess cation-disordered rocksalt-type oxide with nanoscale phase segregation: $Li_{1.25}Nb_{0.25}V_{0.5}O_2$. *Chem. Mater.* **2017,** *29* (16), 6927-6935.

27. Kageyama, H.; Watanabe, T.; Tsujimoto, Y.; Kitada, A.; Sumida, Y.; Kanamori, K.; Yoshimura, K.; Hayashi, N.; Muranaka, S.; Takano, M.; Ceretti, M.; Paulus, W.; Ritter, C.; Andre, G., Spin-ladder iron oxide: $Sr_3Fe_2O_5$. *Angew. Chem. Int. Ed. Engl.* **2008,** *47* (31), 5740-5.

28. Rongeat, C.; Reddy, M. A.; Witter, R.; Fichtner, M., Solid electrolytes for fluoride ion batteries: ionic conductivity in polycrystalline tysonite-type fluorides. *ACS Appl. Mater. Interfaces* **2014,** *6* (3), 2103-10.

29. Blakely, C. K.; Davis, J. D.; Bruno, S. R.; Kraemer, S. K.; Zhu, M.; Ke, X.; Bi, W.; Alp, E. E.; Poltavets, V. V., Multistep synthesis of the $SrFeO_2F$ perovskite oxyfluoride via the $SrFeO_2$ infinite-layer intermediate. *J. Fluor. Chem.* **2014,** *159*, 8-14.

30. Petříček, V.; Dušek, M.; Palatinus, L., Crystallographic computing system JANA2006: general features. *Zeitschrift für Kristallographie-Crystalline Materials* **2014,** *229* (5), 345-352.

31. Momma, K.; Izumi, F., VESTA 3 for three-dimensional visualization of crystal, volumetric and morphology data. *J. Appl. Crystallogr.* **2011,** *44* (6), 1272-1276.

32. Mizutani, U.; Sato, H.; Massalski, T., The original concepts of the Hume-Rothery rule extended to alloys and compounds whose bonding is metallic, ionic, or

covalent, or a changing mixture of these. *Prog. Mater. Sci.* **2021**, 120, 100719.

33. Tsujimoto, Y.; Yamaura, K.; Hayashi, N.; Kodama, K.; Igawa, N.; Matsushita, Y.; Katsuya, Y.; Shirako, Y.; Akaogi, M.; Takayama-Muromachi, E., Topotactic Synthesis and Crystal Structure of a Highly Fluorinated Ruddlesden–Popper-Type Iron Oxide, $Sr_3Fe_2O_{5+x}F_{2-x}$ ($x \approx 0.44$). *Chem. Mater.* **2011**, 23 (16), 3652-3658.

34. Case, G. S.; Hector, A. L.; Levason, W.; Needs, R. L.; Thomas, M. F.; Weller, M. T., Syntheses, powder neutron diffraction structures and Mössbauer studies of some complex iron oxyfluorides: $Sr_3Fe_2O_6F_{0.87}$, Sr_2FeO_3F and $Ba_2InFeO_5F_{0.68}$. *J. Mater. Chem.* **1999,** *9* (11), 2821-2827.

35. Haruyama, J.; Okazaki, K. I.; Morita, Y.; Nakamoto, H.; Matsubara, E.; Ikeshoji, T.; Otani, M., Two-Phase Reaction Mechanism for Fluorination and Defluorination in Fluoride-Shuttle Batteries: A First-Principles Study. *ACS Appl. Mater. Interfaces* **2020**, *12* (1), 428-435.

36. Zhang, L.; Anji Reddy, M.; Fichtner, M., Development of tysonite-type fluoride conducting thin film electrolytes for fluoride ion batteries. *Solid State Ionics* **2015**, *272*, 39-44.

37. Zu, C.-X.; Li, H., Thermodynamic analysis on energy densities of batteries. *Energy Environ. Sci.* **2011**, *4* (8).

38. Rongeat, C.; Reddy, M. A.; Witter, R.; Fichtner, M., Solid electrolytes for fluoride ion batteries: ionic conductivity in polycrystalline tysonite-type fluorides. *ACS Appl. Mater. Interfaces* **2014,** *6* (3), 2103-2110.

39. Yoon, W.-S.; Balasubramanian, M.; Chung, K. Y.; Yang, X.-Q.; McBreen, J.; Grey, C. P.; Fischer, D. A., Investigation of the charge compensation mechanism on the electrochemically Li-Ion deintercalated $Li_{1-x}Co_{1/3}Ni_{1/3}Mn_{1/3}O_2$ electrode system by combination of soft and hard X-ray absorption spectroscopy. *J. Am. Chem. Soc.* **2005,** *127* (49), 17479-17487.

40. Liu, X.; Liu, J.; Qiao, R.; Yu, Y.; Li, H.; Suo, L.; Hu, Y.-s.; Chuang, Y.-D.; Shu, G.;

Chou, F. Weng, T. C.; Nordlund, D.; Sokaras, D.; Wang, Y. J.; Lin, H.; Barbiellini, B.; Bansil, A.; Song, X.; Liu, Z.; Yan S.; Liu G.; Qiao S.; Richardson T. J.; Prendergast D.; Hussain Z.; Groot, Frank M. F. de; Yang, W., Phase transformation and lithiation effect on electronic structure of Li_xFePO_4: an in-depth study by soft X-ray and simulations. *J. Am. Chem. Soc.* **2012,** *134* (33), 13708-13715.

41. Susanto, D.; Cho, M. K.; Ali, G.; Kim, J.-Y.; Chang, H. J.; Kim, H.-S.; Nam, K.-W.; Chung, K. Y., Anionic redox activity as a key factor in the performance degradation of $NaFeO_2$ cathodes for sodium ion batteries. *Chem. Mater.* **2019,** *31* (10), 3644-3651.

42. Yamamoto, K.; Zhou, Y.; Yabuuchi, N.; Nakanishi, K.; Yoshinari, T.; Kobayashi, T.; Kobayashi, Y.; Yamamoto, R.; Watanabe, A.; Orikasa, Y.; Tsuruta, K.; Park, J.; Byon, H. R.; Tamenori, Y.; Ohta, T.; Uchimoto, Y., Charge Compensation Mechanism of Lithium-Excess Metal Oxides with Different Covalent and Ionic Characters Revealed by Operando Soft and Hard X-ray Absorption Spectroscopy. *Chem. Mater.* **2019,** *32* (1), 139-147.

43. House, R. A.; Maitra, U.; Perez-Osorio, M. A.; Lozano, J. G.; Jin, L.; Somerville, J. W.; Duda, L. C.; Nag, A.; Walters, A.; Zhou, K. J.; Roberts, M. R.; Bruce, P. G., Superstructure control of first-cycle voltage hysteresis in oxygen-redox cathodes. *Nature* **2020,** *577* (7791), 502-508.

44. Dai, K.; Wu, J.; Zhuo, Z.; Li, Q.; Sallis, S.; Mao, J.; Ai, G.; Sun, C.; Li, Z.; Gent, W. E.; Chueh, W. C.; Chuang, Y.-d.; Zeng, R.; Shen, Z.-x.; Pan, F.; Yan, S.; Piper, L. F. J.; Hussain, Z.; Liu, G.; Yang, W., High reversibility of lattice oxygen redox quantified by direct bulk probes of both anionic and cationic redox reactions. *Joule* **2019,** *3* (2), 518-541.

45. Gent, W. E.; Abate, I. I.; Yang, W.; Nazar, L. F.; Chueh, W. C., Design rules for high-valent redox in intercalation electrodes. *Joule* **2020,** *4* (7), 1369-1397.

Chapter 4. High Capacity and Zero Strain Iron-based Oxyfluoride Cathodes for All-solid-state Fluoride-ion Batteries

Electrochemical energy storage system with high energy density and safety is significantly important to realize green and sustainable society. All-solid-state fluoride-ion batteries (FIBs), which can achieve a higher energy density and safety than lithium-ion batteries, are promising candidates.[1,2] However, no cathode material for all-solid-state FIBs has been found that exceeds the capacity of cathode materials for lithium-ion batteries, and has a small volume change as well which is extremely important for all-solid-state batteries. Here we report that a perovskite oxyfluoride $SrFeO_2F_x$ obtained from $SrFeO_2$ with infinite layer structure[3] exhibits topotactic fluoride ion (de)intercalation, providing a large reversible capacity of 350 mAh g^{-1} (1843 mAh cm^{-3}) with excellent cycle stability and rate capability. The surprising capacity is obtained by (de)intercalation of 1.3 extra fluoride ion beyond $x = 1$ ($0 \leq x \leq 2.3$ in $SrFeO_2F_x$) and the additional fluoride ion intercalation leads to the formation of molecular O_2 in the perovskite structure for charge compensation, as in $Li_{1.2}Ni_{0.13}Co_{0.13}Mn_{0.54}O_2$ and[4] $Na_{0.75}[Li_{0.25}Mn_{0.75}]O_2$[5]. Moreover, the volume expansion of the $SrFeO_2F_x$ cathode with the excess fluoride ion intercalation ($x = 2.3$) was 0.5%, comparable to that of $Li_4Ti_5O_{12}$ (0.2%), which is known as a strain-free electrode.[6] These results highlight the perovskite oxyfluorides obtained from infinite layer structure as a new class of active materials for the construction of high-performance FIBs.

4.1 Introduction

The development of storage batteries is becoming significantly important for mankind to build a sustainable society. Lithium-ion batteries (LIBs) are successfully commercialized for over 30 years because of their high capacity and long life, and a variety of materials have been developed; starting with the typical $LiCoO_2$,[7] and in recent years, Li-rich cathodes that utilize the charge compensation of oxygen.[8-12] However, as electric vehicles and smart grid systems are becoming more widespread, rechargeable batteries with even higher capacities as well as a high level of safety are required.

Various types of next generation rechargeable batteries using different carrier ions (e.g., Li^+, Na^+, Mg^{2+}, Cl^-, F^-) have been proposed to meet these requirements. [1,13-18]. Among them, all-solid-state fluoride-ion batteries (FIBs), which use fluoride ions as carriers, are promising because of their theoretically high energy density and safety.[1,2,19-25] Moreover, the highest electronegativity of fluorine as well as high redox potential 2.87 V (vs. standard hydrogen electrode) of F^-/F_2 allow choice of electrode materials with high redox potential.[26] Typical conversion-type cathodes (M/MF_x), such as CuF_2 and BiF_3, exhibit high theoretical capacity,[1,19,22] however, the large volume change upon charge/discharge cycling causes contact loss between the active material and the solid electrolyte, leading to reduce cyclability and rate performance.

In order to solve this problem, attention has been focused on the development of intercalation-type cathodes, which benefit from the rigid host lattice and allow the topotactic (de)intercalation reaction of fluoride ions with small volume change. It has been reported various intercalation-type cathodes with a Ruddlesden-Popper perovskite structure such as $LaSrMnO_4$, La_2CoO_4 and Sr_2MnO_3F.[27-30] Although these compounds have the advantage of smaller volume change during charge/discharge compared to metal fluorides, the unsatisfactory capacity due to the large formula of the host compound is the intrinsic disadvantage.

In this study, we applied $SrFeO_2$ compound, which has an infinite layer structure consisting of regularly arranged anion vacancies[3] and is reported to chemically accommodate 1 F^- per unit,[31] to the cathode material for all-solid-state FIBs. After several electrochemical fluoride ion (de)intercalation cycling, this cathode can accommodate reversibly F^- exceeding 1 mol and provide high capacities of 350 mAh g^{-1} and 1843 mAh cm^{-3} with the charge compensation of molecular O_2 formation (anion redox). In addition, the volume change of this cathode material during fluoride ion (de)intercalation is 0.5 %, which is significantly smaller than that of LIBs cathode materials, making it quite attractive as a cathode for all-solid-state batteries. We believe this finding that the intercalation cathode with molecular O_2 formation can provide high capacity gives new design principle for the cathode of all-solid-state FIBs, as well as bring more considerations for developing novel mixed-anion compounds.

4.2 Experimental

4.2.1 Synthesis of materials.

$SrFeO_3$ was prepared by using conventional solid-state reaction similar to previously described.[1] Reagent grade of $SrCO_3$ (99.99%, Kojundo Chemical Laboratory) and Fe_2O_3 (99.9%, WAKO pure chemical industries, ltd.) were used as starting materials. These materials were mixed with a stoichiometric ratio. The mixture was pressed into a pellet and annealed at 1273 K for 24 h in air, ground again, and heat for additional 24 h at 1473 K. The obtained $SrFeO_{3-\delta}$ (0.45 g) was finely ground with a two-molar excess of CaH_2 (0.2 g) in an Ar-filled glove box, sealed in an evacuated Pyrex tube with under vacuum, and reacted at 553 K for two days. The residual CaH_2 and the CaO byproduct were removed from the final reaction phase by washing them with 0.1 M NH_4Cl in dried methanol. $La_{0.9}Ba_{0.1}F_{2.9}$ solid electrolyte with fluoride-ion conductivity, was synthesized as reported in the literature.[2] LaF_3 (99.9%, Kojundo Chemical Laboratory) and BaF_2 (99.9%, Kojundo Chemical Laboratory) were mixed

in a molar ratio of 9:1 and ball-milled at 600 rpm for 12 h using Ar-filled 45 mL ZrO_2 pot and Φ5 mm balls. The mixture was annealed at 600 °C for 10 h in Ar atmosphere.

4.2.2 Cell Assembly and electrochemical measurements

The cathode composite consisted of $SrFeO_2$ powder, $La_{0.9}Ba_{0.1}F_{2.9}$ powder and Vapor-Grown Carbon Fiber (Showa Denko, VGCF, battery grade), with mixed in a weight ratio of 30:60:10 by ball-milling for 10 h at 100 rpm using 45 mL of ZrO_2 pot and ZrO_2 balls. $La_{0.9}Ba_{0.1}F_{2.9}$ was used as a solid electrolyte. $Ca_{0.5}Ba_{0.5}F_2$ was prepared by high-energy ball milling a stoichiometric ratio of BaF_2 and CaF_2 together. The total mass of the mixture was about 2 g. A ball mill pot made of ZrO_2 with a volume of 45 mL was employed. The mixture was mechanically treated 99 h using 140 milling balls (ZrO_2, 5 mm in diameter) at 600 rpm.

PbF_2/acetylene black (Denki Kagaku Kogyo, AB) composites, mixed by ball-milling for 3 h at 600 rpm, are used as a fluorine source on anode side. The electrochemical cells were assembled in disk-shaped pellet by compressed cathode/solid electrolyte/anode layers. At first, 10 mg of cathode composite and 200 mg of $La_{0.9}Ba_{0.1}F_{2.9}$ were compressed for 5 min under 360 MPa. Then, PbF_2/AB composite was added as an anode layer and Au foils were added on both ends as a current collector. These layers were compressed under 360 MPa. The diameter of the pellet was 10 mm. All fabrication processes of the all-solid-state type electrochemical cell were conducted under Ar atmosphere in a glovebox.

Assembled cells were put in a sealed container without exposing to the air atmosphere. Charge and discharge experiments of the all-solid-state fluoride ion cells were conducted in a potential range -1.5~3.0 V vs. Pb/PbF_2 at 140 °C with current density of 5 mA g^{-1} unless otherwise specified. Rate performance of the charge-discharge profiles were measured with various current densities at both charge and discharge processes. The electrochemical properties of the electrochemical test cells were collected using a galvanostat apparatus (HJ1010SD8, Hokuto Denko Corporation).

4.2.3 Materials characterization

High-resolution X-ray powder diffraction data were collected at room temperature in Ar atmosphere, at the BL02B2 and BL19B2 beamlines at the SPring-8 (Hyogo, Japan). The powder samples without electrochemical measurement were conducted at the BL02B2 beamline, where the diffractometer was equipped with six MYTHEN silicon micro-strip photon-counting detectors (Dectris Ltd., Baden, Switzerland), and the measurements were performed in Debye-Scherrer transmission geometry was used.[3] The pellet samples with electrochemical measurement were conducted at the BL19B2 beamline using a Huber multi-axis diffractometer with a scintillation counter in Bragg-Brentano geometry at the BL19B2 beamline.

X-ray absorption spectra for Fe *K*-edge were obtained in the transmission/fluorescence mode using a Si(111) double crystal monochromator at BL14B2 at SPring-8. For Fe, a pair of Rh mirrors with angles of 6 mrad and 2.8 mrad, respectively, were used to eliminate higher order harmonics. The samples were fixed in the laminate cell filled with Ar. X-ray absorption spectra for O and F K-edge were obtained in the fluorescence mode using a varied-line-spacing plane grating as a monochromator with Au mirror at C-branch of BL27SU at SPring-8. The measurements were conducted under vacuum and the samples were transferred from an Ar-filled glove box without exposure to air. Resonant inelastic X-ray scattering (RIXS) measurements were performed at BL07LSU in SPring-8 using a grazing flat-field type high resolution soft X-ray emission spectrometer.[4] The total energy resolution of the RIXS spectra ΔE_tot=√(ΔE_hν^2+ΔE_ana^2) was approximately 150 meV, determined by fitting the elastic scattering from Cu plate. The energy resolution of the incident photon ΔEhv is around 100 meV, so the energy resolution of the soft X-ray emission analyzer at 530 eV ΔEana is estimated to be around 110 meV. The loss energy of RIXS was calibrated as follows. First, the incident X-ray energy was set to 530 eV and 520 eV, the elastic peaks from a Cu plate at both energies were measured, and the emission energy of each elastic peak was determined to be 530 and 520 eV, respectively.

The scaling between the two peaks was then calculated by a quadratic function derived from the optical design, and the conversion equation from the position on the detector to emission energy was obtained. As with the accuracy of the beamline photon energy, the accuracy of the absolute emission energy is about ±0.2 eV, but the relative accuracy is within ±0.5%. Here, the energy loss in RIXS is the energy difference from the elastic scattering, which means that the accuracy of the energy loss is within ±0.5%. The sample powders were supported on the carbon tape in the glovebox filled with Ar gas and transferred to the measurement chamber without exposure to atmosphere. The sample positions were changed at 2.4 μm/s during the RIXS measurements to avoid radiation damage.

4.3 Results and discussion

4.3.1 Fluoride ion (de)intercalation behavior of $SrFeO_2$ before activation

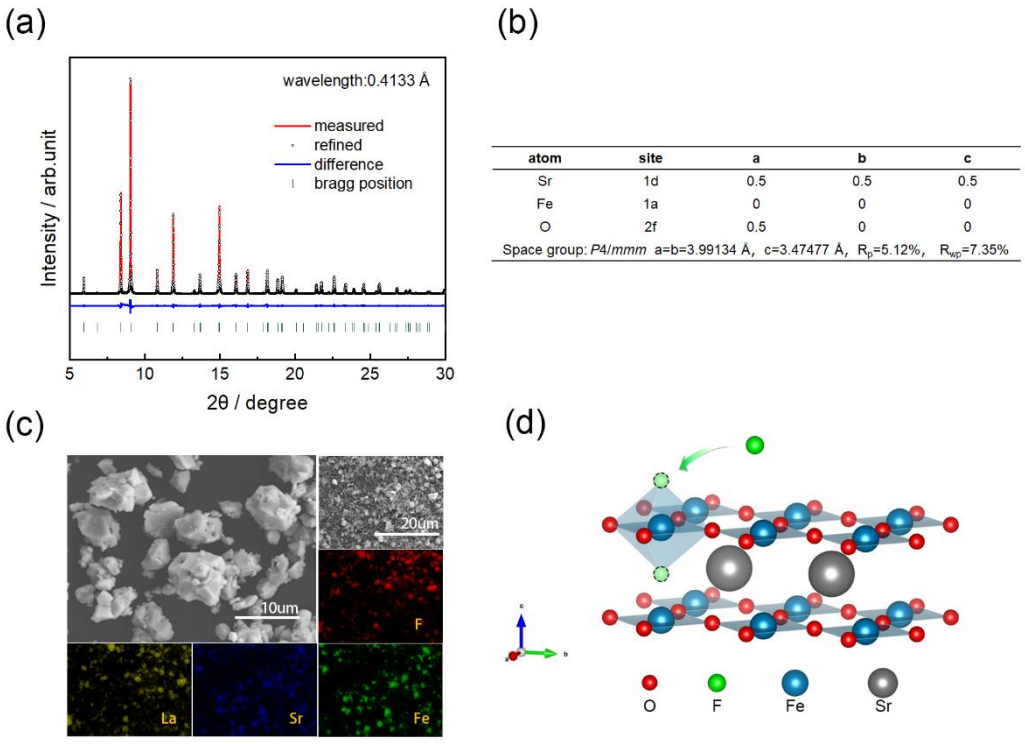

atom	site	a	b	c
Sr	1d	0.5	0.5	0.5
Fe	1a	0	0	0
O	2f	0.5	0	0

Space group: *P4/mmm* a=b=3.99134 Å, c=3.47477 Å, R_p=5.12%, R_{wp}=7.35%

Figure 4.1 (a), X-ray diffraction patterns and Rietveld refinement result of as-prepared $SrFeO_2$. (b), Refined structural data for $SrFeO_2$. (c), SEM-EDX of the

$SrFeO_2$ cathode. (d), Schematic diagram of the crystal structure and the sites that can accommodate fluoride ions.

$SrFeO_2$ was synthesized by reducing pre-prepared $SrFeO_3$ with CaH_2 according to previous study.[3] The details of the synthesis procedure and characterization are described in Figure 4.1. As-prepared $SrFeO_2$ was mixed with solid electrolyte ($La_{0.9}Ba_{0.1}F_{2.9}$) and Vaper-Grown Carbon Fiber (VGCF) by ball milling in a weight ratio of 30: 60: 10 as previous reports.[27,30] To evaluate electrochemical properties of the $SrFeO_2$ cathode, two-electrode cell was assembled, in which excess amount of Pb/PbF_2 composite for the $SrFeO_2$ cathode was used due to the rapid fluorination/defluorination kinetics of PbF_2 and the constant redox potential in the wide fluorine content.[25]

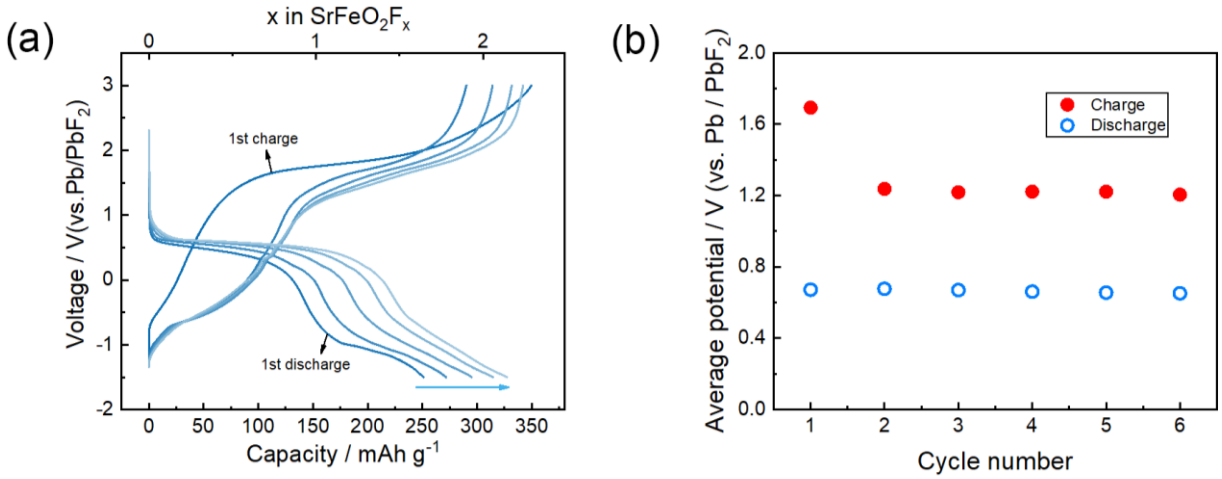

Figure 4.2 (a) Charging/discharging curves during 1st-6th cycling at a rate of 5 mA g^{-1} at 140°C. (b) Average voltage of $SrFeO_2$ cathode during initial 1^{st}-6^{th} cycling.

As shown in Figure 4.2a, the $SrFeO_2$ cathode showed a capacity of 350 mAh g^{-1} with one slope between -1.0 and 1.7 V and one voltage plateau at 1.8 V on the first charging process, and a capacity of 251 $mAhg^{-1}$ with voltage plateaus at 0.5 V and -0.1 V on the subsequent discharging process. The irreversible charge capacity on the first cycle might be originated from partial oxygen release reaction as reported in LIBs[32,33]. After the initial cycling, the cathode showed a charge capacity of 290 mAh g^{-1} with voltage plateaus at -0.5 V and 1.5 V, which is different behavior from the first charging process, and it delivered a discharge capacity of 271 mAh g^{-1} with voltage plateaus at

0.5 V and -1.0 V, which is similar to the first discharging process. In the subsequent cycles, the capacity gradually increased up to six cycles, showing the same charge/discharge curve as in the second cycle. The average voltage of charging/ discharging during the initial six cycles changed largely only from first charging to second charging (Figure 4.2b). These results indicate that the structure of $SrFeO_2$ changes significantly during the first charging process.

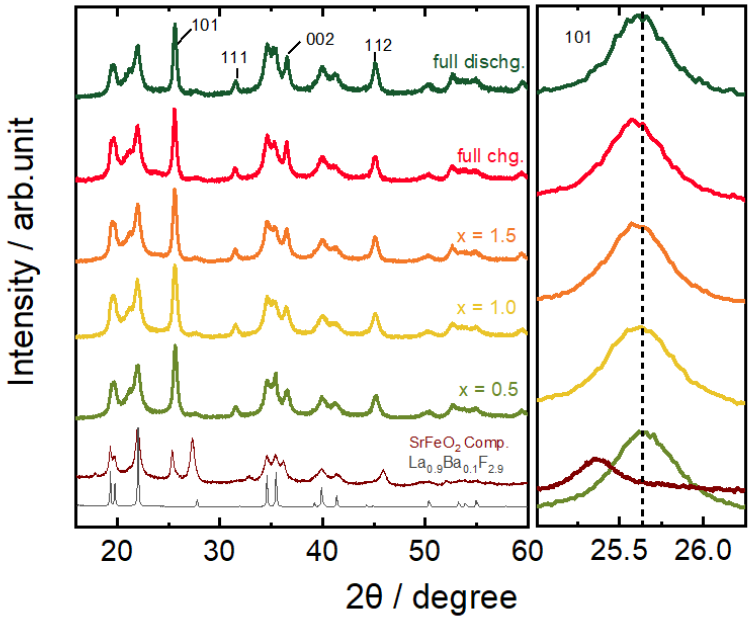

Figure 4.3 XRD patterns of cathode composites containing the $SrFeO_2$ before and after initial charging/discharging. $La_{0.9}Ba_{0.1}F_{2.9}$ solid electrolyte is shown as reference. Inset is enlarged view of the XRD around 25.5°.

The crystal and electronic structural changes during the first charge and discharge were examined by synchrotron X-ray diffraction (XRD) and X-ray absorption spectroscopy (XAS) for Fe and O *K*-edge. In the XRD patterns (Figure 4.3), all diffraction peaks were indexed by $SrFeO_2$ in the space group *P4/mmm* and the $La_{0.9}Ba_{0.1}F_{2.9}$ electrolyte before charging. After charging to $x = 0.5$, the crystal structure of $SrFeO_2$ changed to that with the space group of $Pm\bar{3}m$, which is same as $SrFeO_2F$ obtained by chemically fluorination of $SrFeO_2$.[31] The peak position shifted to the lower angle side with maintaining the same crystal structure in subsequent charging. After discharging process, although the peak position shifted to the higher angle side, the

crystal structure of the $SrFeO_2F_x$ did not return to the pristine one with the space group of *P4/mmm*, but remained with the space group of $Pm\bar{3}m$. This behavior is similar to the previously reported $Li_{1.211}Mo_{0.467}Cr0.3O_2$ (LMCO) compounds, where the transition metal (Mo and Cr) migrates to the Li layers after few charge-discharge cycles, and the overall structure completes the transition from layered structure to disordered rock-salt. The cathode after phase transition exhibits isotropic Li-ion diffusion and a near-zero volume change of ~ 0.12% after charging to 4.3V. [34]

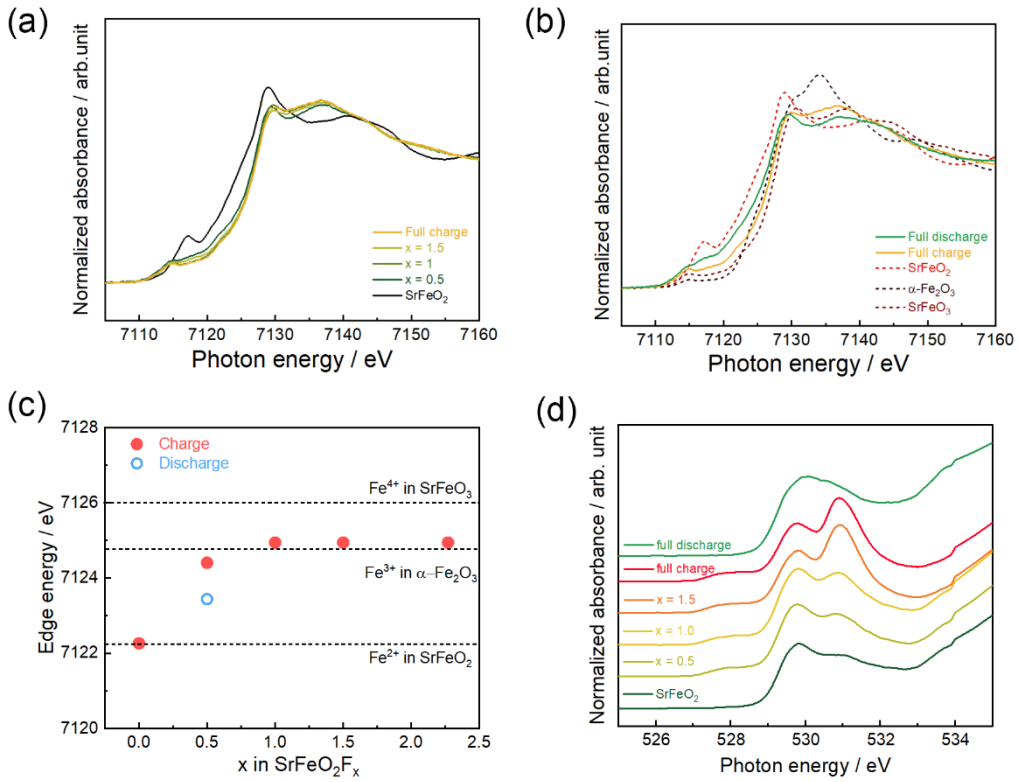

Figure 4.4 Fe *K*-edge XAS spectra (a) during charging, (b) during discharging for various states in charge /discharge profiles shown in Figure 4.2a. The x in the figure represents the fluoride content (x in $SrFeO_2$). (c) Edge energy of Fe *K*-edge XAS spectra, (d) O *K*-edge XAS spectra for various states in charge /discharge profiles shown in Figure 4.2a. The *x* in the figure represents the fluoride content (*x* in $SrFeO_2$).

In the Fe *K*-edge XAS spectra (Figure 4.4a-c), the energy of the absorption edge shifted to the higher energy in the early stage of insertion of fluoride ions (x < 1), but then remained unchanged in the subsequent insertion of fluoride ions (x > 1). The

energy of E_0 partially return to the original energy after full discharge. In the O *K*-edge XAS spectrum (Figure 4.4d), two peaks, which is attributed to the transitions from the O 1*s* level to the hybridized states of the Fe 3*d* and O 2*p* orbitals,[35] was observed around 530 eV before charging ($SrFeO_2$). The intensity at 527.5 eV increased in the early stage of fluoride ion insertion ($x < 1$), which is observed in other iron-based interaction materials.[12,36] On the other hand, further fluoride ion insertion beyond $x \sim 1$ resulted in the appearance of a new O *K*-edge peak at around 530.8 eV, which is similar to oxygen redox behavior observed in the lithium-rich cathodes[4,10,12,36]. Then after full discharge, the shape of the spectrum did not return to the state before charging. These results indicate that the crystal structure of $SrFeO_2$ changes irreversibly from the infinite layer structure (*P4/mmm*) to the $SrFeO_2F_x$ perovskite structure ($Pm\bar{3}m$) during the first cycling, and at the same time the electronic structure of Fe and O changes irreversibly. The large difference in the shape of the charge/discharge curves between the first and second cycles (Figure 4.2a) would be attributed to these irreversible changes. Although the origin of the gradual increase in charge/discharge capacity up to the sixth cycle is not clear, the same shape of the charge/discharge curve suggests that electrochemical (de)intercalation of fluoride ions into the perovskite structure $SrFeO_2F_x$ is occurring. Herein, we consider the initial 6 cycles with the observed increment in capacities as the activation process of the $SrFeO_2$ cathode, the electrochemical properties and the reaction mechanism of the $SrFeO_2F_x$ cathode after the 6th full discharge (at the end of the activation process) will be investigated in the following section.

4.3.2 Fluoride ion (de)intercalation behavior of $SrFeO_2$ after activation

The $SrFeO_2F_x$ after the activation process showed excellent electrochemical properties. As shown in Figure 4.5a, the $SrFeO_2F_x$ provided a capacity of 353 mAh g^{-1}, which exceeds capacity for 1 F^-, with a slope around 0.5 V and a plateau around 1.5 V in the charging process, and then it provided a capacity of 350 mAh g^{-1} with a slope and a plateau in the discharging process. The charge/discharge capacities of $SrFeO_2F_x$

maintained over 320 $mAhg^{-1}$ without voltage decay for at least 30 cycles, and the coulombic efficiency for each cycle was close to 100% (Figure 4.5b, c). Furthermore, the rate characteristics of the $SrFeO_2F_x$ were relatively good (150 $mAhg^{-1}$ at 200 mAg^{-1} as shown in Figure 4.5d), suggesting rapid diffusion of fluoride ions in the bulk. Further, a full cell using the $SrFeO_2F_x$, $Ca_{0.5}Ba_{0.5}F_2$ and $La_{2.9}Ba_{0.1}F_{2.9}$ as cathode, solid electrolyte, and anode, respectively, was tested for electrochemical performance (Figure 4.6 and 4.7). The full cell showed a capacity of 310 mAh g^{-1} with an average voltage of 2.8 V and good cyclability. Based on the active material, the full cell shows a gravimetric energy density of 495 Wh kg^{-1} and a volumetric energy density of 2736 Wh L^{-1}, which are larger than a typical $LiCoO_2$/graphite cell (376 Wh kg^{-1} and 1403 Wh L^{-1}, as shown in Supplementary Table 1).

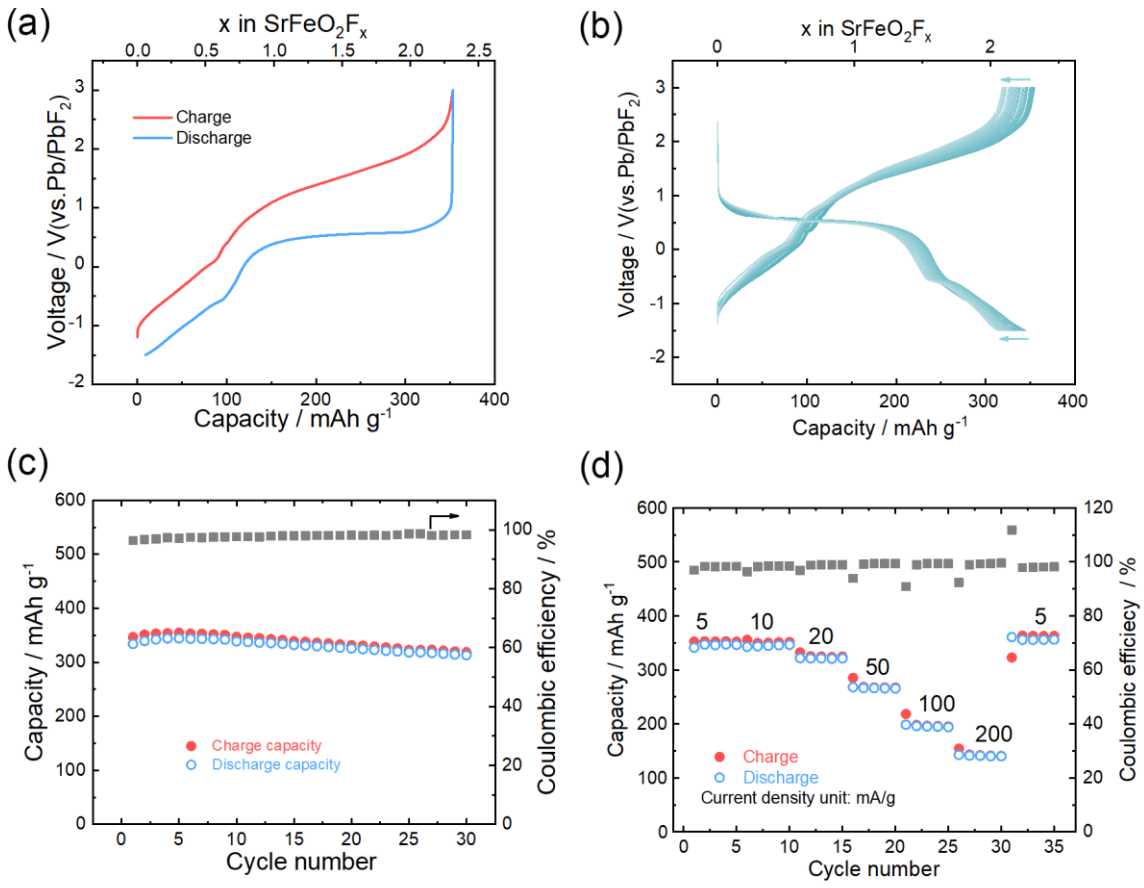

Figure 4.5 Electrochemical properties of the $SrFeO_2F_x$ after activation process. Charging/discharging curves of (a) the first cycle. (b) 1st-30th cycling at a rate of 5 mA g^{-1} at 140°C after activation process. (c) Cycle performance of

charging/discharging capacities and coulombic efficiency at a rate of 5 mA g^{-1} at 140°C. (d) Rate performance and coulombic efficiency with different current density between 5 and 200 mA g^{-1} at 140°C.

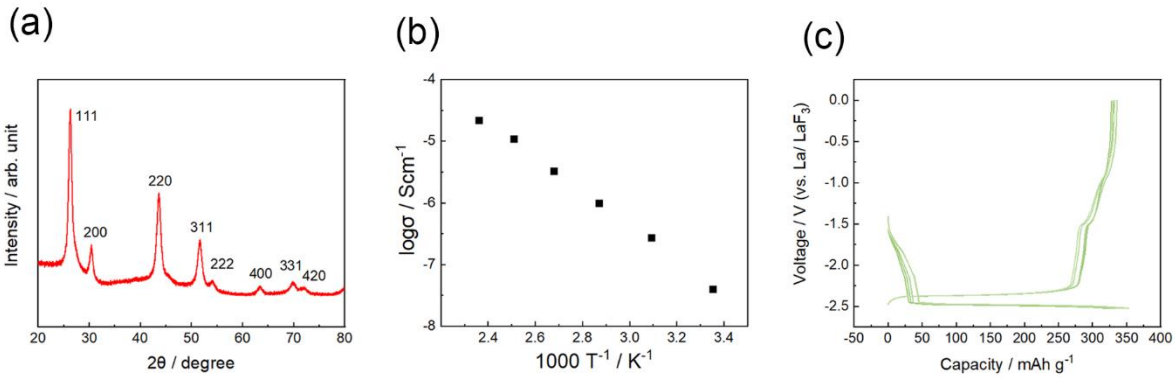

Figure 4.6 (a) XRD patterns of $Ca_{0.5}Ba_{0.5}F_2$. **(b)** ionic conductivity of $CaBaF_4$. **(c)** charge/discharge profiles of $La_{0.9}Ba_{0.1}F_{2.9}$/$Ca_{0.5}Ba_{0.5}F_4$/Pb-PbF_2 cell at a rate of 10 mA/g under 140 °C.

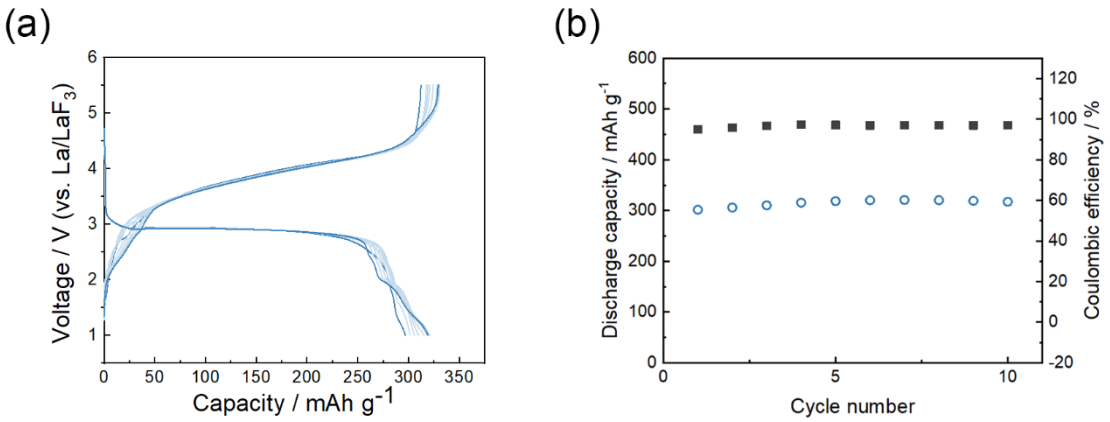

Figure 4.7 (a) Charge/discharge profiles of $SrFeO_2$/$Ca_{0.5}Ba_{0.5}F_2$/$La_{0.9}Ba_{0.1}F_{2.9}$ cell at a rate of 10 mA/g under 140 °C. (b) Capacity and coulombic coefficient with each cycle number.

The crystal structure of the activated $SrFeO_2F_x$ before charging (pristine) was in space group $Pm\bar{3}m$ with a lattice constant of a = 3.9503 Å, which was same as the crystal structure after the first discharge of the non-activated $SrFeO_2$ (Figure 3a). On subsequent charging, the 101 peak of the $SrFeO_2F_x$ shifted continuously to lower angles with the same space group, and then after discharge, it returned to the same state as

before charging, indicating a reversible change in the crystal structure. The lattice constant calculated from the XRD pattern fitting via Le Bail analysis was reversibly changed from 3.9503 Å to 3.9569 Å (the lattice volume expansion ratio ≈ 0.5 %) upon F^- (de)intercalation (Figure 3b). Considering the fact that disordered rock-salt Li-excess (DRX) compounds have been shown to be intrinsically superior in suppressing volume changes during cycling[37], it is self-consistent to use similar nature of anion disordering to achieve negligible volume expansion in FIBs. Figure 3c shows a comparison of volumetric capacity and volume expansion ratio during charge/discharge for the $SrFeO_2F_x$ with those of previously reported LIBs and FIBs cathodes.[30,37-45] The $SrFeO_2F_x$ achieves higher capacity (1843 mAh cm^{-3}) than the previous LIBs and FIBs cathodes with the significantly small volume expansion ratio (0.5%), which is comparable to the values of $Li_4Ti_5O_{12}$, known as a non-strained lithium-ion intercalation electrode.[6]

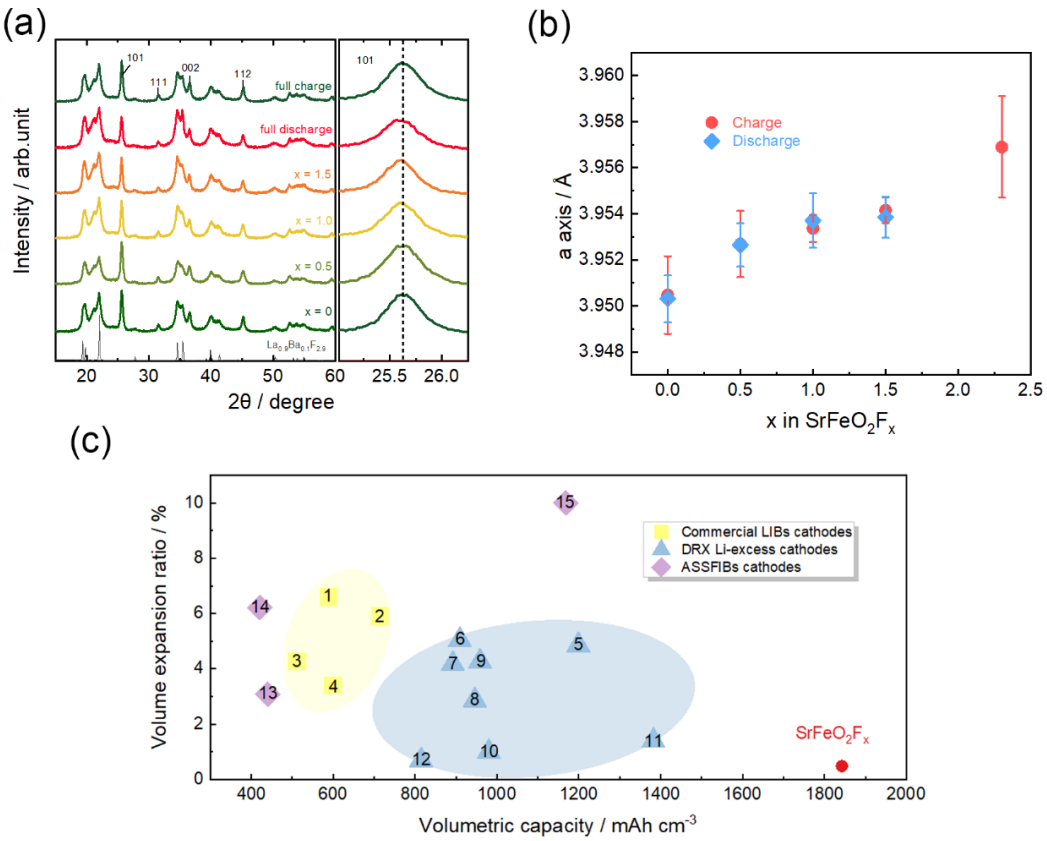

Figure 4.8 (a) XRD patterns of cathode composites containing the $SrFeO_2F_x$ before and after charging/discharging. $La_{0.9}Ba_{0.1}F_{2.9}$ solid electrolyte is shown as

reference. Inset is enlarged view of the XRD around 25.5°. (b**)**. Lattice constant a and volume expansion ratio of the $SrFeO_2F_x$ before and after charging/discharging. (c), Plots of the volume expansion ratio for volumetric capacities for $SrFeO_2F_x$ and cathode materials reported in FIBs and LIBs: 1. $LiFePO_4$[38], 2. $LiNi_{0.8}Co_{0.15}Al_{0.05}O_2$[40], 3. $LiCoO_2$[39], 4, $LiNi_{1/3}Co_{1/3}Mn_{1/3}O_2$[40], 5. $Li_{1.25}Nb_{0.25}Mn_{0.5}O_2$[41], 6. $Li_{1.2}Ni_{0.333}Ti_{0.333}Mo_{0.133}O_2$[42], 7. $Li_{1.15}Ni_{0.45}Ti_{0.3}Mo_{0.1}O_{1.85}F_{0.15}$[42], 8. $Li_{1.2}Mn_{0.2}Ti_{0.4}Cr_{0.2}O_2$[43], 9. $Li_{1.2}Mn_{0.4}Ti_{0.4}O_2$[43], 10. $Li_{1.25}Nb_{0.25}V_{0.5}O_2$[44], 11. $Li_{9/7}Nb_{2/7}Mo_{3/7}O_2$[45], 12. $Li_{1.25}V_{0.55}Nb_{0.2}O_{1.9}F_{0.1}$[37], 13. $Sr_2MnO_3F_2$[30], 14. $LaSrMnO_4F$[30], 15. $La_{1.2}Sr_{1.8}Mn_2O_{7-\delta}F_x$.

4.3.3 Charge compensation mechanism of $SrFeO_2F_x$ after activation

The charge compensation mechanisms of (de)fluorination in the $SrFeO_2F_x$ were examined by synchrotron hard/soft X-ray absorption spectroscopy (XAS) (Figure 4.9). The energy of the absorption edge (E_0) of the Fe *K*-edge shifted to the higher energy in the early stage of insertion of fluoride ions ($x < 1$), but then remained unchanged in the subsequent insertion of fluoride ions ($x > 1$) as shown Figure 4.9c. The energy of the absorption edge decreased reversibly upon fluoride ion extraction. Since the energy at the absorption edge of the $SrFeO_2F_x$ during charging and discharging is between the absorption energy of $SrFeO_2$ and $SrFeO_3$, these results suggest that the Fe^{2+}/Fe^{3+} redox occurs in the range of $x < 1$ for $SrFeO_2F_x$.

In the O *K*-edge XAS spectrum, a broad peak, which is attributed to the transitions from the O 1s level to the hybridized states of the Fe 3*d* and O 2*p* orbitals,[35] was observed around 530 eV before charging ($x \sim 0$) (Figure 4.9 d). The intensity at 527.5 eV increased in the early stage of fluoride ion insertion ($x < 1$), which is observed in other iron-based interaction materials.[12,36] On the other hand, further fluoride ion insertion beyond $x \sim 1$ resulted in the emergence of a new O *K*-edge peak at around 530.8 eV, and this peak increases its intensity with *x*, while it reversibly disappears upon fluoride ion extraction. The increase in the O *K*-edge peak and the unchanged

oxidation of iron for $1 < x < 2$ strongly suggests that oxidized oxygen species are involved in charge compensation, as observed in the lithium-rich cathodes.[4,10,12,36] Upon fluoride ion insertion beyond $x > 1$, the pre-edge region of F *K*-edge spectra (Figure 4.9e) exhibit a small peak that can be attributed to metal-fluorine bond,[46] with its intensity increasing with *x*, suggesting the formation of Fe-F bonds in the structure.

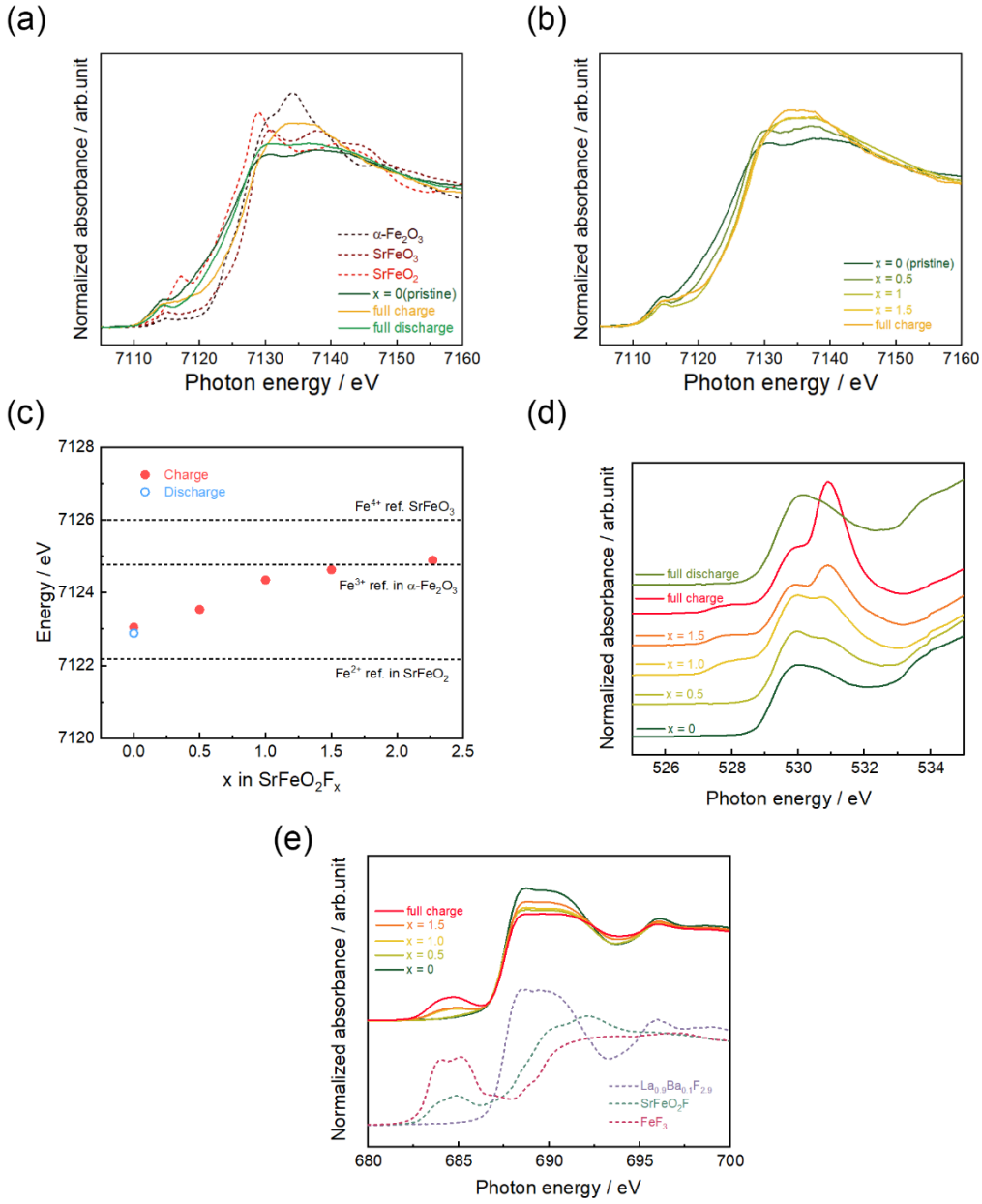

Figure 4.9 Fe *K*-edge XAS spectra of the $SrFeO_2F_x$ after activation process during (a) charging, (b), during discharging for various states in charge/discharge. (c) Edge energy (E_0) of Fe *K*-edge XAS spectra. (d) O *K*-edge XAS spectra. (e) F *K*-edge

XAS spectra. The x in the figure represents the fluoride content (x in $SrFeO_2F_x$ after activation process).

4.3.4 O_2 molecular formation in $SrFeO_2F_x$ cathode

To further confirm the nature of oxidized oxygen species in high fluorine content cathode, we performed resonant inelastic X-ray scattering (RIXS) and Pair distribution function (PDF) analysis against $SrFeO_2F_x$ in different states of charge. Figure 4.10a and Figure 4.11 show the results of RIXS that measured from 527.9 to 533.0 eV in O *K*-edge XAS spectra under high vacuum. The obtained RIXS spectra of $SrFeO_2F_x$ (x = 1) at 527.9 eV did not exhibit whereas the RIXS spectra $SrFeO_2F_x$ (x = full charged) at 530.8 eV exhibited discrete energy-loss peaks around the elastic line from 5 to 0 eV, representing several vibrational levels of the ground state potential energy surface.[47] The frequency of the first vibrational level was approximately 1600 cm^{-1}, similar to the molecular O_2, which has been observed in charged lithium, sodium-ion intercalation cathode materials[4,5] during charge process by RIXS under vacuum. This vibration disappears after full discharge. These results mean that molecular O_2 formation occurs in the $SrFeO_2F_x$ during later charge process and the O_2 formation/breaking is reversible.

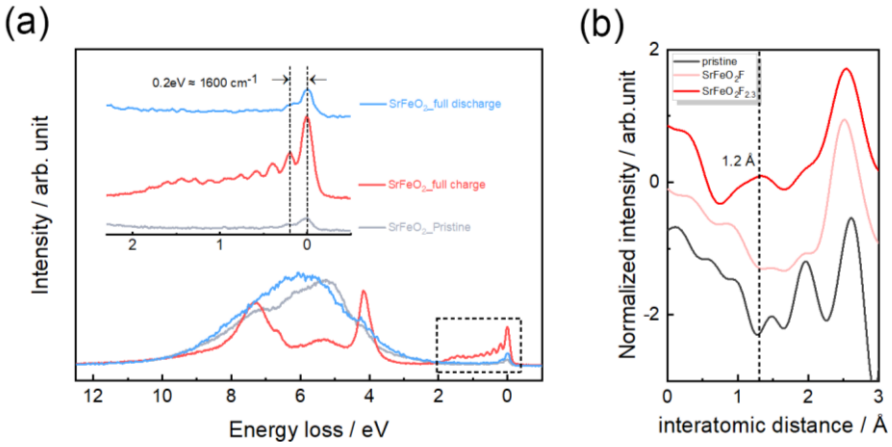

Figure 4.10 Evidences of O_2 molecular formation in $SrFeO_2F_x$ cathode (a) High-resolution RIXS spectra recorded at excitation energies at 530.8 eV for in

$SrFeO_2$, full charge and full discharge states of $SrFeO_2F_x$ after activation process. (b) PDF analysis against synchrotron XRD date of cathodes in different states of charge.

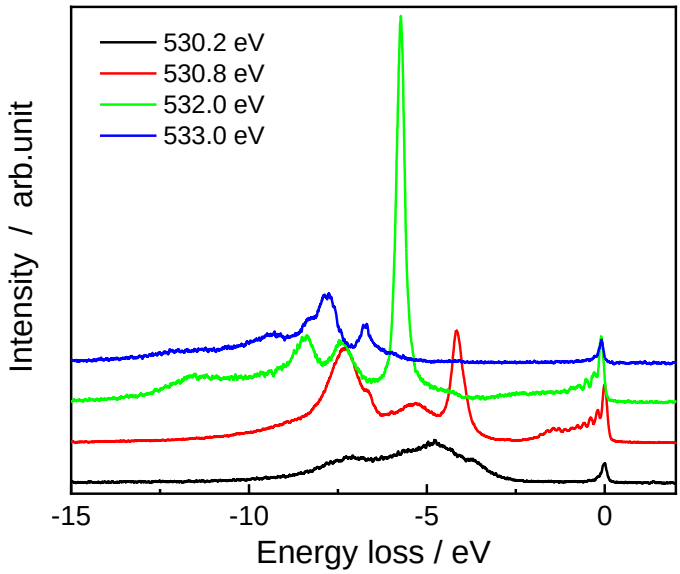

Figure 4.11 Oxygen *K*-edge RIXS spectra recorded at an excitation energy from 530.2 to 533.0 eV for charged (3.0 V) states.

In addition, the PDF analysis results provide a more intuitive signal about the formation of oxygen molecules in $SrFeO_2F_{2.3}$ cathode, the test temperature close to absolute zero suppresses thermal vibrations in the lattice and allows us to directly observe the signal at low interatomic distances.[48] It is clear that after charging to x = 2.3 ($SrFeO_2F_{2.3}$), a new peak appears near 1.2 Å corresponding to the O-O bond in the oxygen molecular, whereas this peak cannot be detected in the pristine and $SrFeO_2F$ electrodes (Figure 4.10b). Since the amount of F^- that can be accommodated in the regular anion vacancies even for $SrFeO_2$ per formula unit is 1, another anion site is needed for the $SrFeO_2F_x$ to accommodate more than 1 F^-. The molecular O_2 that forms in the $SrFeO_2F_x$ during charging observed in RIXS may not only account for charge compensation, but also create additional anion vacancies to accommodate the excess F^-. However, assuming neutral O_2 compensates for the charge of excess F^- insertion (1.3 e^-), the created anion vacancy is approximately 0.33 and a significant F^- should be

accommodated in further irregular sites. Galvanostatic intermittent titration technique (Figure 4.12) showed that polarization was larger for $x > 1$ than $0 < x < 1$ and the larger polarization for $x > 1$ may be caused by the formation of O_2 molecules that could involve local distortions. A similar large polarization has been observed in the cathode for LIBs and sodium ion batteries including the formation of oxygen molecules.[4,5] Although how the molecular O_2 and excess F^- are present in the charged $SrFeO_2F_x$ is not clear, these results indicate that the molecular O_2 and excess F^- may be present in some cavities in the structure, as found in the Li-rich cathode material,[4] the H_2 molecule in $SrTiO_3$[49,50] or the N_2-intercalated WO_3,[51] and the formation of molecular O_2 might create the irregular site of F^-. Such isotropic fluoride ion conduction is similar to disordered rock-salt Li-excess (DRX) compounds, ensuring smooth fluorine ion diffusion while achieving zero-strain of the cathode upon cycling. Further analyses such as scanning transmission electron microscope, quantification of F^- and first-principal calculation is needed to determine how the molecular O_2 and excess F^- exist in the structure.

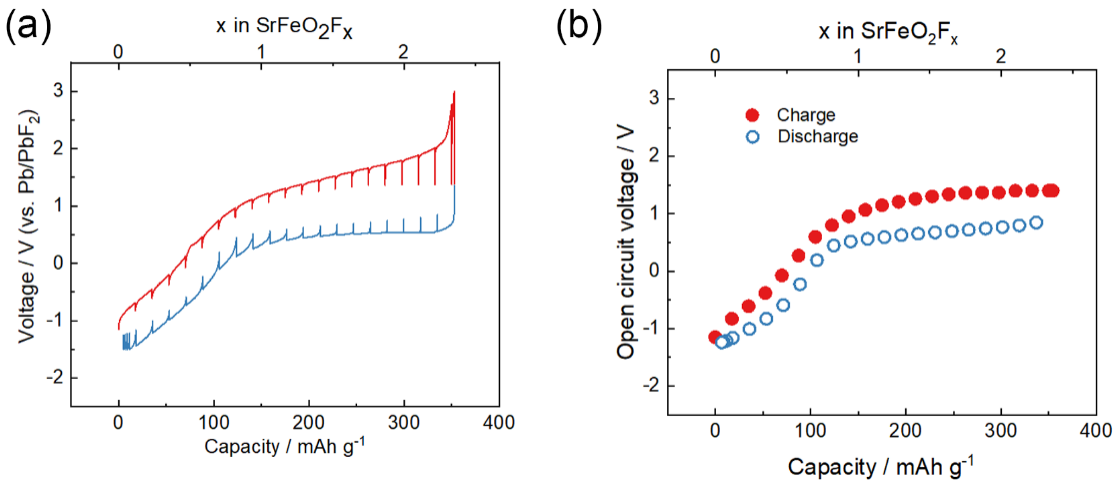

Figure 4.12 (a) The voltage/capacity profile of $SrFeO_2F_x$ obtained by galvanostatic intermittent titration technique, and (b) open-circuit-voltage (OCV) profile obtained from Figure a.

4.4 Conclusion

We demonstrated electrochemical intercalation of fluoride ions with excellent capacity cyclability and rate capability with molecular O_2 formation, using the perovskite oxyfluoride $SrFeO_2F_x$ obtained from $SrFeO_2$ with infinite layer structure. Interestingly, the volume expansion of the $SrFeO_2F_x$ during charging is significantly small, comparable to $Li_4Ti_5O_{12}$ system, which is attractive to construct all-solid-state batteries. It should be emphasized that, like the LIBs, the current FIBs has room for further improvement in terms of electrochemical properties such as cycle stability, rate characteristics, and fluoride ion diffusion; available strategies include chemical substitution with other transition metals, oxygen vacancy control, optimization of composition in an electrode mixture and tuning particle morphologies, in addition to modification of solid-solid interfaces with solid electrolytes (e.g., surface coating, orientation control). Moreover, it is not clear how the molecular O_2 and excess F^- exist in $SrFeO_2F_x$, which is important for designing excellent perovskite oxyfluoride electrodes, more generally, mixed-anion compounds[52] and should be clarified in the future.

Reference

1. Anji Reddy, M.; Fichtner, M., Batteries based on fluoride shuttle. *J. Mater. Chem.* **2011,** *21* (43), 17059-17062.

2. Gschwind, F.; Rodriguez-Garcia, G.; Sandbeck, D. J. S.; Gross, A.; Weil, M.; Fichtner, M.; Hörmann, N., Fluoride ion batteries: Theoretical performance, safety, toxicity, and a combinatorial screening of new electrodes. *J. Fluor. Chem.* **2016,** *182*, 76-90.

3. Tsujimoto, Y.; Tassel, C.; Hayashi, N.; Watanabe, T.; Kageyama, H.; Yoshimura, K.; Takano, M.; Ceretti, M.; Ritter, C.; Paulus, W., Infinite-layer iron oxide with a square-planar coordination. *Nature* **2007,** *450* (7172), 1062-5.

4. House, R. A.; Rees, G. J.; Pérez-Osorio, M. A.; Marie, J.-J.; Boivin, E.; Robertson, A. W.; Nag, A.; Garcia-Fernandez, M.; Zhou, K.-J.; Bruce, P. G., First-cycle voltage hysteresis in Li-rich 3d cathodes associated with molecular O_2 trapped in the bulk. *Nat. Energy* **2020,** *5* (10), 777-785.

5. House, R. A.; Maitra, U.; Perez-Osorio, M. A.; Lozano, J. G.; Jin, L.; Somerville, J. W.; Duda, L. C.; Nag, A.; Walters, A.; Zhou, K. J.; Roberts, M. R.; Bruce, P. G., Superstructure control of first-cycle voltage hysteresis in oxygen-redox cathodes. *Nature* **2020,** *577* (7791), 502-508.

6. Ohzuku, T.; Ueda, A.; Yamamoto, N., Zero-strain insertion material of Li $[Li_{1/3}Ti_{5/3}]O_4$ for rechargeable lithium cells. *J. Electrochem. Soc.* **1995,** *142* (5), 1431.

7. Mizushima, K.; Jones, P.; Wiseman, P.; Goodenough, J. B., Li_xCoO_2 ($0< x<-1$): A new cathode material for batteries of high energy density. *Mater. Res. Bull.* **1980,** *15* (6), 783-789.

8. Sathiya, M.; Rousse, G.; Ramesha, K.; Laisa, C. P.; Vezin, H.; Sougrati, M. T.; Doublet, M. L.; Foix, D.; Gonbeau, D.; Walker, W.; Prakash, A. S.; Ben Hassine, M.; Dupont, L.; Tarascon, J. M., Reversible anionic redox chemistry in high-capacity layered-oxide electrodes. *Nat. Mater.* **2013,** *12* (9), 827-35.

9. McCalla, E.; Abakumov, A. M.; Saubanère, M.; Foix, D.; Berg, E. J.; Rousse, G.; Doublet, M.-L.; Gonbeau, D.; Novák, P.; Van Tendeloo, G., Visualization of O-O peroxo-like dimers in high-capacity layered oxides for Li-ion batteries. *Science* **2015,** *350* (6267), 1516-1521.

10. Luo, K.; Roberts, M. R.; Hao, R.; Guerrini, N.; Pickup, D. M.; Liu, Y. S.; Edstrom, K.; Guo, J.; Chadwick, A. V.; Duda, L. C.; Bruce, P. G., Charge-compensation in 3*d*-transition-metal-oxide intercalation cathodes through the generation of localized electron holes on oxygen. *Nat. Chem.* **2016,** *8* (7), 684-91.

11. Seo, D. H.; Lee, J.; Urban, A.; Malik, R.; Kang, S.; Ceder, G., The structural and chemical origin of the oxygen redox activity in layered and cation-disordered Li-excess cathode materials. *Nat. Chem.* **2016,** *8* (7), 692-7.

12. Yabuuchi, N.; Nakayama, M.; Takeuchi, M.; Komaba, S.; Hashimoto, Y.; Mukai, T.; Shiiba, H.; Sato, K.; Kobayashi, Y.; Nakao, A.; Yonemura, M.; Yamanaka, K.; Mitsuhara, K.; Ohta, T., Origin of stabilization and destabilization in solid-state redox reaction of oxide ions for lithium-ion batteries. *Nat. Commun.* **2016,** *7*, 13814.

13. Kamaya, N.; Homma, K.; Yamakawa, Y.; Hirayama, M.; Kanno, R.; Yonemura, M.; Kamiyama, T.; Kato, Y.; Hama, S.; Kawamoto, K., A lithium superionic conductor. *Nat. Mater.* **2011,** *10* (9), 682-686.

14. Bruce, P. G.; Freunberger, S. A.; Hardwick, L. J.; Tarascon, J. M., Li-O2 and Li-S batteries with high energy storage. *Nat. Mater.* **2011,** *11* (1), 19-29.

15. Kim, S. W.; Seo, D. H.; Ma, X.; Ceder, G.; Kang, K., Electrode materials for rechargeable sodium-ion batteries: potential alternatives to current lithium-ion batteries. *Adv. Energy Mater.* **2012,** *2* (7), 710-721.

16. Aurbach, D.; Lu, Z.; Schechter, A.; Gofer, Y.; Gizbar, H.; Turgeman, R.; Cohen, Y.; Moshkovich, M.; Levi, E., Prototype systems for rechargeable magnesium batteries. *Nature* **2000,** *407* (6805), 724-727.

17. Zhao, X.; Ren, S.; Bruns, M.; Fichtner, M., Chloride ion battery: A new member in the rechargeable battery family. *J. Power Sources* **2014,** *245*, 706-711.

18. Davis, V. K.; Bates, C. M.; Omichi, K.; Savoie, B. M.; Momcilovic, N.; Xu, Q.; Wolf, W. J.; Webb, M. A.; Billings, K. J.; Chou, N. H.; Alayoglu, S.; McKenney, R. K.; Darolles, I. M.; Nair, N. G.; Hightower, A.; Rosenberg, D.; Ahmed, M.; Brooks, C. J.; Miller, T. F., 3rd; Grubbs, R. H.; Jones, S. C., Room-temperature cycling of metal fluoride electrodes: Liquid electrolytes for high-energy fluoride ion cells. *Science* **2018,** *362* (6419), 1144-1148.

19. Thieu, D. T.; Fawey, M. H.; Bhatia, H.; Diemant, T.; Chakravadhanula, V. S. K.; Behm, R. J.; Kübel, C.; Fichtner, M., CuF_2 as reversible cathode for fluoride ion

batteries. *Adv. Funct. Mater.* **2017,** *27* (31), 1701051.

20. Nakano, H.; Matsunaga, T.; Mori, T.; Nakanishi, K.; Morita, Y.; Ide, K.; Okazaki, K.-i.; Orikasa, Y.; Minato, T.; Yamamoto, K., Fluoride-ion shuttle battery with high volumetric energy density. *Chem. Mater.* **2020,** *33* (1), 459-466.

21. Zhang, D.; Nakano, H.; Yamamoto, K.; Tanaka, K.; Yahara, T.; Imai, K.; Mori, T.; Miki, H.; Nakanishi, S.; Iba, H., Rate-determining process at electrode/electrolyte interfaces for all-solid-state fluoride-ion batteries. *ACS Appl. Mater. Interfaces* **2021,** *13* (25), 30198-30204.

22.Zhang, D.; Yamamoto, K.; Ochi, A.; Wang, Y.; Yoshinari, T.; Nakanishi, K.; Nakano, H.; Miki, H.; Nakanishi, S.; Iba, H.; Uchiyama, T.; Watanabe, T.; Amezawa, K.; Uchimoto, Y., Understanding the reaction mechanism and performances of 3*d* transition metal cathodes for all-solid-state fluoride ion batteries. *J. Mater. Chem. A* **2021,** *9* (1), 406-412.

23. Yoshinari, T.; Zhang, D.; Yamamoto, K.; Kitaguchi, Y.; Ochi, A.; Nakanishi, K.; Miki, H.; Nakanishi, S.; Iba, H.; Uchiyama, T.; Watanabe, T.; Matsunaga, T.; Amezawa, K.; Uchimoto, Y., Kinetic analysis and alloy designs for metal/metal fluorides toward high rate capability for all-solid-state fluoride-ion batteries. *J. Mater. Chem. A* **2021,** *9* (11), 7018-7024.

24. Zhang, D.; Yoshinari, T.; Yamamoto, K.; Kitaguchi, Y.; Ochi, A.; Nakanishi, K.; Miki, H.; Nakanishi, S.; Iba, H.; Watanabe, T.; Uchiyama, T.; Orikasa, Y.; Amezawa, K.; Uchimoto, Y., Cu–Pb Nanocomposite Cathode Material toward Room-Temperature Cycling for All-Solid-State Fluoride-Ion Batteries. *ACS Appl. Energy Mater.* **2021,** *4* (4), 3352-3357.

25. Zhang, D.; Yamamoto, K.; Wang, Y.; Gao, S.; Uchiyama, T.; Watanabe, T.; Takami, T.; Matsunaga, T.; Nakanishi, K.; Miki, H.; Iba, H.; Amezawa, K.; Maeda, K.; Kageyama, H.; Uchimoto, Y., Reversible and Fast (De)fluorination of High-Capacity Cu_2O Cathode: One Step Toward Practically Applicable All-Solid-State Fluoride-Ion Battery. *Adv. Energy Mater.* **2021,** *11* (45).

26. Bard, A., *Standard potentials in aqueous solution*. Routledge: 2017.

27. Nowroozi, M. A.; Wissel, K.; Rohrer, J.; Munnangi, A. R.; Clemens, O., $LaSrMnO_4$: Reversible Electrochemical Intercalation of Fluoride Ions in the Context of Fluoride Ion Batteries. *Chem. Mater.* **2017,** *29* (8), 3441-3453.

28. Nowroozi, M. A.; Ivlev, S.; Rohrer, J.; Clemens, O., La_2CoO_4: a new intercalation based cathode material for fluoride ion batteries with improved cycling stability. *J. Mater. Chem. A* **2018,** *6* (11), 4658-4669.

29. Nowroozi, M. A.; Wissel, K.; Donzelli, M.; Hosseinpourkahvaz, N.; Plana-Ruiz, S.; Kolb, U.; Schoch, R.; Bauer, M.; Malik, A. M.; Rohrer, J.; Ivlev, S.; Kraus, F.; Clemens, O., High cycle life all-solid-state fluoride ion battery with La_2NiO_{4+d} high voltage cathode. *Commun. Mater.* **2020,** *1* (1).

30. Wang, Y.; Yamamoto, K.; Tsujimoto, Y.; Matsunaga, T.; Zhang, D.; Cao, Z.; Nakanishi, K.; Uchiyama, T.; Watanabe, T.; Takami, T.; Miki, H.; Iba, H.; Maeda, K.; Kageyama, H.; Uchimoto, Y., Anion Substitution at Apical Sites of Ruddlesden–Popper-type Cathodes toward High Power Density for All-Solid-State Fluoride-Ion Batteries. *Chem. Mater.* **2022,** *34* (2), 609-616.

31. Blakely, C. K.; Davis, J. D.; Bruno, S. R.; Kraemer, S. K.; Zhu, M.; Ke, X.; Bi, W.; Alp, E. E.; Poltavets, V. V., Multistep synthesis of the $SrFeO_2F$ perovskite oxyfluoride via the $SrFeO_2$ infinite-layer intermediate. *J. Fluor. Chem.* **2014,** *159*, 8-14.

32. Xiao, R.; Li, H.; Chen, L., Density functional investigation on Li_2MnO_3. *Chem. Mater.* **2012,** *24* (21), 4242-4251.

33. House, R. A.; Maitra, U.; Jin, L.; Lozano, J. G.; Somerville, J. W.; Rees, N. H.; Naylor, A. J.; Duda, L. C.; Massel, F.; Chadwick, A. V., What triggers oxygen loss in oxygen redox cathode materials? *Chem. Mater.* **2019,** *31* (9), 3293-3300.

34. Lee, J.; Urban, A.; Li, X.; Su, D.; Hautier, G.; Ceder, G., Unlocking the potential of cation-disordered oxides for rechargeable lithium batteries. *science* **2014,** *343* (6170), 519-522.

35. Yoon, W.-S.; Balasubramanian, M.; Chung, K. Y.; Yang, X.-Q.; McBreen, J.; Grey, C. P.; Fischer, D. A., Investigation of the charge compensation mechanism on the electrochemically Li-Ion deintercalated $Li_{1-x}Co_{1/3}Ni_{1/3}Mn_{1/3}O_2$ electrode system by combination of soft and hard X-ray absorption spectroscopy. *J.Am. Chem. Soc.* **2005,** *127* (49), 17479-17487.

36. Yamamoto, K.; Zhou, Y.; Yabuuchi, N.; Nakanishi, K.; Yoshinari, T.; Kobayashi, T.; Kobayashi, Y.; Yamamoto, R.; Watanabe, A.; Orikasa, Y.; Tsuruta, K.; Park, J.; Byon, H. R.; Tamenori, Y.; Ohta, T.; Uchimoto, Y., Charge Compensation

Mechanism of Lithium-Excess Metal Oxides with Different Covalent and Ionic Characters Revealed by Operando Soft and Hard X-ray Absorption Spectroscopy. *Chem. Mater.* **2019,** *32* (1), 139-147.

37. Zhao, X.; Tian, Y.; Lun, Z.; Cai, Z.; Chen, T.; Ouyang, B.; Ceder, G., Design principles for zero-strain Li-ion cathodes. *Joule* **2022**.

38. Nitta, N.; Wu, F.; Lee, J. T.; Yushin, G., Li-ion battery materials: present and future. *Mater. today* **2015,** *18* (5), 252-264.

39. Luo, J.; Dai, C. Y.; Wang, Z.; Liu, K.; Mao, W. G.; Fang, D. N.; Chen, X., In-situ measurements of mechanical and volume change of LiCoO2 lithium-ion batteries during repeated charge–discharge cycling by using digital image correlation. *Measurement* **2016,** *94*, 759-770.

40. Yoon, W.-S.; Chung, K. Y.; McBreen, J.; Yang, X.-Q., A comparative study on structural changes of $LiCo_{1/3}Ni_{1/3}Mn_{1/3}O_2$ and $LiNi_{0.8}Co_{0.15}Al_{0.05}O_2$ during first charge using in situ XRD. *Electrochem. Commun.* **2006,** *8* (8), 1257-1262.

41. Wang, R.; Li, X.; Liu, L.; Lee, J.; Seo, D.-H.; Bo, S.-H.; Urban, A.; Ceder, G., A disordered rock-salt Li-excess cathode material with high capacity and substantial oxygen redox activity: $Li_{1.25}Nb_{0.25}Mn_{0.5}O_2$. *Electrochem. Commun.* **2015,** *60*, 70-73.

42. Lee, J.; Papp, J. K.; Clement, R. J.; Sallis, S.; Kwon, D. H.; Shi, T.; Yang, W.; McCloskey, B. D.; Ceder, G., Mitigating oxygen loss to improve the cycling performance of high capacity cation-disordered cathode materials. *Nat. Commun.* **2017,** *8* (1), 981.

43. Huang, J.; Zhong, P.; Ha, Y.; Kwon, D.-H.; Crafton, M. J.; Tian, Y.; Balasubramanian, M.; McCloskey, B. D.; Yang, W.; Ceder, G., Non-topotactic reactions enable high rate capability in Li-rich cathode materials. *Nat. Energy* **2021,** *6* (7), 706-714.

44. Nakajima, M.; Yabuuchi, N., Lithium-excess cation-disordered rocksalt-type oxide with nanoscale phase segregation: $Li_{1.25}Nb_{0.25}V_{0.5}O_2$. *Chem. Mater.* **2017,** *29* (16), 6927-6935.

45. Hoshino, S.; Glushenkov, A. M.; Ichikawa, S.; Ozaki, T.; Inamasu, T.; Yabuuchi, N., Reversible three-electron redox reaction of Mo^{3+}/Mo^{6+} for rechargeable lithium batteries. *ACS Energy Lett.* **2017,** *2* (4), 733-738.

46. Vinogradov, A. S.; Fedoseenko, S. I.; Krasnikov, S. A.; Preobrajenski, A. B.; Sivkov, V. N.; Vyalikh, D. V.; Molodtsov, S. L.; Adamchuk, V. K.; Laubschat, C.; Kaindl, G., Low-lying unoccupied electronic states in 3*d* transition-metal fluorides probed by NEXAFS at the F 1*s* threshold. *Phys. Rev., B* **2005,** *71* (4).

47. Hennies, F.; Pietzsch, A.; Berglund, M.; Föhlisch, A.; Schmitt, T.; Strocov, V.; Karlsson, H. O.; Andersson, J.; Rubensson, J.-E., Resonant inelastic scattering spectra of free molecules with vibrational resolution. *Phys. Rev. Lett* **2010,** *104* (19), 193002.

48. House, R. A.; Playford, H. Y.; Smith, R. I.; Holter, J.; Griffiths, I.; Zhou, K.-J.; Bruce, P. G., Detection of trapped molecular O_2 in a charged Li-rich cathode by Neutron PDF. *Energy Environ. Sci.* **2022,** *15* (1), 376-383.

49. Iwazaki, Y.; Gohda, Y.; Tsuneyuki, S., Diversity of hydrogen configuration and its roles in $SrTiO_{3-\delta}$. *APL Mater.* **2014,** *2* (1), 012103.

50. Li, H. B.; Lou, F.; Wang, Y.; Zhang, Y.; Zhang, Q.; Wu, D.; Li, Z.; Wang, M.; Huang, T.; Lyu, Y., Electric Field–Controlled Multistep Proton Evolution in $H_xSrCoO_{2.5}$ with Formation of H–H Dimer. *Adv. Sci.* **2019,** *6* (20), 1901432.

51. Mi, Q.; Ping, Y.; Li, Y.; Cao, B.; Brunschwig, B. S.; Khalifah, P. G.; Galli, G. A.; Gray, H. B.; Lewis, N. S., Thermally stable N_2-intercalated WO_3 photoanodes for water oxidation. *J. Am. Chem. Soc.* **2012,** *134* (44), 18318-18324.

52. Kageyama, H.; Hayashi, K.; Maeda, K.; Attfield, J. P.; Hiroi, Z.; Rondinelli, J. M.; Poeppelmeier, K. R., Expanding frontiers in materials chemistry and physics with multiple anions. *Nat. Commun.* **2018,** *9* (1), 772.

Chapter 5. Earth Abundant Ultra-high Capacity Iron-based Oxyfluoride Cathodes for All-solid-state Fluoride-ion Batteries Using Anionic Redox Reactions

With the increasing ownership of electric vehicles (EVs), there is a growing market demand for power batteries with high energy density and safety. All-solid-state fluoride ion batteries (FIBs), which allow the multiple-electron transfer and use solid-state inorganic electrolytes, are noteworthy candidates for reaching high energy densities while ensuring safety. Recently, we reported the application of $SrFeO_2$ cathode for FIBs, achieving an energy density overriding that of lithium-ion batteries with excellent cycle stability, through the in-situ generation of perovskite oxyfluorides $SrFeO_2F_x$ ($0 \leq x \leq 2.3$). In this study, we synthesized a series of cathode materials $Ca_ySr_{1-y}FeO_2$ ($0 \leq y \leq 1$) by using low-cost and lightweight Ca to substitute Sr, which not only reduces the cost but also further increases its energy density. Among them, $Ca_{0.8}Sr_{0.2}FeO_2$ achieves an ultra-high capacity of up to about 600 mAh g^{-1} with rewarding cycle performance, corresponding to an extremely high energy density of 2736 Wh L^{-1}. The large capacity is obtained by (de)intercalation of 2 extra fluoride ion beyond $x = 1$($0 \leq x \leq 3$ in $Ca_{0.8}Sr_{0.2}FeO_2F_x$) and the additional fluoride ion intercalation leads to the formation of molecular O_2 in the perovskite structure for charge compensation, as in $SrFeO_2F_x$. These results highlight the perovskite oxyfluorides obtained from infinite layer structure as a new class of active materials for the construction of high-performance FIBs.

5.1 Introduction

In the past decade, the popularity of lithium-ion batteries (LIBs) as power batteries has enabled the rapid development of electric vehicles (EVs). However, their single-electron transfer mode limits the capacity of LIBs, which leads to the mileage anxiety issue of electric vehicles.[1, 2] Although various multivalent metal ions such as Mg^{2+}, Ca^{2+}, Zn^{2+}, Al^{3+} have been proposed to achieve capacity enhancement by multiple electron transfer[3-8], the low ion mobility of these cations hinders the practical application. In 2011, Anji Reddy and Fichtner first proposed the proof-of-concept of the all-solid-state fluoride ion batteries (FIBs), which again aroused researcher's widespread interest.[9-19] Since fluorine has a small ionic radius and the highest electronegativity, the utilization of fluoride ions as carriers can ensure electrochemically stable migration while achieving high capacity through multiple-electron transfer, which is considered as one of the solutions for next-generation power batteries.

The preliminary all-solid-state FIBs used simple metal/metal fluoride cathodes: Bi/BiF_3 and Cu/CuF_2 electrodes could achieve high capacities of 322 mAh g^{-1} and 385 mAh g^{-1}, respectively, through multiple-electron transfer.[9, 20] However, these electrodes have poor cycling performance due to the large volume changes accompanying the charging and discharging process.[21] Later, Nowroozi et al. reported the application of a series of layered perovskite-related materials with Ruddlesden-Popper phases ($A_{n+1}B_nX_{3n+1}$, where A and B are cations, X is oxygen) as cathode materials, where fluoride ions can be topologically (de)inserted between two MO_6 slabs, like the case of $LiCoO_2$.[22-24] Although these intercalation-type electrodes ensure the structural integrity of the host lattice before and after fluoride ion insertion, and effectively solve the volume expansion problem of metal/metal fluoride electrodes, their redundant lattice composition leads to unsatisfactory theoretical capacity.

Recently, we reported the application of $SrFeO_2$ with infinite-layer structure as a cathode material for FIBs. Compared with the abovementioned layered metal oxides with R-P phase, $SrFeO_2$ has a simplified chemical composition. By using the Fe^{2+}/Fe^{3+}

redox and the formation of oxygen molecular in the bulk, the $SrFeO_2$ cathode contributes an extremely high energy density of 2736 Wh L^{-1}. Here, we propose a series of $Ca_ySr_{1-y}FeO_2$ ($0 \leq y \leq 1$) cathode materials for FIBs using low-cost and lightweight Ca as a substitute for Sr. The electrochemical results indicate that $Ca_{0.8}Sr_{0.2}FeO_2$ cathode achieves an energy density of 643 Wh L^{-1} by reversible 3-electron transfer ((de)insertion of 3 fluoride ions), which is comparable to 2.5 times the value of commercial $LiCoO_2$ electrodes (1403 Wh L^{-1}). The results of X-ray absorption spectroscopy (XAS) demonstrate that $Ca_{0.8}Sr_{0.2}FeO_2$ has a similar charge compensation mechanism to that of $SrFeO_2$.

5.2 Experimental

5.2.1 Material preparation

$Ca_ySr_{1-y}FeO_2$. The precursors $Ca_ySr_{1-y}FeO_{3-\delta}$ ($0 \leq y \leq 1$; $0 \leq \delta \leq 0.5$) was synthesized from $CaCO_3$ (99.99%, Kojundo Chemical Laboratory), $SrCO_3$ (99.99%, Kojundo Chemical Laboratory), and Fe_2O_3 (99.9%, WAKO pure chemical industries, ltd.) in air by a solid-state reaction.[25, 26] $CaCO_3$ was pre-dried before use, then three materials were mixed in a stoichiometric ratio, pelletized and sintered at 1200 °C for 72 hours in three stages; the pellets were crushed at the end of each 24-hour sintering period and re-pressed. To obtain the $Ca_ySr_{1-y}FeO_2$ compounds, the precursors were homogeneously mixed with a 2-molar excess of CaH_2 (99.99%, Sigma-Aldrich), pressed, and sealed in evacuated Pyrex tubes in an argon-filled glovebox. The vacuum tubes were then sintered according to the conditions in the supplementary Table 4.1, which vary for the different Sr and Ca components. Finally, the products of the reduction reaction were washed three times with 0.15 M NH_4Cl/methanol solution to remove the side reaction product CaO and unreacted CaH_2.

Solid Electrolyte. In this study, $La_{0.9}Ba_{0.1}F_{2.9}$ (LBF) was used as a fluoride-ion solid-state electrolyte.[27] LaF_3 (99.9%, Kojundo Chemical Laboratory Co., Ltd.) and

BaF_2 (99.9%, Kojundo Chemical Laboratory Co., Ltd.) were first mixed thoroughly in stoichiometric ratio using a mortar and then the mixture was transferred to a ZrO_2 ball milling vial; the ball milling was carried out under a rotation speed of 600 rpm for 10 h. Finally, the ball-milled product was pressed and sintered at 1000 °C for 4 h. All the above operations were carried out under argon atmosphere.

Table 5.1 Reaction Conditions for $Ca_ySr_{1-y}FeO_2$.

$Sr_{1-x}Ca_xFe_{3-\delta}$	Reaction time/ h
0, 0.2	48
0.4, 0.5, 0.6	96
0.7, 0.8	144
1.0	168

Composite electrode. The cathode composite was produced by ball milling the as-prepared $Ca_ySr_{1-y}FeO_2$ compounds, the solid electrolyte LBF, and VGCF (VGCF, Showa Denko K.K) in the weight ratio of 1:6:3 under a rotation speed of 100 rpm for 12 h. Regarding the anode composite, PbF_2 (99.9%, Kojundo Chemical Laboratory Co., Ltd.), Pb powder (99.9% Kojundo Chemical Laboratory Co. Ltd.), LBF and VGCF were first mixed in a mortar in the weight ratio of 3: 2: 4: 1, and then the mixture was transferred into a ZrO_2 ball mill pot, then produced by ball milling at 100 rpm for 12 h.

5.2.2 Electrochemical measurement

The electrochemical properties of each cathode material were tested using a two-electrode bulk-type cell.[16] The solid electrolyte powder was first molded by applying pressure, followed by adding cathode and anode composites on both sides by applying 360 MPa for 5 min; two gold foils are placed between the electrodes and the metal mold as the current collector. The galvanostatic charge/discharge properties were performed using an HJ1010SD8 (Hokuto Denko Corporation) electrochemical workstation; the applied current density was 5mA g^{-1} and the cutoff voltage range is –1.5 ~ 3 V (vs. Pb/PbF_2) at 150 °C.

5.2.3 Characterization

The X-ray diffraction data was collected at synchrotron radiation facility SPring-8 (BL02B2), Japan. The incident X-ray was monochromatized to a wavelength of 0.4133 Å. The crystal structure information of each cathode was obtained by Rietveld refinement using the Jana2006 package[28], and the crystal structure of each material was depicted using the VESTA program based on the refinement results.[29] Scanning electron microscopy (SEM) images were obtained using a field emission S-3400N scanning electron microscope (Hitachi, Japan). Ex situ Fe *K*-edge, F *K*-edge and O *K*-edge X-ray absorption spectroscopy (XAS) measurement were performed at the BL14B2and BL27SU beamlines at Spring-8, Japan; XAS spectrums were analyzed with the Athena software.[30]

5.3 Result and discussion

5.3.1 Structural evolution with Ca substitution

Figure 5.1a shows the synchrotron XRD data of the $Ca_ySr_{1-y}FeO_2$ compounds, which have similar XRD patterns to $SrFeO_2$, and their diffraction peaks can be calibrated using the tetragonal lattice.[31] With the substitution of Ca, the overall Bragg diffractions shifted to a higher angle, which represents the reduction of the lattice parameters. The Rietveld refinement results of XRD show that the patterns for $0 \leq y \leq 0.8$ converge well using the same infinite layer structure as $SrFeO_2$ (Figure 5.1b and Figure 5.2a-e),[25] however, for $CaFeO_2$, a satisfactory fit could not be obtained using the *P*4/*mmm* space group due to the appearance of some weak super-reflections. Tassel et al. have reported that these super-reflections corresponding to a (1/2, 1/2, 0) modulation vector of tetragonal lattice, the XRD pattern of $CaFeO_2$ could be indexed perfectly by the $P\text{-}42_1m$ (No. 113) space group.[26] Figure 5.2f and Figure 5.1c show the results of the refinement of $CaFeO_2$ and its crystal structure. Due to its small ionic radius (Sr^{2+}: 118

pm; Ca^{2+}: 100 pm)[32], the FeO4 square planar in $CaFeO_2$ underwent a rotation of approximately 5 ° along the *c*-axis compared to the perfect infinite-layer structure (such as $SrFeO_2$), and produce some distortions toward tetrahedra. The above-mentioned structural changes are consistent with previous studies.[25, 26]

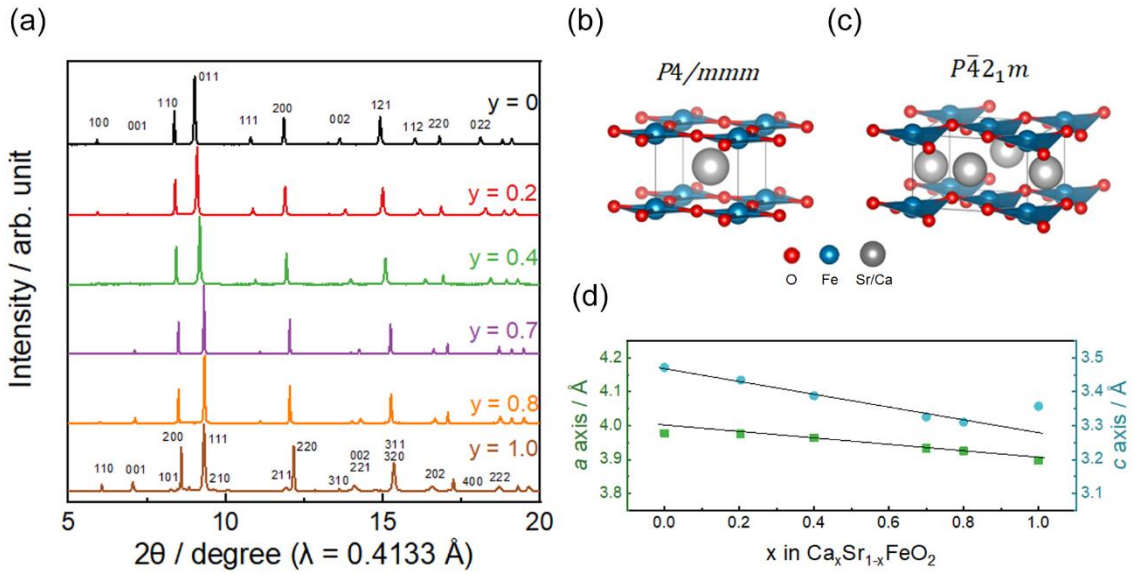

Figure 5.1 (a), X-ray diffraction patterns of as-prepared $Ca_ySr_{1-y}FeO_2$. Lattice structure of (b) $Ca_ySr_{1-y}FeO_2$ ($0 \leq y \leq 0.8$) with space group *P*4/*mmm*, (c) $CaFeO_2$ with space group $P\bar{4}2_1m$. (d) Lattice parameters of *a* and *c* axis obtained by Rietvled refinement.

The results of Rietveld refinement are summarized in Figure 5.1d and Table 5.2, the *a*- and *c*-axis parameter of $Ca_ySr_{1-y}FeO_2$ compounds decrease linearly with increasing Ca content, following Vegard's law. However, this evolution comes to an abrupt end at y = 0.8, where $CaFeO_2$ has a larger *c*-axis parameter compared to the y = 0.8 compound because of the lattice distortion. Finally, Figure 5.3 provides the morphology information of each material, all of which have similar particle sizes of 3-5 um.

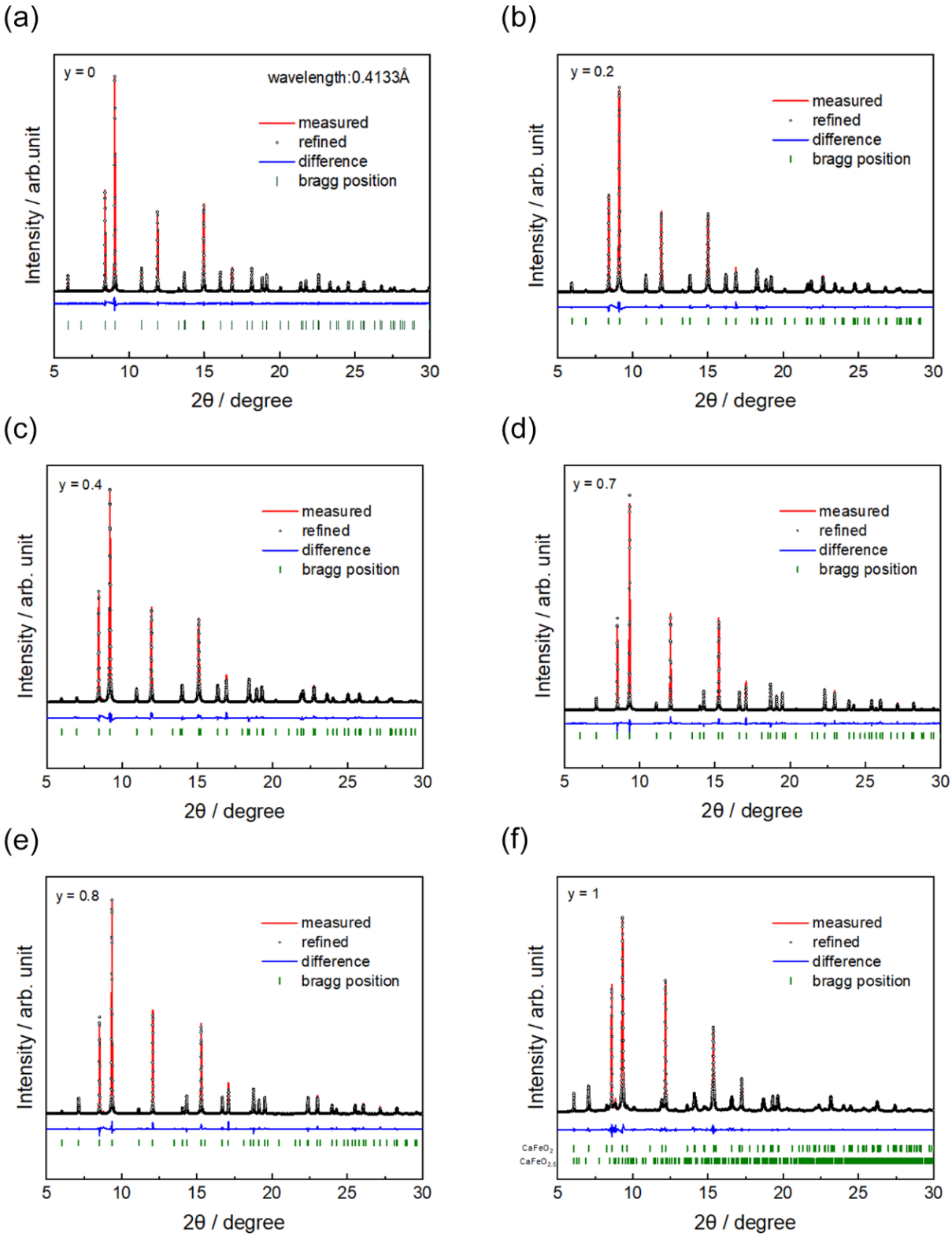

Figure 5.2 Results of Rietveld refinement for $Ca_ySr_{1-y}FeO_2$ ($0 \leq y \leq 1$).

Table 5.2 Results of Rietveld refinement for $Ca_ySr_{1-y}FeO_2$ ($0 \leq y \leq 1$).

	atom	site	x	y	z	occupancy
$SrFeO_2$	Sr	1*d*	0.5	0.5	0.5	1
*P*4/*mmm*	Fe	1*a*	0	0	0	1
a =3.99119(1)	O	2*f*	0.5	0	0	1
c = 3.47466(0)						
R_p = 5.57%						
R_{wp} = 7.70%						
$Sr_{0.8}Ca_{0.2}FeO_2$	Ca	1*d*	0.5	0.5	0.5	0.2
*P*4/*mmm*	Sr	1*d*	0.5	0.5	0.5	0.8
a =3.97792(7)	Fe	1*a*	0	0	0	1
c = 3.43009(4)	O	2*f*	0.5	0	0	1
R_p = 4.45%						
R_{wp} = 6.88%						
	atom	**site**	**x**	**y**	**z**	**occupancy**
$Sr_{0.6}Ca_{0.4}FeO_2$	Ca	1*d*	0.5	0.5	0.5	0.4
*P*4/*mmm*	Sr	1*d*	0.5	0.5	0.5	0.6
a =3.96364(9)	Fe	1*a*	0	0	0	1
c = 3.38783(6)	O	2*f*	0.5	0	0	1
R_p = 4.52%						
R_{wp} = 6.82%						
$Sr_{0.3}Ca_{0.7}FeO_2$	Ca	1*d*	0.5	0.5	0.5	0.7
*P*4/*mmm*	Sr	1*d*	0.5	0.5	0.5	0.3
a =3.93313(5)	Fe	1*a*	0	0	0	1
c = 3.32582(6)	O	2*f*	0.5	0	0	1
R_p = 4.16%						
R_{wp} = 6.05%						
	atom	**site**	**x**	**y**	**z**	**occupancy**
$Sr_{0.2}Ca_{0.8}FeO_2$	Ca	1*d*	0.5	0.5	0.5	0.8
*P*4/*mmm*	Sr	1*d*	0.5	0.5	0.5	0.2
a =3.92576(4)	Fe	1*a*	0	0	0	1
c = 3.31013(7)	O	2*f*	0.5	0	0	1
R_p = 4.86%						
R_{wp} = 7.35%						
$CaFeO_2$	Ca	2*c*	0.5	0	0.5614	0.2
P-42$_1$*m*	Fe	2*a*	0	0	0	1
a = 5.51142(2)	O	4*e*	0.2693	0.7693	0.0967	1
c = 3.35702(3)						
R_p = 3.02%						
R_{wp} = 5.91%						

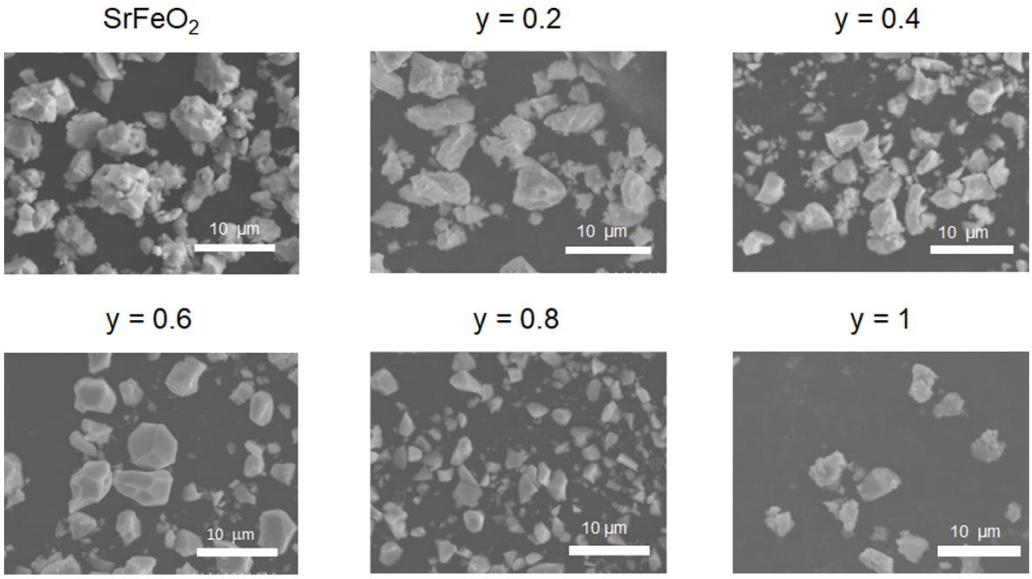

Figure 5.3 SEM images of $Ca_ySr_{1-y}FeO_2$ ($0 \leq y \leq 1$).

5.3.2 Electrochemical performance

The electrochemical performances of $Ca_ySr_{1-y}FeO_2$ cathodes were evaluated using a two-electrode bulk-type cell under a current density of 5mA g^{-1}, and the cut-off potential was set to –1.5 ~ 3 V. The Pb/PbF_2 anode composite is selected as the counter and reference electrode to accurately evaluate the properties of the cathode materials; its potential is always constant because the Pb/PbF_2 transition proceeds via a two-phase reaction. As shown in Figure 5.4, these cathodes exhibit similar two-stage galvanostatic charge/discharge profiles after a similar activation process as $SrFeO_2$. With the increase of Ca content, higher reversible capacity is achieved; the $Ca_{0.8}Sr_{0.2}FeO_2$ cathode exhibited the highest reversible capacity of 580 mAh g^{-1} instead of $CaFeO_2$. This value is higher than not only all commercial Li-ion battery cathodes such as $LiCoO_2$, $LiFePO_4$, but also all known Li-excess system cathodes (Figure 5.5).[33-41] It is speculated that the lattice distortion produced in the infinite-layer structure of $CaFeO_2$ may be unfavorable to the three-dimensional diffusion of fluoride-ions, thus leading to a decrease in the capacity.

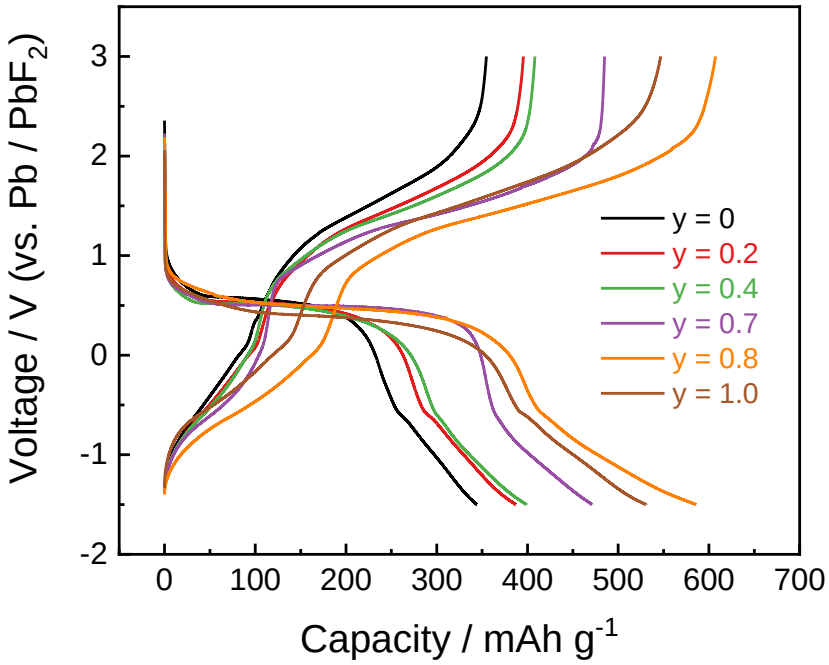

Figure 5.4 Charge/discharge profiles of $Ca_ySr_{1-y}FeO_2$ ($0 \leq y \leq 1$) at a current density of 5 mA g^{-1} under 150℃.

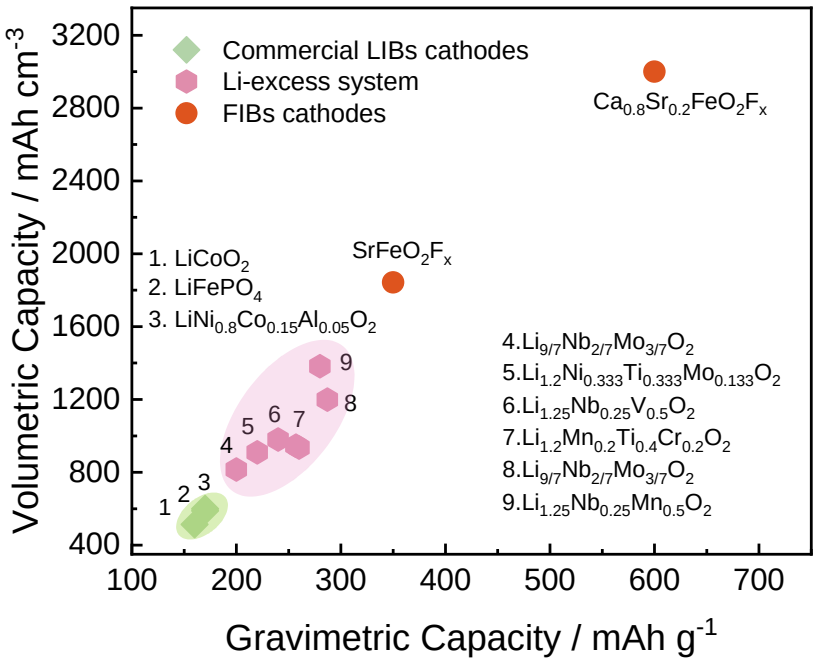

Figure 5.5 Plots of the volume expansion ratio for volumetric capacities for $Ca_{0.8}Sr_{0.2}FeO_2F_x$ and cathode materials reported in FIBs and LIBs

Table 5.3 shows the theoretical capacity corresponding to the insertion of a fluoride ion into each material. The results of charging/discharging show that all cathodes allow the reversible (de)insertion of excess amount of fluoride ions (more than two), especially $Ca_{0.8}Sr_{0.2}FeO_2$, which shows the maximum of three. Figure 5.6 shows the charge/discharge profiles of a $Ca_{0.8}Sr_{0.2}FeO_2$|$CaBaF_4$|LBF full cell, ultra-high energy densities, 650 Wh k g^{-1} gravimetrically or 3643 Wh L^{-1} volumetrically could be realized. To the best of our knowledge, the $Ca_{0.8}Sr_{0.2}FeO_2$ cathode exhibits the highest reversible capacity in all-solid-state fluoride ion batteries to date.

Table 5.3 Theoretical capacities of $Ca_ySr_{1-y}FeO_2$.

$Ca_ySr_{1-y}FeO_2$	F=1	F=2
y = 0	153	306
y = 0.2	162	323
y = 0.4	171	343
y = 0.6	182	365
y = 0.8	195	390
y = 1	210	419

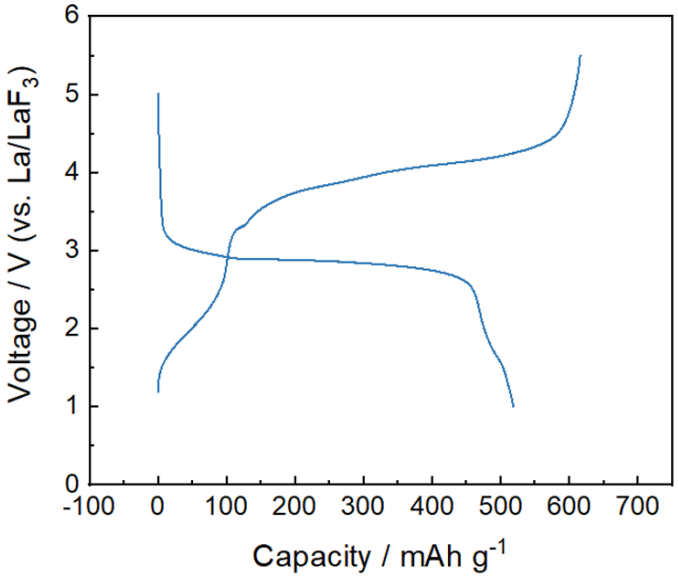

Figure 5.6 Charge/discharge profiles of $Ca_{0.8}Sr_{0.2}FeO_2$ vs. La/LaF_3 anode.

5.3.3 Charge compensation

Since $Ca_{0.8}Sr_{0.2}FeO_2$ exhibits a fluoride ion accommodation capacity well beyond the stoichiometric ratio, it is necessary to probe its chemical state at different fluoride ion contents (different states of charge). Figure 5.7a shows the Fe *K*-edge X-ray absorption spectrums (XAS) obtained upon charging after activation process. During the first fluoride-ion insertion ($0 \leq x \leq 1$), the absorption edge continues to move toward the high energy, representing the oxidation of Fe in this interval. Afterwards, until the full-charge state ($1 \leq x \leq 3$), the position of the absorption edge remains almost constant, indicating that the oxidation state of Fe is virtually unchanged at this stage. The $E_{0.5}$ of the Fe absorption edge for each charging state is summarized in Figure 5.7b, where the evolution in the oxidation state of Fe can be clearly identified by the energy changes. In the starting state ($x = 0$), the energy of the absorption edge is close to that of the FeO reference, indicating that the Fe in $Ca_{0.8}Sr_{0.2}FeO_2$ approximates to divalent. As the fluoride ion content increases, the energy of the absorption edge continues to increase and remains almost constant after x=1. The energy at this point is close to that of the Fe_2O_3 reference, implying that Fe in $Ca_{0.8}Sr_{0.2}FeO_2$ after x=1 remains trivalent. The above results indicate that Fe is involved in charge compensation only during the first fluoride ion insertion.

To probe the redox species beside Fe, we also collected the O *K*-edge and F *K*-edge XAS using the forementioned ex-situ samples. Figure 5.8a summarized the spectrums of O *K*-edge at different fluoride ion content. The broad peak between 528 to 534 eV before charging corresponding to the electron transition from O 1*s* orbital to the O 2*p* – Fe 3*d* hybridized orbital.[42] With the insertion of the fluoride ion, there is no significant change in the spectrum of O in the interval $0 \leq x \leq 1$, however, with further fluoride ion insertion, a new characteristic peak appears near 531 eV and its strength enhances with the increase of fluoride ion content. House et al. observed similar variations in cathode materials of LIBs and NIBs, and this characteristic peak was determined to originate from oxygen molecules formed inside the lattice by resonant inelastic X-ray scattering (RIXS), pair distribution function (PDF), and other analytical methods.

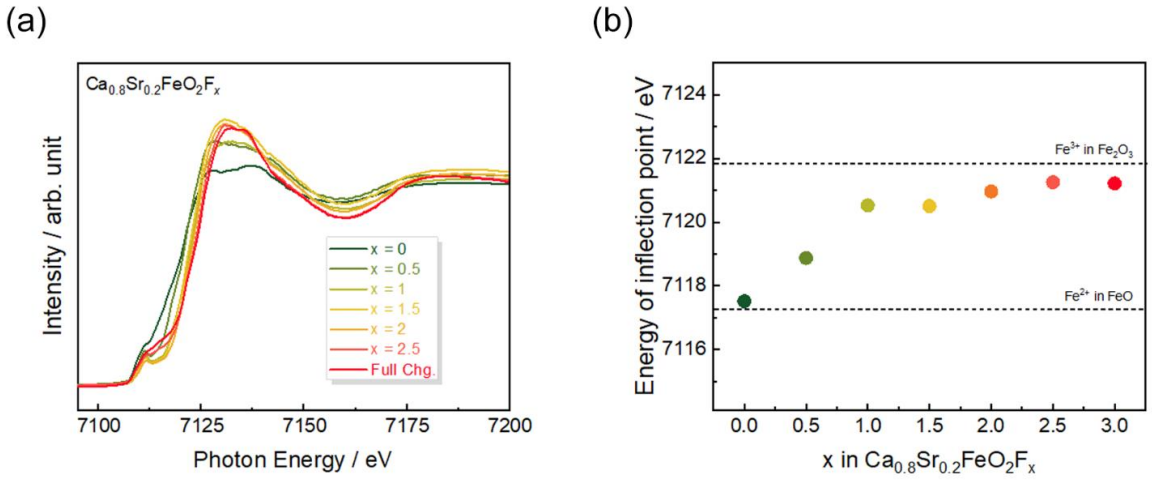

Figure 5.7 (a) Fe *K*-edge XAS spectrums of $Ca_{0.8}Sr_{0.2}FeO_2F_x$ in different states of charge after activation process. (b) Plot of edge energies summarized from Figure 5.7 (a).

In the spectrum of F *K*-edge (Figure 5.8b), the location of the absorption edge did not change with the fluoride ion content.[43-45] After the insertion of one fluoride ion ($x > 1$), a small characteristic peak emerged in the pre-edge region, indicating the formation of Fe-F bonds.[46] Integrating the foregoing XAS results, we came to the following conclusions: during the first fluoride ion insertion ($0 \leq x \leq 1$), Fe^{2+}/Fe^{3+} redox was first engaged in charge compensation from while the chemical state of oxygen did

not change; subsequent fluoride ion insertion did not lead to further oxidation of Fe, the formation of oxygen molecules within the lattice provided additional electrons in this state (x > 1).

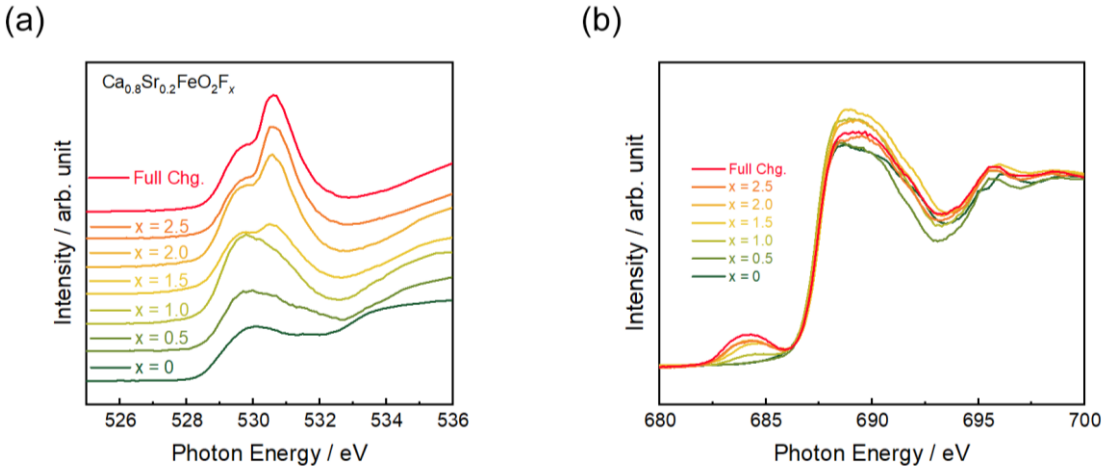

Figure 5.8 (a) O *K*-edge and (b) F *K*-edge XAS spectrums of $Ca_{0.8}Sr_{0.2}FeO_2F_x$ in different states of charge after activation process.

5.4 Conclusions

A series of $Ca_ySr_{1-y}FeO_2$ ($0 \leq y \leq 1$) materials are proposed as cathodes for all-solid-state FIBs. The results of Rietvled refinement using synchrotron XRD data show that the lattice constants of the $Ca_ySr_{1-y}FeO_2$ cathodes continue to decrease with smaller radius Ca^{2+} substitution; after Sr is completely replaced by Ca, the square planar FeO_4 undergoes distortion to stabilize the structure. Their electrochemical performance in the voltage range of –1.5 ~ 3 V was evaluated by a two-electrode bulk-type cell using a current density of 5 mA g^{-1}. Stable and reversible (de)insertion of fluoride ions can be achieved for each material, with $Ca_{0.8}Sr_{0.2}FeO_2$ achieving the highest reversible capacity of 580 mAh g^{-1}; it is speculated that the higher capacity of $CaFeO_2$ is affected by the deviation from the ideal infinite-layer structure due to lattice distortion. The XAS results show that the insertion of the first fluoride ion in $Ca_{0.8}Sr_{0.2}FeO_2$ is achieved by Fe^{2+}/Fe^{3+} redox, and further fluoride ion insertion leads to oxygen oxidation in the bulk, which not only realizes electron transfer but also creates additional fluoride ion

accommodation sites through the formation of stable oxygen molecules. This study has significantly improved the energy density of all-solid-state fluoride ion batteries and educed the cost, and has contributed to their practical application as power batteries in the future.

Reference

1. Li, X.; Wang, Y.; Chen, Z.; Li, P.; Liang, G.; Huang, Z.; Yang, Q.; Chen, A.; Cui, H.; Dong, B., Two-Electron Redox Chemistry Enabled High-Performance Iodide-Ion Conversion Battery. *Angew. Chem. Int. Ed. Engl.* **2022,** *134* (9), e202113576.

2. Lin, Z.; Mao, M.; Yang, C.; Tong, Y.; Li, Q.; Yue, J.; Yang, G.; Zhang, Q.; Hong, L.; Yu, X., Amorphous anion-rich titanium polysulfides for aluminum-ion batteries. *Sci. Adv.* **2021,** *7* (35), eabg6314.

3. Wang, M.; Jiang, C.; Zhang, S.; Song, X.; Tang, Y.; Cheng, H.-M., Reversible calcium alloying enables a practical room-temperature rechargeable calcium-ion battery with a high discharge voltage. *Nat. Chem.* **2018,** *10* (6), 667-672.

4. Aurbach, D.; Lu, Z.; Schechter, A.; Gofer, Y.; Gizbar, H.; Turgeman, R.; Cohen, Y.; Moshkovich, M.; Levi, E., Prototype systems for rechargeable magnesium batteries. *Nature* **2000,** *407* (6805), 724-727.

5. Xu, C.; Li, B.; Du, H.; Kang, F., Energetic zinc ion chemistry: the rechargeable zinc ion battery. *Angew. Chem. Int. Ed. Engl.* **2012,** *124* (4), 957-959.

6. Lin, M.-C.; Gong, M.; Lu, B.; Wu, Y.; Wang, D.-Y.; Guan, M.; Angell, M.; Chen, C.; Yang, J.; Hwang, B.-J., An ultrafast rechargeable aluminium-ion battery. *Nature* **2015,** *520* (7547), 324-328.

7. Ponrouch, A.; Frontera, C.; Bardé, F.; Palacín, M. R., Towards a calcium-based rechargeable battery. *Nat. Mater.* **2016,** *15* (2), 169-172.

8. Orikasa, Y.; Masese, T.; Koyama, Y.; Mori, T.; Hattori, M.; Yamamoto, K.; Okado, T.; Huang, Z. D.; Minato, T.; Tassel, C.; Kim, J.; Kobayashi, Y.; Abe, T.; Kageyama, H.; Uchimoto, Y., High energy density rechargeable magnesium battery using earth-abundant and non-toxic elements. *Sci. Rep.* **2014,** *4*, 5622.

9. Anji Reddy, M.; Fichtner, M., Batteries based on fluoride shuttle. *J. Mater. Chem.*

2011, *21* (43).

10. Rongeat, C.; Reddy, M. A.; Witter, R.; Fichtner, M., Nanostructured Fluorite-Type Fluorides As Electrolytes for Fluoride Ion Batteries. *J. Phys. Chem. C* **2013,** *117* (10), 4943-4950.

11. Rongeat, C.; Anji Reddy, M.; Diemant, T.; Behm, R. J.; Fichtner, M., Development of new anode composite materials for fluoride ion batteries. *J. Mater. Chem. A* **2014,** *2* (48), 20861-20872.

12. Gschwind, F.; Rodriguez-Garcia, G.; Sandbeck, D. J. S.; Gross, A.; Weil, M.; Fichtner, M.; Hörmann, N., Fluoride ion batteries: Theoretical performance, safety, toxicity, and a combinatorial screening of new electrodes. *J. Fluor. Chem.* **2016,** *182*, 76-90.

13. Zhang, L.; Reddy, M. A.; Gao, P.; Diemant, T.; Jürgen Behm, R.; Fichtner, M., Study of all solid-state rechargeable fluoride ion batteries based on thin-film electrolyte. *J. Solid State Electrochem.* **2016,** *21* (5), 1243-1251.

14. Grenier, A.; Porras-Gutierrez, A. G.; Body, M.; Legein, C.; Chretien, F.; Raymundo-Piñero, E.; Dollé, M.; Groult, H.; Dambournet, D., Solid fluoride electrolytes and their composite with carbon: issues and challenges for rechargeable solid state fluoride-ion batteries. *J. Phys. Chem. C* **2017,** *121* (45), 24962-24970.

15. Okazaki, K.-i.; Uchimoto, Y.; Abe, T.; Ogumi, Z., Charge–Discharge Behavior of Bismuth in a Liquid Electrolyte for Rechargeable Batteries Based on a Fluoride Shuttle. *ACS Energy Lett.* **2017,** *2* (6), 1460-1464.

16. Zhang, D.; Yamamoto, K.; Wang, Y.; Gao, S.; Uchiyama, T.; Watanabe, T.; Takami, T.; Matsunaga, T.; Nakanishi, K.; Miki, H.; Iba, H.; Amezawa, K.; Maeda, K.; Kageyama, H.; Uchimoto, Y., Reversible and Fast (De)fluorination of High-Capacity Cu_2O Cathode: One Step Toward Practically Applicable All-Solid-State Fluoride-Ion Battery. *Adv. Energy Mater.* **2021,** *11* (45).

17. Wang, Y.; Yamamoto, K.; Tsujimoto, Y.; Matsunaga, T.; Zhang, D.; Cao, Z.; Nakanishi, K.; Uchiyama, T.; Watanabe, T.; Takami, T.; Miki, H.; Iba, H.; Maeda, K.; Kageyama, H.; Uchimoto, Y., Anion Substitution at Apical Sites of Ruddlesden–Popper-type Cathodes toward High Power Density for All-Solid-State Fluoride-Ion Batteries. *Chem. Mater.* **2022,** *34* (2), 609-616.

18. Zhang, D.; Yoshinari, T.; Yamamoto, K.; Kitaguchi, Y.; Ochi, A.; Nakanishi, K.; Miki, H.; Nakanishi, S.; Iba, H.; Watanabe, T.; Uchiyama, T.; Orikasa, Y.; Amezawa, K.; Uchimoto, Y., Cu–Pb Nanocomposite Cathode Material toward Room-Temperature Cycling for All-Solid-State Fluoride-Ion Batteries. *ACS Appl. Energy Mater.* **2021,** *4* (4), 3352-3357.

19. Zhang, D.; Nakano, H.; Yamamoto, K.; Tanaka, K.; Yahara, T.; Imai, K.; Mori, T.; Miki, H.; Nakanishi, S.; Iba, H., Rate-determining process at electrode/electrolyte interfaces for all-solid-state fluoride-ion batteries. *ACS Appl. Mater. Interfaces* **2021,** *13* (25), 30198-30204.

20. Thieu, D. T.; Fawey, M. H.; Bhatia, H.; Diemant, T.; Chakravadhanula, V. S. K.; Behm, R. J.; Kübel, C.; Fichtner, M., CuF_2 as reversible cathode for fluoride ion batteries. *Adv. Funct. Mater.* **2017,** *27* (31), 1701051.

21. Zhang, D.; Yamamoto, K.; Ochi, A.; Wang, Y.; Yoshinari, T.; Nakanishi, K.; Nakano, H.; Miki, H.; Nakanishi, S.; Iba, H.; Uchiyama, T.; Watanabe, T.; Amezawa, K.; Uchimoto, Y., Understanding the reaction mechanism and performances of 3*d* transition metal cathodes for all-solid-state fluoride ion batteries. *J. Mater. Chem. A* **2021,** *9* (1), 406-412.

22. Nowroozi, M. A.; Wissel, K.; Rohrer, J.; Munnangi, A. R.; Clemens, O., $LaSrMnO_4$: Reversible Electrochemical Intercalation of Fluoride Ions in the Context of Fluoride Ion Batteries. *Chem. Mater.* **2017,** *29* (8), 3441-3453.

23. Nowroozi, M. A.; Ivlev, S.; Rohrer, J.; Clemens, O., La_2CoO_4: a new intercalation based cathode material for fluoride ion batteries with improved cycling stability. *J.*

Mater. Chem. A **2018,** *6* (11), 4658-4669.

24. Nowroozi, M. A.; Wissel, K.; Donzelli, M.; Hosseinpourkahvaz, N.; Plana-Ruiz, S.; Kolb, U.; Schoch, R.; Bauer, M.; Malik, A. M.; Rohrer, J.; Ivlev, S.; Kraus, F.; Clemens, O., High cycle life all-solid-state fluoride ion battery with La_2NiO_{4+d} high voltage cathode. *Commun. Mater.* **2020,** *1* (1).

25. Tassel, C.; Watanabe, T.; Tsujimoto, Y.; Hayashi, N.; Kitada, A.; Sumida, Y.; Yamamoto, T.; Kageyama, H.; Takano, M.; Yoshimura, K., Stability of the infinite layer structure with iron square planar coordination. *J. Am. Chem. Soc.* **2008,** *130* (12), 3764-3765.

26. Tassel, C.; Pruneda, J. M.; Hayashi, N.; Watanabe, T.; Kitada, A.; Tsujimoto, Y.; Kageyama, H.; Yoshimura, K.; Takano, M.; Nishi, M., $CaFeO_2$: A new type of layered structure with iron in a distorted square planar coordination. *J. Am. Chem. Soc.* **2009,** *131* (1), 221-229.

27. Rongeat, C.; Reddy, M. A.; Witter, R.; Fichtner, M., Solid electrolytes for fluoride ion batteries: ionic conductivity in polycrystalline tysonite-type fluorides. *ACS Appl. Mater. Interfaces* **2014,** *6* (3), 2103-10.

28. Petříček, V.; Dušek, M.; Palatinus, L., Crystallographic computing system JANA2006: general features. *Zeitschrift für Kristallographie-Crystalline Materials* **2014,** *229* (5), 345-352.

29. Momma, K.; Izumi, F., VESTA 3 for three-dimensional visualization of crystal, volumetric and morphology data. *J. Appl. Crystallogr.* **2011,** *44* (6), 1272-1276.

30. Ravel, B.; Newville, M., ATHENA, ARTEMIS, HEPHAESTUS: data analysis for X-ray absorption spectroscopy using IFEFFIT. *J. Synchrotron Radiat.* **2005,** *12* (4), 537-541.

31. Tsujimoto, Y.; Tassel, C.; Hayashi, N.; Watanabe, T.; Kageyama, H.; Yoshimura, K.; Takano, M.; Ceretti, M.; Ritter, C.; Paulus, W., Infinite-layer iron oxide with a square-planar coordination. *Nature* **2007,** *450* (7172), 1062-5.

32. Shannon, R. D., Revised effective ionic radii and systematic studies of interatomic distances in halides and chalcogenides. *Acta crystallographica section A: crystal physics, diffraction, theoretical and general crystallography* **1976,** *32* (5), 751-767.

33. Nitta, N.; Wu, F.; Lee, J. T.; Yushin, G., Li-ion battery materials: present and future. *Mater. Today* **2015,** *18* (5), 252-264.

34. Yoon, W.-S.; Chung, K. Y.; McBreen, J.; Yang, X.-Q., A comparative study on structural changes of $LiCo_{1/3}Ni_{1/3}Mn_{1/3}O_2$ and $LiNi_{0.8}Co_{0.15}Al_{0.05}O_2$ during first charge using in situ XRD. *Electrochem. Commun.* **2006,** *8* (8), 1257-1262.

35. Wang, R.; Li, X.; Liu, L.; Lee, J.; Seo, D.-H.; Bo, S.-H.; Urban, A.; Ceder, G., A disordered rock-salt Li-excess cathode material with high capacity and substantial oxygen redox activity: $Li_{1.25}Nb_{0.25}Mn_{0.5}O_2$. *Electrochem. Commun.* **2015,** *60*, 70-73.

36. Sun, J.; Sheng, C.; Cao, X.; Wang, P.; He, P.; Yang, H.; Chang, Z.; Yue, X.; Zhou, H., Restraining Oxygen Release and Suppressing Structure Distortion in Single-Crystal Li-Rich Layered Cathode Materials. *Adv. Funct. Mater.* **2022,** *32* (10), 2110295.

37. Lee, J.; Papp, J. K.; Clement, R. J.; Sallis, S.; Kwon, D. H.; Shi, T.; Yang, W.; McCloskey, B. D.; Ceder, G., Mitigating oxygen loss to improve the cycling performance of high capacity cation-disordered cathode materials. *Nat. Commun.* **2017,** *8* (1), 981.

38. Huang, J.; Zhong, P.; Ha, Y.; Kwon, D.-H.; Crafton, M. J.; Tian, Y.; Balasubramanian, M.; McCloskey, B. D.; Yang, W.; Ceder, G., Non-topotactic reactions enable high rate capability in Li-rich cathode materials. *Nature Energy* **2021,** *6* (7), 706-714.

39. Nakajima, M.; Yabuuchi, N., Lithium-excess cation-disordered rocksalt-type oxide with nanoscale phase segregation: $Li_{1.25}Nb_{0.25}V_{0.5}O_2$. *Chem. Mater.* **2017,** *29* (16), 6927-6935.

40. Hoshino, S.; Glushenkov, A. M.; Ichikawa, S.; Ozaki, T.; Inamasu, T.; Yabuuchi, N., Reversible three-electron redox reaction of Mo^{3+}/Mo^{6+} for rechargeable lithium batteries. *ACS Energy Lett.* **2017,** *2* (4), 733-738.

41. Zhao, X.; Tian, Y.; Lun, Z.; Cai, Z.; Chen, T.; Ouyang, B.; Ceder, G., Design principles for zero-strain Li-ion cathodes. *Joule* **2022**.

42. Yoon, W.-S.; Balasubramanian, M.; Chung, K. Y.; Yang, X.-Q.; McBreen, J.; Grey, C. P.; Fischer, D. A., Investigation of the charge compensation mechanism on the electrochemically Li-Ion deintercalated $Li_{1-x}Co_{1/3}Ni_{1/3}Mn_{1/3}O_2$ electrode system by combination of soft and hard X-ray absorption spectroscopy. *J. Am. Chem. Soc.* **2005,** *127* (49), 17479-17487.

43. House, R. A.; Maitra, U.; Perez-Osorio, M. A.; Lozano, J. G.; Jin, L.; Somerville, J. W.; Duda, L. C.; Nag, A.; Walters, A.; Zhou, K. J.; Roberts, M. R.; Bruce, P. G., Superstructure control of first-cycle voltage hysteresis in oxygen-redox cathodes. *Nature* **2020,** *577* (7791), 502-508.

44. House, R. A.; Rees, G. J.; Pérez-Osorio, M. A.; Marie, J.-J.; Boivin, E.; Robertson, A. W.; Nag, A.; Garcia-Fernandez, M.; Zhou, K.-J.; Bruce, P. G., First-cycle voltage hysteresis in Li-rich 3d cathodes associated with molecular O_2 trapped in the bulk. *Nat. Energy* **2020,** *5* (10), 777-785.

45. House, R. A.; Playford, H. Y.; Smith, R. I.; Holter, J.; Griffiths, I.; Zhou, K.-J.; Bruce, P. G., Detection of trapped molecular O_2 in a charged Li-rich cathode by Neutron PDF. *Energy Environ. Sci.* **2022,** *15* (1), 376-383.

46. Vinogradov, A. S.; Fedoseenko, S. I.; Krasnikov, S. A.; Preobrajenski, A. B.; Sivkov, V. N.; Vyalikh, D. V.; Molodtsov, S. L.; Adamchuk, V. K.; Laubschat, C.; Kaindl, G., Low-lying unoccupied electronic states in 3d transition-metal fluorides probed by NEXAFS at the F 1s threshold. *Phys. Rev., B* **2005,** *71* (4).

Chapter 6. High-capacity Oxyfluoride Cathodes for All-Solid-State Fluoride-ion Batteries with Cationic Substitution toward High-Rate Capability

All-solid-state fluoride-ion batteries with high energy density are considered as advantageous candidates for next-generation energy storage. The intercalation-type cathodes with Ruddlesden−Popper phase using topotactical fluoride ion (de)insertion effectively suppresses the volume change problem of metal/metal fluoride conversion-type cathodes, and exhibit stable cycle ability; however, the energy density of these cathodes is not ideal. Recently, we have proposed $SrFeO_2$ cathode with infinite-layer structure, which has a three-dimensional penetration ion diffusion pathway, achieved high energy density and cycling stability simultaneously by accommodating excess amount of fluoride ions. Based on this material, in this study we have fabricated $Sr_{1-y}Ba_yFeO_2$ ($0 \leq y \leq 0.8$) cathodes with partial substitution by Ba. The results of synchrotron XRD refinements, EXAFS analysis, and electrochemical measurements show that the phase-transition occurs from an infinite-layer phase to an oxygen-deficient $LaNiO_{2.5}$ phase after $y = 0.4$ substitution, and becomes unable to accommodate excess fluoride ions as in the case of $SrFeO_2$. Nevertheless, in the cathode with $0 \leq y \leq 0.3$, $Sr_{0.7}Ba_{0.3}FeO_2$ demonstrates the high-rate performance, because the bottle-neck area for fluoride-ion diffusion increases with increasing Ba content.

6.1 Introduction

Energy drives economies and sustains societies. In the past 30 years, lithium-ion batteries (LIBs) are commercially used in various scenarios as an efficient energy storage system.[1] Researchers have invested a lot of effort to further improve the energy and power density, cycle stability and reliability of LIBs. However, the energy density of conventional LIBs will soon reach its limit[2], the resulting cask effect forces us to develop new battery systems. To meet the growing market demand for next-generation batteries with higher energy density as well as power density, several strategies have been proposed, such as all-solid-state batteries that employ solid electrolyte instead of the liquid counterpart[3], and other battery systems that employ different charge carriers (e.g., Na^+, Mg^{2+}, Cl^- or F^-).[4-8]

All-solid-state fluoride-ion batteries (FIBs), due to the highest electronegativity of fluoride ion carriers, exhibit extraordinary chemical stability and promise high power density by using high-voltage electrodes.[9, 10] Metal/metal fluoride conversion type cathodes (Bi/BiF_3, Cu/CuF_2, etc.) were firstly implied in FIBs owing to their high theoretical capacities. Unfortunately, the dramatic volumetric expansion after fluoride ion insertion, has a negative impact on the reversibility and cyclability.[11-13] To suppress the undesired volume change, a series of layered-perovskite oxides with Ruddlesden−popper structure ($A_{n+1}B_nX_{3n+1}$, where A and B are cations, X is oxygen) were developed as cathode materials for FIBs.[10, 14-18] Although these layered oxides provide rigid host lattices for fluoride ion (de)intercalation, the excessively heavy unit cells hinder the realization of high energy density.

Recently, we published an iron oxide $SrFeO_2$ as cathode material for FIBs. Taking the advantage of a simpler lattice structure in comparison with previous layered compounds (e.g., $LaSrMnO_4$, La_2CoO_4 or La_2NiO_4), $SrFeO_2$ delivered a surprising volumetric energy density of 2736 Wh L^{-1} by using the charge compensation of lattice oxygen. In addition, the unique infinite-layer structure provides a rigid host cell to ensure the structural integrity against fluoride ion insertion, which makes $SrFeO_2$

exhibit outstanding electrochemical reversibility (Coulombic efficiency close to 99% after activation process) and cycling stability (capacity retention of 91.4% after 35 cycles). However, the electrochemical performance at high current densities is not satisfactory.

In this study, we employed a series Ba substituted $Sr_{1-y}Ba_yFeO_2$ ($0 \leq y \leq 0.8$) compounds as cathode materials for FIBs. With the increase of Ba content, the compounds with $x > 0.3$ changes from an infinite-layer structure to a new phase analogous to a "oxygen-deficient" $LaNiO_{2.5}$ structure. The electrochemical performances of each sample are evaluated; the results show that only the materials with infinite-layer structure ($x \leq 0.3$) allow the insertion of excess amount of F, and $Sr_{0.7}Ba_{0.3}FeO_2$ demonstrated the best rate capability. Extended X-ray absorption fine structure (EXAFS) analysis was used to clarify the local structure changes around lattice oxygen and future probe the correlation between it and ionic conductivity.[19, 20] As a result, $Sr_{0.7}Ba_{0.3}FeO_2$ is corroborated to be the material that shows best rate capability owing to the largest bottle-neck area around the lattice oxygen, which enhances the F^- mobility with the lattice.

6.2 Experimental

6.2.1 Material synthesis.

$Sr_{1-y}Ba_yFeO_2$. The oxygen-deficient precursors $Sr_{1-y}Ba_yFeO_{3-\delta}$ (y = 0, 0.1, 0.2, 0.3, 0.4, 0.6, 0.8) were prepared in air by conventional high-temperature ceramic reactions.[21-23] Stoichiometric amount of $SrCO_3$ (99.99%, Kojundo Chemical Laboratory), $BaCO_3$ (99.99%, Kojundo Chemical Laboratory), and Fe_2O_3 (99.9%, WAKO pure chemical industries, ltd.) were thoroughly mixed, pelletized and reacted at 1200°C for 2 days with one intermediate grinding. The as-prepared precursors were subsequently ground well with a 2-molar excess of CaH_2 (99.99%, Sigma-Aldrich) in an Ar-filled glovebox, pelletized, sealed in an evacuated Pyrex tube and heated under various temperatures and durations as listed in Supplementary Table 1. The final

reaction phase was washed with 0.15M NH_4Cl/methanol solution to remove the CaO byproduct and residual CaH_2.

Table 6.1 Reaction Conditions for $(Sr_{1-y}Ba_y)FeO_2$.

$Sr_{1-y}Ba_yFeO_2$	Reaction temperature / °C	Reaction time / days	Reducing agent
y = 0	280	1	CaH_2
y = 0.1 ~ 0.3	280	3	CaH_2
y = 0.4	320	14	CaH_2
y = 0.6, 0.8	320	3	CaH_2
y = 1	140	3	NaH

Solid Electrolyte. $La_{0.9}Ba_{0.1}F_{2.9}$ (LBF) was employed as the electrolyte in this study.[24] A stoichiometric ratio of LaF_3 (99.9%, Kojundo Chemical Laboratory Co., Ltd.) and BaF_2 (99.9%, Kojundo Chemical Laboratory Co., Ltd.) was thoroughly ground using a mortar and the mixture was subsequently sealed into an agate ball milling pot and milled at 600 rpm for 10 h. Finally, the ball-milled mixture was pelletized and sintered at 1000 °C for 4 h. All of the above operations were completed in an Ar-filled glovebox.

6.2.2 Electrochemical measurements.

Electrochemical performances of each sample were evaluated using bulk-type cell. For cathode composites, $Sr_{1-y}Ba_yFeO_2$ was ball-milled with the solid electrolyte, LBF, and vapor-grown carbon fiber (VGCF, Showa Denko K.K) at a ratio of 3: 6: 1 for 10h. For the anode composite, elemental Pb (99.9% Kojundo Chemical Laboratory Co. Ltd.), PbF_2 (99.9%, Kojundo Chemical Laboratory Co., Ltd.), LBF, and VGCF were ball-milled at a wight ratio of 2: 3: 4: 1. The powder of Cathode composite, LBF, and anode composite were pressed into a pellet under 360 MPa for 5min, and finally held by two pieces of gold foil as current collectors.

The electrochemical performances of $Sr_{1-y}Ba_yFeO_2$ were examined on an HJ1010SD8 (Hokuto Denko Corporation) electrochemical workstation. For galvanostatic charge/discharge tests, a current density of 5 mA g^{-1} was employed to evaluate the cycling stabilities; current densities up to 200 mA g^{-1} were used for rate capabilities. The cutoff voltage was set to −1.5 to 3.0 V versus Pb/PbF_2.

6.2.3 Characterization.

Synchrotron X-ray diffraction (XRD) measurements were performed at room temperature at synchrotron radiation facility SPring-8 (BL02B2), Japan. The synchrotron radiation X-rays were monochromatized to a wavelength of 0.41343 Å, which was calibrated using a CeO_2 standard sample. Rietveld refinements were performed using the JANA2006 package[25] to probe the purity of $Sr_{1-y}Ba_yFeO_2$ and local structural information. The crystal structure models for $Sr_{1-y}Ba_yFeO_2$ were depicted using the program VESTA.[26] Extended X-ray absorption fine spectroscopy (EXAFS) for Sr and Ba *K*-edges were performed at beamline BL14B2 in SPring-8 in the transmission mode using a Si (111) monochromator. EXAFS structural analysis was performed with the Artemis software.[27]

6.3 Result and discussion

6.3.1 Crystal structures of $Sr_{1-y}Ba_yFeO_2$.

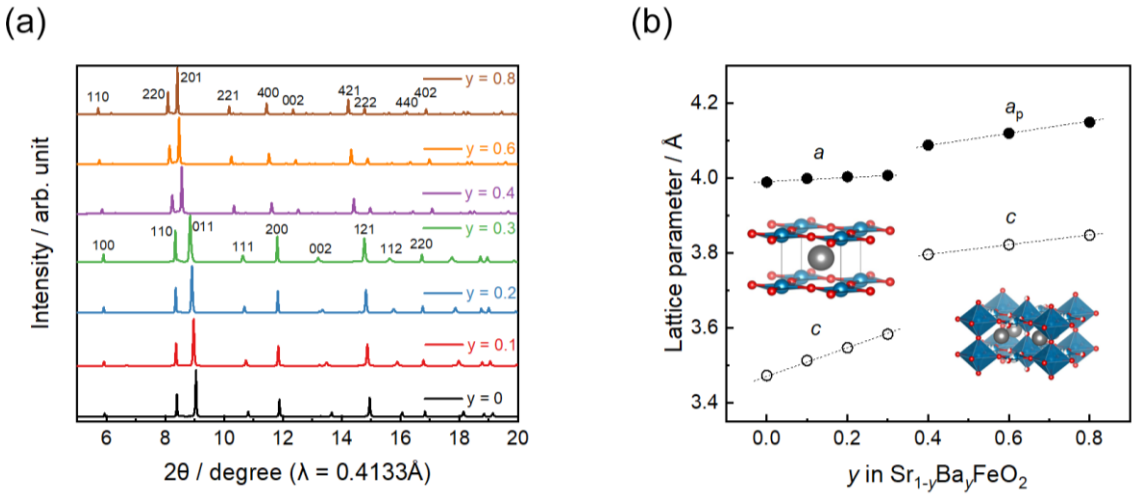

Figure 6.1 (a) Synchrotron XRD pattern of $Sr_{1-y}Ba_yFeO_2$ compounds. (b) Lattice parameter evolution with Ba substitution obtained from Rietveld refinement.

The synchrotron XRD pattern of as-prepared $Sr_{1-y}Ba_yFeO_2$ are shown in the Figure 6.1a. No impurity could be detected within the experimental resolution. All the profiles are readily indexed on the basis of a tetragonal unit cell and gradually shift to lower angles because of the different atomic diameters between Ba and Sr, whereas several

additional superlattice reflections related to the simple perovskite cell emerged in the y = 0.4 ~ 0.8 samples, indicating a structural phase transition after y = 0.4 substituting. Rietveld refinements against synchrotron XRD were performed for all samples, the results are listed in Figure 6.2. In the case of y = 0 ~ 0.3 samples, the profiles could be fitted well using an infinite-layer structure; for y = 0.4 ~ 0.8 samples, the profiles were fitted using the oxygen-deficient $LaNiO_{2.5}$ structure described by Yamamoto et al.[21]

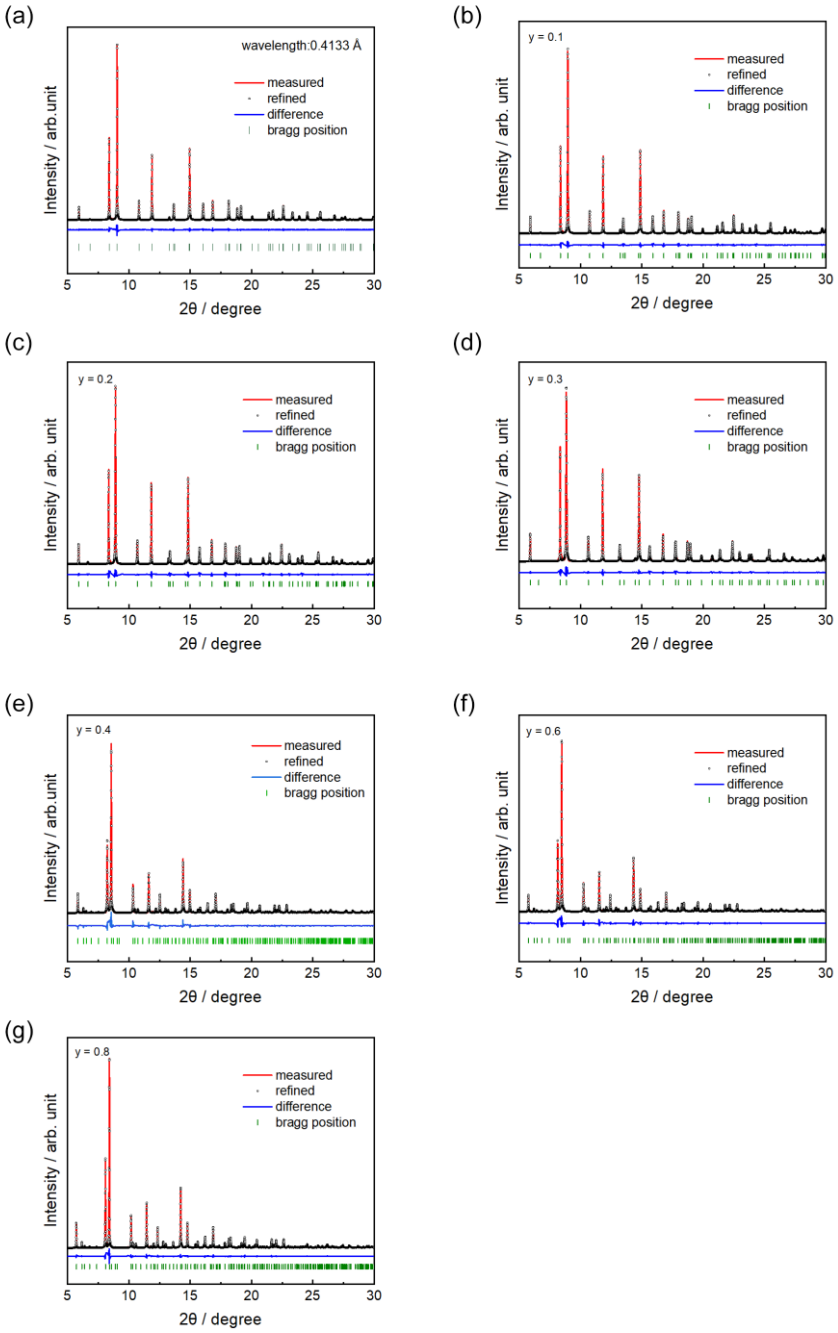

Figure 6.2 Results of Rietveld refinement for $Sr_{1-y}Ba_yFeO_2$ compounds.

Figure 6.1b and Table 6.2 summaries the lattice constants of $Sr_{1-y}Ba_yFeO_2$ compounds; for the sake of comparison, we used the normalized lattice parameter after y = 0.4, where $a_p = 1/2a$. Both the *a* and *c* axis lengthened gradually accompanied by Ba substituting, the *c* axis demonstrated a more significant expansion in compared with *a* axis for y = 0 ~ 0.3 samples (from y = 0 to y = 0.3, *c* axis increases 3.3% while *a* axis increases 0.5%); however, a jump in the lattice parameters of $Sr_{1-y}Ba_yFeO_2$ from y = 0.3 to y = 0.4 strongly suggests that a phase transition has occurred in this region. And for compounds with y ≥ 0.4, their *a* and *c* axis follow Vegard's law exhibiting a linear and continuous increase, indicating that the content of oxygen in them does not vary with y.[21] This kind of phase transition might hinder the perfect pathway for fluoride ion between infinite-layers, might affect the fluoride ion diffusion within the lattice.

Figure 6.3 provides information on the morphology of each material. the SEM images show that the primary particle sizes of the different component materials are similar, with an average particle size of 3 ~ 5 um.

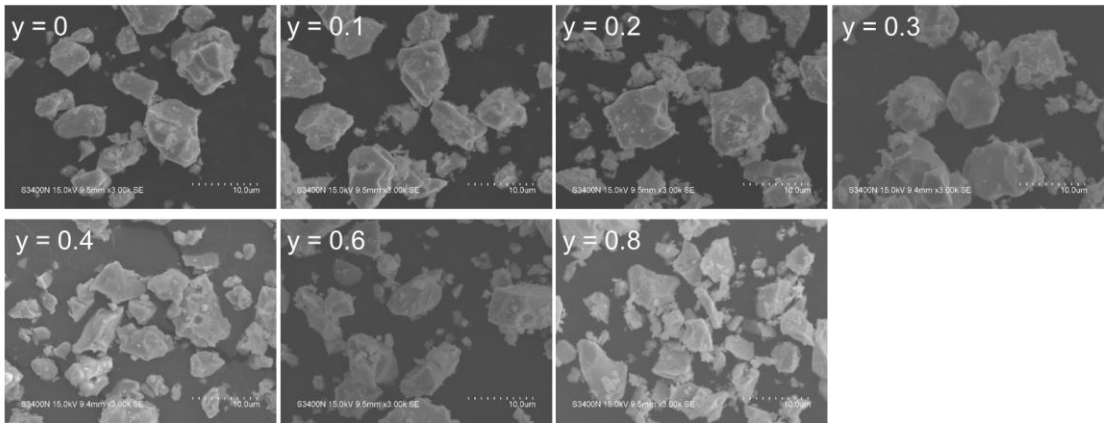

Figure 6.3 SEM images of $Sr_{1-y}Ba_yFeO_2$ compounds.

Table 6.2 Results of Rietveld refinement for $Ca_ySr_{1-y}FeO_2$ ($0 \leq y \leq 1$).

	atom	site	x	y	z	occupancy
$SrFeO_2$	Sr	1*d*	0.5	0.5	0.5	1
*P*4/*mmm*	Fe	1*a*	0	0	0	1
a =3.99119(1)	O	2*f*	0.5	0	0	1
c = 3.47466(0)						
R_p = 5.57%						
R_{wp} = 7.70%						
$Sr_{0.9}Ba_{0.1}FeO_2$	Ba	1*d*	0.5	0.5	0.5	0.1
*P*4/*mmm*	Sr	1*d*	0.5	0.5	0.5	0.9
a =3.99738(9)	Fe	1*a*	0	0	0	1
c = 3.52125(2)	O	2*f*	0.5	0	0	1
R_p = 5.69%						
R_{wp} = 8.52%						

	atom	site	x	y	z	occupancy
$Sr_{0.8}Ba_{0.2}FeO_2$	Ba	1*d*	0.5	0.5	0.5	0.2
*P*4/*mmm*	Sr	1*d*	0.5	0.5	0.5	0.8
a =4.00332(2)	Fe	1*a*	0	0	0	1
c = 3.54869(2)	O	2*f*	0.5	0	0	1
R_p = 5.43%						
R_{wp} = 9.56%						
$Sr_{0.7}Ba_{0.3}FeO_2$	Ba	1*d*	0.5	0.5	0.5	0.3
*P*4/*mmm*	Sr	1*d*	0.5	0.5	0.5	0.7
a =4.01001(6)	Fe	1*a*	0	0	0	1
c = 3.58706(1)	O	2*f*	0.5	0	0	1
R_p = 7.25%						
R_{wp} = 12.49%						

	atom	site	x	y	z	occupancy
$Sr_{0.6}Ba_{0.4}FeO_2$	Sr	4*k*	0.235019	0.235019	0.5	0.4
*P*4/*mmm*	Ba	4*k*	0.235019	0.235019	0.5	0.6
a =8.175213 (5)	Fe1	1*a*	0	0	0	1
c = 3.795612 (1)	Fe2	2*f*	0	0.5	0	0.208
R_p = 7.62%	Fe3	4*n*	0.041060	0.5	0	0.396
R_{wp} = 10.88%	Fe4	1*c*	0.5	0.5	0	1
	O1	4*l*	0.279033	0	0	1
	O2	4*n*	0.252553	0.5	0	0.604
	O3	1*b*	0	0	0.5	1
	O4	1*d*	0.5	0.5	0.5	0.583

	atom	site	x	y	z	occupancy
$Sr_{0.4}Ba_{0.6}FeO_2$	Sr	4*k*	0.235606	0.235606	0.5	0.4
*P*4/*mmm*	Ba	4*k*	0.235606	0.235606	0.5	0.6
a =8.238259 (4)	Fe1	1*a*	0	0	0	1
c = 3.821518 (7)	Fe2	2*f*	0	0.5	0	0.208
R_p = 6.23%	Fe3	4*n*	0.037106	0.5	0	0.396
R_{wp} = 10.63%	Fe4	1*c*	0.5	0.5	0	1
	O1	4*l*	0.280180	0	0	1
	O2	4*n*	0.252553	0.5	0	0.604
	O3	1*b*	0	0	0.5	1
	O4	1*d*	0.5	0.5	0.5	0.583

	atom	site	x	y	z	occupancy
$Sr_{0.2}Ba_{0.8}FeO_2$	Sr	4*k*	0.236463	0.236463	0.5	0.4
*P*4/*mmm*	Ba	4*k*	0.236463	0.236463	0.5	0.6
a =8.296937 (2)	Fe1	1*a*	0	0	0	1
c = 3.84736 (1)	Fe2	2*f*	0	0.5	0	0.208
R_p = 5.51 %	Fe3	4*n*	0.042883	0.5	0	0.396
R_{wp} = 9.35 %	Fe4	1*c*	0.5	0.5	0	1
	O1	4*l*	0.281636	0	0	1
	O2	4*n*	0.256583	0.5	0	0.604
	O3	1*b*	0	0	0.5	1
	O4	1*d*	0.5	0.5	0.5	0.583

6.3.2 Electrochemical performance

The charge/discharge performance of all samples was evaluated in a cutoff voltage range of −1.5 ~ 3V against Pb/PbF_2 anode. Similar to the case of $SrFeO_2$, y = 0.1 ~ 0.3 cathodes exhibited high reversible behavior after a five-cycle activation process (see Figure 6.4a and Figure 6.5). All the samples showed the two-plateau charge-discharge profile, indicating that not only Fe but also O was involved in charge compensation, as we confirmed in the previous study on $SrFeO_2$. Although the charge/discharge capacity gradually decreased with Ba substituting due to the heavier atomic mass of Ba than Sr, each material still allows nearly two F^- intercalation by electrochemical method, while only one F^- was allowed stoichiometrically by using the chemical method.[28, 29] In contrast, for y ≥ 0.4 cathodes, unlike $Sr_{1-y}Ba_yFeO_2$ materials with infinite-layer structure, excess amount of fluoride ions were not allowed even using the electrochemical method, only one F^- was inserted after charging to 3 V vs. Pb/PbF_2 (Figure 6,4b,c and Figure 6.5).

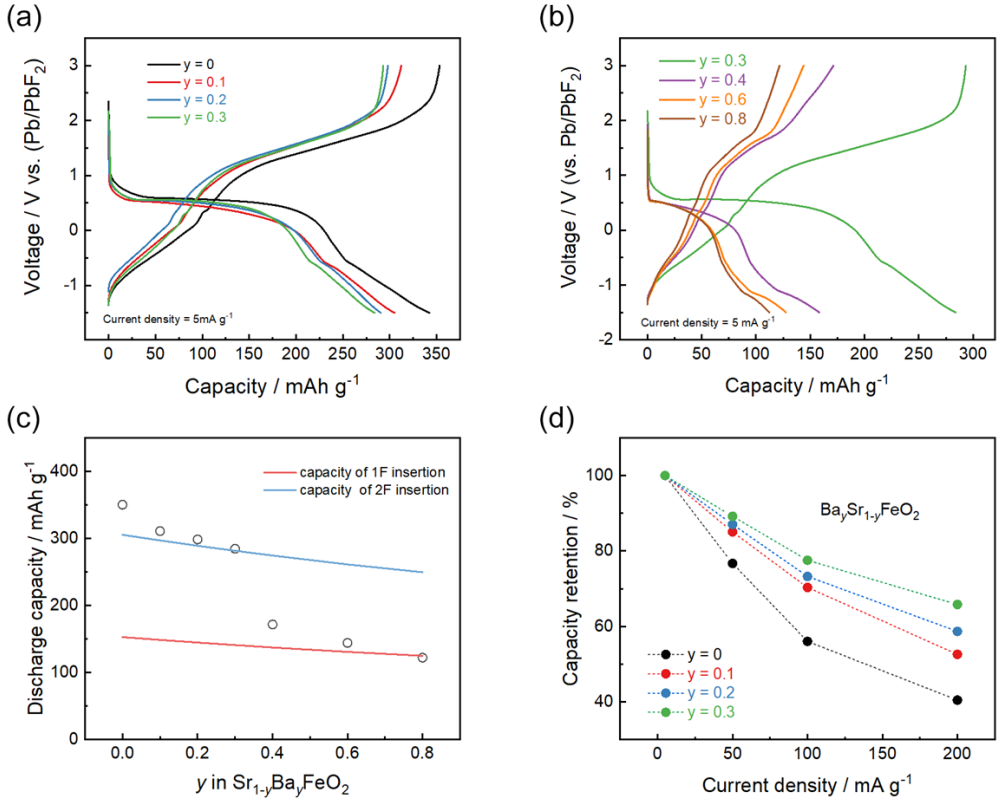

Figure 6.4 (a, b) charge/discharge profiles of $Sr_{1-y}Ba_yFeO_2$ after activation process. (c) 6th discharge capacities of the $Sr_{1-y}Ba_yFeO_2$ cathodes, the red and blue line corresponding to the capacities of 1F and 2F insertion. (d) rate properties of $Sr_{1-y}Ba_yFeO_2$ cathodes (y = 0 ~ 0.3)

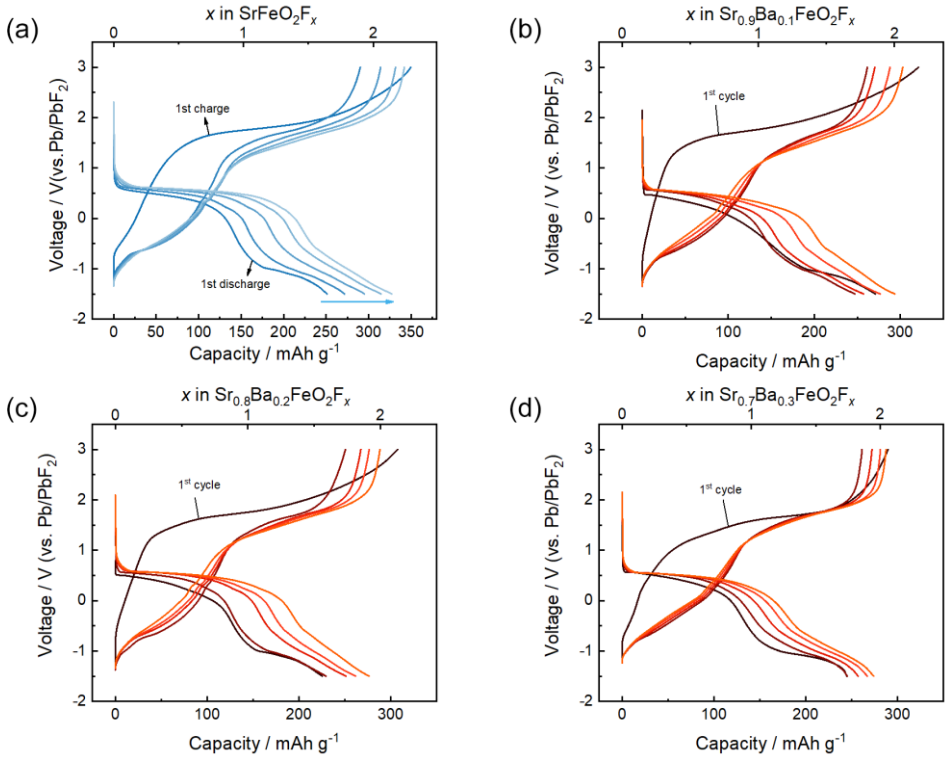

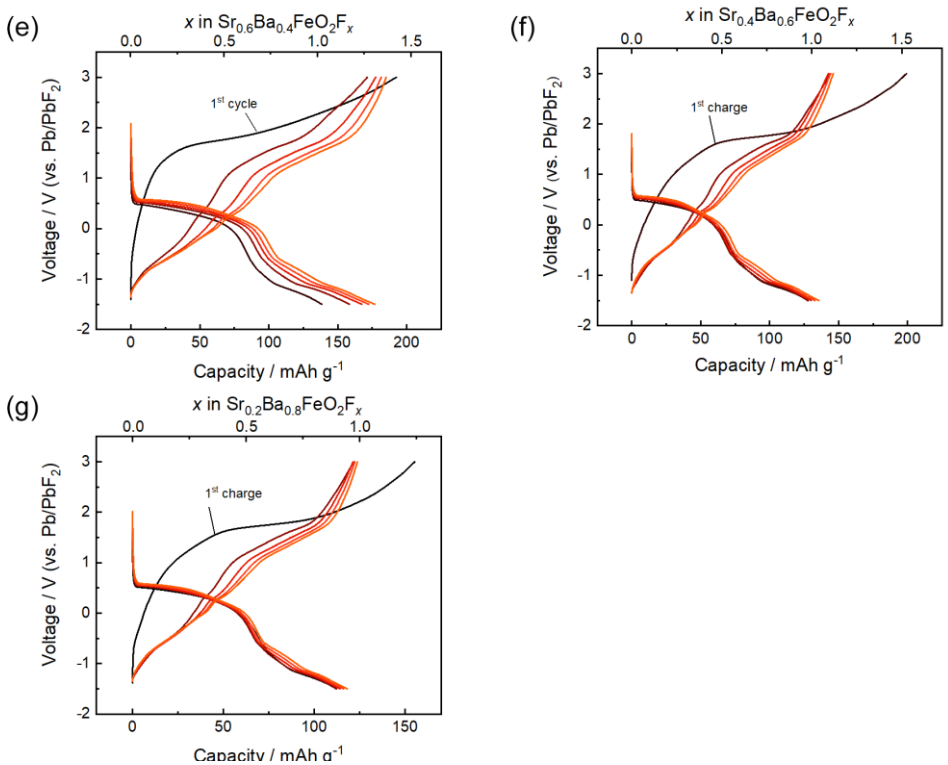

Figure 6.5 Charge/discharge profiles of the initial 5 cycles of $Sr_{1-y}Ba_yFeO_2$ cathodes.

To evaluate the change of rate capability with increasing Ba content, we tested the charge/discharge performance of each material under different current densities. For the cathodes with $y \geq 0.4$ cathodes, which undergo a structural transition from infinite-layer to "oxygen-deficient" $LaNiO_{2.5}$ structure, we did not incorporate them into the comparison. As shown in Figure 6.4b, the material with more Ba content exhibits a higher anionic capacity retention rate under high current density; amount them, $Sr_{0.7}Ba_{0.3}FeO_2$ exhibits the best rate capability, 64% discharge capacity retention was realized at 200mAh g^{-1} while that of $SrFeO_2$ is only 41%.

6.3.3 Charge compensation mechanism

To verify the charge compensation mechanism of $Sr_{1-y}Ba_yFeO_2$ cathodes during the charge/discharge process, the *K*-edge XAS of O and Fe of $Sr_{0.7}Ba_{0.3}FeO_2$ cathode in different states of charge was measured. At the beginning of charging ($0 < x < 1$), the k edge of Fe shifts to higher energies with the insertion of F^-, representing the involvement of Fe in charge compensation (Figure 6.6). Subsequently, the position of

the absorption edge of Fe remains almost constant, implying that the valence state of Fe no longer changes. The absorption edge of Fe shifts back to the initial position (x = 0) after discharging to –1.5V again, revealing that the redox of Fe is reversible during the charge/discharge process. Figure 6.7a summarizes the energy evolution of the Fe *K*-edge with F content.

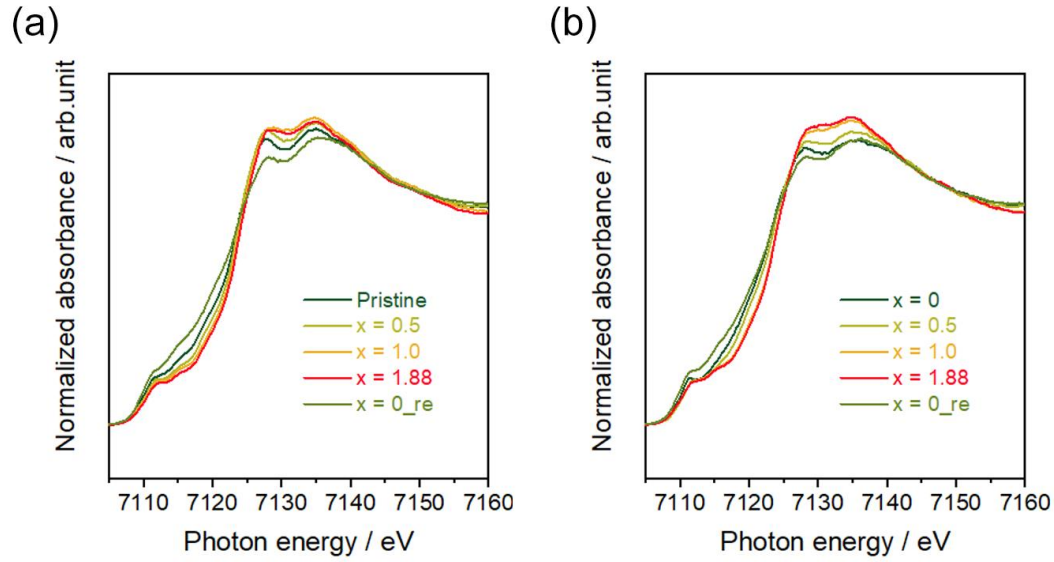

Figure 6.6 Fe K-edge XAS spectrums of $Sr_{0.7}Ba_{0.3}FeO_2F_x$ in different states of charge (a) before activation, (b) after activation.

On the other hand, the trend of the *K*-edge of oxygen is opposite to that of Fe. Figure 6.7b shows the O *K*-edge XAS of the $Sr_{0.7}Ba_{0.3}FeO_2$ cathode. The broad signal in the 530 ~ 535 eV interval come from the electron leap from the O 1*s* orbital to the Fe 3*d* - O 2*p* hybridized orbital, and they do not exhibit significant changes at the initial stage of charging ($0 < x < 1$); however, from $x > 1$ onward, two distinct changes emerge in the spectrum of O *K*-edge XAS: (1) a new peak appeared at the pre-edge area (~ 529 eV), and (2) the intensity of the peak at 532 eV is significantly enhanced. The former is usually considered to originate from superoxide, while the latter is suggested to be a fingerprint feature of oxygen molecular formation within the lattice and is proven in our previous study.[30-33] All of the above evidence suggests that Fe contributes electrons during the first fluoride ion insertion, and thereafter, oxygen is implicated in charge compensation and allows excess fluoride ion insertion through the stable

generation of oxygen molecules.

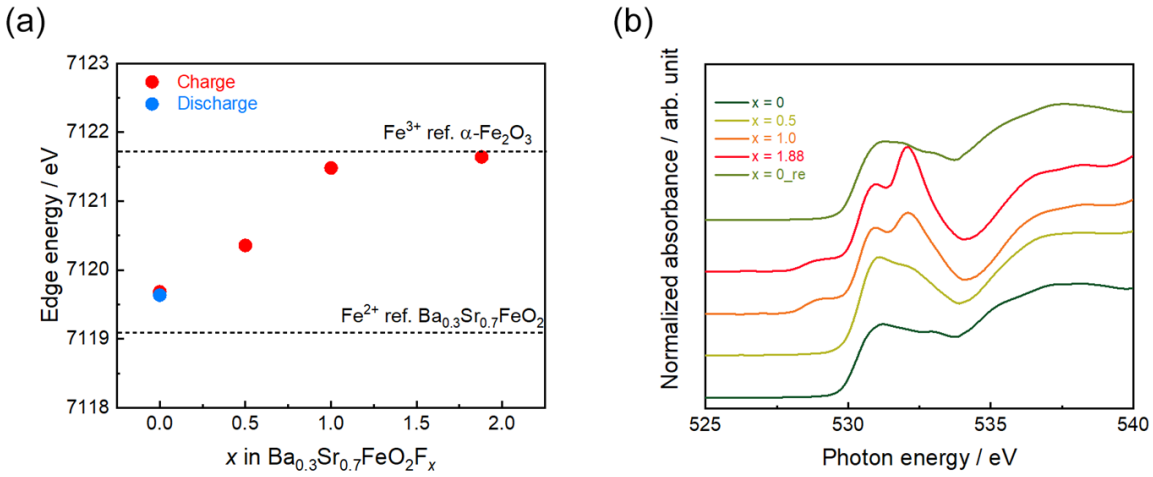

Figure 6.7 (a) Plot of edge energies summarized from Figure 6.6b. (b) O K-edge XAS spectrums of $Sr_{0.7}Ba_{0.3}FeO_2F_x$ in different states of charge.

6.3.4 Local structure changes with the introduce of Ba

It is known from the previous XRD measurement that with the increase of Ba content in $Sr_{1-y}Ba_yFeO_2$, the *c*-axis exhibits more obvious expansion than the *a*-axis. Considering the negligible difference in ionic radii between Ba and Sr (Ba^{2+}: 135 pm; Sr^{2+}: 118 pm)[34], the expansion of the *c*-axis can be attributed to the increase in interlayer distance of the infinite layer. In order to prove our inference, the local structure around Fe, Sr, and Ba atoms is investigated by using EXAFS analysis.

Figure 6.8a shows the radial structure functions (RSFs) around Fe atom obtained from *K*-edge EXAFS. Fourier transformation of the oscillations between 3.5 and 14 Å was used to get RSFs. The first peak observed at 1.5 Å is generated from the first 4-coordinated Fe-O shell. Since $Sr_{1-y}Ba_yFeO_2$ (y = 0 ~ 0.3) compounds have a special infinite-layer structure, the second and the third nearest coordination (Fe-Ba/Sr shell and Fe-O-Fe shell) can be distinguished in R space, corresponding to the peaks located at 3 and 3.6 Å, respectively. Different from the first shell peak, the second peak (Fe-Ba/Sr) showed a significant decrease in intensity with increasing Ba content, which

may be due to the aggravating static distortion of the A site and different phase shifts ($\emptyset_j(k)$ in following Equation of Ba and Sr.[35]

$$\chi(k) = S_0^2 \sum_j \frac{N_j F_j(k_j) \exp(-2k_j{}^2\sigma_j^2)}{k_j r_j^2} \sin(2k_j r_j + \emptyset_j(k)) \quad (6\text{-}1)$$

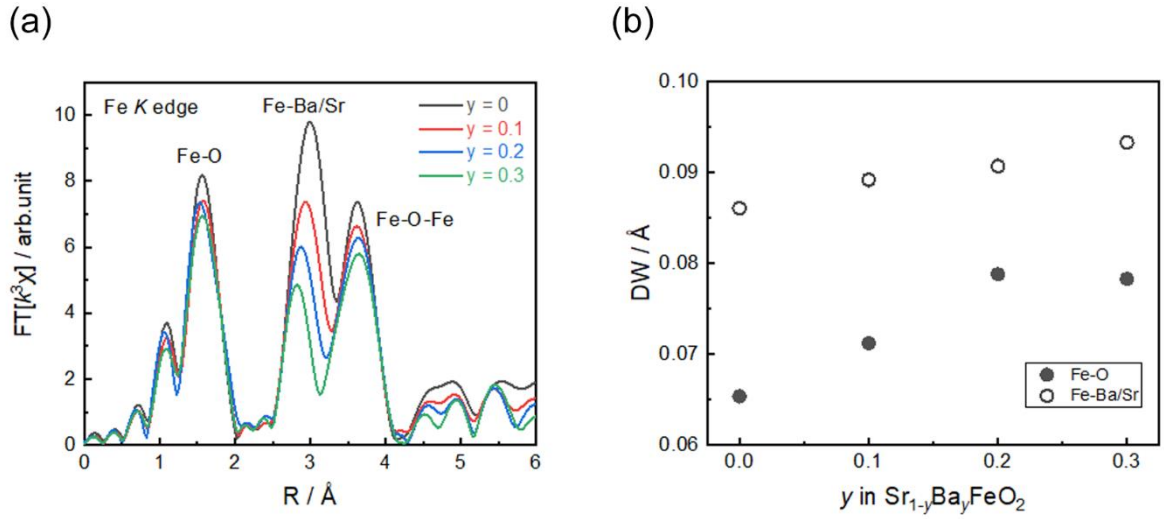

Figure 6.8 (a) Fourier transforms of the Fe K-edge EXAFS of $Sr_{1-y}Ba_yFeO_2$ (y = 0 ~ 0.3). (b) Debye–Waller factor of Fe – O and Fe – Ba/Sr calculated from the Fe K-edge EXAFS analysis as a function of Ba content.

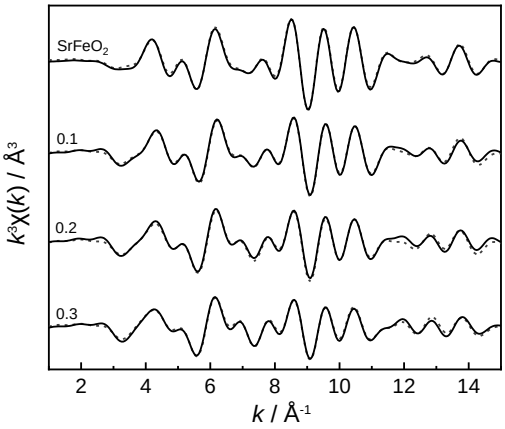

Figure 6.9 Results of the curve-fitting procedure for inverse Fourier transform spectra of Fe K-edge EXAFS.

Figure 6.8b shows the Debye-Waller (DW) factor of the Fe-Ba/Sr shells calculated by the EXAFS fitting as a function of Ba content, each sample was fitted well using an

infinite-layer structure (Figure 6.9). The DW factor of the first two shells increased with increasing Ba content, however, the Fe-Ba/Sr shell showed a more significant increment in static distortion.

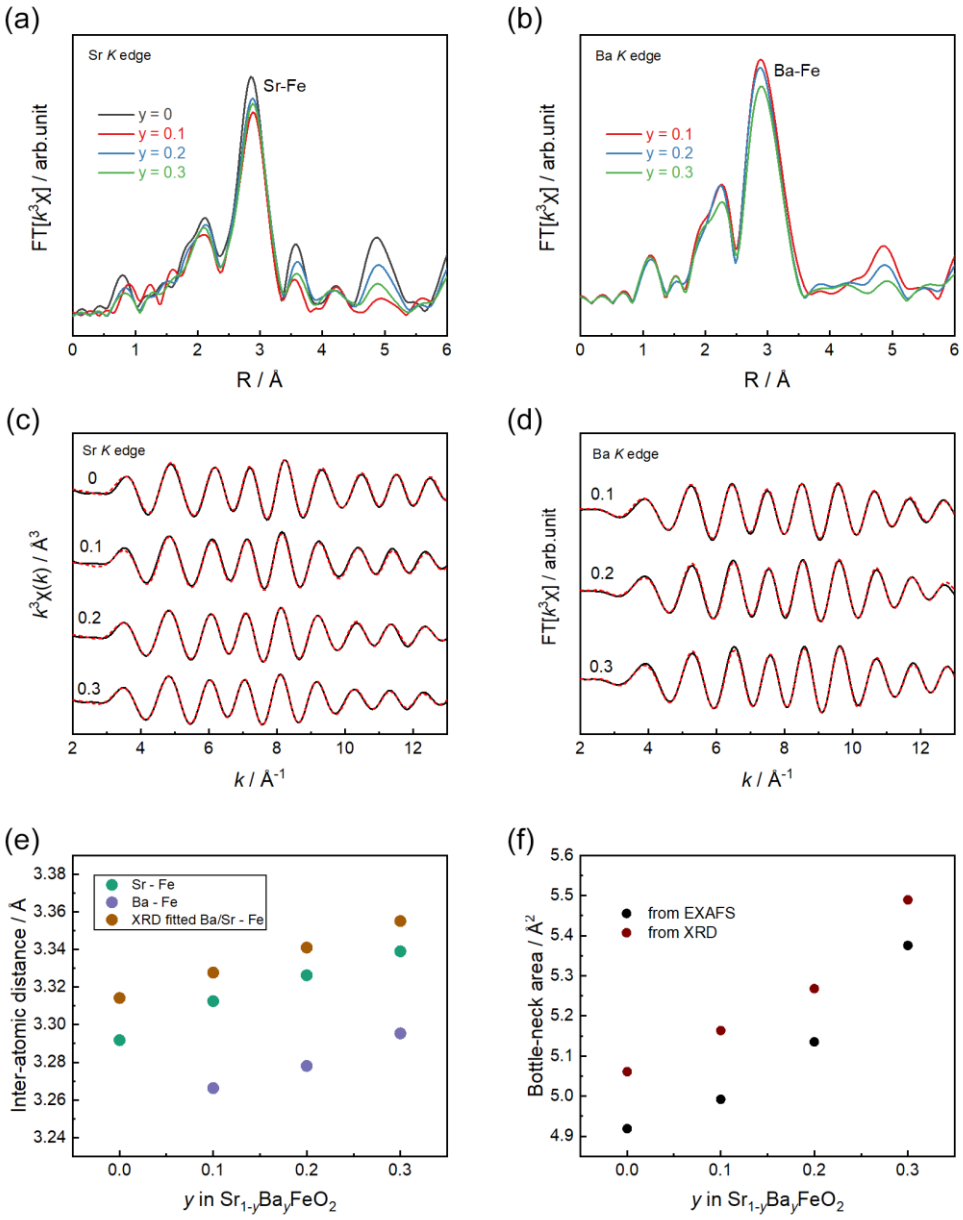

Figure 6.10 Fourier transforms of the (a) Sr, (b) Ba K-edge EXAFS of $Sr_{1-y}Ba_yFeO_2$ (y = 0 ~ 0.3). Results of the curve-fitting procedure for inverse Fourier transform spectra of (c) Sr, (d)Ba K-edge EXAFS. (e) Inter-atomic distance of Sr – Fe and Ba – Fe fitted from synchrotron XRD and EXAFS. (f) The bottle-neck size calculated from Figure 6.10 (e).

The RSFs of the Sr and Ba *K*-edge EXAFS of $Sr_{1-y}Ba_yFeO_2$ compounds is shown in Figure 6.10a-d. The main peak located at around 2.9 Å is corresponded to the signal from the second nearest coordination Sr/Ba – Fe shells. The fitting results of the EXAFS show that the inter-atomic distances of Sr/Ba – Fe lengthens as the Ba content increases, which is consistent with the results of XRD refinement (Figure 6.10e). It is commonly believed that anions migrate along the edges of the MO_6 octahedron in perovskite-type materials (Figure 6.11), so we calculated the bottle-neck area size for fluoride ion diffusion in the $Sr_{1-y}Ba_yFeO_2$ cathodes using the EXAFS fitted interatomic distance. [36, 37] The calculated results suggest that the bottle-neck area increases significantly with the amount of Ba substitution (Figure 6.10f), we believe that this modification enhances the diffusion capacity of fluoride ions.

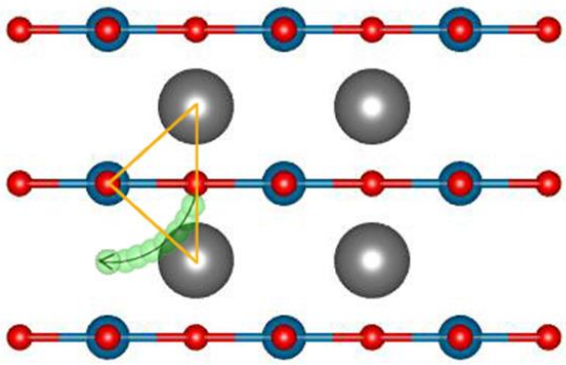

Figure 6.11 Schematic figure for the model of local structure and the bottle-neck for fluoride ion conduction in $Sr_{1-y}Ba_yFeO_2$ compounds ($0 < x < 0.4$) with infinite-layer structure.

6.4 Conclusion

In this study, we synthesized a series of $Sr_{1-y}Ba_yFeO_2$ compounds and tested their electrochemical properties as cathode materials for all-solid-state FIBs. It is known from high-resolution synchrotron XRD measurements that the crystal structure of the $Sr_{1-y}Ba_yFeO_2$ compound changes from an infinite-layer structure to a $LaNiO_{2.5}$-like structure with oxygen defects after 30% Ba substitution. The results of electrochemical testing show that only the $Sr_{1-y}Ba_yFeO_2$ compounds with an infinite-layer structure can

achieve high capacity by inserting excess amount of fluoride ions, and using the charge compensation of iron and oxygen as in the case of $SrFeO_2$. Moreover, $Sr_{0.7}$ $Ba_{0.3}FeO_2$ possesses the best rate capability among them, and the capacity achievement increased from 41% to 64% compared to $SrFeO_2$ at a current density of 200 mA g^{-1}. The bottle-neck area for fluoride-ion diffusion was calculated from the interatomic distances obtained by EXAFS analysis, and the bottle-neck area size increased with the substitution of Ba with larger ionic radius, ensuring faster ion conduction. We believe that the high-rate performance of cathodes for all-solid-state FIBs could be achieved by the local structure modification.

Reference

1. Tarascon, J., The Li-ion battery: 25 years of exciting and enriching experiences. *Electrochem. Soc. Interface.* **2016,** *25* (3), 79.
2. Korthauer, R., *Handbuch lithium-ionen-batterien*. Springer: 2013.
3. Janek, J.; Zeier, W. G., A solid future for battery development. *Nat. Energy* **2016,** *1* (9).
4. Palomares, V.; Serras, P.; Villaluenga, I.; Hueso, K. B.; Carretero-González, J.; Rojo, T., Na-ion batteries, recent advances and present challenges to become low cost energy storage systems. *Energy Environ. Sci.* **2012,** *5* (3).
5. Yoo, H. D.; Shterenberg, I.; Gofer, Y.; Gershinsky, G.; Pour, N.; Aurbach, D., Mg rechargeable batteries: an on-going challenge. *Energy Environ. Sci.* **2013,** *6* (8).
6. Gao, P.; Reddy, M. A.; Mu, X.; Diemant, T.; Zhang, L.; Zhao-Karger, Z.; Chakravadhanula, V. S.; Clemens, O.; Behm, R. J.; Fichtner, M., VOCl as a Cathode for Rechargeable Chloride Ion Batteries. *Angew. Chem. Int. Ed. Engl.* **2016,** *55* (13), 4285-90.
7. Zhao, X.; Zhao-Karger, Z.; Wang, D.; Fichtner, M., Metal oxychlorides as cathode materials for chloride ion batteries. *Angew. Chem. Int. Ed. Engl.* **2013,** *52* (51), 13621-4.
8. Anji Reddy, M.; Fichtner, M., Batteries based on fluoride shuttle. *J. Mater. Chem.* **2011,** *21* (43).
9. Zhang, D.; Yamamoto, K.; Wang, Y.; Gao, S.; Uchiyama, T.; Watanabe, T.;

Takami, T.; Matsunaga, T.; Nakanishi, K.; Miki, H.; Iba, H.; Amezawa, K.; Maeda, K.; Kageyama, H.; Uchimoto, Y., Reversible and Fast (De)fluorination of High-Capacity Cu_2O Cathode: One Step Toward Practically Applicable All-Solid-State Fluoride-Ion Battery. *Adv. Energy Mater.* **2021,** *11* (45).

10. Nowroozi, M. A.; Wissel, K.; Rohrer, J.; Munnangi, A. R.; Clemens, O., $LaSrMnO_4$: Reversible Electrochemical Intercalation of Fluoride Ions in the Context of Fluoride Ion Batteries. *Chem. Mater.* **2017,** *29* (8), 3441-3453.
11. Rongeat, C.; Anji Reddy, M.; Diemant, T.; Behm, R. J.; Fichtner, M., Development of new anode composite materials for fluoride ion batteries. *J. Mater. Chem. A* **2014,** *2* (48), 20861-20872.
12. Thieu, D. T.; Fawey, M. H.; Bhatia, H.; Diemant, T.; Chakravadhanula, V. S. K.; Behm, R. J.; Kübel, C.; Fichtner, M., CuF_2 as reversible cathode for fluoride ion batteries. *Adv. Funct. Mater.* **2017,** *27* (31), 1701051.
13. Zhang, D.; Yamamoto, K.; Ochi, A.; Wang, Y.; Yoshinari, T.; Nakanishi, K.; Nakano, H.; Miki, H.; Nakanishi, S.; Iba, H.; Uchiyama, T.; Watanabe, T.; Amezawa, K.; Uchimoto, Y., Understanding the reaction mechanism and performances of 3d transition metal cathodes for all-solid-state fluoride ion batteries. *J. Mater. Chem. A* **2021,** *9* (1), 406-412.
14. Nowroozi, M. A.; Ivlev, S.; Rohrer, J.; Clemens, O., La_2CoO_4: a new intercalation based cathode material for fluoride ion batteries with improved cycling stability. *J. Mater. Chem. A* **2018,** *6* (11), 4658-4669.
15. Wissel, K.; Heldt, J.; Groszewicz, P. B.; Dasgupta, S.; Breitzke, H.; Donzelli,

M.; Waidha, A. I.; Fortes, A. D.; Rohrer, J.; Slater, P. R.; Buntkowsky, G.; Clemens, O., Topochemical Fluorination of La_2NiO_{4+d}: Unprecedented Ordering of Oxide and Fluoride Ions in $La_2NiO_3F_2$. *Inorg. Chem.* **2018,** *57* (11), 6549-6560.

16. Nowroozi, M. A.; Wissel, K.; Donzelli, M.; Hosseinpourkahvaz, N.; Plana-Ruiz, S.; Kolb, U.; Schoch, R.; Bauer, M.; Malik, A. M.; Rohrer, J.; Ivlev, S.; Kraus, F.; Clemens, O., High cycle life all-solid-state fluoride ion battery with La_2NiO_{4+d} high voltage cathode. *Commun. Mater.* **2020,** *1* (1).
17. Wissel, K.; Schoch, R.; Vogel, T.; Donzelli, M.; Matveeva, G.; Kolb, U.; Bauer, M.; Slater, P. R.; Clemens, O., Electrochemical Reduction and Oxidation of Ruddlesden–Popper-Type $La_2NiO_3F_2$ within Fluoride-Ion Batteries. *Chem. Mater.* **2021,** *33* (2), 499-512.
18. Wang, Y.; Yamamoto, K.; Tsujimoto, Y.; Matsunaga, T.; Zhang, D.; Cao, Z.; Nakanishi, K.; Uchiyama, T.; Watanabe, T.; Takami, T.; Miki, H.; Iba, H.; Maeda, K.; Kageyama, H.; Uchimoto, Y., Anion Substitution at Apical Sites of Ruddlesden–Popper-type Cathodes toward High Power Density for All-Solid-State Fluoride-Ion Batteries. *Chem. Mater.* **2022,** *34* (2), 609-616.
19. Orikasa, Y.; Nakao, T.; Oishi, M.; Ina, T.; Mineshige, A.; Amezawa, K.; Arai, H.; Ogumi, Z.; Uchimoto, Y., Local structural analysis for oxide ion transport in $La_{0.6}Sr_{0.4}FeO_{3-\delta}$ cathodes. *J. Mater. Chem.* **2011,** *21* (36).
20. Sanson, A.; Rocca, F.; Armellini, C.; Dalba, G.; Fornasini, P.; Grisenti, R., Correlation between I-Ag distance and ionic conductivity in AgI fast-ion-conducting glasses. *Phys. Rev. Lett.* **2008,** *101* (15), 155901.

21. Yamamoto, T.; Kobayashi, Y.; Hayashi, N.; Tassel, C.; Saito, T.; Yamanaka, S.; Takano, M.; Ohoyama, K.; Shimakawa, Y.; Yoshimura, K.; Kageyama, H., $(Sr_{(1-x)}Ba_{(x)})FeO_2$ ($0.4 \leq x \leq 1$): a new oxygen-deficient perovskite structure. *J. Am. Chem. Soc.* **2012,** *134* (28), 11444-54.

22. Yamamoto, T.; Li, Z.; Tassel, C.; Hayashi, N.; Takano, M.; Isobe, M.; Ueda, Y.; Ohoyama, K.; Yoshimura, K.; Kobayashi, Y.; Kageyama, H., Synthesis and thermal stability of the solid solution $AFeO_2$ (A = Ba, Sr, Ca). *Inorg. Chem.* **2010,** *49* (13), 5957-62.

23. Tsujimoto, Y.; Tassel, C.; Hayashi, N.; Watanabe, T.; Kageyama, H.; Yoshimura, K.; Takano, M.; Ceretti, M.; Ritter, C.; Paulus, W., Infinite-layer iron oxide with a square-planar coordination. *Nature* **2007,** *450* (7172), 1062-5.

24. Rongeat, C.; Reddy, M. A.; Witter, R.; Fichtner, M., Solid electrolytes for fluoride ion batteries: ionic conductivity in polycrystalline tysonite-type fluorides. *ACS Appl. Mater. Interfaces* **2014,** *6* (3), 2103-10.

25. Petříček, V.; Dušek, M.; Palatinus, L., Crystallographic computing system JANA2006: general features. *Zeitschrift für Kristallographie-Crystalline Materials* **2014,** *229* (5), 345-352.

26. Momma, K.; Izumi, F., VESTA 3 for three-dimensional visualization of crystal, volumetric and morphology data. *J.Appl. crystallogr.* **2011,** *44* (6), 1272-1276.

27. Ravel, B.; Newville, M., ATHENA, ARTEMIS, HEPHAESTUS: data analysis for X-ray absorption spectroscopy using IFEFFIT. *J. Synchrotron Radiat.* **2005,** *12* (4), 537-541.

28. Berry, F. J.; Heap, R.; Helgason, Ö.; Moore, E. A.; Shim, S.; Slater, P. R.; Thomas, M. F., Magnetic order in perovskite-related $SrFeO_2F$. *J. Phys. Condens. Matter.* **2008,** *20* (21).

29. Blakely, C. K.; Davis, J. D.; Bruno, S. R.; Kraemer, S. K.; Zhu, M.; Ke, X.; Bi, W.; Alp, E. E.; Poltavets, V. V., Multistep synthesis of the $SrFeO_2F$ perovskite oxyfluoride via the $SrFeO_2$ infinite-layer intermediate. *J. Fluor. Chem.* **2014,** *159*, 8-14.

30. Yabuuchi, N.; Nakayama, M.; Takeuchi, M.; Komaba, S.; Hashimoto, Y.; Mukai, T.; Shiiba, H.; Sato, K.; Kobayashi, Y.; Nakao, A.; Yonemura, M.; Yamanaka, K.; Mitsuhara, K.; Ohta, T., Origin of stabilization and destabilization in solid-state redox reaction of oxide ions for lithium-ion batteries. *Nat. Commun.* **2016,** *7*, 13814.

31. Yamamoto, K.; Zhou, Y.; Yabuuchi, N.; Nakanishi, K.; Yoshinari, T.; Kobayashi, T.; Kobayashi, Y.; Yamamoto, R.; Watanabe, A.; Orikasa, Y.; Tsuruta, K.; Park, J.; Byon, H. R.; Tamenori, Y.; Ohta, T.; Uchimoto, Y., Charge Compensation Mechanism of Lithium-Excess Metal Oxides with Different Covalent and Ionic Characters Revealed by Operando Soft and Hard X-ray Absorption Spectroscopy. *Chem. Mater.* **2019,** *32* (1), 139-147.

32. House, R. A.; Maitra, U.; Perez-Osorio, M. A.; Lozano, J. G.; Jin, L.; Somerville, J. W.; Duda, L. C.; Nag, A.; Walters, A.; Zhou, K. J.; Roberts, M. R.; Bruce, P. G., Superstructure control of first-cycle voltage hysteresis in oxygen-redox cathodes. *Nature* **2020,** *577* (7791), 502-508.

33. House, R. A.; Rees, G. J.; Pérez-Osorio, M. A.; Marie, J.-J.; Boivin, E.; Robertson,

A. W.; Nag, A.; Garcia-Fernandez, M.; Zhou, K.-J.; Bruce, P. G., First-cycle voltage hysteresis in Li-rich 3d cathodes associated with molecular O_2 trapped in the bulk. *Nat. Energy* **2020,** *5* (10), 777-785.

34. Shannon, R. D., Revised effective ionic radii and systematic studies of interatomic distances in halides and chalcogenides. *Acta crystallographica section A: crystal physics, diffraction, theoretical and general crystallography* **1976,** *32* (5), 751-767.
35. Ashley, C.; Doniach, S., Theory of extended x-ray absorption edge fine structure (EXAFS) in crystalline solids. *Phys. Rev., B* **1975,** *11* (4), 1279.
36. Yashima, M.; Tsuji, T., Structural investigation of the cubic perovskite-type doped lanthanum cobaltite $La_{0.6}Sr_{0.4}CoO_{3-\delta}$ at 1531 K: possible diffusion path of oxygen ions in an electrode material. *J. Appl. Crystallogr.* **2007,** *40* (6), 1166-1168.
37. Yashima, M.; Kamioka, T., Neutron diffraction study of the perovskite-type lanthanum cobaltite $La_{0.6}Sr_{0.4}Co_{0.8}Fe_{0.2}O_{3-\delta}$ at 1260° C and 394° C. *Solid State Ionics* **2008,** *178* (39-40), 1939-1943.

Chapter 7. Properties of composite electrodes for all-solid-state fluoride-ion secondary batteries processed by high-pressure torsion

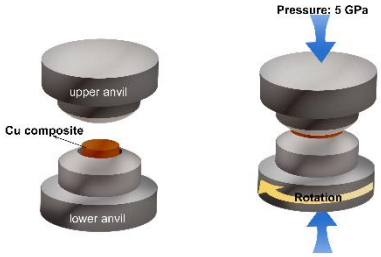

All-solid-state fluoride-ion batteries (FIBs) using metal/metal fluorides are expected to be the next generation of storage batteries because they exhibit high volumetric energy densities by utilizing multielectron reactions, compared to the current lithium-ion batteries. However, method of fabricating a composite electrode for all-solid-state fluoride-ion batteries has not yet been established. A fabrication method for a composite electrode that disperses the active material and solid electrolyte is required. To approach this problem, in this study, we employed a high-pressure torsion (HPT) method, in which an active material, solid electrolyte, and conductive agent can be mixed with size reduction, as a new process and prepared Cu (active material)/$PbSnF_4$ (solid electrolyte)/acetylene black (conductive agent) cathode composites. The crystalline sizes of Cu and $PbSnF_4$ were significantly reduced. The grain boundary resistance was also reduced owing to the more homogeneous distribution in the cathode composites after HPT processing. These structural and morphological changes led to high electrochemical performances, compared to a cathode composite without HPT.

7.1 Introduction

Reducing carbon dioxide emissions is a crucial issue that must be addressed to realize a sustainable society. Full-scale diffusion of electric vehicles (EVs) is required to achieve this goal. As the mainstream power source of EVs, the current lithium-ion batteries (LIBs) are approaching their theoretical limitation in terms of volumetric energy density, and thus it is essential to improve the volumetric energy density of rechargeable batteries for popularity of EVs.[1–3]

To address the demand for batteries with high energy and power densities, a series of candidates that employ Na^+, K^+, Mg^{2+}, Zn^{2+}, Al^{3+}, F^-, or Cl^- as charge carriers have been developed.[4–11] Among them, all-solid-state fluoride-ion batteries (FIBs) using fluoride ions as carriers have attracted widespread attention because of the high volumetric energy density and safety.[11–17] In all-solid-state FIBs, metal/metal fluoride electrodes such as Cu/CuF_2 and Bi/BiF_3 can achieve large capacities using multielectron reactions (Bi/BiF_3: 385 mA h g^{-1} to Bi; Cu/CuF_2: 843 mA h g^{-1} to Cu).[11] Therefore, it is theoretically possible to achieve a high volumetric energy density over 5000 W h L^{-1},[15] which significantly exceeds that of LIB-based systems, by employing combinations of appropriate cathodes and anodes. To fabricate the composite electrode for this battery, the metal active material and solid electrolyte fluoride must be mixed uniformly for the discharge-initiated battery. However, method for this purpose has not yet been established.

It has been reported that diffusion length reduction of fluoride ions in the active material[16] and formation of a good fluoride ion path in the composite electrode[18] are effective approaches to overcome these problems using thin-film model batteries.[15,19] However, for bulk-type battery fabrication, it is necessary to establish a process that can produce fine particles of a powdered active material and form good fluoride ion paths in the composite electrode. Hence, in this study, we focused on high-pressure torsion (HPT) processing, which can effectively refine metal grains and mix metal grains with other materials through the high shear stress generated during the

processing,[20, 21] and used this method to prepare Cu/$PbSnF_4$ solid electrolyte/acetylene black (AB) cathode composites for all-solid-state fluoride batteries. The HPT treatment is effective to prepare refined Cu and $PbSnF_4$ particles and uniformly mixed Cu/$PbSnF_4$/AB cathode composites, which exhibit excellent electrochemical properties. We believe that the HPT treatment will be an important process technology in the preparation of composite electrodes with excellent electrochemical performances for FIBs.

7.2 Experimental

7.2.1 Material preparation

A commercial Cu nano powder (99.8%, US Research Nanomaterials) was used as an active material. A $PbSnF_4$ solid electrolyte was prepared by a conventional solid-state reaction.[17] Stoichiometric amounts of PbF_2 (99.9%, Kojundo, Japan) and SnF_2 (99%, Kojundo, Japan) were thoroughly ground using an agate mortar, and then transferred to a ZrO_2 pod in an Ar-filled glove box. The mixture was milled using planetary ball mills (Fritsch Pulverisette7 premium line, Germany) with a rotation speed of 600 rpm for 12 h. The ball-milled mixture was transferred to the glove box and sintered at 400 ℃ for 1 h. A cathode composite was prepared by mixing the Cu nano powder, $PbSnF_4$ solid electrolyte, and AB, pre-dried under vacuum, in a mass ratio of 40:55:5 by ball milling at 100 rpm for 12 h. The as-prepared cathode composite was pressed into pellets under 180 MPa for 3 min for HPT processing.

7.2.2 HPT process

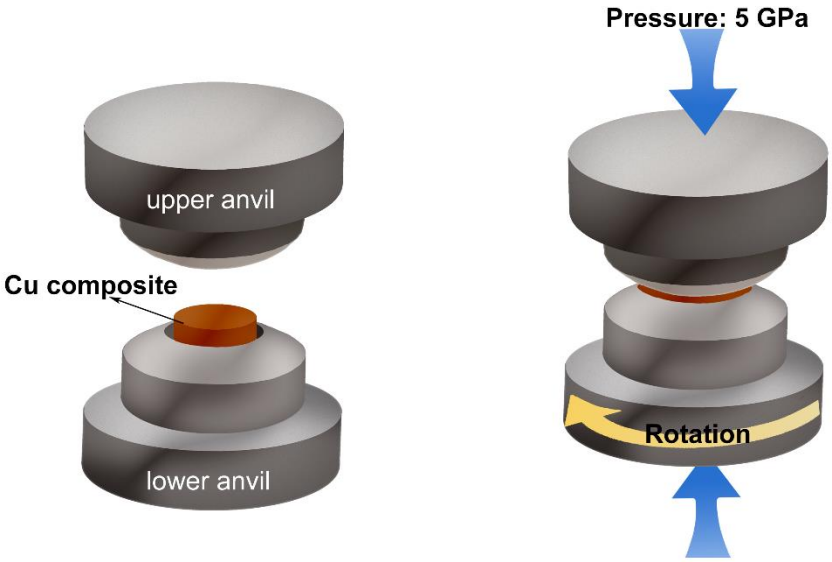

Figure 7.1 Schematic of the HPT process.

The HPT processing illustrated in Fig. 7.1 could introduce large shear strains on a disk-shaped sample.[22] A disk sample with a diameter of 10 mm and thickness of approximately 1 mm was placed between two anvils. A high pressure, typically 5 GPa, was then applied. The lower anvil was rotated under the high pressure. The sample was slightly thicker than the recess on the anvils. A part of the sample flows out into the space between the anvils, which seals the sample. Thus, the sample can be deformed under a quasi-hydrostatic pressure, which minimizes the cracking during straining. In this study, disk pellets of the cathode composite were prepared by cold compaction. They were deformed by HPT under an applied pressure of 5 GPa with an anvil rotation speed of 1 rpm. The number of anvil rotations (N) was 5, 10, 20, 30, and 50. The cathode composites subjected to different N of HPT are hereafter referred to as HPT-0, 5, 10, 20, 30, and 50.

7.2.3 X-ray diffraction (XRD), scanning electron microscopy (SEM), and energy-dispersive X-ray (EDX) spectroscopy mapping

XRD patterns of the cathode composite after HPT with different rotation numbers were acquired using an XRD instrument (Rigaku Ultima IV, Japan) with Cu K_α radiation (λ = 1.54056 Å). The microstructures of cross sections of the cathode composites after HPT with different rotation numbers were observed. The cathode composites were cut into half, mounted in the resin, and mechanically polished. Their morphological structures were observed using a Zeiss Auriga focused-ion beam (FIB)-SEM instrument with an operation voltage of 15 kV in the back-scattered electron mode. In addition, elemental mapping was performed using EDX spectroscopy with an EDAX Octane Elite instrument, equipped on the same FIB-SEM.

7.2.4 Electrochemical measurement

The ionic conductivities of the cathode composites after HPT processing with different rotation numbers were measured using an electron-blocking cell, as shown in Fig. 7.2.[23, 24] The cathode composite was placed into the cell and pressed with a pressure of 180 MPa for 3 min. The $PbSnF_4$ powder was then placed on the opposite side of the cathode composite pellet and pressed under a pressure of 180 MPa for 5 min. Electrochemical impedance spectra were acquired using a ModuLab XM ECS test system (Solartron Analytical) in the frequency range of 0.1 MHz to 10 mHz. The obtained data were fitted using the software ZView4 (Scribner and Associates).

An electrochemical measurement of each cathode composite was performed using a typical bulk-type cell. The $PbSnF_4$ powder was placed into the cell and pressed with a pressure of 90 MPa for 5 min. The cathode composite and Pb foil (99.9%, Nilaco, Japan) were placed on the opposite side of the $PbSnF_4$ pellet and pressed under a pressure of 360 MPa for 5 min. Finally, the cathode composite/$PbSnF_4$/Pb foil was

sandwiched by two pieces of Au foil as current collectors. A galvanostatic charge/discharge test was performed using an HJ1010SD8 (Hokuto Denko Corporation) electrochemical workstation. The cutoff voltage was set to 0.3–1.25 V vs. Pb/PbF_2, and a current density of 8 mA g^{-1} was employed to evaluate the cycling stabilities at 140 ℃.

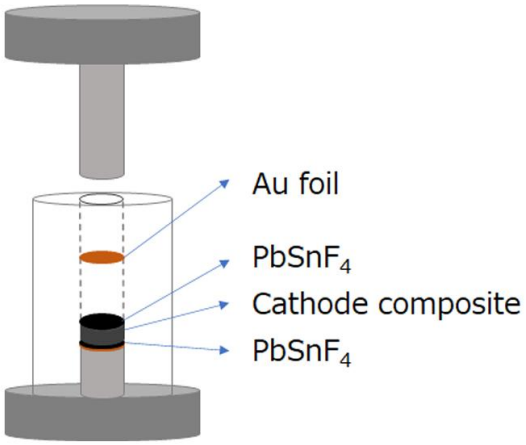

Figure 7.2 Illustration of the testing cell for EIS measurement.

7.3 Result and discussion

7.3.1 Morphological changes after HPT processing

To investigate the crystal structure of each component in the cathode composites after the HPT processing, we measured XRD patterns of the composites with different rotation numbers (*N*) of HPT processing (Fig. 7.3a). All peaks in the XRD pattern of the cathode composite without HPT processing (HPT-0) were indexed to Cu (space group: *Fm*-3*m*), $PbSnF_4$ (space group: $P4_2/n$), and Cu_2O impurity (space group: *Pn*-3*m*). After HPT processing, the peaks attributed to Cu were slightly broadened with the increase in *N*. The lattice parameters of Cu in the cathode composites were not changed with the increase in *N* (Fig. 7.4), which indicates that the chemical composition of Cu was not changed after the HPT. In contrast to Cu in the cathode composite, the peaks attributed to $PbSnF_4$ were largely broadened. Particularly, the peaks attributed to

$PbSnF_4$ almost disappeared for HPT-50. To evaluate the effects on the crystalline sizes of Cu and $PbSnF_4$ in the cathode composite with the HPT processing, we estimated each material's crystalline size by applying the Scherrer equation to the 220 peak of Cu and 102 peak of $PbSnF_4$ (Fig. 7.3b). The crystalline size of Cu was decreased from 35 to 15 nm from $N = 0$ to $N = 20$, and then was almost constant with the increase in N from 20 to 50. In contrast to Cu, the crystalline size of $PbSnF_4$ was largely decreased from 400 to 100 nm with the increase in N from 0 to 5, and then gradually decreased from 100 to 50 nm with the increase in N from 5 to 30. Finally, the crystalline size of $PbSnF_4$ was decreased to 20 nm in HPT-50.

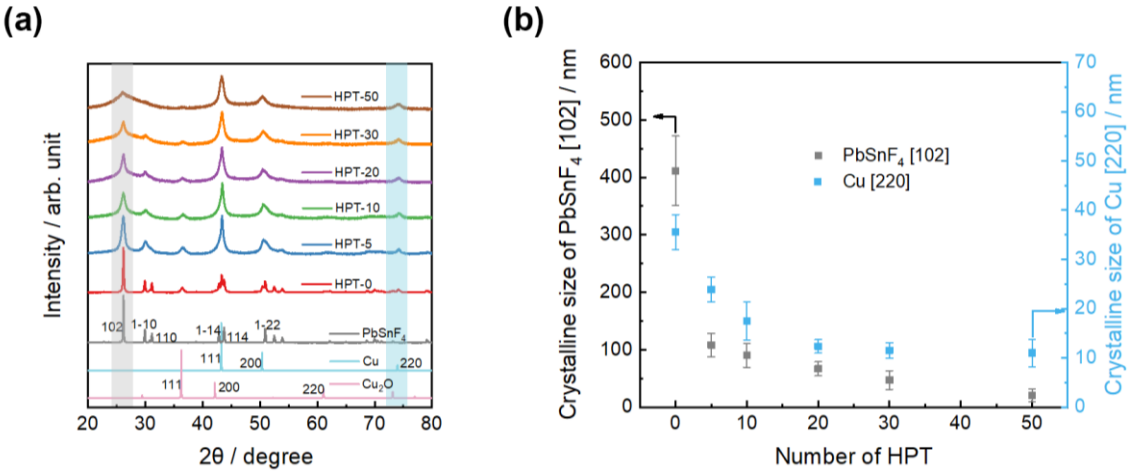

Figure 7.3 (a) XRD patterns and (b) crystalline sizes of Cu and $PbSnF_4$ in the cathode composites with different HPT rotation numbers. The crystalline sizes of Cu and $PbSnF_4$ were calculated by the $PbSnF_4$ [102] and Cu [220] peaks using the Scherrer's equation.

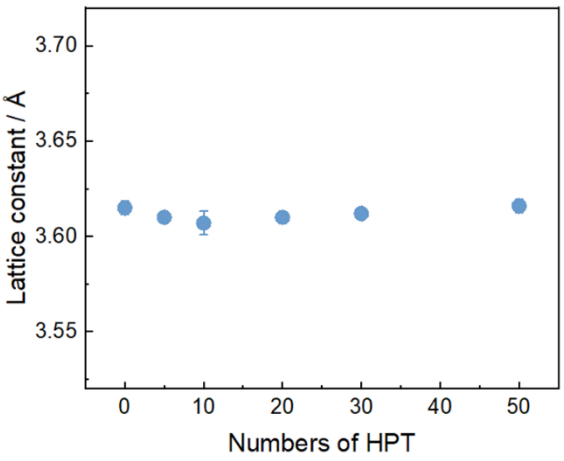

Figure 7.4 Lattice constant of Cu in the cathode composite after HPT processing with different rotation numbers.

The morphologies of the cathode composites before and after HPT with different anvil rotation numbers (N) were analyzed by SEM-EDX measurements. Fig. 7.5 shows the EDX elemental mapping of the Cu-$PbSnF_4$-AB composite after the HPT treatment. The elemental maps of Sn and F exhibit similar tendencies to that of Pb; thus, the Pb-rich area can be regarded as $PbSnF_4$ phase. Before the HPT processing (N = 0), the $PbSnF_4$ particles with sizes of a few micrometers were inhomogeneously distributed in the Cu matrix. With the increase in N to 10, the $PbSnF_4$ particles became more fragmented into smaller particles due to the HPT deformation and finely distributed in the Cu matrix. In the samples with N = 20 and 30, the $PbSnF_4$ particles became finer and more dispersed throughout the Cu active material. At N = 50, although the agglomerated Cu particles remained, the distribution of $PbSnF_4$ was very uniform. The carbon was uniformly distributed regardless of the degree of HPT. The SEM-EDX results indicate that, after the HPT processing, the particle size of the solid electrolyte was significantly reduced and that Cu, $PbSnF_4$, and AB were more homogenously

distributed in the cathode composites.

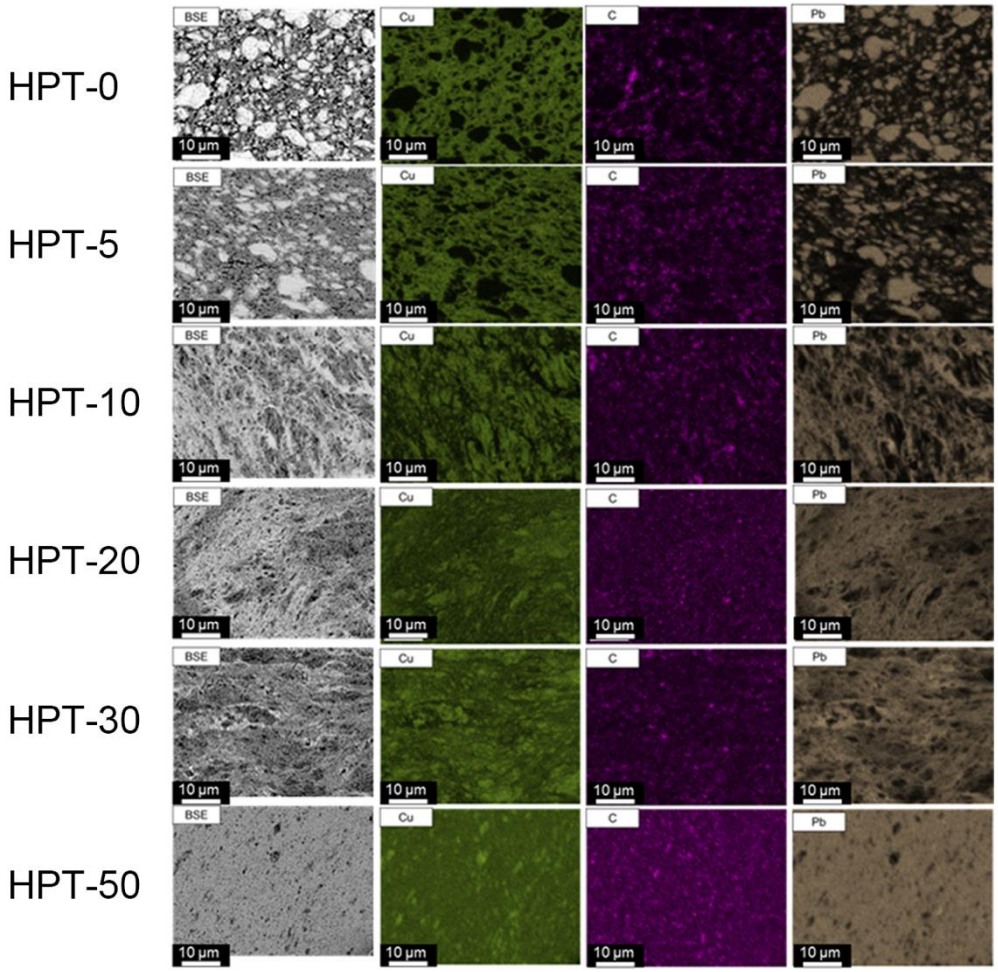

Figure 7.5. EDX mapping of the cathode composites after HPT processing with different anvil rotation numbers *N*.

7.3.2 Changes in the ionic conductivity with the HPT processing

To quantify the effect of the HPT processing on the fluoride-ion diffusion in the cathode composites, the fluoride ion conductivity of the composite was measured using the electron blocking method. Fig. 7.6a and Fig. 7.7 show Nyquist plots for each cathode composite in the range of 25 to 125 °C. A half semicircle was observed in each composite's spectrum. The magnitude of the semicircle decreased from $N = 0$ to $N = 40$, whereas it increased from $N = 40$ to $N = 50$. To quantitatively analyze the impedance spectra, the spectra were fitted with an equivalent circuit, as shown in Fig. 7.6b.[25] The obtained fitting parameters are shown in Table 7.1. The semicircle was attributed to the grain boundary resistance because the obtained capacitance values of the semicircle in each spectrum were in the range of 10^{-11} to 10^{-8} F.[26] Arrhenius plots of the grain boundary resistance and activation energies calculated by the plots for each cathode composite are shown in Fig. 7.6c and 7.6d.

The ionic conductivity of the grain boundary was increased, while its activation energy was decreased from $N = 0$ to $N = 30$, as the crystalline sizes of Cu and $PbSnF_4$ were reduced (Fig. 7.3) and Cu, $PbSnF_4$, and AB were more homogenously distributed in the cathode composites with reduced particle sizes of $PbSnF_4$ (Fig. 7.5). In contrast to the behavior from $N = 0$ to $N = 30$, the ionic conductivity of the grain boundary was decreased, and its activation energy was increased from $N = 30$ to $N = 50$, likely owing to the amorphization of $PbSnF_4$ by excessive HPT processing (Fig. 7.3) as the ionic conductivity of a solid electrolyte is largely influenced by its crystallnitiy.[27]

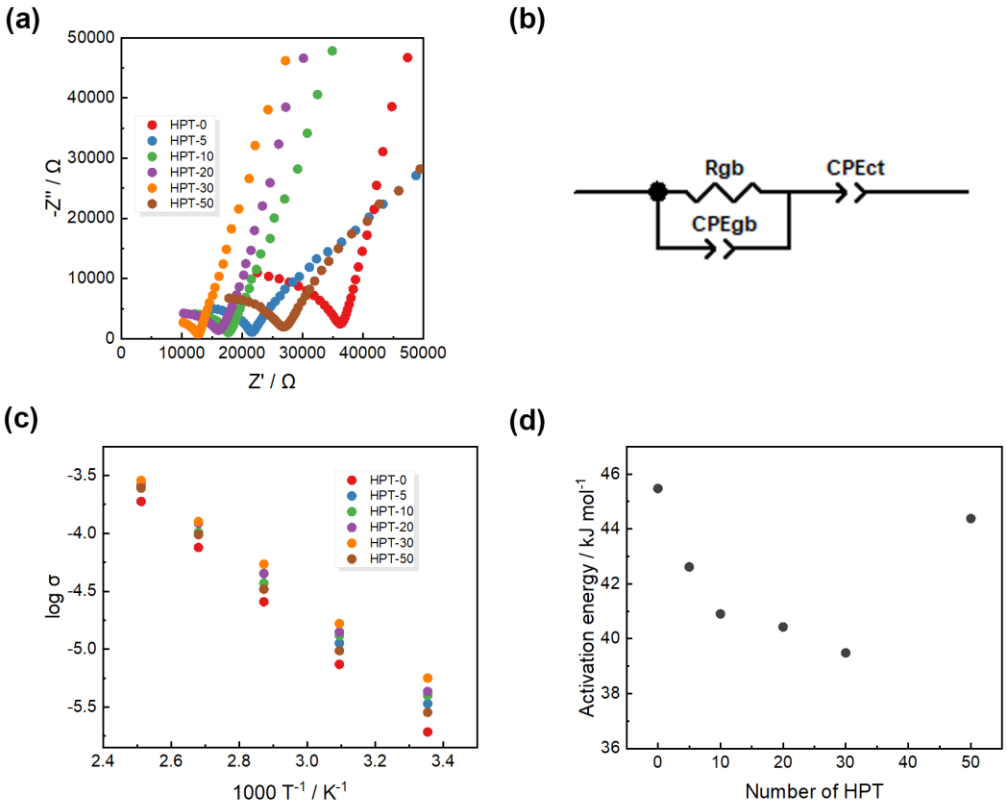

Figure 7.6. (a) Nyquist plots at 25 °C for the cathode composite after the HPT processing with different rotation numbers. (b) Equivalent circuit used for the electrochemical impedance spectroscopy (EIS) fitting. (c) Arrhenius plots for the ionic conductivity of the grain boundary in the cathode composite with the HPT processing: log σ vs. 1000 T^{-1}. (d) Activation energy calculated by the results in (c).

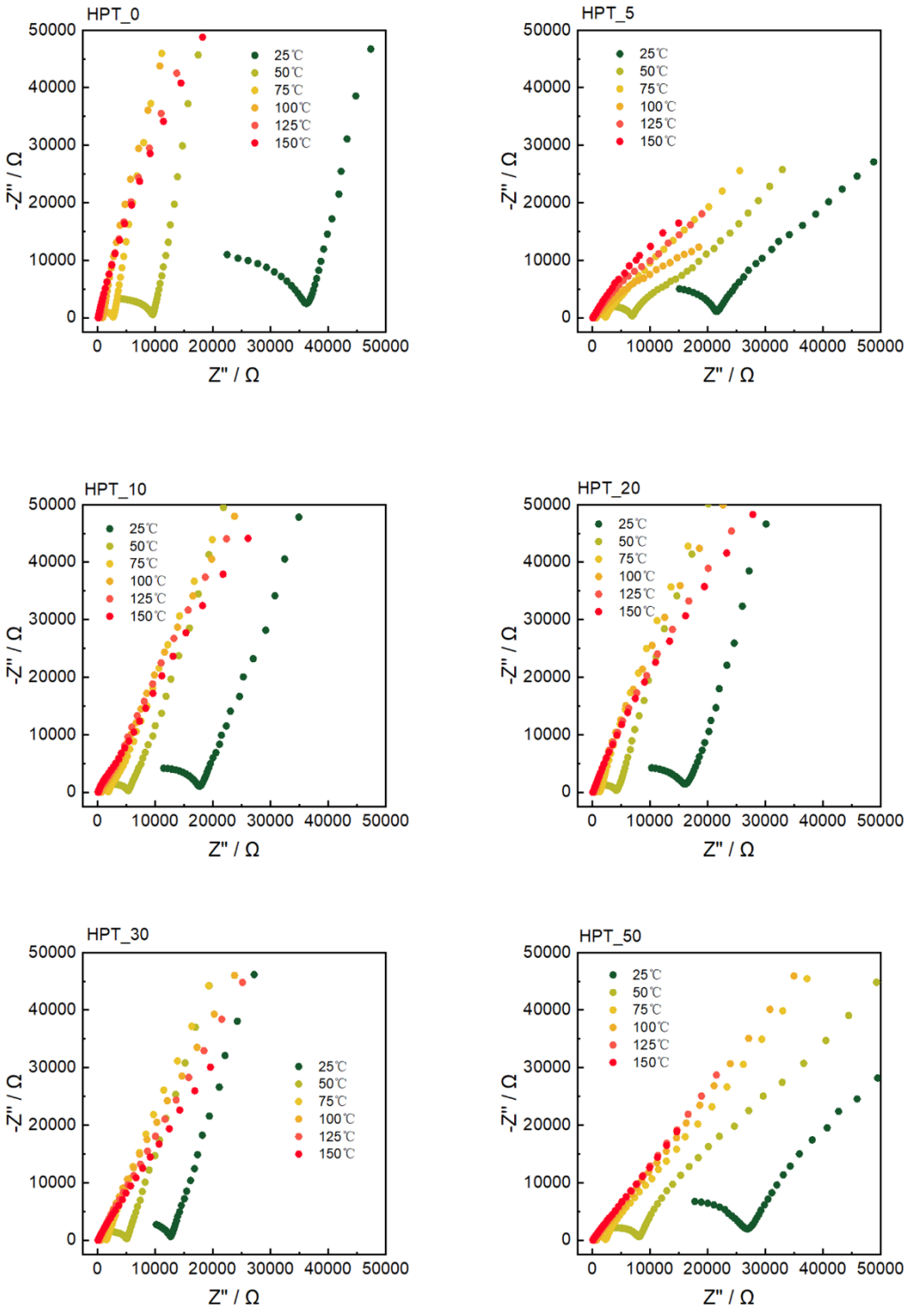

Figure 7.7 Nyquist plots of the cathode composites after HPT processing with different rotation numbers under 25, 50, 75, 100 and 125 ℃.

Table 7.1 The fitting parameters of the EIS results of the cathode composite after HPT processing with different rotation numbers.

Temperature	R2	CPE-T	CPE-P	Capacitance	CPE2-T	CPE2-P	Capacitance
HPT-0							
25	37500	9.29E-09	0.692	2.70E-10	1.45E-06	0.896	2.83E-07
50	9780	8.79E-09	0.724	2.47E-10	1.82E-06	0.891	3.32E-07
75	2820	4.96E-09	0.787	2.42E-10	2.29E-06	0.889	4.02E-07
100	957	1.02E-09	0.904	2.36E-10	2.98E-06	0.881	4.62E-07
125	382	1.94E-10	0.971	1.20E-10	4.45E-06	0.865	5.38E-07
HPT-5							
25	21400	1.15E-08	0.690	2.76E-10	1.45E-05	0.605	2.98E-08
50	6420	3.23E-09	0.798	2.12E-10	3.02E-05	0.571	3.67E-08
75	2190	2.46E-09	0.833	2.15E-10	2.17E-05	0.582	3.12E-08
100	724	5.72E-10	0.948	2.55E-10	3.51E-05	0.596	6.28E-08
125	287	1.28E-10	0.994	1.15E-10	4.30E-05	0.634	1.40E-07
HPT-10							
25	18200	2.77E-08	0.634	3.46E-10	6.56E-06	0.786	2.29E-07
50	5530	4.01E-08	0.614	2.00E-10	9.23E-06	0.778	2.85E-07
75	1950	1.53E-08	0.702	1.85E-10	1.29E-05	0.726	1.78E-07
100	709	1.83E-09	0.866	2.24E-10	1.66E-05	0.696	1.43E-07
125	285	1.97E-10	0.946	7.57E-11	2.07E-05	0.696	1.78E-07
HPT-20							
25	16800	3.86E-08	0.631	5.30E-10	3.72E-06	0.819	2.19E-07
50	4340	4.05E-08	0.656	4.35E-10	5.33E-06	0.808	2.63E-07
75	1330	6.70E-09	0.805	4.01E-10	7.32E-06	0.807	3.59E-07
100	572	1.36E-08	0.768	3.88E-10	1.02E-05	0.798	4.33E-07
125	276	4.92E-08	0.697	3.74E-10	1.55E-05	0.770	4.24E-07
HPT-30							
25	12800	1.09E-08	0.708	2.83E-10	4.59E-06	0.816	2.56E-07
50	5140	1.80E-08	0.679	2.24E-10	5.98E-06	0.797	2.48E-07
75	1610	1.80E-08	0.691	1.67E-10	8.85E-06	0.772	2.50E-07
100	590	6.19E-09	0.774	1.60E-10	1.37E-05	0.742	2.41E-07
125	252	6.91E-10	0.924	1.90E-10	2.16E-05	0.714	2.45E-07
HPT-50							
25	25400	5.48E-09	0.750	2.82E-10	8.05E-06	0.655	3.64E-08
50	7460	7.38E-09	0.734	2.09E-10	9.92E-06	0.657	4.65E-08
75	2200	4.28E-09	0.789	1.93E-10	1.29E-05	0.653	5.68E-08
100	741	3.55E-09	0.802	1.49E-10	2.20E-05	0.607	4.69E-08
125	293	1.92E-09	0.834	1.10E-10	3.49E-05	0.613	8.20E-08

7.3.3 Electrochemical performance

The electrochemical performances of the cathode composites after HPT processing with different rotation numbers were analyzed by the galvanostatic charge/discharge method, as shown in Fig. 7.8 and Supplementary Fig. 7.9. For all cathode composites, a single plateau was observed around 0.8 V during charging and 0.6 V during discharging. The shapes of the charge/discharge curves were consistent with those of the previous studies.[15, 16, 18, 28] These results indicate that, regardless of the rotation number of the HPT treatment, the charge/discharge reactions of the cathodes proceed via the two-phase coexistence reaction of Cu/CuF_2.[15] Although the HPT process did not change the charge/discharge shapes of the cathode composites, it largely influenced the polarization and capacities during the charge/discharge process. As the rotation number increased from 0 (HPT-0) to 30 (HPT-30), the discharge capacity increased from 149 to 435 mA h g^{-1} with the decrease in the polarization. However, the further increase in the rotation number to 50 (HPT-50) led to a decay of the discharge capacity to 322 mA h g^{-1} accompanied by the increase in the polarization.

The discharge capacity was improved from HPT-0 to HPT-30 as the diffusion length in Cu was decreased by the reduction in the crystalline size of Cu[16] and the uniform mixing of Cu and $PbSnF_4$ formed a good ionic conduction path to Cu in the cathode composite.[18] On the other hand, the deteriorated discharge capacity from HPT-30 to HPT-50 is due to the decrease in the ionic conductivity of $PbSnF_4$ by the amorphization via excessive HPT processing. Composite electrodes with excellent electrochemical performances can be fabricated by an appropriate HPT treatment. As the HPT process can be applied to other active materials, this study provides important insights for future research on high-performance composite electrode design.

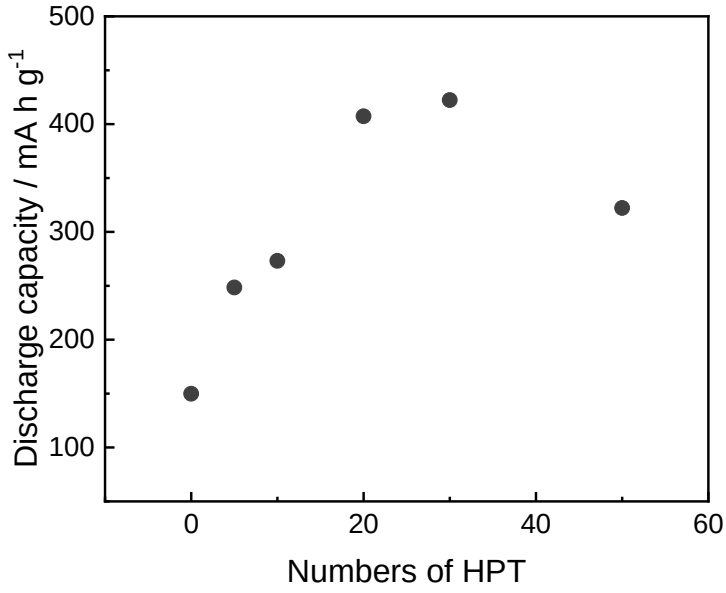

Figure 7.8. Discharge capacities of the cathode composites with different HPT rotation numbers at 0.01 C at 140 °C.

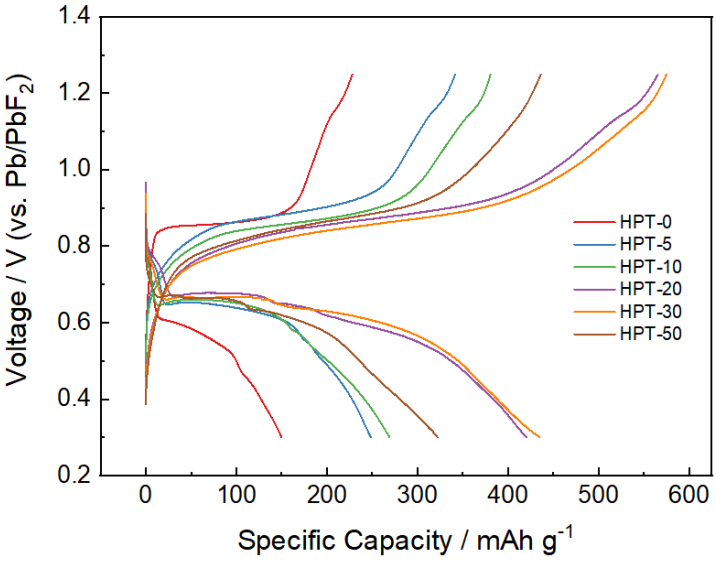

Figure 7.9 Charge/discharge curves of the cathode composites after HPT processing with different rotation numbers at 0.01 C under 140°C.

7.4 Conclusion

In this study, we applied HPT processing to prepare Cu/$PbSnF_4$/AB cathode composites for all-solid-state FIBs, and analyzed their structures and electrochemical properties. Through the HPT processing, the Cu and $PbSnF_4$ particles were refined and uniformly mixed each other in the cathode composites, resulting in a lower grain boundary resistance than that of the cathode composite without HPT. However, $PbSnF_4$ was amorphized after the excessive HPT processing, resulting in an increase in the grain boundary resistance. The cathode composite HPT-30, which underwent a suitable HPT processing, exhibited a significant discharge capacity (435 mA h g^{-1}), 2.5 times that of the cathode composite without HPT (149 mA h g^{-1}). These improvements were achieved as the diffusion length in Cu became small and the uniform mixing of Cu and $PbSnF_4$ formed a good ionic conduction path to Cu in the cathode composite via HPT processing. We believe that the HPT deformation, as a proven process for fabrication of composite electrodes, can have a propulsive role in the construction of high-energy-density all-solid-state FIBs.

Reference

1. Janek, J.; Zeier, W. G., A solid future for battery development. *Nat. Energy* **2016,** *1* (9), 16141.

2. Tarascon, J., The Li-ion battery: 25 years of exciting and enriching experiences. *Electrochem. Soc. Interface* **2016,** *25* (3), 79-83.

3. Armand, M.; Tarascon, J.-M., Building better batteries. *Nature* **2008,** *451* (7179), 652-657.

4. Delmas, C.; Braconnier, J.-J.; Fouassier, C.; Hagenmuller, P., Electrochemical intercalation of sodium in Na_xCoO_2 bronzes. *Solid State Ionics* **1981,** *3*, 165-169.

5. Jian, Z.; Luo, W.; Ji, X., Carbon electrodes for K-ion batteries. *J. Am. Chem. Soc.* **2015,** *137* (36), 11566-11569.

6. Aurbach, D.; Lu, Z.; Schechter, A.; Gofer, Y.; Gizbar, H.; Turgeman, R.; Cohen, Y.; Moshkovich, M.; Levi, E., Prototype systems for rechargeable magnesium batteries. *Nature* **2000,** *407* (6805), 724-727.

7. Xu, C.; Li, B.; Du, H.; Kang, F., Energetic zinc ion chemistry: the rechargeable zinc ion battery. *Angew. Chem. Int. Ed. Engl.* **2012,** *124* (4), 957-959.

8. Lin, M.-C.; Gong, M.; Lu, B.; Wu, Y.; Wang, D.-Y.; Guan, M.; Angell, M.; Chen, C.; Yang, J.; Hwang, B.-J., An ultrafast rechargeable aluminium-ion battery. *Nature* **2015,** *520* (7547), 324-328.

9. Zhao, X.; Zhao-Karger, Z.; Wang, D.; Fichtner, M., Metal oxychlorides as cathode materials for chloride ion batteries. *Angew. Chem. Int. Ed. Engl.* **2013,** *52* (51), 13621-4.

10. Davis, V. K.; Bates, C. M.; Omichi, K.; Savoie, B. M.; Momcilovic, N.; Xu, Q.; Wolf, W. J.; Webb, M. A.; Billings, K. J.; Chou, N. H.; Alayoglu, S.; McKenney, R. K.; Darolles, I. M.; Nair, N. G.; Hightower, A.; Rosenberg, D.; Ahmed, M.;

Brooks, C. J.; Miller, T. F., 3rd; Grubbs, R. H.; Jones, S. C., Room-temperature cycling of metal fluoride electrodes: Liquid electrolytes for high-energy fluoride ion cells. *Science* **2018,** *362* (6419), 1144-1148.

11. Anji Reddy, M.; Fichtner, M., Batteries based on fluoride shuttle. *J. Mater. Chem.* **2011,** *21* (43), 17059–17062.

12. Rongeat, C.; Anji Reddy, M.; Diemant, T.; Behm, R. J.; Fichtner, M., Development of new anode composite materials for fluoride ion batteries. *J. Mater. Chem. A* **2014,** *2* (48), 20861-20872.

13. Zhang, L.; Reddy, M. A.; Gao, P.; Diemant, T.; Jürgen Behm, R.; Fichtner, M., Study of all solid-state rechargeable fluoride ion batteries based on thin-film electrolyte. *J. Solid State Electrochem.* **2016,** *21* (5), 1243-1251.

14. Zhang, D.; Nakano, H.; Yamamoto, K.; Tanaka, K.; Yahara, T.; Imai, K.; Mori, T.; Miki, H.; Nakanishi, S.; Iba, H., Rate-determining process at electrode/electrolyte interfaces for all-solid-state fluoride-ion batteries. *ACS Appl. Mater. Interfaces* **2021,** *13* (25), 30198-30204.

15. Zhang, D.; Yamamoto, K.; Ochi, A.; Wang, Y.; Yoshinari, T.; Nakanishi, K.; Nakano, H.; Miki, H.; Nakanishi, S.; Iba, H.; Uchiyama, T.; Watanabe, T.; Amezawa, K.; Uchimoto, Y., Understanding the reaction mechanism and performances of 3*d* transition metal cathodes for all-solid-state fluoride ion batteries. *J. Mater. Chem. A* **2021,** *9* (1), 406-412.

16. Yoshinari, T.; Zhang, D.; Yamamoto, K.; Kitaguchi, Y.; Ochi, A.; akanishi, K.; Miki, H.; Nakanishi, S.; Iba, H.; Uchiyama, T.; Watanabe, T.; Matsunaga, T.; Amezawa, K.; Uchimoto, Y., Kinetic analysis and alloy designs for metal/metal fluorides toward high rate capability for all-solid-state fluoride-ion batteries. *J. Mater. Chem. A* **2021,** *9* (11), 7018-7024.

17. Zhang, D.; Yamamoto, K.; Wang, Y.; Gao, S.; Uchiyama, T.; Watanabe, T.; Takami, T.; Matsunaga, T.; Nakanishi, K.; Miki, H.; Iba, H.; Amezawa, K.; Maeda, K.;

Kageyama, H.; Uchimoto, Y., Reversible and Fast (De)fluorination of High-Capacity Cu_2O Cathode: One Step Toward Practically Applicable All-Solid-State Fluoride-Ion Battery. *Adv. Energy Mater.* **2021,** *11* (45), 2102285.

18. Zhang, D.; Yoshinari, T.; Yamamoto, K.; Kitaguchi, Y.; Ochi, A.; Nakanishi, K.; Miki, H.; Nakanishi, S.; Iba, H.; Watanabe, T.; Uchiyama, T.; Orikasa, Y.; Amezawa, K.; Uchimoto, Y., Cu–Pb Nanocomposite Cathode Material toward Room-Temperature Cycling for All-Solid-State Fluoride-Ion Batteries. *ACS Appl. Energy Mater.* **2021,** *4* (4), 3352-3357.

19. Nowroozi, M. A.; Mohammad, I.; Molaiyan, P.; Wissel, K.; Munnangi, A. R.; Clemens, O., Fluoride ion batteries – past, present, and future. *J. Mater. Chem. A* **2021,** *9* (10), 5980-6012.

20. Sabirov, I.; Kolednik, O.; Pippan, R., Homogenization of metal matrix composites by high-pressure torsion. *Metall. Mater. Trans. A* **2005,** *36* (10), 2861-2870.

21. Meng, F.; Tsuchiya, K.; Yokoyama, Y., Crystalline to amorphous transformation in Zr–Cu–Al alloys induced by high pressure torsion. *Intermetallics* **2013,** *37*, 52-58.

22. Sakai, G.; Horita, Z.; Langdon, T. G., Grain refinement and superplasticity in an aluminum alloy processed by high-pressure torsion. *Mater. Sci. Eng. A* **2005,** *393* (1-2), 344-351.

23. Vadhva, P.; Hu, J.; Johnson, M. J.; Stocker, R.; Braglia, M.; Brett, D. J.; Rettie, A. J., Electrochemical Impedance Spectroscopy for All-Solid-State Batteries: Theory, Methods and Future Outlook. *Chem. Electro. Chem.* **2021,** *8* (11), 1930-1947.

24. Asano, T.; Yubuchi, S.; Sakuda, A.; Hayashi, A.; Tatsumisago, M., Electronic and ionic conductivities of $LiNi_{1/3}Mn_{1/3}Co_{1/3}O_2$-$Li_3PS_4$ positive composite electrodes for all-solid-state lithium batteries. *J. Electrochem. Soc.* **2017,** *164* (14), A3960.

25. Grenier, A.; Porras-Gutierrez, A. G.; Body, M.; Legein, C.; Chretien, F.; Raymundo-Piñero, E.; Dollé, M.; Groult, H.; Dambournet, D., Solid fluoride electrolytes and their composite with carbon: issues and challenges for rechargeable solid state

fluoride-ion batteries. *J. Phys. Chem. C* **2017,** *121* (45), 24962-24970.

26. Irvine, J. T.; Sinclair, D. C.; West, A. R., Electroceramics: characterization by impedance spectroscopy. *Adv. Mater.* **1990,** *2* (3), 132-138.

27. Yubuchi, S.; Tsukasaki, H.; Sakuda, A.; Mori, S.; Hayashi, A.; Tatsumisago, M., Quantitative analysis of crystallinity in an argyrodite sulfide-based solid electrolyte synthesized via solution processing. *RSC Adv.* **2019,** *9* (25), 14465-14471.

28. Thieu, D. T.; Fawey, M. H.; Bhatia, H.; Diemant, T.; Chakravadhanula, V. S. K.; Behm, R. J.; Kübel, C.; Fichtner, M., CuF_2 as reversible cathode for fluoride ion batteries. *Adv. Funct. Mater.* **2017,** *27* (31), 1701051.

Chapter 8. General conclusion

All-solid-state fluoride ion batteries (FIBs) demonstrated high energy density and excellent stability, which is regarded as a promising successor to lithium-ion batteries (LIBs). Similar to the optimization process that lithium-ion batteries underwent before the concept of $LiCoO_2$|graphite was proposed, all-solid-state FIBs are currently in the materials exploration phase of pre-commercialization. Pioneers' research has provided valuable lessons, and layered metal oxyfluoride currently appears to be one of the excellent candidates for its cathode material. In this thesis, we provide a superficial to in-depth discussion of the research progress and objectives of all-solid-state FIBs based on the working principle and material selection of lithium-ion batteries, and provide a detailed account of the research we have conducted on the design of cathode materials as well as the fabrication process of the composite electrode. The structural evolution of the cathode materials during charge/discharge process and the charge compensation mechanism are analyzed in detail by electrochemical tests and advanced synchrotron radiation characterization techniques.

In Chapter 2, we conducted controlled experiments using oxyfluoride cathode together with its pure oxide analogue, and demonstrated that oxyfluoride cathodes can enhance the rate performance of all-solid-state FIBs by analyzing their electrochemical performance as well as structural evolution during fluoride ion (de)insertion. In Chapter 3, we propose the concept of using anion vacancies for fluoride ion migration, and the cycling stability of the oxyfluoride cathode is dramatically improved by constructing a three-dimensional penetrating fluoride ion diffusion pathway. In Chapter 4, the $SrFeO_2$ with an infinite layer structure is proposed for the first time based on our previous experience on oxyfluoride cathode materials, and by the in-situ generation of the oxyfluoride $SrFeO_2F_x$, we reach an energy density exceeding that of commercial lithium-ion battery cathodes with excellent cycle stability. In Chapters 5 and 6, we modified the local configuration of the $SrFeO_2$ electrode proposed in Chapter 4. By substituting Sr with Ba of larger radius and Ca of lighter weight, we further improved

its rate performance and reached the highest energy density so far, about 2.5 times that of $LiCoO_2$. Finally, we attempted a new method of constructing the composite electrode in Chapter 7. The particle size of the active material and electrolyte were drastically reduced by HPT treatment of the composition electrode, thus a composition electrode with uniform distribution was obtained; the electrochemical performance of the HPT-treated composite electrode was substantially improved compared to the untreated composite cathode. The above study shows that the layered metal oxyfluoride cathodes can achieve high energy densities, excellent cycling stability and low cost, showing great potential for future practical applications.

Acknowledgement

Time has wings, and the 5-year research life in Kyoto University is coming to the focus. Now that I can complete this doctoral thesis, there are so many people I need to express my gratitude to.

First of all, I would like to thank my supervisor Professor Yoshiharu Uchimoto, who lit the pilot light for me when I first came to Japan and was confused about the way forward, providing me with patient guidance, adequate support, as well as excellent experimental conditions during these five years. Tomoki Uchiyama and Kentaro Yamamoto, who were assistant professors at the time, gave me a lot of guidance and help in electrochemistry and synchrotron radiation experiments. Also, Professor Toshiyuki Matsunaga imparted valuable experience to me in crystal diffraction studies.

The sudden outbreak of the COVID-19 pandemic spanned my entire doctoral career, perhaps a special three years in the entire history of mankind. Everyone was physically and mentally exhausted by the long quarantine period, and I was grateful to have the company of several of seniors and juniors. Zhiwei Mu would detect my emotional loss and console me in time; Datong Zhang was my close and reliable navigator; and Zulai Cao, Yao Xiao, Chen Liu, I hope we will have the opportunity to enjoy the beautiful scenery of our country together.

I drifted away from home for 3 years without being able to reunite with my parents, and could only watch their aging faces from the screen of cell phone. Confucius remarked, “While his parents are living, a son should not go far abroad; if he does, he should let them know where he goes.” I always comforted myself with this during my years of studying abroad, and there is no way to repay them for the kindness they have given me, not to mention that a few words of thanks can express my feelings.

The following professors, staffs and fellow students are acknowledged as well: Seunghoon Yang, Yadan Ren, Saeko Otani, Prof. Koji Nakanishi (SPring-8), Prof. Tsuyoshi Takami, Prof. Yoshihiro Tsujimoto, Dr. Toshiki Watanabe, Ms. Shigeki

Shimura, Ms. Yumiko Saito, Ms. Yukiko Nakaji Ms. Aki Gakiuchi, Dr. Xiao Gao, Dr. Takahiro Yoshinari, Dr. Yingying Zhou, Dr. Chen Liu, Dr. Feilure Tuerxun, Dr. Masakuni Takahashi, Hiroyuki Nakaki, Aika Ochi, Shuo Cao, Ryusei Yamaguchi, Nozomi Kawakami, Zhuoran Li, Yuki Sakaguchi, Xian Shi, Xiaohan Mei, Aierxiding, Weijie Cao, Wenli Pan, Yunfei Gao, et al.

List of Publications

1. **Y. Wang**, K Yamamoto, Y. Tsujimoto, T. Matsunaga, D. Zhang, Z. Cao, K. Nakanishi, T. Uchiyama, H. Kageyama, and Y. Uchimoto. *Chemistry of Materials,* 2022, 34,2,609-616. (**Chapter 2**)

2. **Y. Wang**, D. Zhang, K. Yamamoto, T. Matsunaga, K. Nakanishi, T. Uchiyama, T. Watanabe, H. Miki, H. Iba, K. Maeda, H. Kageyama, Y. Uchimoto. *Chemistry of Materials*, 2022, 34, 23, 10631–10638. (**Chapter 3**)

3. **Y. Wang**, S. Lee, K. Yamamoto, T. Matsunaga, H. Miki, H. Iba, K. Tsuchiya, T. Uchiyama, T. Watanabe, T. Takami and Y. Uchimoto. Batteries. *Electrochemistry*, in press. (**Chapter 7**)

4. D. Zhang, K. Yamamoto, **Y. Wang,** S. Gao, T. Uchiyama, T. Watanabe, T. Takami, T. Matsunaga, K. Nakanishi, H. Miki, H. Iba, K. Amezawa, K. Maeda, Y. Uchimoto, *Advanced Energy Materials* 2021, 11 (45), 2102285.

5. D. Zhang, K. Yamamoto, A. Ochi, **Y. Wang,** T. Yoshinari, K. Nakanishi, H. Nakano, H. Miki, S. Nakanishi, H. Iba, T. Uchiyama, K. Amezawa, Y. Uchimoto, *Journal of Materials Chemistry A* 2021, 9 (1), 406-412.

※著作権等

Anion Substitution at Apical Sites of Ruddlesden–Popper-type Cathodes toward High Power Density for All-Solid-State Fluoride-Ion Batteries

Yanchang Wang, Kentaro Yamamoto, Yoshihiro Tsujimoto, Toshiyuki Matsunaga, Datong Zhang, Zulai Cao, Koji Nakanishi, Tomoki Uchiyama, Toshiki Watanabe, Tsuyoshi Takami, Hidenori Miki, Hideki Iba, Kazuhiko Maeda, Hiroshi Kageyama, and Yoshiharu Uchimoto

Chemistry of Materials, 2022, 34, 609-616.

doi: 10.1021/acs.chemmater.1c03189

Oxyfluoride Cathode for All-solid-state Fluoride-ion Batteries with Small Volume Change using Three-dimensional Diffusion Paths

Yanchang Wang, Tsuyoshi Takami, Zhuoran Li, Kentaro Yamamoto, Toshiyuki Matsunaga, Tomoki Uchiyama, Toshiki Watanabe, Hidenori Miki, Toshihiko Inoue, Hideki Iba, Uichiro Mizutani, Hirokazu Sato, Kazuhiko Maeda, Hiroshi Kageyama, and Yoshiharu Uchimoto

Chemistry of Materials, 2022, 34, 10631-10638.

doi: 10.1021/acs.chemmater.2c02736

Properties of Composite Electrodes for All-solid-state Fluoride-ion Secondary Batteries Processed by High-pressure Torsion

Yanchang Wang, Sangmin Lee, Kentaro Yamamoto, Toshiyuki Matsunaga, Hidenori Miki, Hideki Iba, Koichi Tsuchiya, Tomoki Uchiyama, Toshiki Watanabe, Tsuyoshi Takami, and Yoshiharu Uchimoto

Electrochemistry, in press

doi: 10.5796/electrochemistry.22-00133